Photoelectrochemical Biosensing

Design and Optimization of TiO_2 Nanomaterial-based Photoelectrochemical Biosensors

By

Sadman Sakib

B.Eng (McMaster University)

A Thesis Submitted to the School of Graduate Studies in

Partial Fulfillment of the Requirements for the Degree

Doctor of Philosophy in Engineering Physics

Doctor of Philosophy (2022) McMaster University

(Engineering Physics) Hamilton, Ontario, Canada

TITLE: Design and Optimization of TiO_2 Nanomaterial-based Photoelectrochemical Biosensors for Rapid Point-of-care Applications

AUTHOR: Sadman Sakib, B. Eng (McMaster University)

SUPERVISORS: Dr. Leyla Soleymani, Associate Professor, Department of Engineering Physics, McMaster University

Dr. Igor Zhitomirsky, Professor, Department of Materials Science and Engineering, McMaster University

PAGES: xxvi, 257

Lay Abstract

Biosensors show great promise for use in point-of-care diagnostics and health monitoring systems. Such deceives combine biorecongition with signal transduction for analyzing biologically relevant targets. Photoelectrochemical (PEC) mode of signal reading, particularly those based on TiO_2 nanomaterials, have shown great promise in delivering point-of-care biosensors that have excellent diagnostic performance. In this thesis, our goal was to develope new techniques for creating low-cost, easy-to-use and ultrasensitive photoelectrochemical biosensors. To achieve this goal, our work here can broadly be split into three objectives. Firstly, we focused on developing new material synthesis methods to improve traditional TiO_2 nanomaterials so they can be more useful in PEC biosensors. These methods involved combining TiO_2 with organic molecules known as catecholates and metal nanoparticles. This work created material systems that are able to generate high signals and more easily interface with biomolecules for improving PEC biosensor sensitivity. For the second objective, we used our newly developed enhanced TiO_2 nanomaterials as the foundation for designing various bioassays for the detection of a wide range of different biological targets such as DNA, RNA, proteins and bacteria. This served to demonstrate the robustness of PEC signal reading as a tool for various markers of diseases. Despite PEC biosensors being a powerful tool in healthcare, they have seen very little commercial breakthrough, which can primarily be attributed to needing bulky benchtop instruments and light sources for signal reading. For the last objective, we worked on designing a handheld smartphone-operated signal-reader for PEC biosensing with its own built-in light source.

Abstract

Recently, there has been a shift in the global healthcare paradigm, which is prioritizing a more patient-centric approach causing an increase in the demand for rapid and point-of-care (PoC) biomolecular detection. Electrochemical (EC) signal transduction has been used to great effect to meet some of this demand by constructing biosensors with high sensitivity and low limit-of-detection (LOD). However, signal generation in EC biosensors requires input bias potentials to activate electrochemical redox reactions. This means EC systems are inherently built-in with high background noise that limits the performance of biosensors. Biosensors with photoelectrochemical (PEC) signal transduction have recently shown great promise in being able to deliver biomolecular detection on par with, if not better than, EC biosensors. PEC biosensing directly improves upon EC signal transduction by combining EC signal readout with optical excitation as the bias input, and generally being able to achieve similar performance with simpler bioassay designs. In this scheme, the input and output of the signal transduction are decoupled from each other, significantly reducing background signal in biosensors to enhance their sensitivity. Despite being highly effective, PEC biosensors have yet to find commercial breakthrough as they have so far only shown quantitative analysis on a limited set of biomarkers and have not shown to be PoC-capable. In this thesis, we developed new strategies to improve PEC signal transduction so that it could be applied to build robust ultrasensitive PoC biosensors with high dynamic range, simple operation, and low LOD for detecting a wide variety of different disease biomarkers.

The most popular photoactive materials used in the fabrication of PEC biosensors are TiO_2 nanomaterials on account of their availability, chemical stability, high catalytic efficiency, tunable morphology, and ideal band energy levels for driving useful EC reactions. However, unmodified TiO_2 suffers from several drawbacks that limit its photocurrent generation efficiency, such as poor visible range absorbance due its wide bandgap and fast charge carrier recombination. Alongside the additional difficulty of biofunctionalization, PEC biosensors fabricated from TiO_2 nanomaterials are limited in their bioanalytic performance. In order to make improvements on PEC biosensors, we modified the surface of TiO_2 nanomaterials by chelating them with catecholate molecules. The surface modification with catecholates formed charge transfer complexes on TiO_2, which resulted in enhanced photoexcitation due to enhanced electron injection attributable to intermolecular orbital excitations in the catecholate molecules. The catecholate ligands also added improved colloidal stability and additional functional groups that aided with biofunctionalization. This resulted in multifunctional TiO_2 nanoparticles with improved photocurrent signal generation and enhanced visible range photoabsorption. We took this one step further by taking advantage of the high binding affinity of catecholates on TiO_2 surfaces to create novel synthesis methods that created high surface area nanostructures. Photoelectrodes fabricated from these new TiO_2 nanostructures had nanoporous morphology and were able to capture biomolecules more efficiently. Using our novel TiO_2 nanomaterials, we fabricated signal-off biosensors that were able to detect DNA biomarkers and IL-6 protein (cancer and inflammatory biomarker) in urine with an LOD of 1.38 pM and 3.6 pg mL^{-1}, respectively.

We further explored hybrid semiconductor structures by combining TiO_2 nanomaterials with other materials such semiconductors with different bandgaps or plasmonic metal nanoparticles

(NP). Using the aforementioned catechol-assisted synthesis techniques, we were able to produce different morphologies of TiO_2 nanomaterials with distinct phases: anatase TiO_2 nanorod assemblies and rutile TiO_2 NP. The two different TiO_2 nanomaterials have different bandgaps and can be used to form semiconductor heterostructures. By combining rutile TiO_2 NPs with DNAzymes, a type of synthetic functional nucleic acid, we created a photoactive molecular switch that worked by making and breaking heterostructures between the two TiO_2 nanomaterials. We used DNAzymes specific to *E. coli* bacteria to develop a highly sensitive signal-on bacterial detection platform that was able to detect *E. coli* in lake water samples with an LOD of 18 CFU mL^{-1}. Using catecholate-assisted photoreduction synthesis, we developed an efficient and novel method for decorating TiO_2 NP with silver (Ag) NP. The resultant nanomaterial featured TiO_2 NP surfaces modified with Hematoxylin (HTX) dyes and covered with sub-nanometer sized silver NP. The band structure of TiO_2/HTX/Ag NP hybrid material involved high energy electron generation through decay of surface plasmons in the Ag NP and then enhancing the photoelectron injection process between HTX and TiO_2. This significantly enhances the photoexcitation and photoabsorbtion, resulting in the material with the highest photocurrent generation as presented in this thesis. By taking advantage of thiol-metal bonds, we used the TiO_2/HTX/Ag NP material system in the fabrication of a highly sensitive signal-off microRNA (prostate cancer biomarker) sensor with an LOD of 172 fM in urine.

Special attention was paid to the design of PEC bioassays in this work so that they are miniaturized and easy to use, and thus suitable for PoC applications. Because PEC signal transduction generates ultrahigh signals compared to other transduction methods, it allows bioassay designs to remain simple without sacrificing performance. This allowed us to create bioassays with very few operational steps, that excel in reliability and ease-of-use. To further

improve PoC capability, we explored multiplexing with the biosensor made from TiO_2/HTX/Ag NP. Here we were able to demonstrate multiplexing with PEC signal transduction for the first time. Another major barrier to PEC biosensors becoming widespread is the requirement of large benchtop instrumentation such as potentiostats and light sources. To address this challenge, we designed a portable smartphone-interfacing potentiostat with a built-in LED light source to support PEC biosensing. This device, named the PECsense was as versatile as any commercial potentiostats, having features such as adjustable recording periods, variable illumination periods, automatic data processing and being able to record both anodic and cathodic photocurrents. The PECsense was demonstrated to be used successfully as a signal reader in a PEC DNA detection assay.

Ultimately, we designed several ultrasensitive PEC biosensors used for the detection of four different diagnostic biomarkers. Combined with the exploration of miniaturized design, multiplexing and portable signal-reading, our designed PEC biosensors were made PoC-capable. The work in this thesis presented innovations in areas of nanotechnology, material synthesis, solid-state physics, biotechnology and embedded systems for the advancement of biomolecular detection and PoC diagnostics.

Acknowledgements

First and foremost, I'd like to thank both of my supervisors, Dr. Leyla Soleymani and Dr. Igor Zhitomirsky for their constant support – both in research and otherwise – throughout my thesis. I am thankful to have supervisors who have consistently provided invaluable insight into my work, pushed me to learn beyond what is necessary, and have advocated for success at every opportunity. Thank you for willing to put up with my wild ideas and guiding me to make them achievable. I am very proud of the work we have done together over the years, and I hope to continue to do more innovative research together in the future.

In would also like to thank members of my supervisory committee, Dr. Katheryn Grandfield and Dr. Adrian Kitai for always providing me with thoughtful feedback while continuing to inspire me in my work. Discussions with you have yielded many innovative experiments and design ideas that have strengthened our research.

Over the years, I have had the pleasure of working with many brilliant graduate and post-doctoral researchers from the Soleymani Group and the Zhitomirsky Group. I greatly value the close collaboration I shared with Fatemeh Bahkshandeh, Alexander Scott, Rodrick Maclachlan, Enas Osman, Ryan Poon, Wenjuan Yang, Wenyu Liang, Aseeb Syed, Farhaan Kanji, Dr. Sudip Saha, Dr. Richa Pandey, and Dr. Amin Hosseini. All of my lab mates have taught me a great number of things during the course of my graduate studies. Their influence has positively impacted my research in ways both big and small. Your company and wisdom have made it an absolute joy to be a researcher.

A very special thank you goes out to my parents and sister. Despite many hardships, you have always provided me with unending support. Your belief in me has kept me going, not to mention the practical supports you have provided like shuttling food over to my apartment, helping me practice presentations, and making sure I wasn't getting sick. Visiting you guys has always been the exact thing I need to replenish my mental batteries. I look forward to lounging with you guys after my thesis and filling your heads with nerdy science stuff.

Last, and definitely not least, I'd like to thank my partner and best friend, Emily Laevens. Thank you for going through this journey alongside me and for your unwavering support. There is an entire thesis' worth of things I could write thanking you. But, in short I am extremely proud of us and can't wait for what comes next.

Finally, I would like to acknowledge McMaster University for their financial support.

Table of Contents

List of Figures

List of Tables

List of Abbreviations

3D	Three-dimensional
AA	Ascorbic Acid
ADC	Analog-to-Digital Converter
API	Application Programming Interface
BSA	Bovine Serum Albumin
CA	Caffeic Acid
CApm	Control Amplifier
CB	Conduction Band
CE	Counter Electrode
CFU	Colony-forming Unit
CM	Carbonaceous material
CNT	Carbon Nanotubes
CT	Charge Transfer
DAC	Digital-to-Analog Converter
DFT	Density Functional Theory
DHB	3,4-dihydroxybenzoic acid
DHBA	3,4-Dihydroxybenzaldehyde
DHPL	3,4-dihydroxyphenylacetic acid
DNA	Deoxyribonucleic Acid
DOPA	3,4-dihydroxy-L-phenylalanine
dsDNA	Double-stranded DNA
DSSC	Dye-Sensitized Solar Cell
EC	Electrochemistry
EDC	1-ethyl-3-(3-dimethylaminopropyl)carbodiimide hydrochloride
EDS	Energy-Dispersive X-Ray Spectroscopy
EELS	Electron Energy Loss Spectroscopy
EIS	Electrochemical Impedance Spectroscopy

ELISA	Enzyme-linked Immunosorbant Assay
EWG	Electron-Withdrawing Group
FTIR	Fourier Transform Infrared Spectroscopy
HAADF	High-Angle Annular Dark Field
HOMO	Highest Occupied Molecular Orbital
HTX	Hematoxylin
IL-6	Interleukin-6
IPCE	Incident Photon-to-Current Conversion Efficiency
IPS	In-situ and Post-situ
IS	In-situ
ITO	Indium-Tin Oxide
LED	Light Emitting Diode
LOB	Limit of Blank
LOD	Limit of Detection
LPF	Low-pass Filter
LSPR	Localized Surface Plasmon Resonance
LUMO	Lowest Unoccupied Molecular Orbital
MES	2-(N-morpholino)ethanesulfonic acid
miRNA	MicroRNA
ML	Machine Learning
NAAT	Nucleic Acid Amplification Test
NC	Non-complimentary
NHE	Normal Hydrogen Electrode
NHS	N-hydroxysulfosuccinimide
NMR	Nuclear Magnetic Resonance
NP	Nanoparticle
NR	Nanorod
PBS	Phosphate Buffered Saline
PCB	Printed Circuit Board
PDA	Polydopamine

PEC	Photoelectrochemistry
PET	Poly(ethylene terephthalate)
PoC	Point-of-Care
PS	Post-situ
PWM	Pulse-width Modulation
QD	Quantum Dots
RE	Reference Electrode
RNA	Ribonucleic acid
SEM	Scanning Electron Microscopy
STEM	Scanning Transmission Electron Microscopy
ssDNA	Single-stranded DNA
TEM	Transmission Electron Microscopy
TGS	Thermogravimetric Analysis
THB	2,3,4-trihydroxybenzoic acid
THBA	2,3,4-trihydroxybenzaldehyde
TIA	Transimpedance Amplifier
UV	Ultraviolet
UV-vis	Ultraviolet/Visible
VB	Valence Band
VF	Voltage Follower
WE	Working Electrode
WHO	World Health Organization
XRD	X-Ray Diffraction

Declaration of Academic Achievement

This dissertaion was written to fulfill the requirements of the doctoral degree in the department of Engineering Physics at McMaster University. The work described here was performed between the time period of May 2017 to August 2022.

The majority of the work presented in this written document including conceptualization, design, methodology, experimental work, data analysis, data visualization, literature review and writing was done by the author of this thesis, in consultations with the supervisors Dr. Leyla Soleymani and Dr. Igor Zhitomirsky, with the exception to the following:

Chapter 2: Fatemeh Bahkshandeh contributed to writing the manuscript equally.

Chapter 3: Dr. Richa Pandey illustrated Figure 2-1 and helped with the calculation of the LOD.

Chapter 4: Dr. Amin Hosseini assisted with the conceptualization of the PEC IL-6 Immunosensor.

Chapter 5: Dr. Zijie Zhang performed ligation and purification of the DNAzyme strands. Enas Osman partially illustrated Figure 5-3. Farhaan Kanji tested the lake water media for bacterial contamination. Fatemeh Bahkshandeh assisted with the preparation of photoelectrode substrates.

Chapter 7: Alexander Scott contributed to writing the manuscript equally. Alexander Scott also conceptualized the design for the initial portable electrochemical reader on which the PECsense was adapted from.

Chapter 1

Introduction

Preface:

This first chapter serves as the introduction to the key ideas, motivations, and objectives of this thesis. Here we will provide technical background on point-of-care biosensing and discuss the projected market growth of this technology, in addition to the challenges facing its development and deployment in the field of healthcare. We will review existing techniques for biosensing in the different signal transduction methods commonly utilized. Then we will shift our focus to the main subject of this thesis – photoelectrochemical biosensing. We will discuss the basics of photoelectrochemistry and justify its use as a signal transduction method in point-of-care biosensing by highlighting its advantages over more traditional methods. Finally, this chapter will discuss the objectives of this thesis and outline how the thesis is organized.

1.1 Background

1.1.1 Point-of-care Biosensing – Overview, Technical Challenges and Future Needs

The World Health Organization (WHO) estimates that non-communicable diseases such a cardiovascular diseases, respiratory illnesses, cancer, and diabetes kill around 41 million people each year.[17,18] The prevalence of non-communicable diseases as a result of chronic health conditions is expected to increase globally due to factors such as aging populations, rapid unplanned urbanization, and globalization of unhealthy lifestyles.[17,19–22] Globally, this has a significant economic impact on both governments and households in increased burden on healthcare resources and increases cost of treatment.[18,21,22] It is interesting to note that while chronic diseases remain the leading cause of mortality in high-income countries, non-communicable diseases (including respiratory infections, water-borne illnesses, mosquito-bourse infections, and human immunodeficiency virus acquired immunodeficiency syndrome (HIV/AIDS)) account for higher mortality in low-income countries.[18,20] In the last few decades, detection of communicable diseases resulting from viral or bacterial pathogens has become a key public safety priority for the prevention of outbreaks that represent a high risk for disruption of healthcare systems and disastrous socio-economic impacts.[23,24] Environmental pathogenic contamination leading to water-borne and food-borne diseases have become an important public health problem, resulting in significant global rates of morbidity and mortality.[25–27] This problem is expected to be further exacerbated by climate change-induced trends such as increasing temperatures, more frequent rainfall, rising sea level leading to increased dispersal and proliferation of pathogens in the environment.[27–30] Rapid urbanization and destruction of natural habitats are increasing the risk of zoonotic transmission of infectious diseases.[22] In the last decade, we have seen the emergence of several deadly zoonotic diseases such as swine flu,

Ebola, Zika, Middle East respiratory syndrome (MERS), coronavirus disease 2019 (COVID-19) and Monkeypox.[19,31–33] Furthermore, the overuse of antibiotics is contributing to the emergence of multidrug resistant pathogens, which severely increases the difficulty of treatment.[23,34,35] The WHO closely monitors and a publishes a list of epidemic-potential diseases requiring priority research attention for this reason.[32,33,36]

The global rise in non-communicable and communicable diseases is best combatted through preventative healthcare.[37,38] Driven by this mandate, there has been a growing interest towards advancements in the field of biosensing and in the development of point-of-care (PoC) readout instruments.[37,39,40] Biosensors are chemical sensing devices capable of detecting specific types of biochemical parameters such as protein interaction, enzyme activity, bioanalyte concentration, DNA damage, or cell/tissue detection. The "bio" aspect refers to specific biorecognition elements in the biosensors that recognize specific bioanalytes, whereas the "sensor" aspect refers to a transducer which is responsible for converting the recognition event into a measurable signal.[41,42] The advancements in the field of biosensing hold great promise for revolutionizing healthcare through early diagnosis, disease prevention and patient self-management.[39,40,43] In order to deliver on this promise, we have to transition away from our standard for disease diagnostics, which involve laboratory-based testing where samples are sent to a centralized location for analysis and shift towards PoC testing.[39] The practice of PoC testing involves performing diagnostic or prognostic tests near a patient with the promise of rapid results. PoC-capable devices aim to provide rapid diagnostic information outside of a typical laboratory setting and prove to be substantially more affordable and faster than gold standard techniques.[39,44] Currently, there is a great deal of research taking place on PoC biosensors in the area of medical diagnostics.[39,40,44] The major advantages of PoC biosensors over conventional

diagnostic methods include: fast sample-to-result times, increased capacity for preventative healthcare, being able to rapidly control outbreaks, reduced cost of testing, and being able to provide remote and low-income communities with high quality health management capabilities.[39,40,43,44]

Due to rapid advances in the field of PoC biosensing and the global shift towards patient-centric medical care,[37] proper guidelines for PoC biosensing must be established. The WHO has established one such guideline known as ASSURED, which stands for Affordable, Sensitive, Specific, User-friendly, Rapid and robust, Equipment-free, and Deliverable to end-users.[45,46] The challenge inherent in developing biosensors that meet this criteria is that it is difficult to achieve laboratory-quality test results, while also delivering a device with a simple miniaturized design (i.e. in terms of chemical reactions needed for biorecognition and data processing) that is not operationally complex thus requiring minimal training.[47,48]

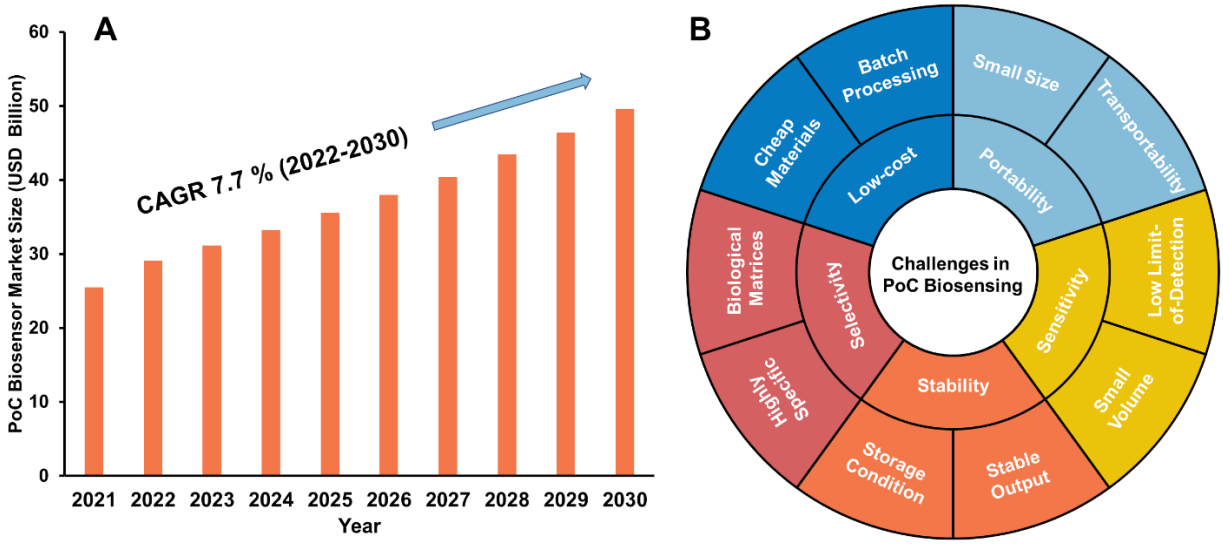

Figure 1-1. A) Projected Market share for PoC diagnostic biosensors by the year 2030. The market size expected to surpass US$ 49.6 billion and have an expanding growth at a CAGR of 7.7 %. Data collected from various reports of market research.[1–3] B) Technical challenges associated with the design of PoC Biosensing.

In spite of a growing market size and clinical interest (**Figure 1-1A**), there is a very small selection of PoC biosensors available on the market. These include, electrochemical-based systems such as blood glucose monitors, and blood gas analyzers,[49] real time PCR systems for pathogen-based gene detectors,[50] and colorimetry-based systems for pregnancy tests, cancer tests, and COVID-19 tests.[51–53] The design criteria of PoC biosensors that require them to be low cost, portable, stable, highly sensitive, and highly specific are difficult to implement and are major obstacles that slow their transition from research labs into the hands of patients (**Figure 1-1B**).[54] Keeping costs low is a challenging endeavor since biosensors require a variety of different materials, reagents and mechanical parts that need to be integrated into a single device.[54] Many biosensors are designed as single-use devices which adds to their cost.[54] The bioreagents commonly used in biosensors are unstable if there are large temperature fluctuations and often need refrigeration. These elements vary depending on the type of biosensor, and their cost of manufacturing further drives up the cost. The fabrication process for the biosensors and their components also needs to be suitable for batch processing. Paper or plastic-based devices are commonly used in lieu of PoC biosensors due to their suitability for batch processing.[55,56]

The user-free, equipment-free, and deliverable to end-users criteria of the ASSURED guideline require that PoC biosensors are designed in a way such that all the stages in their operation from sample collection to data processing need to be seamlessly integrated and automated. Ideally minimal training and intervention is required on the part of the end-users. Therefore, PoC biosensors need to have an accessible process workflow that simplifies tasks like sample collection, sample processing and diagnostic evaluation. [54,57] For example, sample purification stages like plasma separation usually require the use of centrifuges and pipettes, equipment normally unavailable outside of laboratories.[54,58] Microfluidics and lateral flow based designs

aim to address some of these challenges.[51,59] However best scenarios would involve designs that can achieve high performance with simple assays with fewer stages. Other challenges in this category also include safe disposal of biohazardous samples.[54,60] Furthermore, it is desirable for biosensors to be portable, which allow these devices to be properly usable in point-of-care settings, especially in remote areas where medical testing is hard to access. Here, research is focused on portable signal-readers which address the data acquisition and processing aspects of biosensors.[61–63]

In order to be clinically useful, PoC biosensors must achieve high sensitivity. Different diseases have different biomarker concentration thresholds for detection and diagnostics, and early detection and preventative healthcare is highly reliant on PoC biosensors having a low limit-of-detection (LOD).[41,64,65] Generally, when LOD for existing technology is improved, it opens up opportunities for new insight into disease prevention and progression.[66] Additionally, special attention must be directed towards the minimum sample volumes required to achieve good sensitivity in biosensors, as it directly impacts their portability, ease-of-use and cost. But too low of a volume is also likely to introduce large errors in the quantification of biomarkers.[61,67] Designing biosensors requires careful balancing of sensitivity, sample volume and reproducibility.[68] Automated sample processing techniques such as using absorption pads and microfluidics can be used to solve this issue but introduce a higher probability of sample contamination.[68,69]

Achieving high specificity is a major concern for biosensors. It is crucial that deployed biosensors only generate signal in response to the specific target biomarkers they were designed to look for. This can be particularly difficult as practical applications of these devices require them to analyze complex biological matrices such as urine, saliva or blood. Selectivity of a

biosensor is defined as the degree to which a bioanalyte of interest can be detected without interference from other biomolecules present in the clinical sample being analyzed. Non-specific adsorption due to bio-fouling of proteins is a major challenge in all biological samples.[70,71] Various surface modification techniques are employed to reduce the effect of non-specific absorption to maintain high specificity and avoid false positive or false negative outcomes.[72]

It is also important that the bioreceptors and reagents used in biosensors are thermally and chemically stable with a long shelf-life. Many bioreceptors (e.g. antibodies, DNA or enzymes) and many reagents (e.g. L-ascorbic acid) are unstable in room temperature or in solution form. This can lead to inaccurate testing and irreproducibility at the user-end, therefore care must be taken when selecting the chemical and biomolecular components for a bioassay.[73] Currently, to circumvent these issues, commercial devices ship these components in sealed foil pouches, desiccated chamber or temperature-controlled containers. These measures also further add to the cost of biosensors.[54,69] Moreover, since biosensors deal with very small concentrations of biomolecules and reagents, reaction kinetics play a major role in signal generation,[74,75] and therefore conditions must also be controlled during the operation of biosensors.

1.1.2 Biorecognition and Signal Transduction in Biosensing

Biosensors can generally be separated into two distinct components: the biorecognition element and the transducer element (**Figure 1-2**). The biorecognition element are biomolecules which interact with a specific target analyte by immobilizing it, going through conformational changes or catalyzing a chemical reaction.[41,42,60,64] Examples of biorecognition elements include nucleic acids, antibodies, enzymes, or cells. It is important to choose biorecognition elements with a high degree of specificity so that they only interact with the target analyte of interes, thereby

minimizing false positive reults.[41,42,60] The transducer element is responsible for converting the biorecognition event into a measurable signal. The signals produced by the transducer element can be either threshold-based or proportional to the target analyte. The output signal from the transducer usually requires some additional processing (e.g. filtering, amplification, analog-to-digital conversion) for quantitative analysis. [41,42,60] The choice of biorecognition elements is largely dependent on the analyte to be detected. The choice of transducer element is not subject to such constraints, and by exploring different options, designers of biosensors have great flexibility to optimize various requirements of biosensors such as cost, reliability, sensitivity, dynamic range detection threshold, and limit-of-detection.[76] It is crucial to recognize the advantages and disadvantages of different biosensor transduction techniques, while also keeping in mind that these techniques are undergoing constant optimization and innovations to overcome their limits. Commonly used transduction methods are colorimetric, optical, thermal, piezoelectric, magnetic, electrochemical and photoelectrochemical (PEC) techniques.

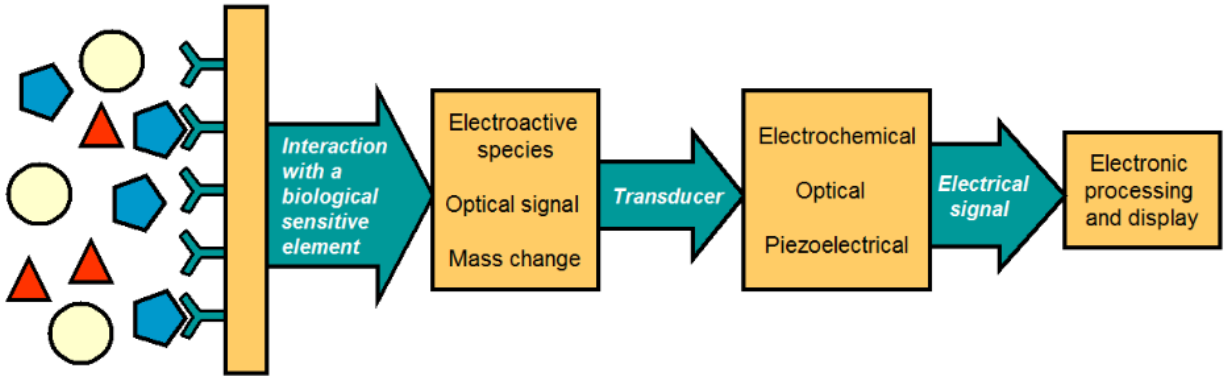

Figure 1-2. Scheme of the basic integrated units that conform a biosensor. Reproduced with permission.[4] Copyright 2012, IntechOpen.

Colorimetric biosensors rely on color changes to indicate target detection. Most designs aim for

these color changes to be detectable to by the naked eye, eliminating the need for costly instrumentation.[77,78] Most designs that make use of colorimetric transduction tend to be paper-based lateral flow assays, which excel as threshold-based indicator type tests.[51,77,78] The biorecognition elements are generally cross-linked within porous polymer or paper membranes. These types of devices make excellent PoC devices as they are low-cost, simple to operate and require minimal instrumentation. However, colorimetric biosensors have poor sensitivity and are unsuitable for quantitative analysis making them unsuitable for disease monitoring and accurate prognosis.[77,79]

Optical signal transduction can be viewed as a more active form of colorimetry, where photons are emitted from dyes or other photoactive materials in response to target biomolecule interaction.[80,81] Usually in the optical transduction scheme, biorecognition elements are modified or labelled with various photoactive materials that endow them with special optical characteristics such as fluorescence, phosphorescence, chemiluminescence, and change in absorbance or reflectance.[80–82] Target analyte interaction brings about chemical or conformational changes that activate these new optical properties, which can detected. Unlike colorimetry, optical transduction requires the use of complex instrumentation to perform.[80,81] While optical transduction is significantly more sensitive than colorimetry, it also hard to achieve testing that is both inexpensive and miniaturized. Additionally, degradation of modified biorecognition elements due to photobleaching is a major obstacle to achieving stable and reliable devices.[80,81]

Thermal transduction relies on measuring changes in temperature to detect the presence of target bioanalytes.[83,84] A typical thermal biosensing device uses enzymes as its biorecognition element, which can catalyze either an exothermic or an endothermic biochemical reaction to produce the

temperature change.[83,84] Thermal biosensors can operate non-invasively and are very well suited for continuous monitoring. However, these devices demonstrate poor specificity, due to non-specific external heating/cooling effects. Interfering reactions can cause enthalpy changes in the system and affect the temperature measurements.[83,84]

Magnetic signal transduction involves the use of magnetic NPs, which are usually conjugated with the biorecognition elements to create magnetic probes. Typically, in these setups, the magnetic probes possess a high binding affinity towards the target biomolecules so as to immobilize them onto the magnetic NP. The magnetic NPs can be manipulated with the help of external magnetic fields and microfluidics to set up the detection scheme. [85,86] Since most biological samples are not magnetic, this type of biosensor suffers only limited effects from background noise, making it superior to most optical biosensors. [85,86] Although magnetic biosensors can be easy to operate, they require additional instruments for magnetic field manipulation which limit their portability and make them expensive for a PoC device. [85,86]

Piezoelectric signal transduction makes use of piezoelectric crystals which change their electrical oscillation frequency based on mass loading.[87–89] The typical setup involves quartz crystal microbalances coated with a gold electrode, which is used to due to its proven reliability and availability.[87–89] This transduction mechanism does not depend on any additional reagents or labels as it is primarily a mass change-based biosensor. [87–89] Piezoelectric biosensors are generally inexpensive, simple and able to provide fast responses. However, the piezoelectric crystals used can be very unstable to external conditions such as temperature changes or humidity, making them unsuited long-term stability. [87–89]

Electrochemical transduction converts biorecognition into a measurable electrical signal by having the target analyte participate in or eaffect the rate of an electrochemical redox reaction.

Various electrochemical techniques such as amperometry, potentiometry or electrochemical impedance spectroscopy can be used for quantitative analysis for target bioanalytes.[49,90,91] The most commonly used electrochemical PoC biosensor is the glucometer, which utilizes screen printed electrodes modified with enzyme biorecognition elements as a test strip, and a pocket sized potentiostat as the signal reader.[92] Another commercially available PoC biosensor that utilizes electrochemical transduction is the iSTAT blood analyzer, which was designed to analyze various biomarkers in blood. Electrochemical transduction has many advantages such as low-cost, high sensitivity, high specificity, easy miniaturization and being able to work with small sample volumes.[93] This transduction mechanism usually requires bias voltage, which produces a high background signal and thus limiting the performance of electrochemical biosensors.[49,90,94]

PEC signal transduction is very similar to electrochemical signal transduction, relying on electrochemical redox reactions to convert biorecognition into electrical signals. However, the key difference between the two methods is that the source of bias for PEC is external light illumination rather than applied voltage.[64,95–97] This effectively decouples the input signal and output signal of the PEC system, resulting in significantly lower background signal.[64,94] PEC signal transduction has all the benefits of electrochemistry while minimizing its greatest disadvantage. Furthermore, PEC transduction can typically generate significantly higher signals than electrochemical transduction resulting in biosensors that can be much more operationally simple while achieving the same level of performance as their electrochemical counterparts.[64,94,98] Although no PEC biosensor has been commercialized yet, this transduction method holds great promise to meet the demands of the new PoC diagnostics paradigm.

1.1.3 Basics of Photoelectrochemistry

Photoelectrochemical (PEC) cells are a subtype of solar cells based on semiconductor-electrolyte interfaces. The basic three-electrode PEC cell consists of a working electrode (WE), a reference electrode (RE), and a counter electrode (CE) (**Figure 1-3A**).[5,95,99] A common choice of reference electrode for PEC biosensing applications is Ag/AgCl which has an electrochemical potential of 0.197 V *vs.* normal hydrogen electrode (NHE).[64,100] The voltage in the PEC cell is measured with respect to the RE, and the current in the PEC cell is measured with respect to the CE. The final element of the PEC cell is the photoexcitation source, which is often an external light source. Depending on the application, the light source can consist of a wide range of frequencies (e.g. Xenon arc lamps for simulating solar spectra) or single frequencies (e.g. lasers).[5,64,95]

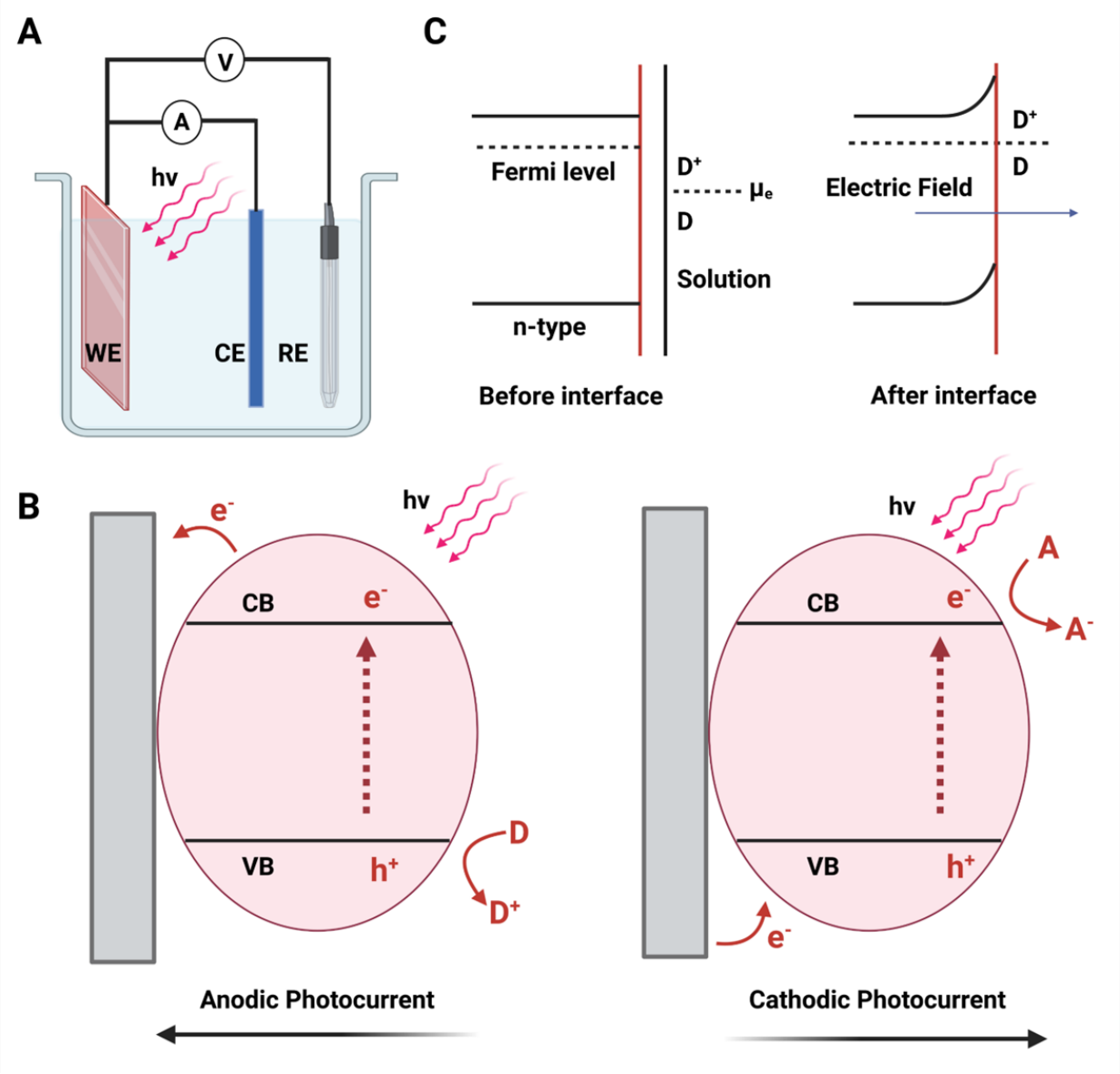

Figure 1-3. A) Setup of the standard three-electrode PEC cell. B) Generation of anodic and cathodic photocurrent through electron-hole pair charge separation after photoexcitation. C) Example of the formation of space charge region in the semiconductor/electrolyte interface shows using an n-type semiconductor and D/D^+ redox couple.

The WE are fabricated from photoactive semiconductor material (*S*) which generate electron-hole pairs when then absorb photons with energies ($h\nu$) higher than its bandgap energy (E_g). After photo absorption, *S* will transition to an excited state, S^*. In order to return to a more stable

energy state, electrone-hole pair recombination usually follows. However, the semiconductor/electrolyte interface proves a pathway for separation of the charge carriers before the recombination process (**Figure 1-3B**). The electrolyte species consists of either electron donor species (*D*) or acceptor species (*A*). The electron donor neutralizes the hole at the VB, and is oxidized from *D* to D^+, resulting in the generation of an anodic photocurrent. Alternatively, an electron acceptor neutralizes the electron from the CB, and is reduced from *A* to A^-, resulting in a cathodic photocurrent. Through this process, PEC cells convert light energy into chemical energy and the light source here acts as an electron pump.[95–97,100]

$$S + h\nu \rightarrow S^*$$

$$S^* + A \rightarrow S^+ + A^-$$

$$S^* + D \rightarrow S^- + D^+$$

The reaction between S^+ and A^- or S^- and D^+ is usually spontaneous, and therefore to utilize the converted chemical energy from PEC cells, these electrolyte species must be separated first. The semiconductor/electrolyte interface provides a mechanism for this separation through its intrinsic electric field (**Figure 1-3C**). [95,101] Semiconductors usually have a narrow bandgap and their CBs are nearly vacant while the VB is mostly full. The immersion of a bulk piece of semiconductor results in the formation of a solid/liquid junction. In equilibrium and without any external excitation, the electrochemical potential (μ_e) of the semiconductor and the electrolyte must attain equilibrium.[102] It should be noted that μ_e the of a semiconductor is equal to its Fermi level (E_F). The Fermi level is typically expressed with respect to vacuum energy level in contrast to electrochemical potentials which are expressed with respect to NHE. The μ_e of the NHE is equal to -4.5±0.1 eV.[102]

Let us consider a junction between an n-type semiconductor and an electrolyte solution containing donor species, a common scenario for PEC biosensing.[64,96,97] Charge transfer occurs at this interface due to the difference in electrochemical potential between the semiconductor and the electrolyte. In a scenario like this, the μ_e will be lower than the semiconductor Fermi level, and electrons will flow from the semiconductor to the electrolyte until Fermi level equilibrium is achieved. This results in upward band bending at this interface, which creates a charge depletion layer. The depletion layer has a built-in electric field that points from the semiconductor to the electrolyte.[102]This electric field can act as a charge separator when electron-hole pairs are formed after absorption of photons. The direction of the electric friend forces electrons to flow away from the electrolyte while the holes move towards the electrolyte.[102]

1.1.4 Materials used in PEC Biosensors

In PEC biosensors, a wide variety of different photoactive materials serve as the building blocks for their transducer elements. The photoactive materials can serve as the base photoelectrode material or as signaling labels/reporters.[64,94] Biorecognition elements of PEC biosensors are usually immobilized onto the photoelectrode or conjugated with these signaling labels/reporters. Photoactive materials used in PEC biosensing must be carefully chosen based on their electronic and optical properties such as incident photon-to-current conversion efficiency (IPCE), optical absorption spectra, charge carrier mobility, band edge levels, and response time.[64,94] The electronic and optical properties of the chosen material must make it suitable for generating charge carriers with sufficient energy levels (indicated by the band structure of the material) to drive desired electrochemical redox reactions.[94,96,97,103] In order to design PEC biosensors with high sensitivity, high dynamic range and low LOD, the photoactive material used to fabricate the biosensor must be able to generate high photocurrent and photovoltage signal. This is

accomplished by maximizing the IPCE and having a wide optional absorption band for the photoactive material.[94,96,97] Having a high surface area-to-volume ratio is critical to achieving high performance in biosensors, and therefore materials used in biosensors, including PEC biosensors, tend to be nanoscale materials.[104,105] Fine tuning the size and shape of nanoscale photoactive materials is also important for enhancing the PEC performance of the biosensor as structure tenability on the nanoscale changes the band structure of materials. Resistance nanoscale to photodegradation is also important as it allows PEC biosensors to be stable and effective for a longer period of time.[106–108] Lastly, it is critical that photoactive materials be easily biofunctionalizable in order to interface with the biorecognition elements present in biosensors. Usually this requires being able to react and bind to various terminal functional groups found in biomolecules such as thiol, carboxyl, amine, hydroxyl and aldehyde groups.[109–111] There are three major classes of photoactive materials that are used in PEC biosensors: inorganic semiconductors, organic semiconductors and hybrid semiconductors. These are discussed below.

Inorganic semiconductors are made from oxides or chalcogenides of solid-state structures of group III, IV, and V elements, and exclude carbonaceous materials (**Figure 1-4**). Generally, in transducers made from this type of materials, absorption of photons with energies higher than the bandgap energy leads to excitation of electron from the VB to the CB.[95,112] Here photoexcitation leads to electron-hole pair generation, which facilitates electrochemical redox reactions to generate a photocurrent in the context of PEC biosensors (see section 1.3). Mobile charge carriers in the semiconductor traverse the bulk of the electrode while the minority charge carriers take part in the redox reactions at the semiconductor/electrolyte interface. Therefore, n-type semiconductors produce anodic photocurrent and p-type semiconductors produce cathodic

photocurrent.[95–97] Inorganic semiconductors generally exhibit higher stability under mechanical, electrical and chemical stress compared to other materials.[112,113] There exists a variety of cost-effective synthesis methods for precision fabrication of nanoscale inorganic semiconductors such as hydrothermal synthesis, solvothermal synthesis, chemical vapor deposition, lithography, and sol-gel process, to name a few.[113,114] Inorganic semiconductors usually require lower bias voltages due to their higher charge mobility and charge-carrier separation efficiency and exhibit faster response time in the generation of charge carriers upon excitation.[112,115] While being very popular for use in PEC biosensing, inorganic semiconductors have two major drawbacks. Their excellent physical and chemical stability make it very difficult to implement biofunctionalization which it difficult to properly integrate biorecognition elements. Additionally, their high photoexcitation signal is heavily impacted by non-specific absorption of biomolecules. To counteract these disadvantages, researchers focus on integrating inorganic semiconductors into hybrid semiconductor structures, where the presence of other materials can provide easier biofunctionalization and improved anti-fouling properties.[64,70,98]

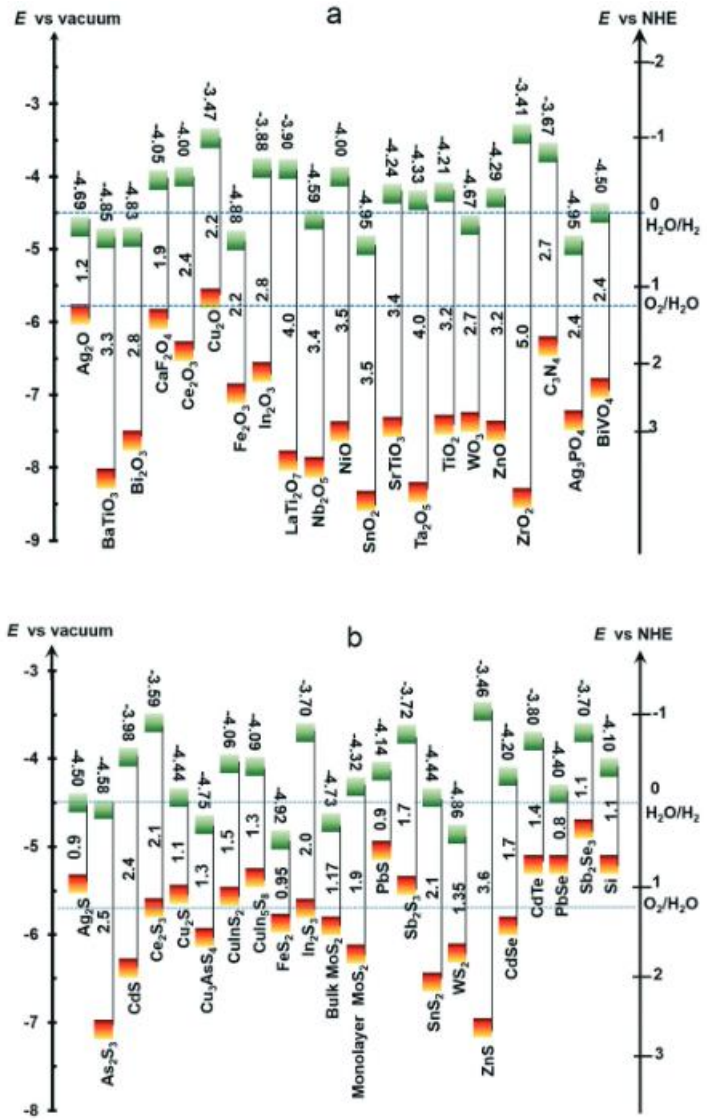

Figure 1-4. Band edge positions with respect to vacuum level and NHE for various photoactive semiconductors used for constructing photoelectrodes for PEC biosensors A) oxides, phosphates and carbides. B) quantum dots. Reproduced with permission.[5] Copyright 2015, Royal Society of Chemistry.

Organic semiconductors are made up materials whose building blocks comprises of pi-bonded molecules made from carbon and hydrogen.[64,116] Thee include materials such as dyes, carbon nanomaterials (e.g. graphene quantum dots, carbon nanotubes), bacteriorhodopsins, porphyrins and semiconducting polymers (e.g. poly(thiophene), phthalocyanine, phenylenevinylene, polymer dots).[116–118] The biggest advantages offered by organic semiconductors are their

mechanical pliability and their amenability to low-temperature solution-based processing, which allow for inexpensive fabrication of thin films on small, irregularly shaped or flexible substrates.[64,116,119] This opens up interesting avenues for designs of PEC biosensors by taking advantage of special geometries, surface microstructuring or microfluidics to create portable, low-cost miniaturized biosensors that do not sacrifice performance.[11,120,121] The organic chemical structure of these materials mean that they come pre-equipped with useful functional groups, that make biofunctionalization easy.[9,64,116,122] Despite these advantages, organic semiconductors have low quantum efficiency, making photoexcitation signal generation lower than that of inorganic semiconductors. Unlike ionic or covalent bonds seen in inorganic semiconductors, weak Van der Waals interactions are more prevalent in organic semiconductors making them less conductive.[116,123,124] For these reasons, organic semiconductors are usually coupled with other photoactive materials in order to fabricate effective photoelectrodes.[116,123,124]

Hybrid semiconductors structures are formed in three different ways: (i) coupling two inorganic semiconductors with different bandgaps,[125,126] (ii) complexing an inorganic semiconductor with an organic semiconductor,[113,122] or (iii) combining plasmonic metal NPs with organic/inorganic semiconductors.[127,128] Coupling two or more different inorganic semiconductors creates co-sensitization through the formation of a multi-state band structure, where the effective bandgap of the composite material is lower than each of the components individually. As a result, the absorption spectra and the IPCE of the hybrid structure is improved, which increases their photoexcitation signal generation.[5,129,130] Complexing inorganic semiconductors with organic semiconductors, such as dyes and photoactive polymers, is a strategy that combine the best traits of both these material classes. The organic semiconductor improves charge transfer and reduces electron work function to enhances generated photocurrent. This strategy is particularly useful

for improving the optical absorption spectra and IPCE of wide bandgap inorganic semiconductors.[60,122] The presence of inorganic molecules also endows the inorganic semiconductor material with the use of functional groups for biofunctionalization.[60,122] Coupling inorganic or organic semiconductors with plasmonic metal NPs such as gold, silver or platinum is an increasingly favoured strategy in PEC biosensing. [127,128] This type of hybrid structure results in a Schottky barrier which captures excited electrons generated by the localized surface plasmon resonance (LSPR) effect in the metal NP. Similar to the previous two strategies, this also results in improved signal generation, which is important for enhancing the performance of biosensors. [127,128]

1.2 Motivations

The increasing demand for cost-effective and reliable biosensors has led to the development of nanomaterials-based PEC biosensors. .[64,94] TiO_2 nanomaterials have been identified as a promising material for use in such biosensors due to their unique light-harvesting properties useful for driving electrochemical redox reactions involved in biomolecular detection.[114,131,132] However, the efficiency of TiO_2 nanomaterials for photoelectrochemical biosensors is still limited. This research aims to develop a new generation of PEC biosensors based on TiO_2 nanomaterials coupled with various other materials improve its base photoactive properties. This research is motivated by the need for reliable, low-cost, and highly sensitive biosensors that can detect specific biological molecules in real-time. Therefore, this research will focus on the characterization of hybrid semiconductor structures made from TiO_2 nanomaterials, the optimization of photoenhancement strategies, and the evaluation of the performance of photoelectrode signal transducers made from modified TiO_2 nanomaterials for PEC biosensing. This research will provide valuable insights into photoenhancement engineering, nanostructure

engineering, photoelectrode fabrication, bioassay design, which will be beneficial for the development of more cost-effective and reliable PEC biosensors. The outcome of this research will provide a valuable contribution to the fields of biosensor development, nanotechnology and solid state engineering, to enable the development of more sensitive, efficient, and cost-effective biosensors for various applications.

1.3 Research Objectives

The main goal of this research is to develop low-cost, easy-to-use and ultrasensitive PEC biosensors that is PoC capable. This was done by utilizing various photocurrent signal enhancement strategies on TiO_2 nanomaterial which were used to fabricate the photoelectrode signal transducer and designing portable signal-readers. In order to achieve this objective, the following specific goals were defined:

I. Exploring ideal TiO_2-based photoactive nanomaterials for sensitive PEC biosensing

To build a PEC biosensor with high sensitivity, high dynamic range and low LOD, its transducer element (i.e. photoactive working electrode) must have high photocurrent signal generation.[64,96,133,134] In addition to this, the transducer must also be highly biofunctionalizable in order to implement various bioassays.[109,135] TiO_2 nanomaterials have been extensively studied for its use as a metal oxide photoelectrode material in PEC biosensing owing to its high photocatalytic efficiency, tunable morphology and ideal conduction band (CB) & valance band (VB) levels for photoelectrochemistry.[136] Despite this unmodified TiO_2 has poor visible light absorption, high photogenerated charge carrier recombination rate that limit its photocurrent generation efficiency,[6,9,137] in addition to being hard to functionalize.[109,138] Our goal in this work was to build upon existing research into TiO_2 nanomaterial-based photoelectrodes to make more

effective PEC biosensors. To accomplish this, we synthesized various novel morphologies of TiO_2 nanomaterials and combined them with other materials such as catecholate ligands, functional nucleic acids, other metal oxide semiconductors with differing bandgaps and plasmonic nanoparticles to make composite TiO_2 material systems. These novel material systems provided signal enhancement to TiO_2 and also created many avenues for easier biofunctionalization.

II. *Designing and implementing bioassays with PEC signal transduction for a wide variety of bioanalytes*

In order prove the robustness and suitability of photoelectrochemistry as a signal transduction mechanism for biosensing, it had to be applied in a wide variety of different bioassays to detect different types of bioanalytes. Biomarkers are specific bioanalytes that are monitored as substitutions for predicting a clinically relevant outcome that difficult to observe. There exists a wide variety of biomarkers that are used by physicians do diagnose screening, diagnosis characterization, prognostic indication, and for observing drug reactions.[139–141] We designed various bioassays using our composite TiO_2 material systems for detecting various biomarkers such as nucleic acids, proteins and bacteria cells.

III. *Adding PoC-capabilty to PEC biosensors by designing bioassays that have fast sample-to-result time, while being operationally simple and also by designing portable signal-readers*

While the interest in the research of PEC biosensors is at all-time high,[39,40,44] these devices have seen little to no commercial breakthrough.[62] This can particularly be attributed to the fact that PEC biosensors require the use of bulky benchtop potentiostats and optical fixtures to provide

photoexcitation, which runs counter to PoC biosensing.[62,142] In order to challenge this status quo, we worked on designing a handheld smartphone-operated potentiostat for PEC biosensing with its own built-in LED photoexcitation source. Additionally, keeping PoC applications in mind, we designed our bioassays to be operationally simple single-step devices that deliver rapid sample-to-result time. Lastly, we also explored multiplexing with PEC biosensors in order to further deliver on PoC-capable PEC biosensors.

1.4 Thesis Overview

The remainder of this thesis is organized as follows:

Chapter 2 provides the literature review for catecholate surface functionalization of metal oxide and its photocurrent signal enhancement mechanism, which is foundational basis for all our composite TiO_2 material systems.

Chapter 3 discusses the PEC characterization of various catecholate ligand modification of TiO_2 nanoparticles (NP) and presents the design for a simple signal-off PEC biosensor based on caffeic acid modified TiO_2 NP for detecting DNA in blood plasma samples. The catecholate-TiO_2 is the foundational material system that all subsequent material systems and bioassays presented in thesis are based off of.

Chapter 4 explores the synthesis of one-dimentional TiO_2 nanostructure morphologies using a novel acid-hydrothermal synthesis method, where catecholate ligands were added in *in-situ* during the synthesis process to tune nanostructure morphology. This method formed TiO_2 nanorod clusters, which were used to fabricate nanoporous photoelectrodes with high surface area which resulted in high probe biomolecule immobilization efficiency. The catecholate ligand modification on the TiO_2 nanostructures resulted in significant photocurrent enhancement and

allowed biofunctionalization through Schiff-base reactions, making it highly suitable for PEC biosensing. A signal-off PEC biosensor for the detection of IL-6 protein (an imflammatory cytokine) in human blood plasma was developed using this material system.

Chapter 5 details the development of a photoelectrochemical bacterial assay that uses RNA-cleaving DNAzymes to modulate photocurrent by breaking and then rebuilding of TiO_2 nanomaterial-based heterostructures as a signaling mechanism. This assay uses the previous TiO_2 rutile nanorod cluster developed in the previous chapter and combines it with newly created ultrasmall (1-6 nm) TiO_2 NP to achieve semiconductor heterostructure that is significantly more photoactive than the base materials by themselves. The anatase TiO_2 NP were linked to the DNAzyme to create photoactive barcodes. The DNAzymes react to specific bacteria species causing release of photoactive barcodes from one photoelectrode (where signal decreased) and subsequent capture on a second photoelectrode (where signal increased). The assay was able to detect *E. Coli* contamination of *native* water samples with a high degree of specificity and a low limit-of-detection.

Chapter 6 describes the development of dye-assisted synthesis of Ag NP decorated TiO_2 NP. The synthesis technique involved photoreduction of Ag NP on the surface of haematoxylin (HTX, a dye containing catecholate functional groups) modified TiO_2 by taking advantage of dye-sensitized photocurrent enhancement. The TiO_2/HTX/Ag NP shows significantly enhanced photocurrent due to localized surface plasmon resonance effect and allowed for easy biofunctionalization through thiol-metal binding. This material system was used to build a multiplexed signal-off PEC biosensor for detecting microRNA in human blood plasma.

Chapter 7 describes the design and validation of the PECsense, a portable smartphone-operated potentiostat with built-in LED matrix as photoexcitation for PEC biosensing. The

microelectronic embedded systems design is discussed along with the device specifications. The performance of the device is characterized though noise analysis tests, performing PEC chronoampermetery at different bias voltages and stability tests involving rapid photoexcitation cycling and long-term exposure tests. Lastly, the PECsense was used to demonstrate PoC biosensing by repeating the signal-off DNA bioassay described in chapter 2.

Chapter 8 discusses the conclusions of this research and contributions made in the field of PEC biosensing. This section provides a summary of the key findings on this theses and potential future work.

Chapter 2

Background on surface functionalization of metal oxides with catecholate ligands

Preface:

In chapter 1, we discussed the challenges associated with PEC biosensing. In particular, we highlighted the need to develop photoactive material systems both highly biofunctionalizable and have high baseline photocurrent generation. This chapter contains a literature survey on the use of catecholates ligands for surface modification metal oxide semiconductors for photoabsorbtion amplification and colloidal stability enhancement strategies. The mechanisms for the surface adsorption of catecholates and how this leads to photoabsobtion enhancement are discussed in detail. Finally, we review recent advances and emerging trends for the use catecholate-modified metal oxides in various applications of photocatalysis, PEC biosensing and solar cell technology.

Authors: Sadman Sakib, Fatemeh Bahkshandeh, Sudip Saha, Leyla Soleymani and Igor Zhitomirsky (Equal contribution with Fatemeh Bahkshandeh)

Publication: Published in Solar RRL in September 2021

2.1 Abstract

Metal oxide nanostructures are increasingly important materials for various emerging photocatalytic, photovoltaic and photoelectrochemical (PEC) applications. They are commonly used as photoelectrode materials due to their unique functional properties such as wide bandgap, reactive electronic transitions, and high stability. To increase the effectiveness of semiconductor metal oxides photoelectrodes, researchers seek to use various photoabsorption amplification and colloidal stability enhancement strategies. An effective method for achieving this is the surface functionalization of metal oxide semiconductors with catechol-type ligands. Catechol-type ligands are a family of organic molecules that adsorb very strongly onto metal oxides by forming complexes with metal atoms through adjacent phenolic -OH groups. Once adsorbed, catechol-type ligands facilitate improved particle dispersion by inhibiting agglomeration and enhance photoexcitation in metal oxide semiconductors by improving visible light absorption. Herein, the surface complexation of catechol-type ligand onto metal oxide semiconductor surfaces and their photoabsorption enhancement mechanisms is described. In addition, recent advances and trends in this area are described by presenting recent advancements made in applications of catechol-modified metal oxide systems in photocatalysis, PEC biosensing, and solar cells.

2.2 Introduction

In recent years, researchers have dedicated significant effort into the study of transition metal oxide semiconductors and their applications. The electrostatic interaction between the metal and oxygen ions within the metal oxide crystal gives rise to strong chemical, electrochemical, and photoelectrochemical (PEC) stability in electrolytes, which is critically important for achieving good performance in various applications such as PEC biosensors, photovoltaic devices, and water splitting.[5,114,143,144] The band structure of transition metal oxides is composed of overlapping

2p orbitals from oxygen anions forming the low energy and highly populated valence band (VB), whereas overlapping d orbitals of the metal cations form the high energy and sparsely populated conduction band (CB).[145–147] This results in unique attributes such as wide bandgaps,[148,149] reactive electronic transitions,[103,150] high electron mobility, and low work function.[151,152] These properties make metal oxide semiconductors favorable materials for a wide range of applications such as heterogeneous catalysis, photocatalytic water splitting, photovoltaics, optoelectronics, and PEC biosensing.[153]

The rapid development of nanotechnology and the resultant advancements in the synthesis of functionally tunable nanomaterials have greatly motivated researchers to incorporate metal oxides into emerging photocatalytic, photovoltaic, and PEC sensing devices.[153–155] Despite showing high chemical stability, the use of transition metal oxides is limited by their wide bandgap that reduces their light absorption in the visible range. Therefore, it is important to enhance the range of the photoabsorption spectrum in these materials. Among different types of transition metal oxides, TiO_2 and ZnO have been extensively studied as photoelectrode materials due to their corrosion resistance, relative abundance, physical/chemical stability, and nontoxicity compared with other transition metal oxide semiconductors.[13,114,131] Moreover, WO_3, SnO_2, Al_2O_3, Fe_2O_3, and $BiOIO_3$ are seeing considerable interest in PEC applications.[10,156–159] To increase the effectiveness of semiconductor metal oxides photoelectrodes, researchers seek to use various photoabsorption amplification strategies including the coupling of metal oxides with plasmonic nanostructures,[128] bimetallic NPs,[160] graphene,[161] and quantum dots (QDs),[162] as well as dye sensitization[154] to create heterojunctions.

Despite the impressive advancements in the development of photoabsorption amplification strategies, there is a need for simple and versatile method for achieving photoabsorption

amplification that can also improve particle dispersion. While the techniques described earlier can be very effective, their implementation often involves complex multistep procedures.[163–165] Moreover, these techniques do not help to prevent particle agglomeration which creates photoelectrodes with poor film morphology that limit their usefulness.[114,166,167] Functionalization transition metal oxides with small organic ligands have also proven to be highly effective, while being significantly easier to implement.[9,168–170] One of the simplest and most effective photoabsorption strategies is the surface functionalization of metal oxide semiconductors with catechol-type ligands. Molecules from the catechol organic ligand family adsorb exceptionally well onto metal oxides due to their strong capability to complex with metal atoms by phenolic –OH groups, and present opportunities for one-step preparation of metal oxide particles with enhanced photoabsorption.[9,170,171] The strong adsorption of the catecholate molecules on metal oxide particles facilitates particle dispersion.[6,9] Catechol-type ligands create a charge transfer (CT) complex that helps enhance light absorption into the visible region.[172,173] In addition, catechol-type ligands are also commonly used as stable anchoring groups for binding coabsorbing organic dyes on metal oxide surfaces and as a sensitizer for dye-sensitized solar cells (DSSCs).[174] These metal oxide/ligand/dye systems have larger absorption coefficients due to the intramolecular π–π^* transitions.[9,175] Finally, catechol-type ligands can also be exploited as a bifunctional linker for various metal oxide-based PEC biosensors, wherein they are used to anchor peptides or nucleic acids.[176,177] The use of metal oxide/catechol ligand systems have allowed researchers to significantly improve the performance of various PEC and photocatalytic devices. In the field of PEC biosensing, adding catechol-type ligands significantly improves limits of detection of devices.[6,9,178] With photovoltaics, DSSCs are often augmented via the addition of catechol-type ligands, which are commonly used as a molecular linker to anchor

more complex dyes to metal oxides to improve photocurrent density.[15,179,180] The improved absorption of visible light of metal oxide/catechol ligand is leveraged into designing photocatalysts with very high efficiency.[13,173,181]

The goal of this review is to explore the surface complexation mechanism of catechol-type ligand onto transition metal oxide semiconductor surfaces and their photoabsorption enhancement mechanism. In addition, this review describes recent advancements made in applications of catechol-modified metal oxide systems in applications of photocatalysis, PEC biosensing, and solar cells.

2.3 Enhancement of Photoabsorption by Catechol

PEC signal generation involves generation of electron–hole pairs at the electrode/electrolyte interface upon optical excitation.[101,182] The electrodes are usually prepared using semiconductor materials of certain bandgap energies, which determines the energy of the excited electrons and holes. Optically generated electron–hole pairs are able to drive redox reactions that depends on the energy of these charge carriers, which in turn depends on VB and CB position of the electrode material. In the electrolyte, the reduced species are known as electron donor, whereas the oxidized species are known as electron acceptor. If the relevant ion concentrations and the standard redox potential of the redox species cause an overlap of unoccupied redox states with occupied semiconductor states or vice versa, CT occur in the system.[183]

Generally, n-type semiconductors produce anodic photocurrent, whereas p-type semiconductors yield cathodic photocurrent.[64,96] However, the direction of the photocurrent can also be modulated by applied electrode potential as it controls the position of the Fermi level of semiconductor relative to the electrochemical potential of the electrolyte.[183] Under illumination during open-circuit conditions, the photovoltage between the two electrodes is the same as the

difference between the Fermi level in the semiconductor and the redox potential of the electrolyte. In closed-circuit conditions, although there is not any photovoltage between the electrodes during illumination, there is a net charge flow.[183] The minor photogenerated charge carriers in the semiconductor are pushed to the surface and then injected into the electrolyte for driving a redox reaction. For example, in n-type semiconductors, an anodic reaction is driven by the injected minority holes, whereas for p-type semiconductors, the injected minority electrons can make a cathodic reaction. The major photogenerated charge carriers move to the semiconductor bulk at the working electrode (WE) and then leave the bulk by an ohmic contact, pass through an external circuit to the counter electrode (CE) for driving a redox reaction opposite to that happening at the semiconductor.[183]

There are two types of electron injection mechanisms from a surface-adsorbed molecule to the semiconductor metal oxide (**Figure 2-1**). The first mechanism (type I) occurs when a photoexcited electron from an excited state of a surface-adsorbed ligand molecule is transferred to the metal oxide CB. The second mechanism (type II) is a direct transition of photoexcited electrons from the highest occupied molecular orbital (HOMO) of the ligand to the semiconductor CB.[184] As type II is a direct transition, none of the intramolecular ligand excited states are involved in photoelectron injection process.[175,185] In principle, the type II mechanism is considered to be more efficient in electron injection due to the direct electron transfer from the ligand HOMO to the semiconductor CB.[175] However, it has some disadvantages including recombination (back electron transition) processes from the lowest states, and the low oscillator strength related to direct transition. In a direct transition, the final and initial electronic levels involved in the electron transfer have dissimilar spatial localization. Considering these

drawbacks, in practice, type II mechanism with respect to the type I has limited efficiency.[175,180,186]

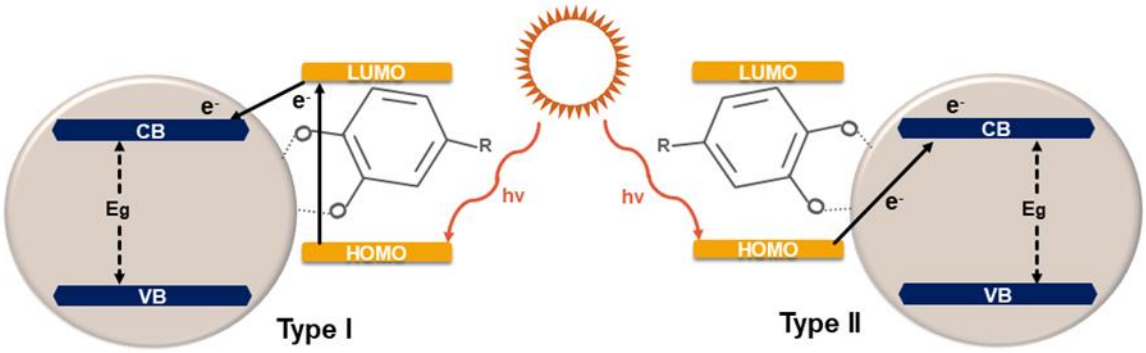

Figure 2-1. Schematic illustration of type I and type II photoelectron injection mechanism. Catechol molecules can make a type II ligand-to-metal CT complex by absorption on the metal oxides like TiO_2. Upon illumination a photoexcited electron can transfer directly from the HOMO catechol to CB of metal oxide.

TiO_2–catechol ligand complexes are one of the most well studied photoabsorption enhancement systems in the literature.[175,180,186] TiO_2 shows excellent absorption of light in the UV region and poor absorption in the visible region due to its wide bandgap (≈3.2 eV). Catechol-type ligands form a CT complex with TiO_2 to expand the absorption range into the visible region.[175] Catechol ligands are attractive as surface modifiers of TiO_2 because they greatly improve optical absorption of TiO_2 above 300 nm (4.14 eV), which is the lowest wavelength of intramolecular excitation of TiO_2.[174,185] Catechol-type ligands strongly bind to tetrahedral Ti^{4+} ions on the surface of TiO_2 and a bulk-like octahedral structure is formed.[173] It has been shown that TiO_2–catechol-type ligand systems facilitate type II electron transfer[173,180,185] resulting in fast electron injection (<100 fs) where the photoexcited electrons transit from the HOMO of the catechol-type ligands to the TiO_2 CB occurs.[180] However, type I electron transfer is also possible in this system

through which an electron is excited from the catechol ground state to a TiO_2 d-orbital and subsequently to TiO_2 CB.[180] The type II CT mechanism in TiO_2–catechol ligand complexes has been reported as the reason to have photosensitized TiO_2 system with broaden light absorption over the visible range.[173] Also, catechol-type ligands have been introduced as a photosensitizer and a catalyst, simultaneously. Indeed, the broadened photoabsorption into visible range and lower required overpotential for electrochemical oxygen evolution reaction compared with TiO_2 was the result of complexing TiO_2 with catecholate molecule.[185]

2.4 Surface Adsorption Mechanism

Organic molecules from the catechol family, such as dopamine, caffeic acid (CA), and gallic acid are well known to readily adsorb onto the surfaces of metal oxides.[168–170] The common structural feature shared by all catechol ligands is the presence of an aromatic ring with two phenolic –OH groups, bonded to adjacent carbon atoms of the aromatic ring. Gallates have three phenolic –OH groups and can be adsorbed on the surfaces by the catecholate type bonding mechanism. In addition, such molecules may have a short hydrocarbon chain with various other functional groups such as –COOH, –COH, and $–NH_2$. **Figure 2-2A** shows the chemical structures of several common catecholate molecules.[170,187] Surface adsorption was shown to be achieved by simply suspending metal oxide particles in aqueous solutions of catecholate or gallate molecules.[6,9] Alternatively, the molecules can be added in situ during the synthesis of metal oxide nanostructures, where in addition to surface adsorption, they can tune the morphology by acting as capping agents.[171,188] The morphology regulation is attributed to the preferential binding affinity of catechol-type ligands to certain crystal facets of metal oxides, which experience reduced growth during the synthesis process. Crystal facets with low ligand adsorption and higher surface energies experience more anisotropic growth.[189–191] Nanostructures

produced through this in situ surface adsorption method typically have smaller dimensions than those without any added modifier molecules during synthesis, due to reduced agglomeration.[171,191] The adsorption event can be verified by observing increased light absorption and a redshifting in the UV–vis spectrum of the modified metal oxide particles.[6,9,156,192,193] Catecholates, such as dopamine, have also been reported to form polymers.[15,194] Catechol ligands can bind onto metal oxide surfaces through two adjacent phenolic –OH groups to form bonds based on bidentate chelating, bidentate inner sphere bridging or bidentate outer sphere bridging.[170,187,195,196]

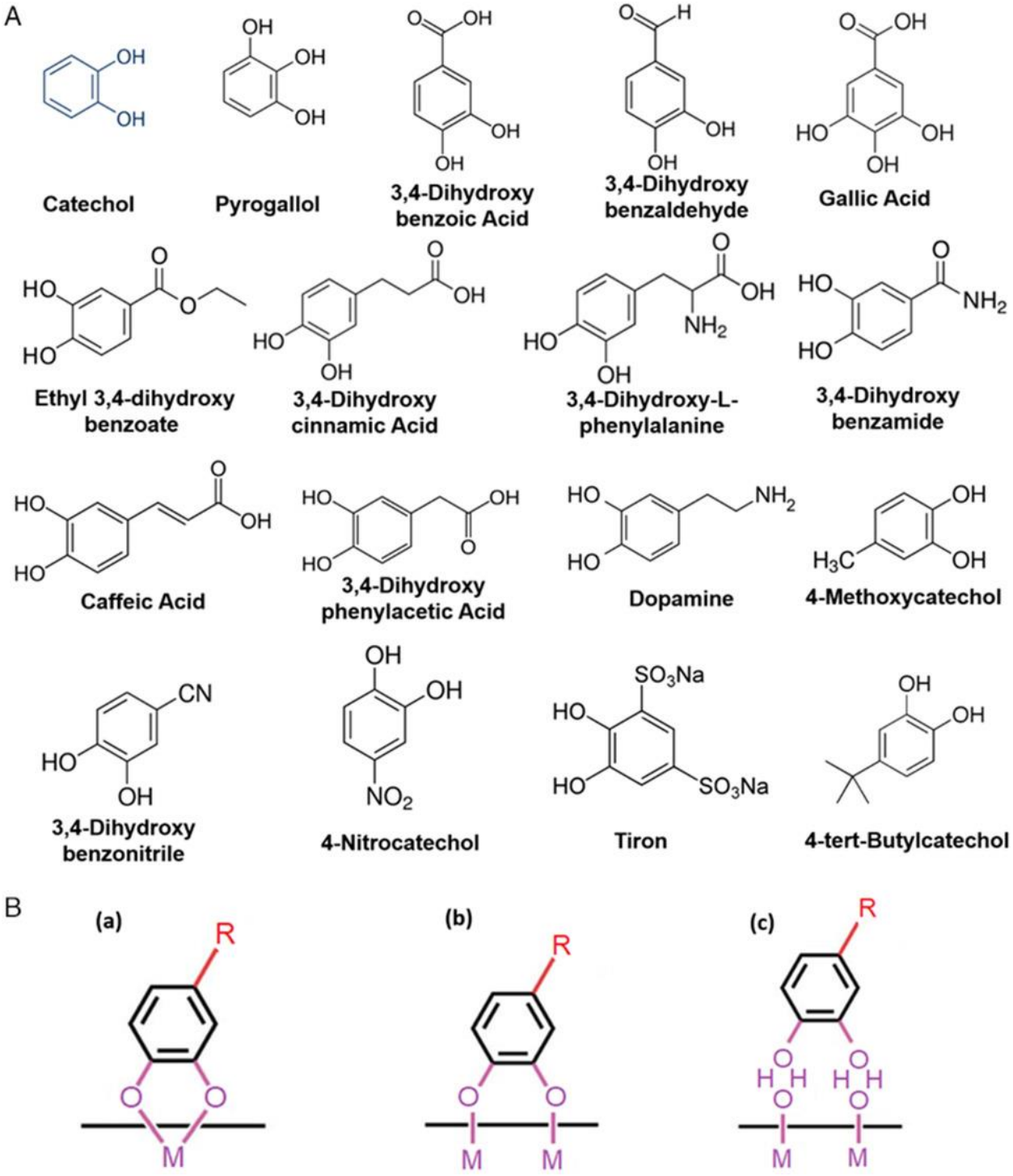

Figure 2-2. A) Chemical structures of commonly used catechol-type ligands and B) bonding mechanisms of a catechol group to metal oxide surface: a) bidentate chelating bonding, b) bidentate bridging bonding (inner sphere), and c) bidentate bridging bonding (outer sphere).

To understand the binding behavior of catechol-type ligands on metal oxides, the surface chemistry of metal oxide surfaces must be examined. The approach to studying the surface structure of metal oxide generally involves the assumption that the surfaces are generated from cleavages along the planes of the bulk crystal structure. The bulk atomic arrangement is maintained at the surface plane.[197,198] The newly formed surface planes contain metal atoms and bonded oxygen atoms with a lowered coordination index. To minimize surface Gibbs energy, dissociation of water molecules near the surface plane oxygen atoms will produce a hydroxylated metal oxide surface.[199,200] The catechol-type ligand form a bidentate-type bonding configuration via their phenolic –OH groups with the metal oxide surface hydroxyl groups.[199,200] The bidentate-type bonding occurs during the surface adsorption process, when two adjacent phenolic –OH groups of the catechol ligands are deprotonated and coordinate with the metal cation through dehydration. The bidentate bonding mechanisms can have several variations, which are bidentate chelating, bidentate inner sphere bridging, or bidentate outer sphere bridging of a catechol group to the metal ions (**Figure 2-2B**).[156,193,197,201,202] Catechol-type ligands are shown to form ordered densely packed monolayers on metal oxide surface, which give rise to additional electronic states above the VB level of metal oxide bandgap.[199,203,204] This results in the formation of CT complexes on the metal oxide surface that when photoexcited enable electron injection: direct electron transfer from the complex into the bulk metal oxide.[153,197]

Nanomaterials often agglomerate due to attractive van der Waals forces forming aggregates of heavier particles that precipitate from suspensions. Deposition of particles in this state results in poor film morphology composed of large agglomerates, which can reduce the overall photoactive surface area and reduce their performance as photoelectrodes.[166,167,205] Adsorbed catecholates act as dispersants and reduce agglomeration of metal oxide nanostructures. Films

created from the deposition of catechol-modified metal oxide nanostructures display improved morphology and distribution compared with nanostructures with no catechol surface modification, due to the higher stability of their suspension.[9] Upon surface adsorption of catechol molecules, metal oxide nanostructures develop a ligand shell around them, that provides a barrier that prevents further nanostructure growth or agglomeration via attractive van der Waals forces.[170,206] This suspension stabilizing effect is particularly strong for catechol-type ligands that contain long hydrocarbon chains.[170,207,208] Alternatively, through an alternative electrostatic repulsion mechanism, molecules with anionic or cationic functional groups impart a surface charge that reduces agglomeration.[209] Catecholate molecules with hydrocarbon chains terminating with –COOH or $–NH_2$ functional groups are able to dissociate or absorb protons to form a charged surface, providing electric charge and reducing agglomeration through electrostatic repulsion.[9,210] Catechol ligands can also act as versatile molecular linkers between metal oxide surfaces and many different types of materials[6,9,187] binding to carbon nanostructures,[194] other metal oxides nanostructures,[173] dyes,[7] polymers,[6] nucleic acids,[9] and peptides.[211] Catechol ligands with hydrocarbon chains containing –COH end groups bind to $–NH_2$ groups of other material through Schiff base reactions forming an imine bond. This binding mechanism has been used to integrate TiO_2 nanoparticles in a polymeric framework as an effective strategy for forming photoelectrodes for a PEC DNA biosensor. In this system, TiO_2 was functionalized with –COH group containing 3,4-dihydroxybenzaldehyde (DHBA) for binding with chitosan, a polymer with $–NH_2$ groups on its monomeric units (**Figure 2-3A**).[6] Such Schiff base reactions have been used to bind TiO_2 nanoparticles to poly-l-lysine, another polymer with $–NH_2$ groups on its monomeric units, using DHBA as a linker. The modified TiO_2 nanoparticles were electrodeposited for creating biocompatible film (**Figure 2-3C**).[8] Schiff base

reactions are thermodynamically favorable at room temperature and occur readily in aqueous media without additional catalysts.[6,8] Similarly, ligands with –COOH groups at the end of their hydrocarbon tail can also bind to $–NH_2$ groups of other materials via carboxamide binding to form an amide bond. This is demonstrated by Sakib et al., [9] where –COOH group of CA binds $–NH_2$-terminal single-stranded DNA to TiO_2 NP photoelectrodes, which forms the basis of a signal-off PEC DNA biosensor (**Figure 2-3D**). Carboxamide binding is not as thermodynamically favorable as Schiff base reactions and needs the use of additional catalysts.[9,176,177] Molecular linking through Schiff base reactions can also be achieved if the catechol molecule contains an $–NH_2$ group, whereas the other material contains –COH/–COOH, as the Schiff base reaction and carboxamide binding happens regardless of the location of the functional groups.[7,194,211] Burger et al. demonstrated this using dopamine, an $–NH_2$-containing catecholate molecules to establish linking between ZnO nanorods and –COOH-containing porphyrins, which are macrocyclic organic molecules commonly used as photoactive sensitizers (**Figure 2-3D**).[7,212,213]

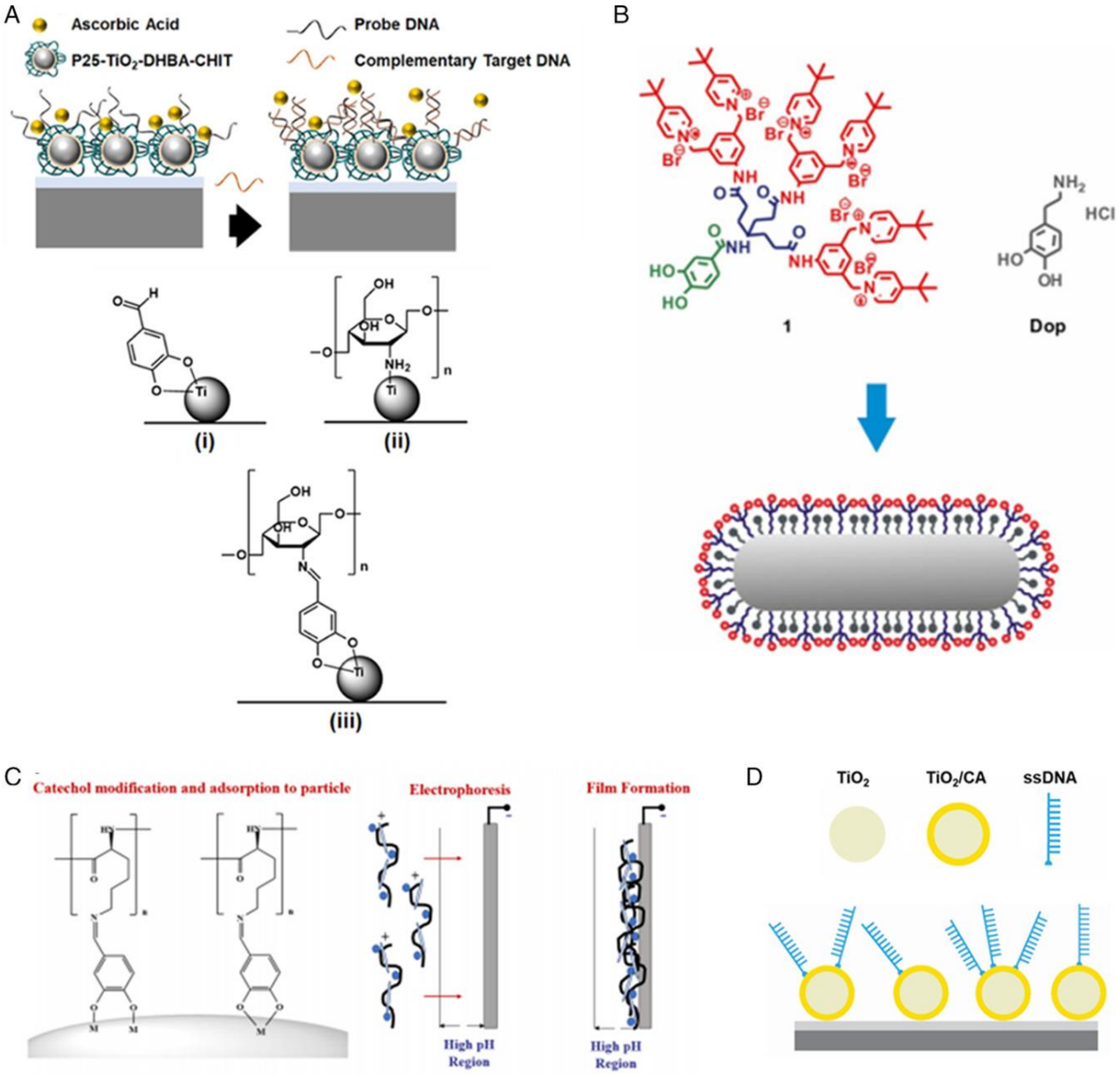

Figure 2-3. Catechol-type ligands acting as molecular linkers. A) TiO_2 NP and polymeric chitosan linked together using DHBA and used for PEC biosensing application. Reproduced with permission.[6] Copyright 2019, American Chemical Society. B) ZnO NRs and porphyrins are linked together using dopamine for the fabrication of solar energy converters. Reproduced with permission.[7] Copyright 2018, John Wiley and Sons. C) TiO_2 NP and poly-l-lysine are linked with DHBA to form adhesive films that can be deposited via electrophoretic deposition. Reproduced with permission.[8]Copyright 2019, Elsevier. D) TiO_2 NP being linked to single-stranded DNA probes using CA to form the basis of a signal-off PEC DNA biosensor. Reproduced with permission.[9] Copyright 2020, John Wiley and Sons.

2.5 Characterization of Metal Oxide/Catechol Systems

Various characterization techniques such as Fourier transform infrared spectroscopy (FTIR), thermogravimetric analysis (TGS), ultraviolet–visible absorption (UV–vis) spectroscopy, nuclear magnetic resonance (NMR) spectroscopy, photoemission spectroscopy, and density functional theory (DFT) calculations have been used to analyze and model the binding between metal oxides and catechol-type ligand. FTIR spectroscopy has been used to detect bidentate or monodentate binding between catechol-type ligands and metal oxides.[9,158,191,214,215] In the FTIR spectra of catechol-modified metal oxides, the development of C–O stretch and a decrease in –OH band intensity of the bonded catechol ligand is typically observed, which indicates deprotonation of the phenolic –OH groups, thereby providing support for the formation of bidentate-type bonding.[195–197,216] TGA is another technique used to investigate the surface adsorption of catechol ligands onto metal oxides, particularly looking at the changes in the stability of metal oxide–catechol ligand complexes over a wide range of temperatures.[158,198,217,218] Surface adsorption is also verified using UV–vis as catechol surface functionalization generally shows redshifting and an increase in the absorbance peak. This results in improved photoabsorption in the visible range and increased photocurrent density.[9,169,172,193,204,214,219] Other spectroscopic techniques used for the characterization of metal oxide/catechol systems include NMR spectroscopy for determining whether catechol-type ligands link other molecules,[220] Raman spectroscopy for quantifying the amount of catechol ligand bonded to metal oxide nanostructure surface,[197,208] and photoemission spectroscopy for experimentally obtaining the occupied and unoccupied states of the adsorbed catechol ligands.[174] TGA studies allow for the calculation of the maximum grafting density of ligands, adsorption coefficient, and negative-free binding energies of the surface functionalization of metal oxide nanostructures. These parameters

provide a toolbox for predicting adsorption/desorption, co-adsorption and ligand exchange behavior, which can be used to identify the optimal metal oxide and ligand concentration when preparing substrates for various applications.[158,217,218] DFT calculations can be used to quantitatively assess the binding affinity of catechol ligands and model their absorption on various metal oxide surfaces, and to evaluate changes of their optical absorption spectra and vibrational properties.[191,200,221] DFT studies show that the surface modification of metal oxides with catechol-type ligands lowers the bandgap of metal oxides. In TiO_2–catechol systems, surface modification by catechol reduces the bandgap of TiO_2 from 3.2 to 2.4 eV.[12] DFT studies show that this can be attributed to the fact that a donor level is constructed in the metal oxide midband. The various catecholate molecules that were used for surface modification can be divided into the following groups: molecules containing electron donating functional groups such as $–CH_2$, $–OCH_3$, or $–NH_2$ groups (e.g., 4-methoxycatechol, dopamine, 4-tert-butylcatechol) and molecules containing electron-withdrawing groups (EWGs) such –COOH, –COH, or $–NO_2$ groups (e.g., 3,4-dihidroxybenzaldehyde, 3,4-dihidroxybenzoic acid, and 4-nitrocatechol).[12,203] Typically, molecules containing EWGs carry out better in improving photoabsorption in the visible range and increasing the photocurrent response.[9,203]

2.6 Applications

The most common transition metal oxide/catechol-type ligand systems are often implemented through the surface modification of TiO_2 nanostructures. TiO_2 has attracted widespread attention in PEC biosensing, photocatalytic and photovoltaic applications due to its photocorrosion resistance, relative abundance, physical/chemical stability, and nontoxicity compared with other transition metal oxide semiconductors. However, the wide bandgap of TiO_2 (3.2 eV) makes it impractical for many applications as it has poor optical absorption in visible light range.

Therefore, there is significant interest in TiO_2–catechol ligand systems, which enhance photoabsorption properties of TiO_2 and improve its photocatalytic and PEC performance in visible light.[114,131,132] ZnO is another wide bandgap (~3.37 eV) metal oxide that is commonly used in photocatalysis and PEC applications which has comparable bandgap energy levels to that of TiO_2, high electron mobility, charge carrier lifetime, and physical/chemical stability.[13,114,131] Similar to TiO_2, ZnO is also limited by its wide bandgap and can have its photoabsorption enhanced by surface modification through catechol-type ligands.[13,131] Catechol surface functionalization has also been explored for metal oxide semiconductors such as WO_3,[10] SnO_2,[158] Al_2O_3,[193] and $BiOIO_3$.[156]

A summary of various catechol-modified metal oxide systems and their applications are shown in **Table 2-1**. In these systems, the nanoparticles of metal oxides are primarily utilized due to their high surface-area-to-volume ratio, which is an attribute that is greatly useful for photocatalytic and biosensing applications.[114,222] Various nanoscale morphologies such as nanoparticles, nanorods, nanowires, and nanoplatelets, as well as mesoporous or nanoporous substrates are used as photoactive building blocks of metal oxide-catechol systems.[114,153,223] Some of these systems are shown in **Table 2-1**. In most cases, these systems utilize catechol-type ligands as bifunctional linkers between metal oxides and other photoabsorption enhancement materials such as dyes,[7,179] QDs,[178] and noble metal nanoparticles.[10,224] Large organic dyes and catechol-type ligands synergistically strengthen type II electron injection processes wherein a photoexcited electron is transmitted from the HOMO level to the LUMO level of the dye catechol complex, which is near the CB edge of the metal oxide.[180] Metal nanoparticles or QDs are coupled to metal oxides through catechol-type ligands to enable photoabsorption enhancement through surface plasmon resonance (LSPR)[128] or dual sensitization,[133,225]

respectively. Co-adsorbant materials such as polymers are also commonly used within metal oxide/catechol systems for providing additional functionality such as improved coating adhesion,[204]enabling electrophoretic deposition,[8] or introducing additional functional groups that could be used for attaching other structures such as probe molecules for biosensors.[6] However, there are reports where the catechol-type ligand is not acting as linker, but rather it is a material complexed onto the metal oxide surface alongside it. In these systems, the third coadsorbate material is present for enhancing colloidal stability, typically a bile acid salt such as deoxycholic acid,[186,226] or a molecule with long hydrocarbon tails such as oleic acid.[207,227] The function of these coabsorbates is to act as dispersants to provide additional colloidal stability enhancement, whereas the catechol-type ligands continue to provide photoabsorption enhancement.[186,227]

Table 2-1: Summary of catechol-modified metal oxide systems and their applications.

Metal Oxide	Ligand	Surface Function	Application	Peak Performance	Ref.
ZnO NP	3,4-Dihydroxy-L-phenylalanine *	Linker, Stabilizer	N/A	N/A	[220]
Nanoporous TiO_2	3,4-Dihydroxy benzaldehyde *	Linker	Solar cell	$J=2.5$ $mA\ cm^{-2}$	[180]
WO_3 NP	Dopamine	N/A	Chemical sensing (Dopamine)	N/A	[228]
TiO_2 NP	Catechol	Stabilizer	N/A	N/A	[196]
TiO_2 NP	Gallic acid	Stabilizer	N/A	N/A	
TiO_2 NP	Catechol *	Linker	Solar cell	N/A	[175]
TiO_2 NP	Dopamine *	Linker, Stabilizer	Solar cell	$J=22$ $\mu A\ cm^{-2}$	[210]
TiO_2 NP	3,4-Dihydroxybenzoic acid *	Linker, Stabilizer	Solar cell	$J=24$ $\mu A\ cm^{-2}$	

ZnO NR	Dopamine *	Linker, Stabilizer	Solar cell	*J=0.1 μA cm^{-2}*	7
ZnO NR	3,4-dihydroxybenzoic acid *	Linker, Stabilizer	N/A	N/A	229
ZnO NP	Catechol	Stabilizer	N/A	N/A	
ZnO NP	3,4-Dihydroxybenzoic acid	Stabilizer	N/A	N/A	
ZnO NP	4-Nitrocatechol	Stabilizer	N/A	N/A	221
ZnO NP	3,4-Dihydroxybenzamide	Stabilizer	N/A	N/A	
ZnO NP	Catechol	N/A	N/A	N/A	230
TiO_2 NP	3,4-Dihydroxy benzaldehyde *	Linker, Stabilizer	Biomimetic Coating	N/A	8
Mesoporous TiO_2 film	3,4-Dihydroxy-L-phenylalanine	Linker	Bio-functionalization	N/A	
Mesoporous TiO_2 film	3,4,6-Triihydroxy-L-phenylalanine	Linker	Bio-functionalization	N/A	231
Mesoporous TiO_2 film	6-Nitro-3,4-Dihydroxy-L-phenylalanine	Linker	Bio-functionalization	N/A	
Al_2O_3 NP	Catechol	Stabilizer	N/A	N/A	
Al_2O_3 NP	Caffeic acid	Stabilizer	N/A	N/A	193
Al_2O_3 NP	Dopamine	Stabilizer	N/A	N/A	
Al_2O_3 NP	Gallic acid	Stabilizer	N/A	N/A	
TiO_2 NP	Catechol	N/A	Solar cell	N/A	232
TiO_2 NP	Catechol	N/A	Solar cell	N/A	233
TiO_2 NP	Dopamine	N/A	N/A	N/A	
TiO_2 NP	3,4-Dihydroxyphenylacetic acid	N/A	N/A	N/A	198
TiO_2 NP	Dopamine	Linker, Stabilizer	Bio-functionalization	N/A	
TiO_2 NP	3,4-Dihydroxyphenylacetic acid	Linker, Stabilizer	Bio-functionalization	N/A	211
ZnO NP	3,4-Dihydroxybenzoic acid *	Linker, Stabilizer	Solar cell	*J=1.4 mA cm^{-2}*	179

TiO_2 NP	Catechol	N/A	Water splitting	H_R=*3 µM/ 5 h*	12
TiO_2 NP	3-methoxycatechol	N/A	Water splitting	H_R=*1 µM/ 5 h*	
TiO_2 NP	3,4-dihydroxybenzonitrile	N/A	Water splitting	H_R=*30 µM/ 5 h*	
TiO_2 NP	2,3-Dihydroxybenzoic acid	N/A	Water splitting	H_R=*18 µM/ 5 h*	
TiO_2 NP	Tiron	N/A	Water splitting	H_R=*30 µM/ 5 h*	
TiO_2 NP	4-*tert*-Butylcatechol	N/A	Water splitting	H_R =*1 µM/ 5 h*	
ZnO NP	Dopamine	Stabilizer	Photoluminescense	N/A	171
TiO_2 NP	Catechol	Stabilizer	N/A	N/A	215
TiO_2 NP	Pyrogallol	Stabilizer	N/A	N/A	
TiO_2 NP	Gallic acid	Stabilizer	N/A	N/A	
Mesoporous TiO_2 film	Phenol	Stabilizer	Photocatalytic dye degradation	*J=1.2 µA* cm^{-2}	126
Mesoporous TiO_2 film	Catechol	Stabilizer	Photocatalytic reduction of Cr(VI) to Cr(III),	η= 60%*/5 m*	153
Mesoporous TiO_2 film	Catechol	Stabilizer	Water splitting	H_R =*10925 µM* g^{-1}	
SnO_2 NP	Tiron	Stabilizer	N/A	N/A	158
SnO_2 NP	Catechol	Stabilizer	N/A	N/A	
ZnO NR	Polydopamine	Linker, Stabilizer	Photocatalytic dye degradation	η=65%*/ 3 h*	13
ZnO NR	Polydopamine	Linker, Stabilizer	Antimicrobial Coating	CCR= 10^{4}*/3 h*	
ZnO NP	Dopamine *	Linker, Stabilizer	N/A	N/A	
ZnO NP	Dopamine	Stabilizer	N/A	N/A	217
ZnO NP	3,4-Dihydroxy-L-phenylalanine	Stabilizer	N/A	N/A	
TiO_2 NP	Catechol	Stabilizer	N/A	N/A	197
TiO_2 NP	Catechol	N/A	Solar cell	N/A	199

TiO_2 NP	2-Hydrixy-5-methoxy benzaldehyde	N/A	Photocatalytic oxidation of amines to imines	η= *77-85%/ 1 h*	234
ZnO NP	Catechol	Stabilizer	Photoluminescense	N/A	
ZnO NP	4-*tert*-Butylcatechol	Stabilizer	Photoluminescense	N/A	
ZnO NP	4-Nitrocatechol	Stabilizer	Photoluminescense	N/A	204
ZnO NP	Ethyl 3,4-dihidroxy benzoate	Stabilizer	Photoluminescense	N/A	
ZnO NP	Ethyl 3,4-dihidroxy benzoate	N/A	Solar cell	N/A	192
Nanoporous TiO_2	Phenol	N/A	Photocatalysis	$J=85\ \mu A\ cm^{-2}$	
Nanoporous TiO_3	Catechol	N/A	Photocatalysis	$J=0.1\ mA\ cm^{-2}$	223
TiO_2 NP	Catechol	N/A	Solar cell	N/A	235
Mesoporous TiO_2 film	Catechol	N/A	Chemical sensing	IPCE=*3%*	236
TiO_2 NP	Polydopamine	Stabilizer	Solar cell	$J=5.5\ \mu A\ cm^{-2}$	15
TiO_2 NP	Catechol *	Linker	Photocyanation of amines	η=*96%/3 h*	237
TiO_2 NP	Catechol *	Linker	Photocyanation of amines	η=*96%/3 h*	
TiO_2 NP	Catechol	N/A	Water splitting	$H_R = 130\ \mu M\ g^{-1}$	
TiO_2 NP	3,4-Dihydroxybenzoic acid	N/A	Water splitting	$H_R = 160\ \mu M\ g^{-1}$	
TiO_2 NP	3,4-Dihydroxycinnamic acid	N/A	Water splitting	$H_R = 175\ \mu M\ g^{-1}$	173
TiO_2 NP	Caffeic acid	N/A	Water splitting	$H_R = 275\ \mu M\ g^{-1}$	
Bulk crystalline TiO_2	Catechol	N/A	N/A	N/A	174

Bulk crystalline ZnO	Catechol	N/A	N/A	N/A	
TiO_2 NP	3,4-Dihydroxyphenylacetic acid	Linker, Stabilizer	Bio-functionalization	N/A	238
TiO_2 NP	Dopamine	Linker, Stabilizer	Bio-functionalization	N/A	239
TiO_2 NP	Catechol	N/A	Antimicrobial Coating	$J=4\ \mu A\ cm^{-2}$	240
TiO_2 NP	Catechol	N/A	Photocatalytic pollutant degradation	$J=0.2\ \mu A\ cm^{-2}$	241
TiO_2 NP	Pyrogallol	N/A	Photocatalytic pollutant degradation	$J=50\ nA\ cm^{-2}$	
TiO_2 NP	Caffeic acid	Linker	DNA biosensing	$J=22\ \mu A\ cm^{2}$	
TiO_2 NP	3,4-Dihydroxybenzaldehyde	N/A	DNA biosensing	$J=16\ \mu A\ cm^{2}$	
TiO_2 NP	3,4-Dihydroxybenzoic acid	N/A	DNA biosensing	$J=9\ \mu A\ cm^{-2}$	
TiO_2 NP	2,3,4-Trihydroxybenzaldehyde	N/A	DNA biosensing	$J=12\ \mu A\ cm^{-2}$	
TiO_2 NP	2,3,4-Trihydroxybenzoic acid	N/A	DNA biosensing	$J=7\ \mu A\ cm^{-2}$	9
TiO_2 NP	3,4-Dihydroxyphenylacetic acid	N/A	DNA biosensing	$J=13\ \mu A\ cm^{-2}$	
TiO_2 NP	3,4-Dihydroxy-L-phenylalanine	N/A	DNA biosensing	$J=4\ \mu A\ cm^{-2}$	
TiO_2 NP	Catechol	N/A	Solar cell	N/A	184

TiO_2 NP	Catechol	Stabilizer	N/A	N/A	[242]
TiO_2 NP	Catechol	Stabilizer	Solar cell	N/A	
TiO_2 NP	3-Methylcatechol	Stabilizer	Solar cell	N/A	
TiO_2 NP	4-Methylcatechol	Stabilizer	Solar cell	N/A	
TiO_2 NP	3-Methoxycatechol	Stabilizer	Solar cell	N/A	[203]
TiO_2 NP	3,4-Dihydroxybenzaldehyde	Stabilizer	Solar cell	N/A	
TiO_2 NP	4-Nitrocatechol	Stabilizer	Solar cell	N/A	
TiO_2 NP	Catechol *	Stabilizer	Photocatalysis	N/A	[227]
ZnO NP	Ethyl 3,4-dihidroxy benzoate	Stabilizer	N/A	N/A	
ZnO NP	3,4-Dihydroxy-L-phenylalanine *	Linker, Stabilizer	N/A	N/A	[208]
WO_3 NP	Dopamine *	Linker	Photothermal therapy	T_P=*42 ºC/5 m*	[243]
TiO_2 NP	Catechol	N/A	N/A	N/A	[200]
TiO_2 NP	Catechol	N/A	Water splitting	J=*90 μA* cm^{-2}	[185]
TiO_2 NP	Catechol	Stabilizer	Solar cell	J=*0.11 mA* cm^{-2}	
TiO_2 NP	Dopamine	Stabilizer	Solar cell	J=*0.1 mA* cm^{-2}	[186]
Nanoporous TiO_2	Catechol *	N/A	Solar cell	*J=1.28 mA* cm^{-2}	
Nanoporous TiO_2	Dopamine *	N/A	Solar cell	*J=0.31 mA* cm^{-2}	

Amorphous TiO_2 film	Dopamine	N/A	N/A	N/A	214
TiO_2 NP	Dopamine	N/A	N/A	N/A	172
TiO_2 NP	Catechol	N/A	N/A	N/A	
TiO_2 NP	3,4-Dihydroxy benzaldehyde *	Linker	DNA Biosensor	J=*1 μA cm*$^{-2}$	6
WO_3 NR	Polydopamine *	Linker	Chemical sensor (Insulin)	*J=15 μA cm*$^{-2}$	178
TiO_2 NP	Catechol	Stabilizer	N/A	N/A	244
Nanoporous TiO_2	Dopamine	N/A	Chemical sensing (NADH)	J=*0.2 μA cm*$^{-2}$	245
ZnO NR	Catechol	Stabilizer	Solar cell	N/A	14
ZnO NR	Polydopamine	Linker, Stabilizer	Immunosensor	*J=22 μA cm*$^{-2}$	11
TiO_2 NW	Poly(dopamine) *	Linker	Photocatalytic dye degradation	η= *97% /2h*	194
TiO_2 NP	4-*tert*-Butylcatechol	Stabilizer	N/A	N/A	
TiO_2 NP	4-Nitrocatechol	Stabilizer	N/A	N/A	218
TiO_2 NP	3,4-dihydroxybenzonitrile	Stabilizer	N/A	N/A	
$BiOIO_3$ NP	2,3-Dihydroxybenzoic acid	Stabilizer	Photocatalytic pollutant degradation	J=1.*2* *μA cm*$^{-2}$	156
WO_3 nanoplatelets	Polydopamine *	Linker	Immunosensor	J=*9.5* *μA cm*$^{-2}$	10
ZnO NR	Caffeic acid	Stabilizer	N/A	N/A	191
TiO_2 NP	Tiron	Stabilizer	N/A	N/A	246
TiO_2 NP	Dopamine	Stabilizer	N/A	N/A	

Fe_3O_4 NP	Dopamine *	Linker, Stabilizer	Biocompatible Hydrogel	N/A	[247]
Fe_2O_3 NP	Catechol	N/A	Wastewater Treatment	N/A	[159]
TiO_2 NP	Catechol	N/A	Wastewater Treatment	N/A	
TiO_2 NP	Catechol	Stabilizer	Photocatalytic dye degradation	η= *1.7%*	[248]

* catechol ligand is co-absorbed alongside an additional material

NP = nanoparticle, NW = nanowire, NR = nanorod

J- photocurrent density, H_R- H_2 production rate, T_P- Photothermal temperature, IPCE- incident photon to converted electrons, CCR- cell count reduction factor, η-photocatalysis efficiency

2.6.1 Photoelectrochemistry and Photocatalysis

PEC and photocatalytic systems have attracted a great amount of scientific interest for different types of sensing applications and solving environmental contamination issues.[249,250] In addition, these systems can also be used for splitting water into H_2 and O_2, which can pave the way for efficient mass generation of renewable fuels.[249,250] Utilizing these systems into water splitting is a green and environmentally friendly method to generate solar hydrogen.[126,251] Nanostructured metal oxides like TiO_2 and ZnO are most frequently used as photoactive materials in these systems.[153,251] However, due to their large band gap, they can only show photocatalytic activity under UV light which is just 5% of the sun light spectrum. Therefore, surface modifying of metal oxides with dyes is a well-established strategy for tailoring the optical and physicochemical properties of semiconductors to convert them to visible light active materials.[126,173,237,248,252]

Generally, a PEC cell is composed of an electrochemical cell with working, counter, and reference electrodes (REs) submerged in an electrolyte and excited by a photonic source (**Figure**

2-4A). In these cells, the WE acts as a photoelectrode that drives redox reactions.[6,253] The photoelectrodes are typically fabricated from organic or inorganic semiconductors immobilized on conductive substrates. When the photoelectrode absorbs photons with energy greater than its bandgap energy, charge separation occurs where electrons migrate to the CB and holes are left behind in the VB. Redox reactions occur on the photoelectrode at the electrode/electrolyte interface,[134] generating a photocurrent or a photopotential.

In contrast, a photocatalytic cell is composed of two electrodes (WE and CE) submerged in an aqueous solution of pollutants or pure water for water splitting applications (**Figure 2-4C**). Similar to PEC cells, when a photocatalytic cell is illuminated by an excitation source, it absorbs photons with energy greater than its bandgap energy, charge separation occurs, and photoexcited electron-hole pairs are generated. In a photocatalytic degradation process, the photogenerated holes will ionize water to form hydroxyl radicals (•OH) and the photogenerated electrons cause oxygen ionosorption where dissolved oxygen (O_2) species are reduced to form anionic superoxide radicals (O_2^-).The superoxide may be further protonated to form hydroperoxyl radicals (HO_2•), and subsequently forming hydrogen peroxide (H_2O_2), which further dissociates into high reactive hydroxyl radicals (•OH) The radicals cause oxidation or reduction of pollutants which result in their neutralization and complete degradation.

(1) $Photoexcitation$: $TiO_2 + hv \rightarrow TiO_2\left(e^-(CB) + h^+(VB)\right)$

(2) $Ionization\ of\ water$: $H_2O(ads) + h^+(VB) \rightarrow \bullet OH(ads) + H^+(ads)$

(3) $Oxygen\ ionosrption$: $O_2 + e^-(CB) \rightarrow O_2^{-\cdot}(ads)$

(4) $Protonation\ of\ superoxide$: $2O_2^{-\cdot}(ads) + 2H^+ \rightarrow 2HOO^{\cdot}(ads) \rightarrow H_2O_2(ads) \rightarrow 2 \bullet OH$

In water-splitting applications, the CB energy level of the photoactive semiconductor must be more negative than the reduction potential of water to produce H_2, and the VB energy level must be more positive than the oxidation potential of water to produce O_2. At the cathode, electrons reduce hydrogen cations (H^+) to form H_2. At the anode, holes oxidize hydroxide anions (OH^-) to produce O_2.[144,249,250,254] Another novel application of photoactive semiconductors are as photocatalytically active antimicrobial coatings. Charges generated by photoexcitation participate in redox reactions at the surface of antimicrobial coatings, which causes the inactivation of microorganisms such as bacteria.[13,240]

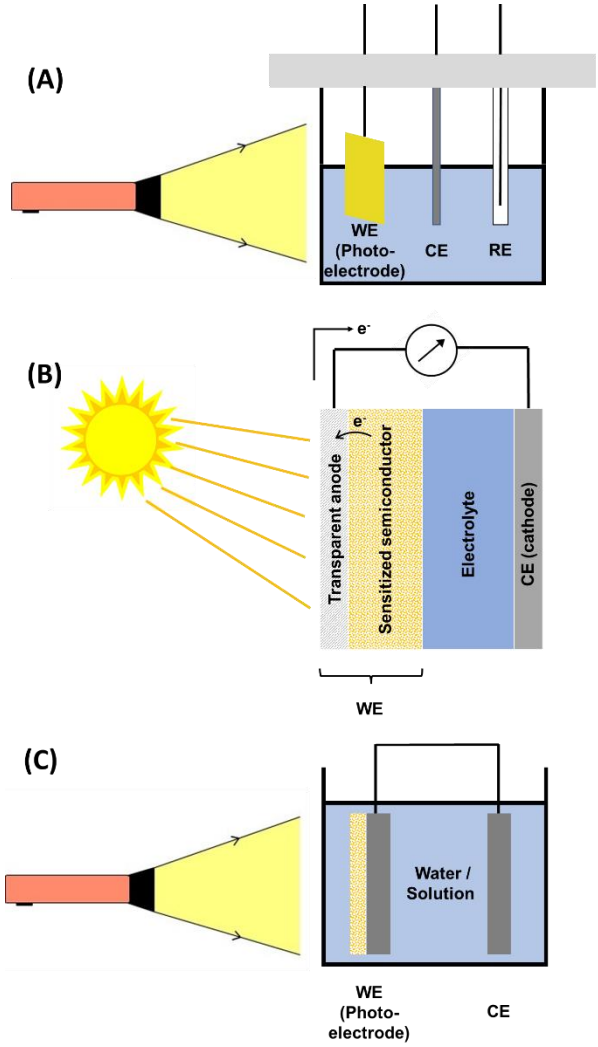

Figure 2-4. A) Three-electrode PEC cell setup showing WE/photoelectrode, CE, RE, and the photoexcitation source. B) General configuration of a DSSC showing the WE cathode (porous dye-sensitized photoactive semiconductor layer deposited onto a transparent anode), an electrolyte layer, and a CE cathode. C) General configuration of the two-electrode photocatalytic cell showing the WE and CE submerged in an aqueous solution of pollutants or pure water.

Karimi-Maleh et al.[255] showed using ZnO/CNTs nanocomposite/catechol derivative modified photoelectrode in a PEC cell that were able to differentiate and detect glutathione and amoxicillin simultaneously for the first time although the oxidation peak potentials of amoxicillin overlapped with that of glutathione. In addition, this modified electrode shows higher selectivity in voltametric measurements.[255] Murata et al. studied adsorption properties of catechol-adsorbed TiO_2 as a model biosensing system. In this study, they showed that adsorption of a catechol containing molecule on TiO_2-induced CT improved photoabsorption in the whole visible region.[236] Sakib et al.[9] fabricated a PEC DNA biosensor using TiO_2-modified different catechol molecules. As these molecules enhanced light absorption in the visible range, they allowed for much higher photocurrent than that of bare TiO_2. The CA-modified TiO_2 photoelectrodes showed the required photocurrent value to distinguish between complementary and non-complementary DNA sequences with a limit of detection of 1.4 pM.[9] As shown in **Figure 2-5A**, for fabricating a PEC immunosensor of human epididymal protein 4, Zhang et al. used a catechol-containing molecule, polydopamine (PDA), in the materials system including WO_3 and Au nanoparticles. PDA significantly suppressed electron–hole pairs recombination in the system, facilitated their separation, and increased their density and lifetime. Because of the plasmon resonance energy transfer effect of Au nanoparticles and the sensitization effect of PDA, improved signal and a limit of detection of 1.56 pg mL^{-1} were obtained for this sensor.[10] As shown in **Figure 2-5B**, Yang and Hu reported a PEC immunosensor composed of ZnO and PDA, in which PDA has both roles of an efficient sensitizer for light absorption and photogenerated carrier separation and a biocompatible functional matrix for attachment of

biological probe. This catecholate molecule, PDA, improved photocurrent generation of the sensor which offered a limit of detection of 10 pg mL^{-1} to distinguish target protein.[11] Victorious et al.[6] used catechol-containing molecule, DHBA in addition to TiO_2 and chitosan to develop a PEC DNA biosensor. They showed that DHBA enhanced the optical and electronic properties of TiO_2 nanoparticles by improving light absorption and photo generated carrier separation, and binding sites for biorecognition probes attachment. The developed photoelectrodes enhanced the obtained photocurrent by a factor of 10 and distinguished between complementary and noncomplementary DNA sequences at a concentration of 0.5 μM.[6]

Orchard et al.[173] developed a new route for fabricating metal-free photoelectrodes by preparation of a CT catechol-sensitized TiO_2 complexes for the photocatalysis system. They studied different catechol derivatives like 1,2-dihydroxybenzene, 3,4-dihydroxybenzoic acid (DHBA), 3,4-dihydroxyhydrocinnamic acid, CA, 2-(3,4-dihydroxybenzene) thiophene, and 2,3-naphthalenediol and showed that the highest activity for driving sacrificial H_2 evolution was obtained with CA. They reported that the modified TiO_2 with catechol are effective photosensitizers by facilitating type II CT complex and exhibited broad light absorption over the visible range. They also showed that the obtained photocurrents with these photoelectrodes are comparable to those that sensitized with type I dyes.[173] Tachan et al. presented a catechol molecule that act not only as a photosensitizer but also a catalyst. They reported that TiO_2-catechol complex expand the photoabsorption into visible range, oxidized water to oxygen very efficiently and reduced the required overpotential for electrochemical oxygen evolution reaction by 500 mV compared with TiO_2.[185] Higashimoto et al. studied visible light-sensitive TiO_2 photocatalyst for hydrogen (H_2) production from aqueous triethanolamine in the presence of Pt cocatalyst.[12] To obtain interfacial surface complexes (type II CT complex), they modified TiO_2

with catechol and its derivatives. Also, they investigated the effects of catechol derivatives with electron-donating groups (EDGs) and EWGs on the photocatalytic activity. They reported that modified TiO_2 by catechol derivatives with EWG like 3,4-dihydroxybenzonitrile and tiron showed much higher photocatalytic activity than catechol-containing molecule with EDG like 4-*tert*-butylcatechol, 4-methoxycatechol. The catechols with EWG not only enlarge the bandgap energy but also make an anodic shift of the donor levels. As shown in **Figure 2-5C**, the excitation from these donor levels created in TiO_2 midgap affects the visible-light sensitivity of the interfacial surface complexes. **Figure 2-5C** also shows the reaction mechanism for photocatalytic H_2 evolution from aqueous triethanolamine on modified TiO_2 with dihydroxybenzonitrile. By visible-light irradiation, TiO_2– dihydroxybenzonitrile complex induces electron–hole separation. The reduction of protons on the CB to produce H2 through the Pt cocatalyst and the oxidation of triethanolamine in the interfacial TiO_2– dihydroxybenzonitrile complex are happened by photogenerated electrons and holes, respectively.[12] Sadowski et al. demonstrated that TiO_2 films modified with catechol on polypropylene foils can act as antimicrobial coatings. They reported inactivation of E. coli and S. aureus bacteria by showing a three order of magnitude population decrease after 8 h of visible-light (405 nm) irradiation.[240] As shown in **Figure 2-5D**, Kim et al. used PDA to link ZnO nanoparticles to polyurethane nanofibers. The ZnO nanoparticles acted as seeds for growing larger ZnO nanorods on the polyurethane nanofibers via a hydrothermal process. This structure was used to make films that demonstrate excellent antimicrobial properties as demonstrated by the inactivation of E. coli by three orders of magnitude after 3 h of UV irradiation. It also shows excellent photocatalytic degradation of organic pollutants, as demonstrated by 65% reduction in concentration of methylene blue after 3 h of UV irradiation. and antimicrobial activity.[13] In recent years,

researchers have greatly advanced the efficiency of photocatalytic systems using metal phosphides rather than metal oxides[256] or coupling metal oxides with carbonaceous materials (CMs). Despite their significant application potential, CMs suffer from poor dispersion in aqueous solutions and are hard to bind to functional materials.[256,257] Catechol-type ligands can be used for providing coupling between metal oxides and CMs by being used as a functional linker.[194,256,257] Yu et al. demonstrated this by fabricating a photocatalytic membrane made from PDA-modified TiO_2 nanowires intercalated with graphene oxide nanosheets. This system demonstrated high photocatalytic efficiency with a removal rate of 98% on a dye–water emulsion.[194]

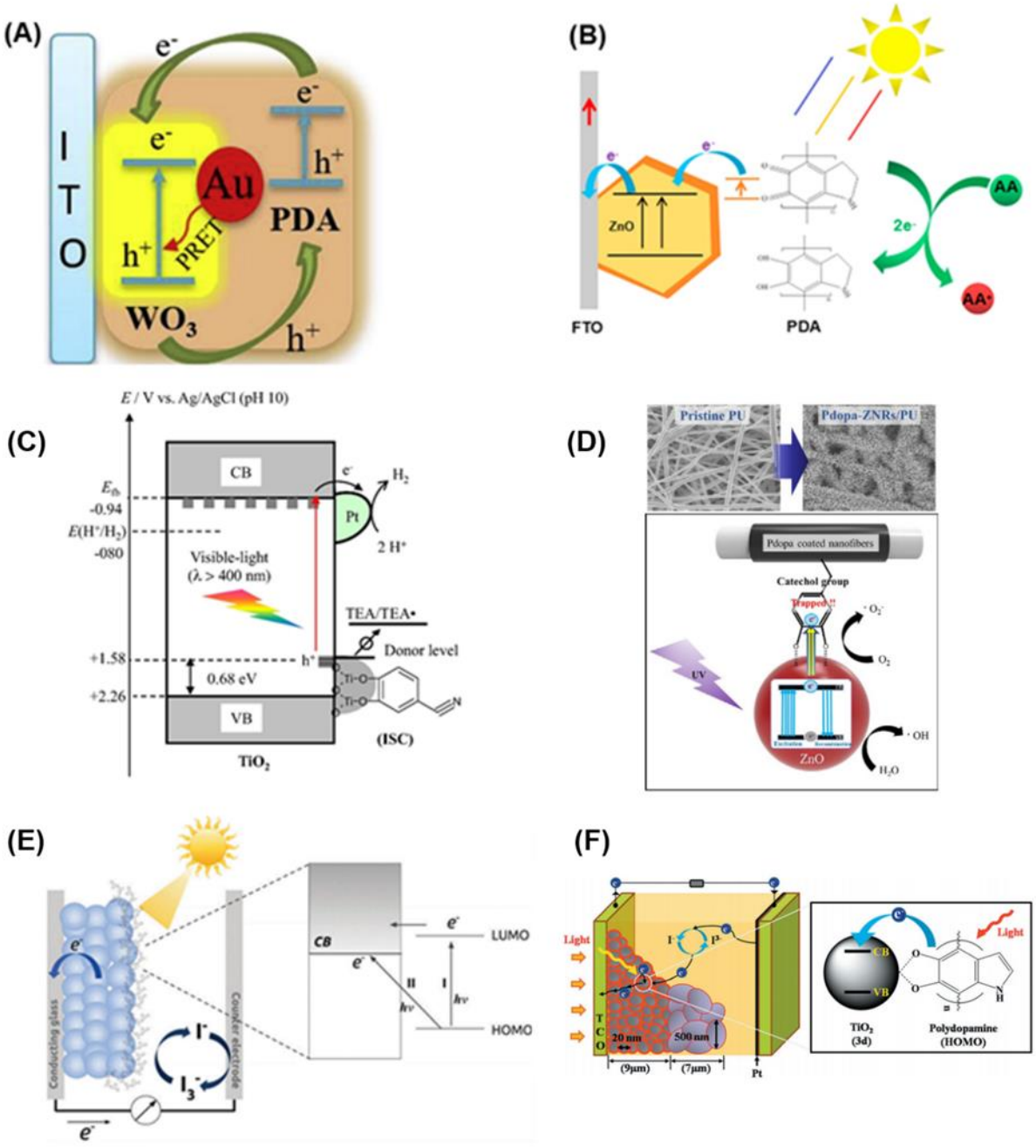

Figure 2-5. Applications of metal oxide and catechol ligand heterostructures in PEC applications. A) The possible photogenerated CT mechanism at WO_3/Au/PDA interface from a PEC immunosensor. Reproduced with permission.[10] Copyright 2020, Elsevier. B) The possible photogenerated CT mechanism at PDA–ZnO nanorods PEC immunosensor in ascorbic acid (AA) electrolyte. Reproduced with permission.[11] Copyright 2017, Elsevier. C) A possible mechanism of H_2 evolution from aqueous triethylamine solutions in the presence of Pt cocatalyst for modified TiO_2 with 3,4-dihydroxybenzonitrile catalyst under visible-light irradiation. Reproduced with permission.[12] Copyright 2015, Elsevier. D) Schematic of the mechanism of

increased electron–hole pair generation and synthesis of radical product on ZnO/PDA-coated polyurithane nanofiber photocatalyst. Reproduced with permission.[13] Copyright 2018, Elsevier. E) A diagram of the operation of a DSSC made from ZnO nanoparticles modified with catechol and of the injection mechanisms. Reproduced with permission.[14] Copyright 2018, Royal Society of Chemistry. F) Schematic illustration of PDA-sensitized solar cells proposing the photogenerated CT mechanism. Reproduced with permission.[15] Copyright 2012, John Wiley and Sons.

2.6.2 Photovoltaic Applications

Considering rising demand for clean energy in recent years, researchers introduced the third generation of solar cells, DSSCs, that are a type of photovoltaic devices.[14,180,258] A photovoltaic cell can directly convert solar energy. In general, DSSC photovoltaic cells are composed of the following elements: a WE constructed from a porous dye-sensitized photoactive semiconductor layer deposited onto a transparent anode, an electrolyte layer, and a CE cathode (**Figure 2-4B**). The anode and the cathode of the DSSC are connected to an external load and a closed circuit is established.[143,259,260] When excited by sunlight, the sensitizer dye is excited, and an electron is injected into the CB of semiconductor. This causes the sensitizer to be oxidized and the electrolyte to be reduced. The injected electrons diffuse through the semiconductor layer and arrive at the anode. From the anode, the electrons travel to the external load, where work is carried out. The electrons then arrive at the cathode before oxidizing the electrolyte to complete the cycle. [143,259,260] In DSSCs, light transmittance has to be maximized and therefore the anode must be transparent. Most commonly the anode is constructed from indium-doped tin-oxide (ITO) glass or fluorine doped tin-oxide glass.[261] The redox couple most commonly used as the liquid electrolyte is iodide and triiodide (I^-/I_3^-), whose redox potential is high enough to regeneration reaction with a redox mediator.[143,262]

Fabrication cost and sunlight to electricity conversion efficiency are main challenges in the solar cells research area.[14] TiO_2, ZnO, and SnO_2 metal oxides are commonly used as photoanodes in

DSSCs.[14] Excellent electrochemical properties, strong bonding ability to form CT complexes with metal oxides, and photovoltaic performance of dyes containing catechol make them promising candidates.[15] Upon photoexcitation, an electron of catechol dye HOMO transfers to metal oxide CB by direct one-step process (type II).[14,15] In fact, oxidizing catechol dye by a metal oxide is known as "sensitizing" of the photoanode to the solar spectrum.[180] Then the oxidized catechol dye is reduced via a redox couple in electrolyte such as iodide/triiodide. By regenerating of the electrolyte in the cathode (CE) the circuit will be completed.[14,180] Efficient (near-unity quantum yield) and fast (femtosecond timescale) transfer of light-generated charge carriers across the interface of catechol–photoanode determine the power conversion of the device and prevent photocurrent reduction by inhibiting parasitic back reactions.[180]

Ullah et al. fabricated a photoanode for DSSC using holmium-doped TiO_2 and ZnO (Ho–TiO_2 /ZnO) using pyrocatechol violet dye as a photosensitizer. The catechol containing molecule boosted the efficiency of their device from 1.12% (for Ho–TiO_2/ZnO) to 1.51% (for Ho–TiO_2 /ZnO/dye).[263] Adineh et al.[258] investigated DSSCs using dyes with catechol anchoring moiety and studied photogenerated electron injection mechanism in TiO_2/catechol. They reported the high stability of catechol anchoring group on the TiO_2 surface and showed the DSSC fabricated using this catecholic dye have inconsiderable desorption of dye from the TiO_2 surface after days.[258] Wettstein et al.[14] fabricated a DSSCs using dyes with catechol anchoring moiety and studied photogenerated electron injection mechanism in ZnO/catechol. They reported that the injection of the photoexcited electron is one of the most important processes in DSSC devices. The type of the injection process depends mainly on the anchoring group of the dye. Catechol anchoring group showed type II or direct process. A photoexcited electron of the dye was transferred into the CB of the metal oxide and generated oxidized dye (**Figure 2-5E**). The

process is followed by CT from the electrolyte to the sensitizer (dye). So, a redox couple such as I^-/I_3^- reduced the oxidized dye and regenerated it back. Finally, the circuit is closed by regeneration of the electrolyte in the CE.[14] Also, Nam et al.[15] showed (**Figure 2-5F**) excellent photovoltaic results for the DSSC fabricated from modified TiO_2 with PDA. They reported that larger current density and efficiency values are results of a strong bidentate complex with Ti atoms which leads to the efficient electron injection from PDA to TiO_2 (**Figure 2-5F**).[15]

2.7 Conclusion

Catechol-modified metal oxide systems have garnered significant interest due to their improved stability and enhanced photoabsorption range. Complexation between organic ligands and inorganic metal oxide semiconductors allows the heterosystem to achieve better performance than just metal oxide devices. In this review, we describe how catechol-type ligands enhance the photoabsorption of transition metal oxide semiconductors by creating CT complexes and facilitating type I and type II electron injection processes. Furthermore, the mechanism of the surface adsorption of catechol-type ligands onto metal oxides and the resulting colloidal stability enhancement is also discussed. Various characterization techniques for analyzing and modeling interaction between metal oxide and catechol-type ligand are detailed. Enhancing the absorption spectrum of the metal oxides improves their photoactivity, which allows them to be used in photocatalysis, PEC biosensing, and solar cells applications. Here, we described the principle working mechanisms for these applications and recent trends in how metal oxide/catechol ligand systems are utilized by researchers to achieve high performance in them.

As illustrated in this review, the two most common catechol-type ligands implemented in metal oxide/catechol ligand systems are catechol and dopamine. Although using these two ligands can result in great improvements in colloidal stability and photoabsorption enhancement, there exists

a large group of other catechol-type ligands with potential to offer greater performance. Therefore, further development of new catechol ligands for use in metal oxide/catechol ligand systems is emerging as a new area of technological and scientific interest. Particularly, ligands with a variety of different functional groups are being explored as they can be used as molecular linkers to expand upon the biofunctionalization aspect present in many biomedical applications.[9,239] Despite enhancing optical absorption of metal oxide via catechol-type ligand modification, a significant portion of the solar spectrum remain unused. Therefore, there is a high demand to improve these structures to cover the entire solar spectrum. One of the approaches that is gaining traction in achieving this is to introduce an additional metal oxide or dye molecule in the system to create semiconductor heterostructures, where catechol-type ligands are used as linker.[133,180,225] In these approaches, catechol initially adsorbs at the metal oxide surfaces, which then helps to bind another smaller bandgap semiconductor or dye molecule to create a multitiered band structure that able to significantly enhance photoexcitation and photoabsorption across a broad wavelength range. Finally, another area for potential development is to use catechol ligands as a linker between metal oxides and polymers to create an assortment of different functional materials that can be used as biomimetic materials or antimicrobial coatings.[6,8,240]

2.8 Acknowledgements

This research was funded by the Natural Sciences and Engineering Research Council of Canada.

Chapter 3

Surface modification of TiO_2 for photoelectrochemical DNA biosensors

Preface:

In the previous chapter, we provided background on how catecholate surface modification can be used to enhance photoexcitation efficiency of transition metal-oxide semiconductors in various photocatalytic and photovoltaic applications. The work presented in this chapter uses this background knowledge on catecholate ligands and applies them to TiO_2 NP in order to make material systems suitable for high performance PEC biosensing. The objective of this work was to analyze the influence of various chelating molecules with different functional groups from the catecholate family of ligands to ascertain their influence on the photoabsorption and photoexcitation efficiency of TiO_2 NP.[122] The second objective was to use these results to fabricate an ideal photoelectrode for a high-performance signal-off PEC DNA biosensor[96] by optimizing the catecholate-modified TiO_2 NP material system.

This work primarily focuses on research objective I, in laying the foundation for an ideal TiO_2-based photoactive nanomaterials sensitive PEC biosensing. The catecholate-modified showed significant enhancement in photoexcitation compared to unmodified TiO_2 NP, as demonstrated via UV/vis absorbance spectroscopy, photocurrent density measurements and incident photon-to-electron conversion efficiency tests. Addition of catecholate also improved film morphology of TiO_2 NP, which made for higher quality photoelectrodes with more active sites for biomolecule

binding. In particular, it was found that caffeic acid (CA)-modified TiO_2 and 3,4-dihydroxybenzaldehyde (DHBA)-modified TiO_2 NP are exceptional for improving the base photocurrent signal generation of TiO_2-based photoelectrodes. The CA-modified TiO_2 and DHBA-modified TiO_2 became the foundational material system that all subsequent material systems and bioassays presented in thesis are built upon. CA and DHBA also contain -COOH and -COH functional groups, which will repeatedly prove useful for biofunctionalization probe/capture biomolecules such as ssDNA, antigens, and functional nucleic acids.

The second half of this chapter attends to research objective II, in designing a bioassay with PEC signal transduction using the optimized TiO_2-based material system. We designed a an operationally simple signal-off PEC biosensor[96] for detecting DNA biomarkers in human blood plasma using CA-TiO_2 NP photoelectrodes. This assay was based on the principle of steric hinderance, where obstruction of the photoelectrodes with large molecules limits access to electrolyte species, thereby reducing PEC current generation.; -NH_2 terminated capture probe ssDNA strands were bound to the photoelectrode through carboxamide linking,[264] which can capture target ssDNA strands through DNA hybridization. The deposition of probes and capture of target caused signal decrease; the higher the target concentration was the lower the signal. The specificity of this bioassay was evaluated by comparing complimentary ssDNA target with non-complimentary ssDNA target. A calibration curve was plotted for target range of 100 fM – 100 nM, and the assay showed a linear-logarithmic relation between photocurrent density and target concentration. The LOD was found to be 1.4 pM. Similar to the catecholate-modified TiO_2 material system, this signal-off bioassay became the blueprint for several subsequent assays to be built on. This work also established the optimized protocol for fabrication of photoelectrodes through drop-deposition of TiO_2-bases suspensions on transparent conductive polymer films.

Authors: Sadman Sakib, Richa Pandey, Leyla Soleymani and Igor Zhitomirsky

Publication: Published in Medical Devices and Sensors in February 2020

3.1 Abstract

A photoelectrochemical (PEC) DNA biosensor is developed using surface-modified TiO_2 nanoparticles (NPs) as a sensitive transducer. Different catecholates and gallates are used as sensitizers for TiO_2 NPs. The molecules are adsorbed on TiO_2 via the catecholate type bonding mechanism to enhance light absorption in the visible range. The adsorbed molecules act as charge transfer mediators and enhance photocurrent. Despite the similar bonding mechanism of the molecules, the TiO_2 NPs exhibit significant differences in photocurrent. The modified TiO_2 films showed photocurrent increase in the order: 3,4-dihydroxy-L-phenylalanine < 2,3,4-trihydroxybenzoic acid < 3,4-dihydroxybenzoic acid < 2,3,4-trihydroxybenzaldehyde < 3,4-dihydroxy-phenylacetic acid < 3,4-dihydroxybenzaldehyde < caffeic acid. Testing results provide an insight into the influence of the structure and properties of the organic molecules on their adsorption and photocurrents of modified TiO_2 films. The TiO_2 NPs modified with caffeic acid are used for the fabrication of PEC DNA biosensor by forming photoelectrodes and immobilizing probe single-stranded DNA on their surface. The caffeic acid-modified TiO_2-based photoelectrodes offer the required signal magnitude to distinguish between complementary and non-complementary DNA sequences in the 100 nM–1 pM DNA concentration range and with a limit of detection of 1.38 pM, paving the way towards PEC DNA sensing.

3.2 Introduction

Biosensors are devices that integrate biorecognition with signal transduction for analysing biologically relevant analytes.[104] Recent investigations highlighted the importance of DNA detection, development of advanced detection methods and signal amplification strategies. [265–267] In DNA biosensors, capture event of specific DNA targets through DNA hybridization is translated to a detectible electrochemical,[268] photoelectrochemical,[269] optical[270] or a

mechanical[271] signal. Photoelectrochemical (PEC) signal transduction combines optical excitation with electrochemical readout to increase the sensitivity and reduce the background signal of biosensors (Zhao, Xu, & Chen, 2014).[96] Particularly in PEC DNA biosensors, DNA hybridization is translated to a change in photocurrent[253] with a signal change that is proportional to the concentration of the target DNA sequence.

TiO_2 nanoparticles (NPs) are commonly used for the fabrication of photoelectrodes for PEC DNA biosensors[6,133] and other PEC applications, such as photovoltaic devices[272] and photocatalysis.[173] In PEC devices, photoexcitation leads to charge carrier generation that catalyses an electrochemical reaction.[272] TiO_2 NPs are ideal for PEC-based application due to their high photocatalytic activity, chemical stability, tunability of morphology and crystallinity, ideal conduction band and valence band levels for kick-starting many electrochemical reactions, water insolubility, non-toxicity and low manufacturing cost.[137] In order to fabricate effective PEC biosensors, the photoelectrodes must have a high incident photon-to-electron conversion efficiency (IPCE), which allows for a high electrochemical reaction rate and high photocurrent. The photoelectrodes must be fabricated from materials that offer high photon absorption and low charge carrier recombination rates.

Despite of its suitability as a photoelectrode material, TiO_2 has poor absorption in the visible range, while showing strong absorption in the UV range. This severely limits total light absorption of TiO_2 NPs, which in turn limits IPCE and photocurrent generation. Using UV light as an excitation source would lead to poor performance of PEC biosensors, as many biomolecules, such as DNA, are unstable under UV irradiation. Therefore, TiO_2 NPs must be modified in order to enhance their absorption and photocurrent generation in the visible light range. Several photocurrent amplification strategies have been developed, which allow for

enhanced absorption in the visible light range, improved charge mobility or reduced charge carrier recombination rates of TiO_2 NPs. Such strategies include TiO_2 doping,[273] formation of disordered surface layers,[274] surface modification with quantum dots,[275] plasmonic noble metal NPs[276] and organic ligands.[277] The modification of TiO_2 NPs with various organic ligands is a promising photocurrent amplification strategy[278] due to its relative ease of implementation and effective photoenhancement.

The objective of this investigation was the fabrication of high-performance PEC DNA biosensors and analysis of the influence of chemical structure and properties of organic surface modifier molecules on TiO_2 light absorption properties and photocurrent amplification. Various chelating molecules from the catechol and gallic acid family, containing aldehyde and carboxylic groups, were used. The adsorption mechanism was based on the catecholate type of bonding. The modified TiO_2 NPs showed significant enhancement of photocurrent, compared to the unmodified NPs. Despite the similar bonding mechanism, the different molecules resulted in a significant difference in photocurrent when used for the surface modification of TiO_2 NPs. The results presented below shed new light on the development of surface modifier molecules for TiO_2-based DNA biosensors.

3.3 Experimental Procedures

Materials and Photoelectrode Fabrication:

Caffeic acid (CA), 3,4-dihydroxybenzaldehyde (DHBA), 3,4-dihydroxybenzoic acid (DHB), 3,4-dihydroxy-L-phenylalanine (DOPA), 3,4-dihydroxyphenylacetic acid (DHPL), 2,3,4-trihydroxybenzaldehyde (THBA), 2,3,4-trihydroxybenzoic acid (THB) and indium tin oxide/poly(ethylene terephthalate) (ITO/PET) were purchased from Sigma-Aldrich. TiO_2 nanoparticles (P25, containing 80% anatase and 20% rutile) were obtained from Nippon Aerosil

Co. Ltd. Aqueous suspensions of TiO_2 without additives or containing CA, DHB, DHBA, DOPA, DHPL, THBA and THB additives were prepared. The concentration of TiO_2 in DI water was 0.25 g/L. The mass ratio of TiO_2 to additive was 10:1.

ITO/PET substrates with dimensions of 1.2 cm × 0.7 cm were masked with vinyl to preserve electrical contact area. Substrates were subjected to (oxygen) plasma treatment for 1 min. The substrates were then coated with TiO_2 or modified TiO_2 by dropping 10 µl of the suspension on the substrate surface and baking them in the oven at 85°C for 6 min. This process was repeated three times to deposit three layers.

Material Characterization:

Ultraviolet/visible (UV/Vis) spectroscopy was performed using an OceanviewOptics flame-S-UV-vis-ES assembly. The samples used for UV/vis spectroscopy were solid photoelectrodes. Incident photon-to-electron conversion efficiency measurements were obtained using a Zahner CIMPS-QE/IPCE3 Phtotoelectrochemical Workstation containing a wavelength-adjustable light source (350–650 nm). Incident photon to converted electron measurements were carried out in a three-electrode cell set-up with an electrolyte solution containing 0.1 M phosphate buffered saline (PBS) and 0.1 M ascorbic acid (AA). The following formula was used to convert photocurrent values at specific measured light wavelengths into percentage efficiency:

$$(1) \quad IPCE\ (\%) = \frac{1240 \times J_{photo}(mA\ cm^{-2})}{\lambda(nm) \times I_{inc}(mW\ cm^{-2})}$$

Photoelectrochemical measurements are carried out in a three-electrode cell set-up with a white light source as the photoexcitation source. Platinum (Pt) wire was used as the counter electrode, a silver/silver chloride (Ag/AgCl) electrode for the reference electrode and the TiO_2/catechol-

modified TiO_2 photoelectrodes acting as the working electrodes. The electrolyte solution used contained 0.1 M phosphate buffered saline (PBS) and 0.1 M ascorbic acid (AA). Chronoamperometric PEC curves were measured using a CHI660D electrochemical station, under illumination at 20-s intervals for 100 s. Scanning electron microscopy (SEM, JEOL JSM-7000F microscope) was used for microstructure characterization. Fourier transform infrared (FTIR) spectroscopy data were obtained using a Bruker Vertex 70 spectrometer.

DNA Hybridization and Detection Experiments:

CA-modified TiO_2 photoelectrodes were used for PEC-based DNA detection testing. A solution of 20 mM 1-ethyl-3-(3-dimethylaminopropyl)carbodiimide hydrochloride (EDC), 10 mM N-hydroxysulfosuccinimide (NHS) and 10 mM 2-(N-morpholino)ethanesulfonic acid (MES) was deposited on the photoelectrodes and incubated for 1 hr. This was done in order to facilitate carboxamide linking between CA and amine-terminated probe single-stranded DNA (ssDNA). In the next step, 1 μM amine-terminated probe DNA was deposited on the photoelectrode surface and incubated for 2 hr. Photocurrent was measured at this point to get the after-probe photocurrent. This was followed by deposition of target DNA, which was incubated for 1 hr. The target DNA contained 100 pM of non-complementary (NC) DNA and a variable amount of complementary DNA, ranging from 100 nM to 100 fM. The photoelectrodes were washed between each deposition step with DI water. Photocurrent was once again measured at this point to get after-target photocurrents. Photocurrent measurements of DNA-modified photoelectrodes were done using a CHI660D electrochemical workstation and using a PBS/AA electrolyte solution. All the photocurrents are normalized by adjusting the after-probe photocurrents to the same level and multiplying the after-target photocurrent with the same adjustment factor.

Limit of Detection (LOD) Calculation:

A calibration graph was plotted as a function of the photocurrent density and the concentration of the complementary target DNA used to hybridize with the probe DNA immobilized on the surface of the electrode. All target DNA concentration for LOD measurements were done in the presence of 100 pM NC DNA in order to simulate the effect of non-specific absorption of non-target molecules. The NC DNA can be successfully quantified experimentally with a sensitivity of 0.2 A cm^2 nM^{-1}. Limit of blank (LOB) is calculated by the using equation:

$$(2) \quad LOB = I_{Blank} + 3 \times \sigma_{Blank}$$

where σ_{Blank} is the standard deviation of the blank signal and the factor 3 is used to calculate the limit of detection within a 95% confidence interval. The LOD is then calculated from the regression line by substituting the y value with the LOB.

3.4 Results and Discussion

It was hypothesized that catechol-modified TiO_2 will have enhanced photocurrent generation due to an improvement in absorption spectra. This material can be used to form the basis of a signal-off PEC DNA biosensor (**Figure 3-1**) that has a high dynamic range and low LOD. In such a scheme, the catechol molecules will act as molecular linkers between probe single-stranded DNA (ssDNA) and the photoelectrode. In the presence of target ssDNA, the probe and target will hybridize to from double-stranded DNA (dsDNA) that is attached to the photoelectrode. This event reduces the photocurrent generated by the photoelectrode due to steric hindrance, as the dsDNA makes charge transfer between the photoelectrode and the electrolyte more difficult.

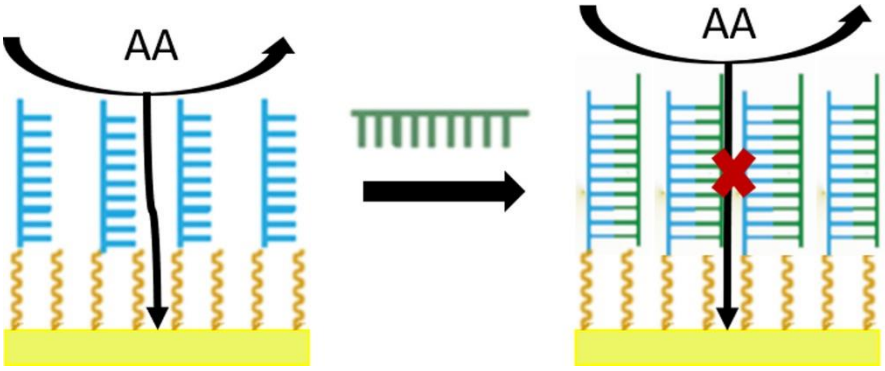

Figure 3-1. DNA detection scheme; the probe DNA (blue) immobilized on the catechol-modified TiO_2 in the presence of ascorbic acid (AA) generates a photocurrent which decreases following the target DNA (green) hybridization due to steric hinderance.

Figure 3-2A shows chemical structures of molecules used in this investigation for modification of TiO_2 NPs. The molecules can be adsorbed by the catechol-type bonding (**Figure 3-2B**), which involves two adjacent phenolic OH groups. The bonding mechanism can be based on bidentate chelating, bidentate inner sphere bridging or bidentate outer sphere bridging of a catechol group to the Ti atoms.[170,187] It is important to note that THB and THBA contain three phenolic OH groups. However, similar to catechol, the bonding mechanism of such molecules involves two adjacent OH groups.[170] Literature data on dopamine adsorption on TiO_2 indicated that functionalization of TiO_2 NPs with catechol enhances electronic and optical properties of TiO_2 by forming charge transfer complexes.[279] DHB, THB, CA and DHPL molecules contain a carboxylic group, which imparts anionic properties to the molecules. The adsorption of the anionic molecules on the TiO_2 NPs allows for electrostatic dispersion and reduced agglomeration. The total charge of the zwitterionic DOPA is influenced by the ionization of amino and carboxylic groups. The amino group of DOPA is protonated below pH = 10, and the positive charge of the protonated amino group compensates the negative charge of the carboxylic group.[170] The carboxylic groups of DHB, THB, CA, DHPL and DOPA can also be involved in the adsorption of such molecules on TiO_2. It was shown that carboxylic groups of aromatic

molecules were involved in their adsorption on surface Ti sites of anatase by forming complexes.[280] However, the interactions of aromatic carboxylic acids with TiO_2 surfaces are relatively weak.[170,216] Investigations showed that carboxylic group of CA was not involved in the CA adsorption on TiO_2.[281] The comparison of catecholates containing different hydrocarbon chains showed that catecholate molecules with longer hydrocarbon chain provided enhanced dispersion of oxide particles and allowed for higher electrophoretic deposition rate.[170]

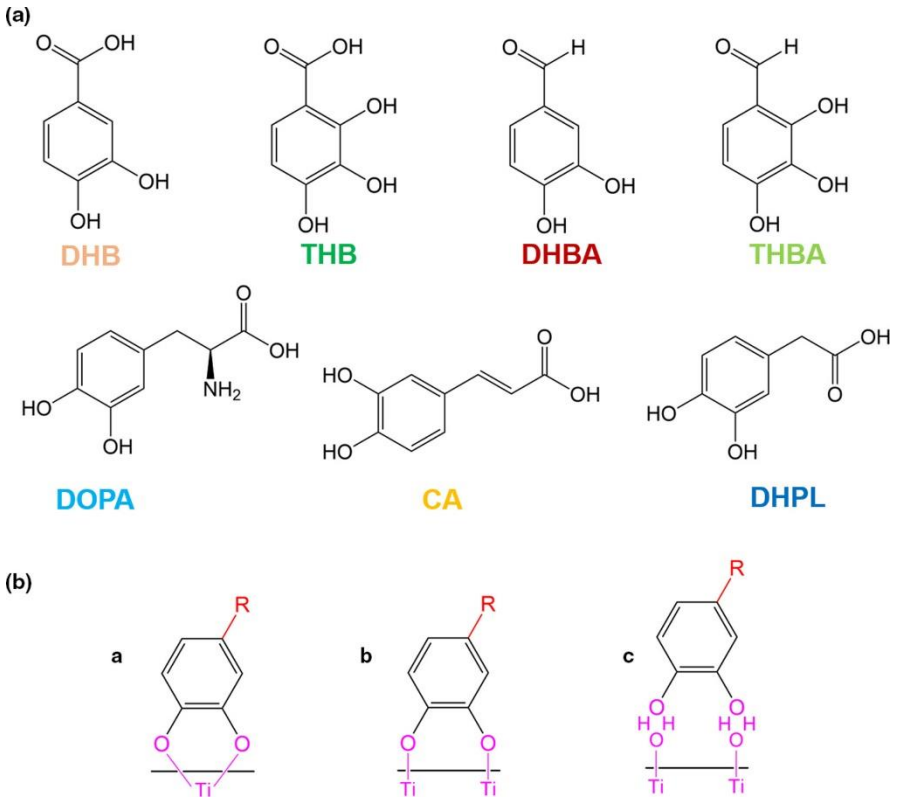

Figure 3-2. (A) Chemical structures of catechol-type molecules and (B) bonding mechanisms of a catechol group to TiO_2 surface: (a) bidentate chelating, (b) bidentate bridging (inner sphere) and (c) bidentate bridging (outer sphere) bonding of catechol group.

Ultraviolet–visible (UV-vis) spectroscopy (**Figure 3**) was performed to confirm the adsorption of the catechol ligands of the selected molecules and study the effect of surface modification on the light absorption of TiO_2 NPs. TiO_2 is a wide-bandgap semiconductor with bandgap ranging from 3.0 to 3.2 eV, which allows for light absorption in the UV range and very poor absorption

in the visible range. Adsorption of catechol molecules on TiO_2 NPs forms complexes that can be excited by visible light and can inject electrons into the conduction band of TiO_2.[168] This has the effect of the semiconductor absorbing more light in the visible range and having higher overall light absorption.[282,283] In comparison with non-functionalized TiO_2, the UV–visible spectra of all the catechol-functionalized TiO_2 samples showed red shifting, thus confirming adsorption. The TiO_2 NPs, modified with CA, DHBA, DHPL and THBA, showed an increase in absorbance across their entire spectra. The improved absorption of the catechol-modified TiO_2 NPs was expected to correlate with their improved photocurrent.

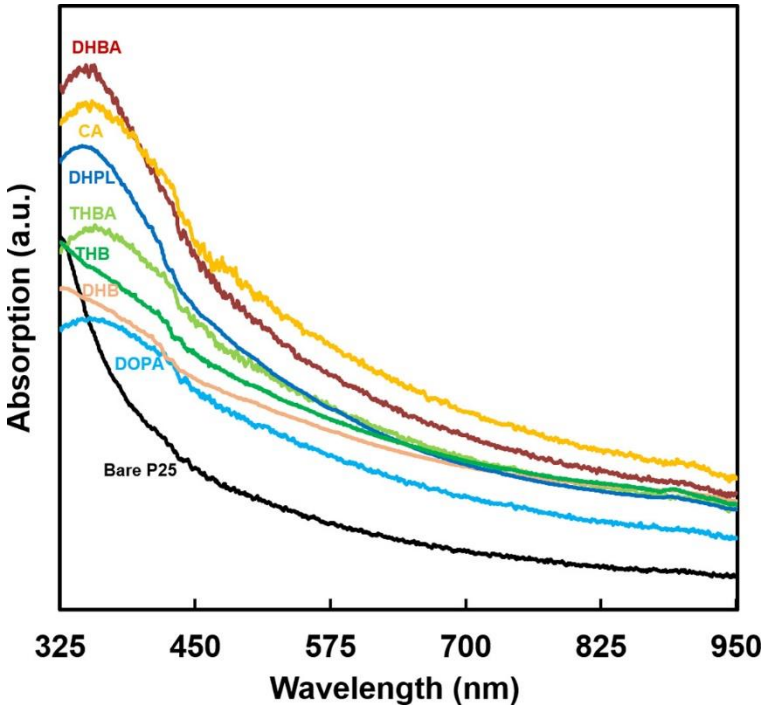

Figure 3-3. UV/vis absorbance spectroscopy of catechol-modified TiO_2.

Scanning electron microscopy (SEM) was used to characterize the surface of photoelectrodes fabricated from CA-modified TiO_2. **Figure 3-4A** shows an SEM image of the surface of a photoelectrode fabricated from unmodified TiO_2. Similarly, **Figure 3-4B** shows an SEM image

of the surface of a photoelectrode fabricated from CA-modified TiO_2. Bare TiO_2 demonstrates agglomerates and has poor surface coverage. Modification via CA resulted in reduced agglomeration and improved surface coverage. The improved film morphology was beneficial in order to achieve increased photocurrent by optimizing charge transfer throughout the film. Fourier transform infrared (FTIR) spectroscopy was also performed on the TiO_2 samples to confirm the CA adsorption on TiO_2. **Figure 3-4C** displays the FTIR spectra of powdered forms of bare TiO_2, CA and CA-modified TiO_2. In the wavenumber range of 1,000–2,000 cm^{-1}, bare TiO_2 shows no discernable peaks. CA showed several series of peaks in the 1,500–1,620 cm^{-1} range corresponding to C–C and C=C ring vibrations, a major peak at 1,148 cm^{-1} corresponding to aromatic C=C stretching, a peak at 1,641 cm^{-1} corresponding to acyclic C=C stretching and peaks in the 1,100^{-1}, 300 cm^{-1} corresponding to C–O stretching (Kim, & Hwang, 2016; Li, Wu, & Zhitomirsky, 2010; Wu et al., 2010). [187,284,285] These peaks were also observed in the CA-modified TiO_2 samples, which confirmed that CA molecules were indeed absorbed onto the surface of the TiO_2 NP.

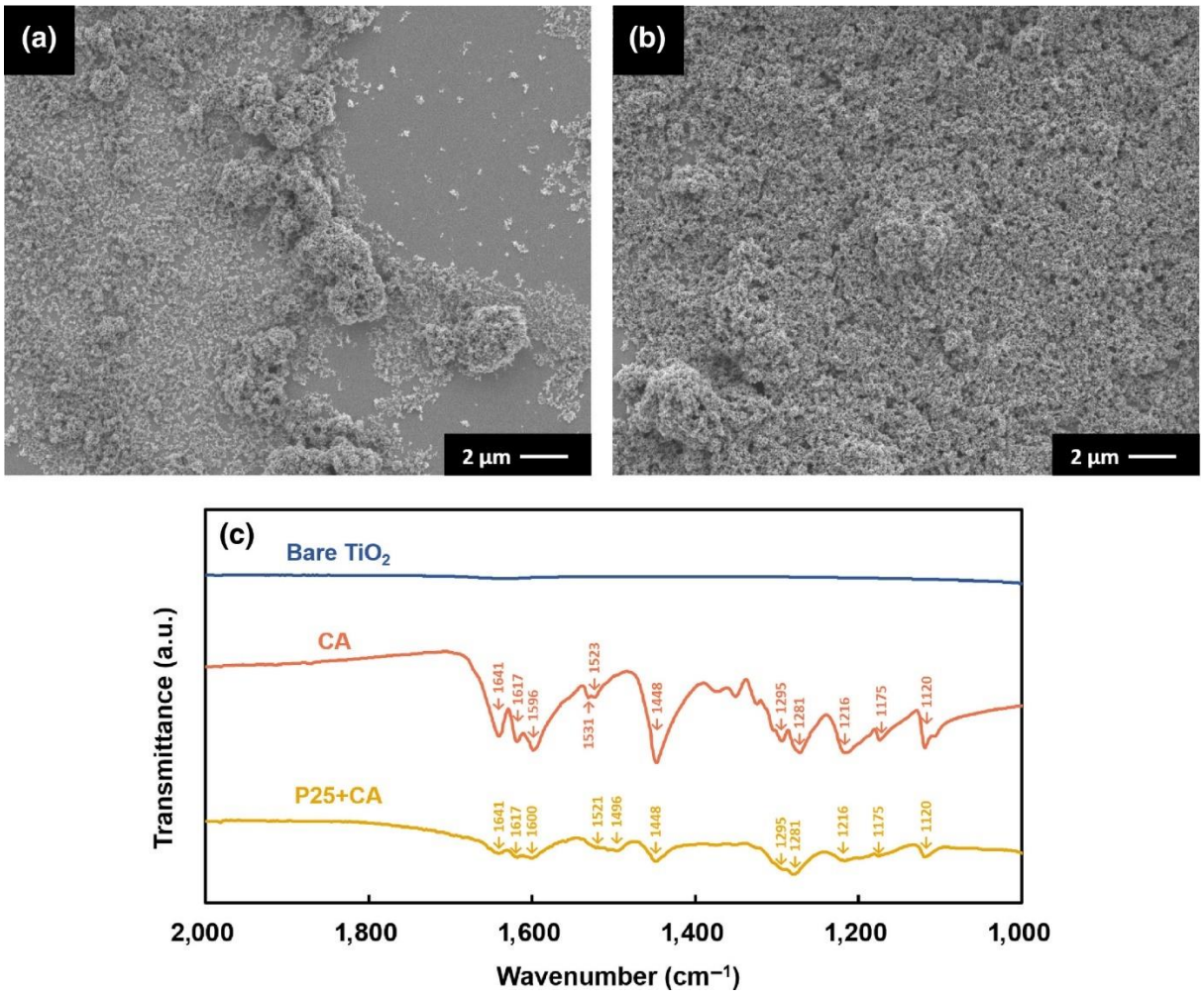

Figure 3-4. SEM image of photoelectrodes fabricated from (A) bare TiO_2 and (B) CA-modified TiO_2; (C) FTIR spectroscopy of bare TiO_2, CA and CA-modified TiO_2 powders.

The catechol-modified TiO_2 NPs were used to fabricate photoelectrodes, which were tested to see whether they would improve PEC current generation. This photocurrent testing was performed in a three-electrode electrochemical cell, with the photoelectrode acting as the working electrode and using an electrolyte containing AA as a hole scavenger. **Figure 3-5** shows the photocurrent density measurements for each sample. The potential of the PEC cell was held constant, and the working electrode was irradiated with white light at 20 s intervals for 100 s, in order to generate a chronoamperometric curve (**Figure 3-5A**). When TiO_2 is irradiated with light having energy greater than its bandgap, an electron–hole pair is generated that initiates a redox

reaction.[132] Ascorbic acid is oxidized at the working electrode/electrolyte interface by the holes in the valence band of TiO_2. This action generates a measurable anodic PEC current (**Figure 3-6, inset**).[286] **Figure 3-5B** shows a summary of the average photocurrent density generated by tested samples and their standard deviation. The averages were calculated by taking the moving average of the ON periods of the chronoamperometric curves. Significant improvement in the photocurrent density from bare TiO_2 was observed when TiO_2 NPs were functionalized with catechol molecules. The catechol-modified systems when ordered from highest to lowest photocurrent density are CA > DHBA > DHPL > THBA > DHB > THB > DOPA. The photocurrent density measurements confirmed that the improved UV/vis absorption also correlates with improved PEC current generation. This behaviour is consistent with the known phenomenon of density of state of TiO_2 shifting from the forbidden energy band into the CB and allowing for visible light to excite TiO_2 and improve charge carrier generation.[287] By comparing the photocurrents to the corresponding catechol molecule chemical structures (**Figure 3-2A**), it can be observed that ligands with -COH groups (e.g., DHBA, THBA) give higher photoenhancement than those containing -COOH groups (e.g., DHB, THB). It is further observed that ligands with longer hydrocarbon chains (e.g., CA, DHPL) tend to provide better photoenhancement than those with short chains (e.g., DHBA, THB, DHB). To further analyse the relationship between catechol ligand length, functional groups and photoenhancing properties, IPCE measurements were performed. **Figure 3-6** displays the IPCE measurements for bare TiO_2, CA-modified TiO_2, DHBA-modified TiO_2 and DHB-modified TiO_2. DHBA has a -COH groups, whereas DHB has a -COOH group, but both molecules have similar structures. CA and DHB both have a -COOH group at the end of their hydrocarbon chains, but the chain in CA is longer than that in DHB. The longer hydrocarbon chain can result in better dispersion of TiO_2

particles, which in turn is beneficial for their interaction with CA. Moreover, the poor solubility of CA in water is beneficial for CA adsorption on TiO_2. The IPCE results show that catechol functionalization enhanced PEC response of TiO_2 in the near-UV region and visible part of the spectra, while reduced PEC response in the UV region. This is why irradiation with white light results in very high photocurrent generation in catechol-functionalized TiO_2, when compared with no functionalization. CA exhibits broader IPCE peak that results in higher PEC response in the visible range and allows for better photoenhancement. It is important to note that the electric charge of dissociated CA and longer hydrocarbon chain are beneficial for dispersion of TiO_2 NPs. The reduced agglomeration of TiO_2 in CA solutions and poor solubility of CA in water are beneficial for CA adsorption on TiO_2. As a result, the CA-modified TiO_2 NPs system displays the best photocurrent compared to the all the other catechol-modified TiO_2 systems in the photocurrent data in **Figure 3-5A and 3-5B**. Therefore, CA-modified TiO_2 was chosen as the basis for a PEC DNA biosensor.

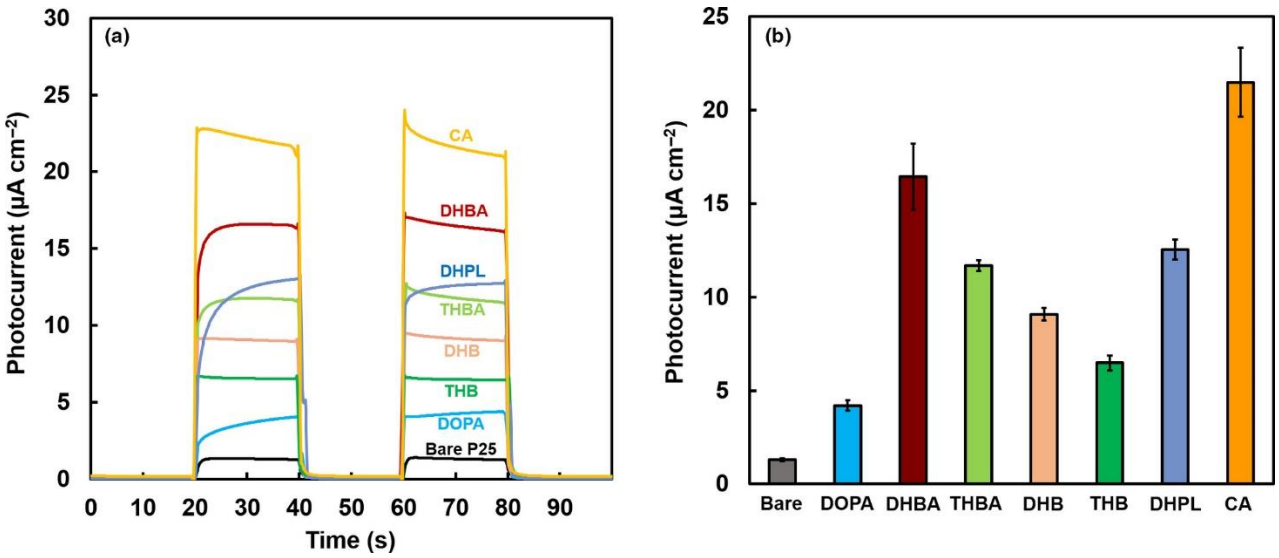

Figure 3-5. Photocurrent densities for photoelectrode films of TiO2 modified with different catechol-type molecules: (A) chronoamperometric curves and (B) photocurrent response summary.

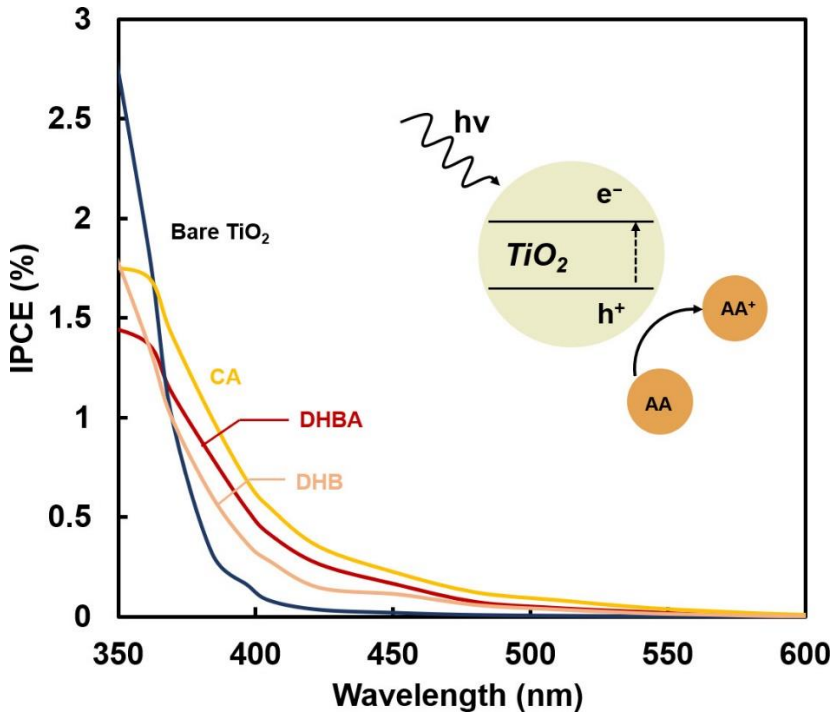

Figure 3-6. IPCE for bare TiO_2, CA-modified TiO_2, DHBA-modified TiO_2 and DHB-modified TiO_2 photoelectrodes. The inset illustrates photocurrent generation via the oxidation of ascorbic acid when TiO_2 is photoexcited**.**

The key to fabricating effective PEC biosensors is to have signal transduction elements that provide high dynamic range and a low limit of detection (LOD), which can be achieved by having a high photocurrent.[41,96] Surface modification with CA provided dual functionality to the TiO_2 NPs photoelectrodes: It enhanced their PEC response and through the -COOH functional group provided a molecular linker for attaching -NH_2 terminated probes that capture target DNA. **Figure 3-7** illustrates different steps in the fabrication and operation of the DNA biosensor. The biorecognition elements in PEC DNA biosensors are composed of probe single-stranded DNA (ssDNA). Target ssDNA is captured by the probes via the DNA hybridization process, in which two complementary ssDNA combine to produce double-stranded DNA (dsDNA).[96,288] The main principle for PEC DNA detection is that the photocurrent would undergo amplification or attenuation due to DNA hybridization on the photoactive substrate; therefore, DNA can be detected by comparing the signal before and after hybridization. **Figure 3-7B** shows the first

operational step in which CA-modified TiO_2 NPs were deposited on an ITO substrate to form a photoactive film. **Figure 3-7C** shows the probe immobilization step, in which a layer of -NH_2 terminated ssDNA is deposited on the CA-modified TiO_2 layer. The -COOH groups of the CA ligands were covalently bonded to the -NH_2 termination of the ssDNA to form a carboxamide link.[177,264] **Figure 3-7D** shows the target capture stage, in which a solution containing complementary target ssDNA is deposited on top of the probe layer and DNA hybridization occurs.

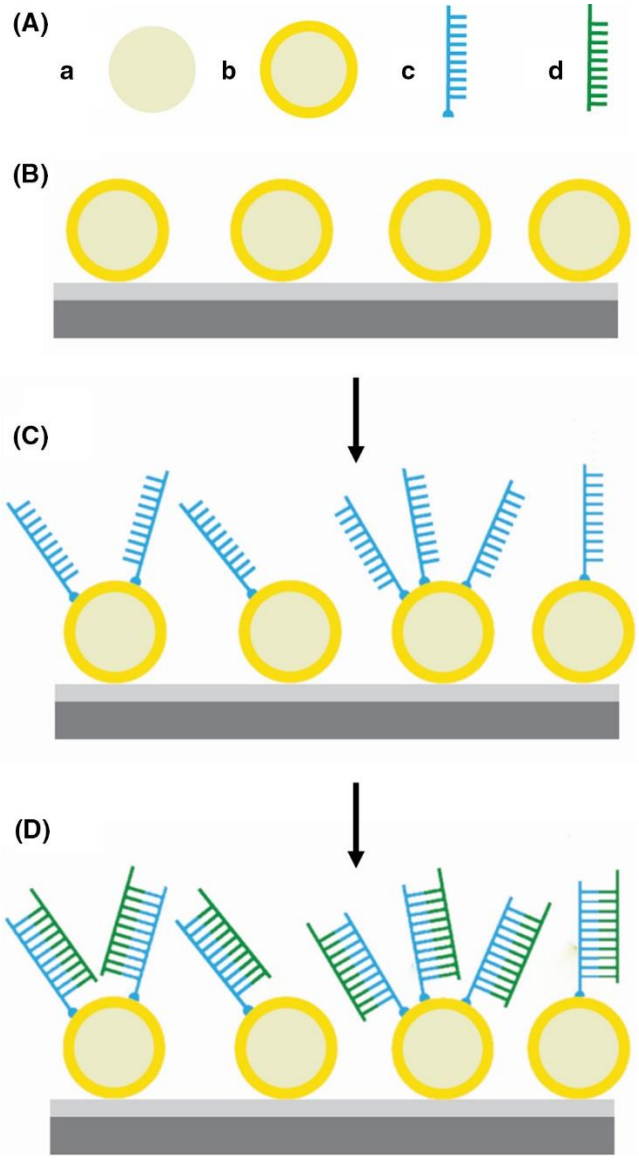

Figure 3-7. (A) Schematic of (a) unmodified TiO_2, (b) CA-modified TiO2, (c) probe DNA and (d) target DNA, and (B–D) fabrication of films on ITO-PET substrate: (B) deposition of CA-modified TiO2, (C) modification with probe DNA and (D) hybridization with target DNA.

Figure 3-8A shows the change in photocurrent of the CA-modified TiO_2 photoelectrodes after the probe deposition stage and the target capture stage (100 nM complementary + 100 pM NC, only 100 nM complementary and 100 nM complementary in undiluted human plasma). The photocurrent decreases after probe deposition and decreases further after target capture. Probe immobilization causes photocurrent decrease by limiting the access of AA from the solution to the photoelectrode surface.[253] Complementary target causes further photocurrent decrease by causing increased steric hindrance when it hybridizes with the probe to form dsDNA.[289] Depositing non-complementary ssDNA results in a slight decrease in photocurrent (less than 10%), which could be attributed to non-specific DNA adsorption on the photoelectrode surface .[96,290] The photocurrent signal decreases by around 18% if the target DNA detection is done in plasma rather than in DI water, due to the non-specific binding protein onto the photoelectrode surface.[291] This forms the basis for a signal-off type PEC DNA biosensor.[96,274] Under optimized experimental conditions, an amperometric technique was utilized to demonstrate the DNA biosensing ability of the CA-modified TiO_2 photoelectrodes under visible light irradiation.

Figure 3-8B shows the photocurrent measurement of the fabricated sensor with logarithmically decreasing target ssDNA concentration, ranging from 100 fM to 100 nM. Current density was observed to decrease gradually as target concentration was increased. A linear dynamic range between the current density and the log of concentration of the DNA was obtained in the linear range of 1 pM–100 nM, which resulted in a LOD of 1.4 pM The dashed line in the graph represents the average signal of the blank measurement with the positive and negative standard deviation for a signal-to-noise ratio of 3. Hence, the concentration falling above this line is not resolvable from the blank signal. All target DNA concentration measurements were done in the

presence of 100 pM NC DNA in order to simulate the effect of non-specific absorption of non-target molecules. The NC DNA can be successfully quantified experimentally with a sensitivity of 0.2 nA cm^2 nM^{-1}. It is evident from this investigation that the TiO_2 modification with CA is the basis for high-performance signal-off PEC DNA biosensors with a high dynamic range and low LOD. Some recent examples in literature[64] of PEC DNA biosensors are as follows: CdS/MoS_2 heterojunction-based electode (LOD = 0.39 fM, linear range = 1 fM–100 pM),[292] CdS/Ag NP electrodes (LOD = 0.2 fM, linear range = 1 fM–100 pM)[293] and Au NP-modified TiO_{2-X} electrodes (LOD = 0.6 pM, linear range = 100 nM).[294] The main advantage our system offers is its ease of fabrication and operation due to the ease of surface modification of TiO_2 with caffeic acid. Additionally, our system boasts a very high linear range when compared against similar systems in literature.

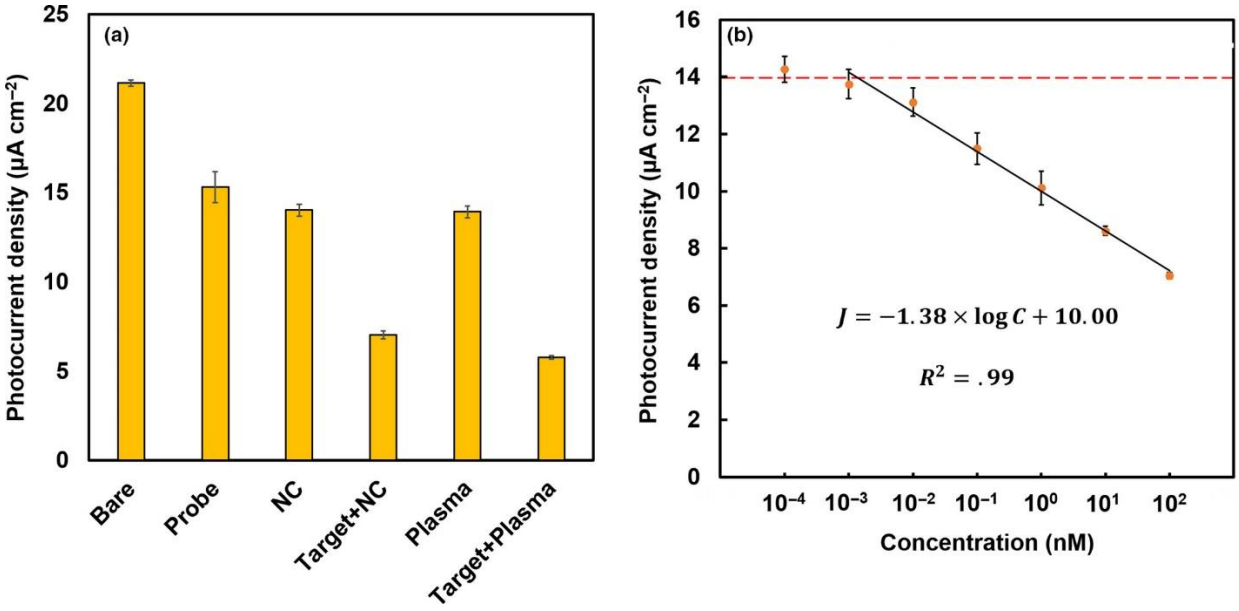

Figure 3-8. (A) Photocurrent density of CA-modified TiO_2: bare, after probe modification, after target hybridization (only NC), after target hybridization (both complementary and NC), after target hybridization in undiluted blood plasma (no complementary target) and after target hybridization in plasma (complementary target present). (B) Calibration curve plotting photocurrent density as a function of complementary target DNA concentration. The inset shows the slope of the linear trendline fitted to the curve showing the dynamic range of the biosensor,

represented by the equation $J = 1.38 * log\ C + 10$ (J = photocurrent density [μA cm^{-2}], C = concentration of target ssDNA [nM]) with $R^2 = .99$. The red dashed line delineates the average signal and the standard deviation of the blank measurement.

3.5 Conclusions

A PEC DNA biosensor has been developed using modified TiO_2 as a sensitive transducer. Different catecholates and gallates were used as sensitizers for TiO_2 nanoparticles. The molecules were adsorbed on TiO_2 via the catecholate type bonding mechanism and enhanced light absorption in the visible range. The adsorbed molecules acted as charge transfer mediators and enhanced photocurrent. Despite the similar bonding mechanism, the modified TiO_2 NPs exhibited significant difference in photocurrent from the different molecules tested. The modified TiO_2 films showed photocurrent increase in the order: DOPA < THB<DHB < THBA < DHBA < CA. The enhanced PEC performance of CA-modified TiO_2 films can be attributed to reduced agglomeration of the modified particles and enhanced adsorption of CA. The TiO_2 nanoparticles modified with CA were used for the fabrication of PEC DNA biosensors by immobilization of probe single-stranded DNA using the carboxamide The TiO_2–CA-based photoelectrodes showed the required signal magnitude to distinguish between complementary and non-complementary DNA sequences in the linear range of 1 pM–100 nM and with an LOD of 1.4 pM, paving the way towards PEC DNA sensing.

3.6 Acknowledgement

The authors gratefully acknowledge the Natural Sciences and Engineering Research Council of Canada for the financial support. Soleymani is the Canada Research Chair (Tier II) in Miniaturized Biomedical Devices and is supported by the Canada Research Chair Program.

Chapter 4

Photoelectrochemical IL-6 Immunoassay Manufactured on Multifunctional Catecholate-Modified TiO_2 Scaffolds

Preface:

Chapter 3 detailed the benefits of surface modification of TiO_2 with catecholate ligands for photoexcitation enhancement, colloidal stabilization and improved biofunctionalization. This chapter builds on the work in the previous chapter in introducing nanomorphology tuning for TiO_2 further improve PEC biosensors by creating nonporous photoelectrode with high internal surface area. The most commonly used TiO_2 nanomaterial morphology for PEC applications are NPs due to their high surface area-to-volume ratio.[64,122,272] Despite this, films fabricated from TiO_2 NP have relatively small usable surface areas due to the compact form factor of TiO_2 NP, which makes the interior of the photoelectrode inaccessible to reactive species.[5,97,114,272] The work in this chapter addresses this by synthesizing three-dimentional (3D) TiO_2 nanostructures as alternates to TiO_2 NP as a photoelectrode material. Additionally, 3D TiO_2 nanostructures showed also improved photoexcitation compared to their NP counterparts due to increased charge carrier migration and reduced charge carrier recombination rates, due to electron-hole pairs being less localized.[5,114]

This chapter continues the work on research objective I and the search for ideal TiO_2-based photoactive material system for use in PEC biosensors. The work in this chapter aims to improve

TiO_2-based material systems by through nanomaterial morphology tuning. In the course of this work, we developed a novel acid-hydrothermal synthesis technique for TiO_2 nanostructures, that allowed us to tune TiO_2 nanostructures to form radially symmetric clusters of nanorods. From the previous work, we learned that catecholate ligands like CA or DHBA have strong binding affinity to TiO_2 surface and will easily bind in an aqueous suspension without any special conditions such increased temperature or non-neutral pH.[9] We took advantage of this phenomenon and added CA and DHBA *in-situ* during synthesis. It was found through XRD analysis that CA and DHBA preferentially bind to specific crystal facets of TiO_2 and inhibit their growth to create nanorod clusters.[189,190,295] FTIR spectroscopy results showed that after synthesis via this method degrades the ligands on the TiO_2 nanostructure surface, so they were fortified with additional CA or DHBA after synthesis for increased PEC signal generation.

The work in this chapter also continues furthering research objective II, by creating another bioassay for detecting ilterleukin-6 (Il-6) antigens using 3D TiO_2 nanostructures. IL-6 is a protein biomarker that plays key roles in immunomodulation, hematopoiesis and inflammatory processes in the human body.[296] Elevated levels of IL-6 can be used as evidence for diagnosis of various cancers and autoimmune disorders and even show the progression of COVID-19.[296,297] In this work, we developed a direct signal-off immunoassay for IL-6 detection in human blood plasma using DHBA-modified 3D TiO_2 nanostructures as photoelectrode material. Surface modification with DHBA was used to modify the properties of TiO_2 nanostructures in a three-pronged approach of nanomorphology tuning, photocurrent signal enhancement, and facilitating bioconjugation. This bioassay works very similar to the previous assay presented in chapter 3, except the capture antibody (anti-Il-6) is bound to the photoelectrode through Schiff-base interaction between -COH functional groups of DHBA and free -NH_2 groups of the capture

antibody. The specificity of this assay was evaluated by comparing signal change against a non-specific protein target (bovine serum albumin (BSA)). A calibration curve was plotted for target range of 0 – 2000 pg mL^{-1}, and the assay showed a linear-logarithmic relation between photocurrent density and target concentration. The LOD was found to be 3.6 pg mL^{-1}. Immunesensors like this device are critically important in clinical settings due to their roles in detecting inflammatory processes, autoimmune disorders, cardiovascular disorders and cancers. Detection of proteins in addition to DNA further helped demonstrate the robustness of PEC signal transduction in biosening.

Authors: Sadman Sakib, Amin Hosseini, Igor Zhitomirsky, and Leyla Soleymani

Publication: Published in ACS Applied Materials & Interfaces in October 2021

4.1 Abstract

There is an increasing interest in using photoelectrochemistry for enhancing the signal-to-noise ratio and sensitivity of electro-chemical biosensors. Nevertheless, it remains challenging to create photoelectrochemical biosensors founded on stable material systems that are also easily biofunctionalized for sensing applications. Herein, a photoelectrochemical immunosensor is reported, in which the concentration of the target protein directly correlates to a change in the measured photocurrent. The material system for the photoelectrode signal transducer involves using catecholate ligands to modify the properties of TiO_2 nanostructures in a three-pronged approach of morphology tuning, photoabsorption enhancement, and facilitating bioconjugation. The catecholate-modified TiO_2 photoelectrode is combined with a signal-off direct immunoassay to detect interleukin-6 (IL-6), a key biomarker for diagnosing and monitoring various diseases. Catecholate ligands are added during hydrothermal synthesis of TiO_2 to enable the growth of three-dimensional nanostructures to form highly porous photoelectrodes that provide a three-dimensional scaffold for immobilizing capture antibodies. Surface modification by catecholate ligands greatly enhances photocurrent generation of the TiO_2 photoelectrodes by improving photoabsorption in the visible range. Additionally, catecholate molecules facilitate bioconjugation and probe immobilization by forming a Schiff-base between their−COH group and the−NH_2 group of the capture antibodies. The highest photocurrent achieved herein is 8.89 μA cm^{-2}, which represents an enhancement by a factor of 87 from unmodified TiO_2. The fabricated immunosensor shows a limit-of-detection of 3.6 pg mL^{-1} and a log−linear dynamic range of 2−2000 pg mL^{-1} for IL-6 in human blood plasma.

4.2 Introduction

Biosensors are devices that couple biorecognition elements with signal transduction mechanisms to quantify and analyze biologically relevant analytes.[104] Research in the field of biosensing is increasingly focusing on improving real-time health monitoring, point-of-care diagnosis, treatment selection, and monitoring of treatment response.[64,97,104,134,298] Recent investigations have highlighted the importance of protein biosensing for the reliable detection of inflammatory processes, autoimmune disorders, cardiovascular disorders, and cancers.[140,299–301] Among the signal transduction methods used for signal readout in biosensors, photoelectrochemical (PEC) readout has generated tremendous interest due to its low limit-of-detection (LOD),[302] high sensitivity,[97] and broad linear dynamic range.[96] In PEC signal transduction, light and electricity are used as input and output signals, respectively. This decoupling of input and output signals in conjunction with photo amplification strategies allows for the creation of highly sensitive biosensors.[64,97,133] Given the possibility of optical biasing in PEC biosensors, these systems are operated at lower applied electrical potentials compared to their electrochemical counter-parts, which reduces the background signals caused by interfering electrochemical signals, thus enhancing the signal-to-background ratio and limit-of-detection of PEC biosensors.[64,97,133] In PEC immunosensors used for protein biosensing, biorecognition occurs on the surface of the photoelectrode, on which photon-enabled electrochemical reactions are measured.[97] It is desirable for photoelectrodes used in PEC biosensing to have high incident photon-to-converted electron efficiency to increase the electrochemical reaction rate and the resultant photocurrent.[97,133]

TiO_2 is commonly used as the photoactive material in PEC biosensing[6,9,303–306] due to its high photocatalytic efficiency, chemical stability, tunable morphology, water insolubility, low

toxicity, low cost, and ideal conduction and valence band levels for driving electrochemical reactions.[64,137,272] However, unmodified TiO_2 has poor light absorption in the visible range[6,9] along with high photogenerated charge carrier recombination rate, limiting its photocurrent generationefficiency.[137,272] To overcome these limitations, researchers have employed various photoabsorption and photocurrent amplification strategies that couple TiO_2 with plasmonic noble metal nanoparticles (NP),[128] quantum dots,[307] metal-oxides with different bandgaps,[5] and organic ligands.[260] The surface modification of TiO_2 nanostructures with organic ligands, particularly catecholate ligands, is a very promising photo-absorption and photocurrent amplification strategy due to their strong adsorption onto the surface of metal oxides and the resultant formation of charge transfer complexes.[5,9,170]

The most commonly used TiO_2 structures used in PEC biosensing are nanoparticles due to their high surface area to volume ratio.[64,97,272,304] In spite of this, when TiO_2 nanoparticles are made into films deposited onto photoelectrodes, a large fraction of their surface area is inaccessible due to their compact form factor, thus limiting their interaction with the electrolyte and their available surface area for modification with biorecognition layers. Three dimensional (3D) nanostructures mitigate this problem by forming porous photoelectrodes, through which they improve electrolyte and biomolecular access. Additionally, 3D nanostructures improve photocurrent generation by increasing charge carrier migration and reducing charge recombination rate, since charge carriers are less localized compared to nanoparticles.[5,97,114,272]

Here, we sought to create 3D TiO_2 nanostructures that yielded a porous architecture desirable for biosensing, had enhanced PEC current generation in the visible light compared to unmodified TiO_2 nanostructures, and could be easily functionalized with biorecognition elements for biosensing. For this purpose, we used multifunctional catecholate molecules. Catecholate

ligands are known to strongly adsorb onto the surface of TiO_2.[9,170,187] As such, researchers have demonstrated that surface modification of TiO_2 nanostructures with catecholate ligands is an excellent photoexcitation enhancement strategy.[9,173,180,185] The TiO_2−catecholate ligand complex is utilized in various applications such as PEC biosensing,[6,9] water splitting,[12,173,185] solar cells,[34−36] and photocatalytic pollutant degradation.[13,159,194] Previous studies have primarily focused on enhancing the photoexcitation of the TiO_2-catecholate ligand complex by adding catecholate ligands to pre-synthesized TiO_2 nanostructures. The formation and performance of TiO_2−catecholate complexes is influenced by the chemical structure of the catecholate molecules. The chemical properties and electric charge of the functional groups of catecholate ligands influence their solubility, adsorption on TiO_2 particles, strength as dispersing agents, photovoltaic performance of the complexes, and their interactions with other components of the biosensors. As such, in situ modification of TiO_2 using catecholates as capping and dispersing agents for synthesis is promising for tuning the morphology and properties of TiO_2 structures. The goal of this work was to take advantage of the strong surface adsorption property of catecholate ligands to tune the morphology of TiO_2 during synthesis to produce 3D TiO_2 nanostructures that were able to form highly porous photoelectrodes. The catecholate surface modification was also hypothesized to enhance photocurrent generation in the 3D TiO_2 nanostructures by improving photoabsorption and charge. Lastly, the functional groups on the catecholate molecules would allow facile functionalization of the photoelectrodes with biorecognition elements.

The developed 3D TiO_2 photoelectrodes were functionalization with biorecognition elements for creating a biosensor for analyzing interleukin-6 (IL-6), a biomarker with key roles in immunomodulation, hematopoiesis, and inflammation processes in the human body. IL-6 levels

in the body are linked to several cancers and diseases such as meningitis, Alzheimer's disease, rheumatoid arthritis, lymphoma, myeloma, or psoriasis.[296,308,309] The results presented below reveal key insights into development of new material systems for the fabrication of high performance PEC biosensors.

4.3 Results and Discussion

With the purpose of creating 3D TiO_2 nanostructures, we explored the addition of catecholate molecules during the acid-hydrothermal synthesis of TiO_2. 3,4-Dihydroxybenzaldehyde (DHBA) and caffeic acid (CA) were the catecholate molecules used for the TiO_2 synthesis process (**Figure 4-1A**). The common structural features shared by catecholate molecules is the presence of an aromatic ring with two adjacent phenolic −OH groups. The chemical structures of the molecules also included a short hydrocarbon chain that ends in various functional groups. In the case of DHBA and CA, their hydrocarbon chains end in −COH and −COOH groups, respectively.[170,187] Catecholate ligands readily adsorb onto the surface of metal oxide particles via bidentate bonding (**Figure 4-1B**).[9,170,187] In this bonding mechanism, surface Gibbs energy is minimized when adsorbed water molecules dissociate to produce a hydroxylated surface. The bidentate type bonding occurs via the surface adsorption process, when two adjacent phenolic −OH groups are deprotonated and coordinate with the metal cation through dehydration of the surface hydroxyl groups or by outer sphere bonding.[195,199,200]

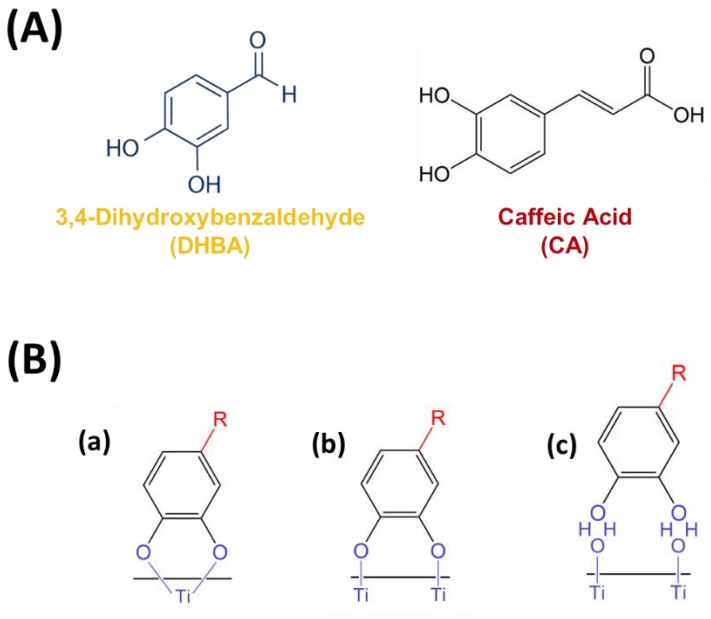

Figure 4-1. (A) Chemical structures of catecholate molecules used for modifying TiO_2, (B) bonding mechanisms of a catechol group to TiO_2 surface: (a) bidentate chelating, (b) bidentate bridging (inner sphere), and (c) bidentate bridging (outer sphere) bonding of catechol group. R group represents −CH−CH−COOH for CA and −COH for DHBA.

Seven different TiO_2 nanostructures were synthesized using a standard acid-hydrothermal synthesis procedure[310] and CA or DHBA was added in situ to observe changes in the morphology and PEC response of the nanostructures: bare TiO_2, CA-TiO_2 (IS), DHBA-TiO_2 (IS), CA-TiO_2 (PS), DHBA-TiO_2 (PS), CA-TiO_2 (IPS), and DHBA-TiO_2 (IPS). Bare TiO_2 refers to the unmodified sample that did not have any catecholate molecules added during or after the synthesis process. CA-TiO_2 (IS) and DHBA-TiO_2 (IS) refer to samples that had CA or DHBA added during synthesis. CA-TiO_2 (PS) and DHBA-TiO_2 (PS) are samples that were first synthesized as the bare TiO_2, but had CA or DHBA added to them after synthesis. Lastly, the CA-TiO_2 (IPS) and DHBA-TiO_2 (IPS)samples had CA or DHBA added both during and after synthesis. The bare TiO_2 were composed of aggregated nanorods that radially extended outward; whereas, the CA-TiO_2 (IS) and DHBA-TiO_2 (IS) were made of more loosely packed nanorods and were surrounded by nanoparticles (**Figure 4-2A**). These new morphologies are attributed to

DHBA and CA readily adsorbing onto the surface of TiO_2 nanostructures as they form, stabilizing their surface to prevent aggregation. When the TiO_2 nanostructures are deposited on to a planar substrate they form a nanoporous surface, as shown by SEM imaging (**Figure 4-2B**). As shown in the XRD data, both the CA-TiO_2 (IS) and DHBA-TiO_2 (IS) predominantly contain the rutile phase, with small amounts of anatase and negligible amount of brookite phase impurities (**Figure 4-2C**). The shape of the diffraction peaks suggests that all the synthesized particles have high crystallinity; however, the CA-TiO_2 (IS) and DHBA-TiO_2 (IS) showed lower crystallinity than the unmodified particles. With the addition of surfactants that have preferential binding affinity for specific crystal facets, it is possible to control the growth of TiO_2 nanostructuresduring synthesis.[189,190,295] On the basis of density functional theory models, catecholate ligands are known to preferentially adsorb on to the {110} facet of rutile TiO_2.[191] It is proposed that CA and DHBA, preferentially adsorb onto the {110} facet of TiO_2 during acid-hydrothermal synthesis, preventing further growth. This encourages anisotropic growth of TiO_2 on other crystal facets with high surface energies. This is supported by the XRD data, where we see that the {211} diffraction of peak of the CA-TiO_2 and DHBA-TiO_2 are higher than the {110} diffraction peaks, whereas the opposite is the case for the bare TiO_2.

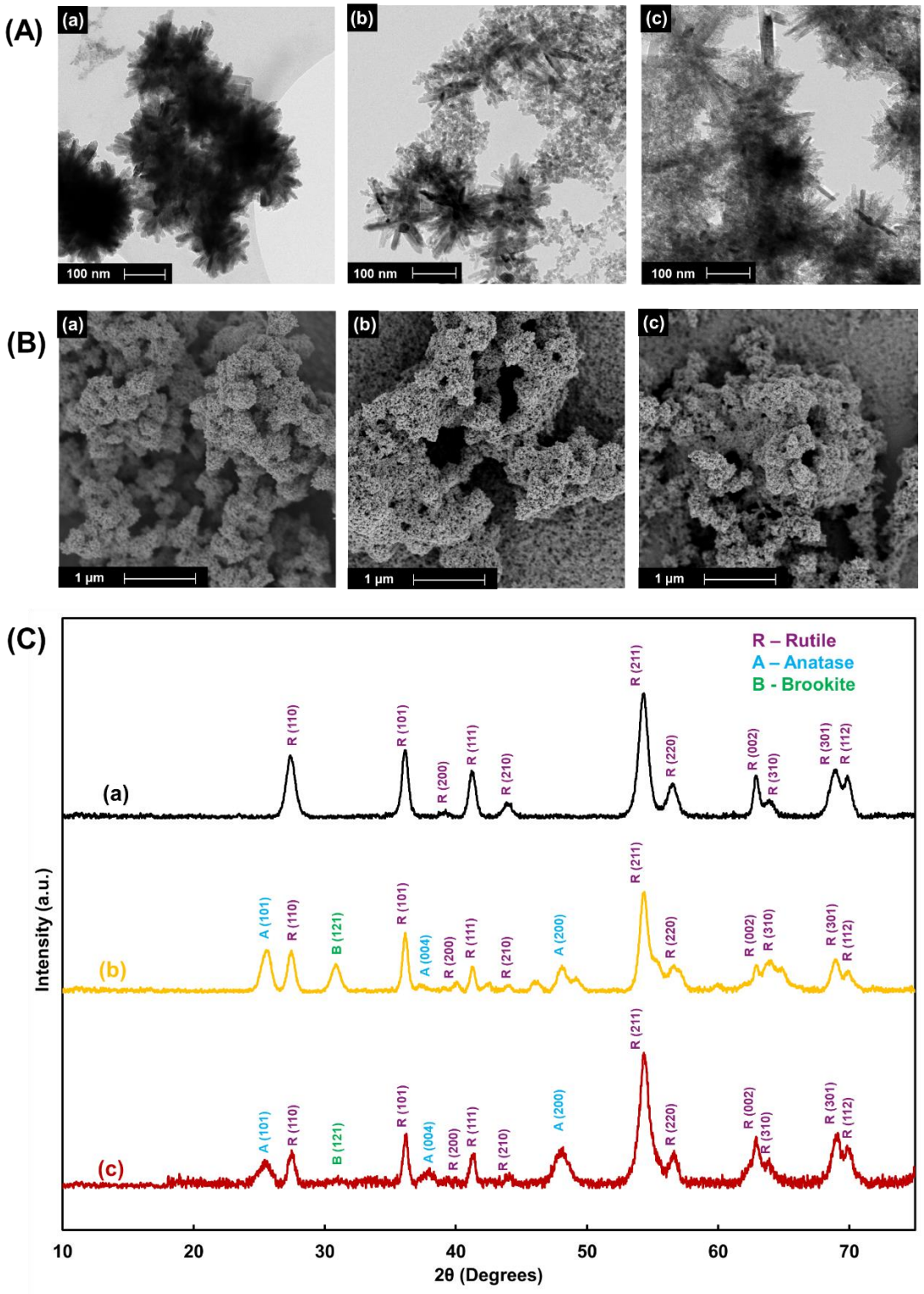

Figure 4-2. (A) TEM images of synthesized TiO_2 nanostructures. (B) SEM images of synthesized TiO_2 nanostructures deposited onto ITO-PET substrate. (C) XRD data of acid-hydrothermally synthesized TiO_2 nanostructures (a) bare TiO_2, (b) DHBA-TiO_2 (IS), and (c) CA-TiO_2 (IS).

The expected bidentate bonding of catecholate molecules to metal oxides was evaluated using FTIR spectroscopy (**Figure 4-3**) for a subset of the above-mentioned nanostructures. In the wavenumber range of 1000−2000 cm^{-1}, bare TiO_2 does not have any discernible peaks; however, CA and DHBA show several peaks. These CA and DHBA peaks were also observed in the CA-TiO_2 (PS) and DHBA-TiO_2 (PS) samples, with minor shifting. It was also observed that the peaks related to C−O stretching and bending (1528, 1597, and 1296 cm^{-1} are intensified, while other peaks are reduced. This indicates the formation of bidentate-type bonding between TiO_2 and CA/DHBA. In the CA-TiO_2 (IS) and DHBA-TiO_2 (IS) samples, most peaks not related to C−O stretching and bending are significantly reduced compared to bare TiO_2 suggesting that the surface adsorbed CA and DHBA may be partially decomposed during synthesis after binding to the surface of TiO_2.

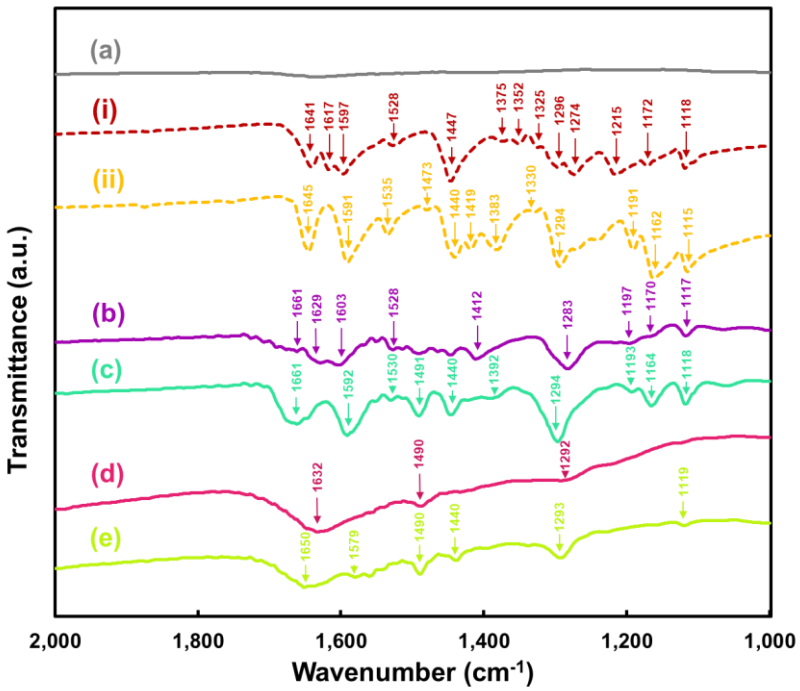

Figure 4-3. FTIR spectroscopy data for (a) bare TiO_2, (b) CA-TiO_2 (PS), (c) DHBA-TiO_2 (PS), (d) CA-TiO_2 (IS), and (e) DHBA-TiO_2 (IS). (i) and (ii) are CA and DHBA, respectively.

All the TiO_2 nanostructures, modified with catecholate molecules during or after synthesis, were optically and photoelectrochemically characterized (**Figure 4-4**). For bare TiO_2, we observe excellent light absorption in the UV range (<380 nm) and poor light absorption in the visible range (380−700 nm) (**Figure 4-4A**). The UV/vis spectroscopy confirms that all TiO_2 nanostructures with the catecholate surface modification show significantly enhanced absorption in both the visible range and the near UV range, compared to the bare TiO_2. Adsorption of catecholate ligands on the surface of TiO_2 forms charge transfer complexes that greatly improve light absorption in the visible and the near UV range by facilitating improved photoexcited electron injection into the TiO_2 conduction band.[168,173,174] Photocurrent measurements were performed by exciting the TiO_2 photoelectrodes using white light (**Figure 4-4C**). Photons with energies high enough to overcome the TiO_2 bandgap generate electron−hole pairs. The holes in the valence band oxidize ascorbic acid at the electrode/electrolyte interface, generating an anodic photo-current.[99,286] The photocurrent density of the TiO_2 nanostructures when ordered from highest to lowest are CA-TiO_2 (IPS)> CA-TiO_2 (PS) > DHBA-TiO_2 (IPS) > DHBA-TiO_2 (PS) >CA-TiO_2 (IS) > DHBA-TiO_2 (IS) > bare TiO_2. The sample with the highest photocurrent is CA-TiO_2 (IPS) at 8.89 μA cm^{-2}, which demonstrates an enhancement by a factor of 87 from bare TiO_2. CA-modified TiO_2 had higher photocurrents compared to their DHBA-modified counterparts. This is consistent with our previous experiments,[9] where it was shown that catecholate ligands with longer hydrocarbon tails demonstrate a larger photocurrent enhancement. The IS samples demonstrate lower photocurrents compared to the PS or IPS samples. The IPS samples slightly outperform PS samples, which can be explained by their crystalline composition. Based on the XRD data (**Figure 4-2C**), IPS samples contain both rutile and anatase phases, whereas the PS samples only contain the rutile phase. The combination of

rutile (~3.0 eV) and anatase (~3.2 eV) phases improves the photocurrent of IPS samples via dual sensitization. Coupling large bandgap and small bandgap semiconductors results in a multistaged bandgap that improves electron−hole pair generation efficiency by allowing lower energy photons to excite the system; this process results in improved absorbance in the visible range.[125,311,312]

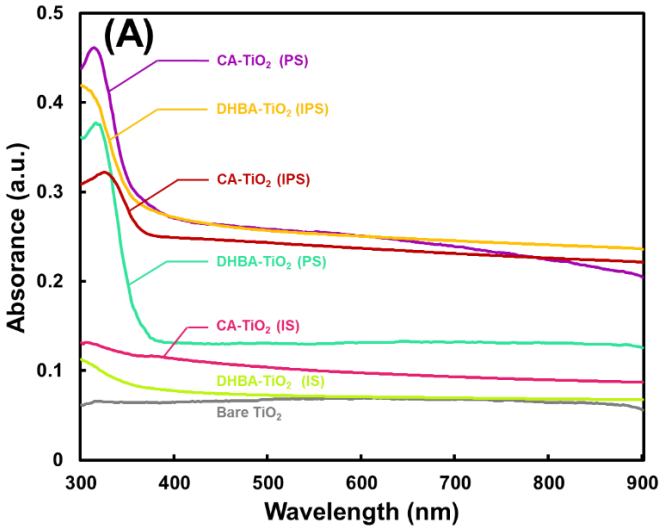
(A)
CA-TiO2 (PS)
DHBA-TiO2 (IPS)
CA-TiO2 (IPS)
DHBA-TiO2 (PS)
CA-TiO2 (IS)
DHBA-TiO2 (IS)
Bare TiO2
Absorance (a.u.)
Wavelength (nm)

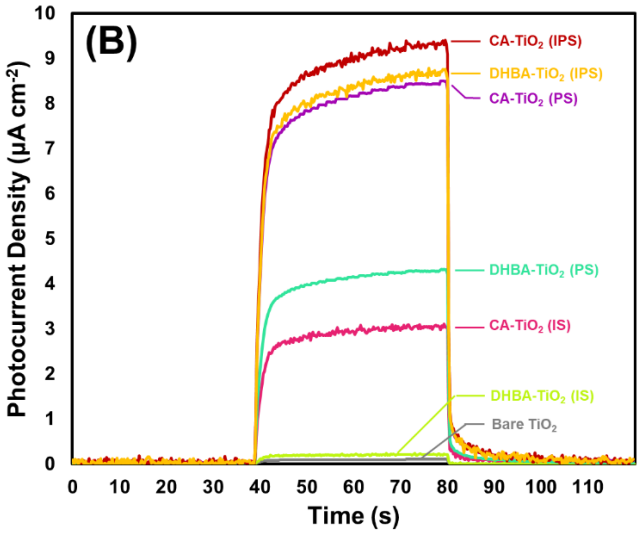
(B)
CA-TiO2 (IPS)
DHBA-TiO2 (IPS)
CA-TiO2 (PS)
DHBA-TiO2 (PS)
CA-TiO2 (IS)
DHBA-TiO2 (IS)
Bare TiO2
Photocurrent Density (μA cm-2)
Time (s)

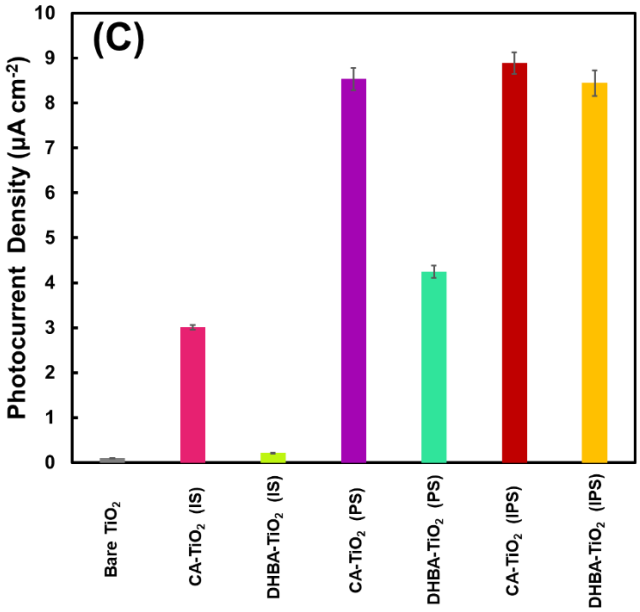
(C)
Photocurrent Density (μA cm-2)
Bare TiO2
CA-TiO2 (IS)
DHBA-TiO2 (IS)
CA-TiO2 (PS)
DHBA-TiO2 (PS)
CA-TiO2 (IPS)
DHBA-TiO2 (IPS)

Figure 4-4. Optical and photoelectrochemical characterization of TiO_2 nanostructures. (A) UV/vis absorbance spectroscopy of TiO_2 nanostructures. (B) Chronoamperometric curves of TiO_2 nanostructures with and without optical illumination. (C) Summary of photocurrent densities for various TiO_2 nanostructures. The bars represent the mean value obtained from at least three separate electrodes, with the error bars representing the standard deviation. The photocurrent measurements were performed at 0 V potential vs Ag/AgCl using 0.1 M ascorbic acid in 0.1 M PBS as the electrolyte. The photoelectrodes were irradiated with white light and the average photocurrent density was measured by taking the running average of the last 10 s of the irradiation period.

It has been reported that 3D metal-oxide nanostructures such as nanorod arrays,[313] nanoflowers,[314] and mesoporous films[315] demonstrate higher charge carrier separation, reduced charge carrier recombination rate, and lower charge transfer resistance, compared to their NP counterparts.[5,107] This has been attributed to the increased length-scale of 3D nanostructures, which provides a "highway" for charge transport along their longitudinal direction.[5,316] 3D nanostructures also boast higher light absorption than NP morphologies due to increased internal light scattering.[5,313] All of these qualities generally endow 3D nanostructured metal oxides with enhanced photocurrent generation over metal oxide NP. The observed surfaces in **Figure 4-2B** have a similar morphology to the 3D nanostructured metal oxides found in literature and are expected to have similar photocurrent generation enhancement. Additionally, it has been reported that 3D nano-structured electrodes can increase the sensitivity of a biosensor by a 100-fold compared to their planar counterparts made from nanoparticles.[34,253,317] The use of 3D nanostructures gives photoelectrodes a higher electroactive surface area compared to planar photoelectrodes of the same footprint, which in turn increases the probe molecule immobilization density and the target capture density.[34,253,317] The photocurrent enhancement, solely attributed to the physical features of the nanostructures, could not be directly quantified here due to the presence of photoabsorption enhancing catecholate ligands. The DHBA-TiO_2 (IPS) nanostructures were used for the creation of PEC biosensors due to their high photocurrent and the presence of $-COH$ group on their surface that can react with the $-NH_2$ groups of antibodies

through Schiff-base reactions. The PEC biosensor is created by immobilizing anti-IL-6 capture anti-bodies on the photoelectrode, which can then bind to the target IL-6 antigen (**Figure 4-5A**). It is expected that in the presence of IL-6, the measured photoelectrochemical current would decrease due to the reduced access of the ascorbic acid to the electrode surface. Other 3D nanostructured electrodes composed of nanorod arrays,[313,318,319] nanoflakes,[314,320,321]and mesoporous films [315] (Supporting Information, **Table 4-S1**), have been reported in the literature for PEC applications. These 3D nanostructured electrodes are generally made from metal oxides such as TiO_2, ZnO, and BiOI.[107] Some of these structures also include functionalization with other photoactive materials such as plasmonic NPs, quantum dots, and other metal oxide nanoparticles as part of a broader photoexcitation enhancement strategy.[5,107,128,307] Hydrothermal synthesis is the most common method for fabricating these 3D nanostructured photoelectrodes, followed by chemical vapor deposition, electrodeposition, and successive ionic layer adsorption and reaction. However, all of these fabrication methods require initial seeding of a substrate with a precursor structure to create the 3D nanostructuring.[107] This makes the fabrication of 3D nanostructured electrodes highly inefficient, lengthy, and costly, as the production is limited by the geometric area of the substrate able to fit inside the instrument used for synthesis. The synthesis method presented in this work does not suffer from such a drawback. Acid-hydrothermal synthesis of TiO_2 combined catecholate-induced morphology tuning can produce hierarchical 3D TiO_2 nanostructures without the need for substrate seeding, resulting in high volume and high concentration suspensions of 3D nanostructures.

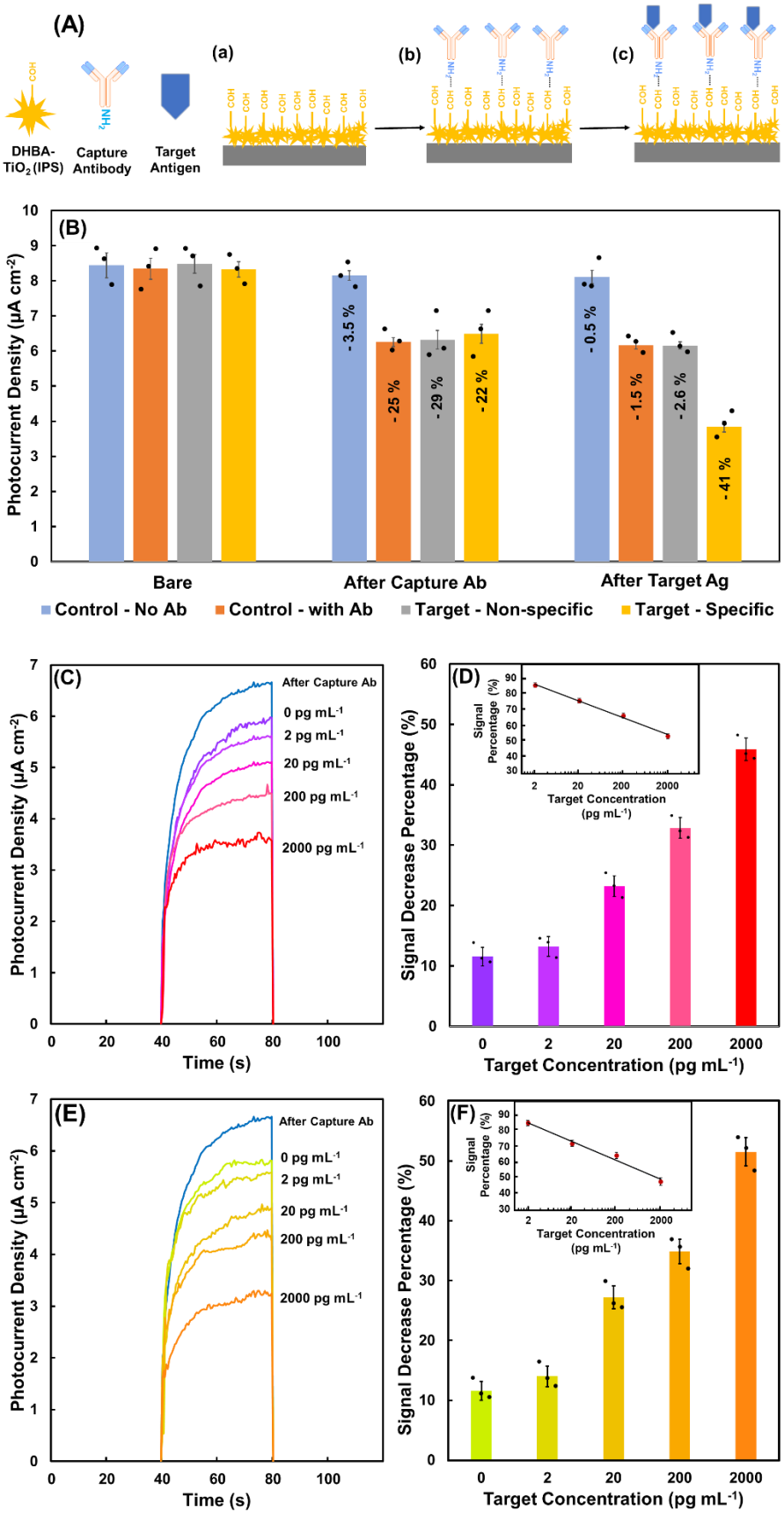
(A)
(a)
(b)
(c)
DHBA-TiO2 (IPS)
Capture Antibody
Target Antigen
(B)
Photocurrent Density (μA cm-2)
- 3.5 %
- 25 %
- 29 %
- 22 %
- 0.5 %
- 1.5 %
- 2.6 %
- 41 %
Bare
After Capture Ab
After Target Ag
Control - No Ab
Control - with Ab
Target - Non-specific
Target - Specific
(C)
After Capture Ab
0 pg mL-1
2 pg mL-1
20 pg mL-1
200 pg mL-1
2000 pg mL-1
Photocurrent Density (μA cm-2)
Time (s)
(D)
Signal Decrease Percentage (%)
Signal Percentage (%)
Target Concentration (pg mL-1)
(E)
(F)

Figure 4-5. Characterization of the PEC immunoassay (A) Fabrication of the signal-off immunoassay: (a) deposition of DHBA-TiO_2 (IPS) on the substrate (b) modification with capture antibody and (c) complexation with target protein. (B) Photocurrent density of DHBA-TiO_2 (IPS) photoelectrodes at bare, probe immobilization, and target capture stages of immunosensor operation in buffer. (C) PEC curves demonstrating the signal response at various target concentrations in buffer. (D) Photocurrent signal decrease at various IL-6 concentrations obtained from the PEC immunosensor in buffer. The inset shows a calibration curve with the data points fitted to a line by equation $S = 10.76 \times logC + 9.43$ and with $R^2 = 0.99$. (E) PEC curves demonstrating the signal response at various target concentrations in 20% human blood plasma. (F) Photocurrent signal decrease at various IL-6 concentrations ontained from the PEC immunosensor in 20% human blood plasma. The inset shows a calibration curve with the data points fitted to a line by equation $S = 12.02 \times logC + 10.25$ and with $R^2 = 0.98$.

In order to validate each step involved in the development of the PEC biosensor, we measured the photocurrent before and after each step in buffer solution, and quantified the signal change caused as a result (**Figure 4-5B**). The immobilization of probe antibodies on the photoelectrodes resulted in a signal decrease (−22% to−29%) for all the data sets, that was significantly larger in magnitude compared to the observed signal decrease with a blank solution that did not contain any antibody (−3%). This indicated the successful biofunctionalization of the photoelectrode. The immobilization of the capture antibody decreases the photocurrent by limiting the access of ascorbic acid from the electrolyte to the photo-electrode surface.[322,323] Incubation with the specific target IL-6 demonstrated a significantly larger signal change (−41%) compared to incubation with the nonspecific target (−3%), bovine serum albumin (BSA), and the blank (−1%) solution, demonstrating the ability of the PEC sensor in detecting the specific target. Target complexation results in further steric hindrance leading to more signal decrease. In order to determine the analytical performance of the PEC biosensor, we assessed it with logarithmically increasing IL-6 concentrations in buffer (**Figure 4-5C and 4-5D**) and 20% human blood plasma, ranging from 2−2000 pg mL^{-1} (**Figure 4-5E and 4-5F**). As expected, the PEC current decreased in magnitude with increasing target concentration in both mediums (**Figure 4-5D and 4-5F**), and the percentage change in PEC current increased in magnitude with increasing the target

concentration. The signal decrease measured in plasma was in good agreement with that measured in buffer, demonstrating negligible signal change dueto biofouling (<6%). The sensor demonstrated a log−linear operational range of 2−2000 pg mL^{-1}, with a limit-of-detection (LOD) of 3.6 pg mL^{-1} in plasma and 1.6 pg mL^{-1}in buffer solution.

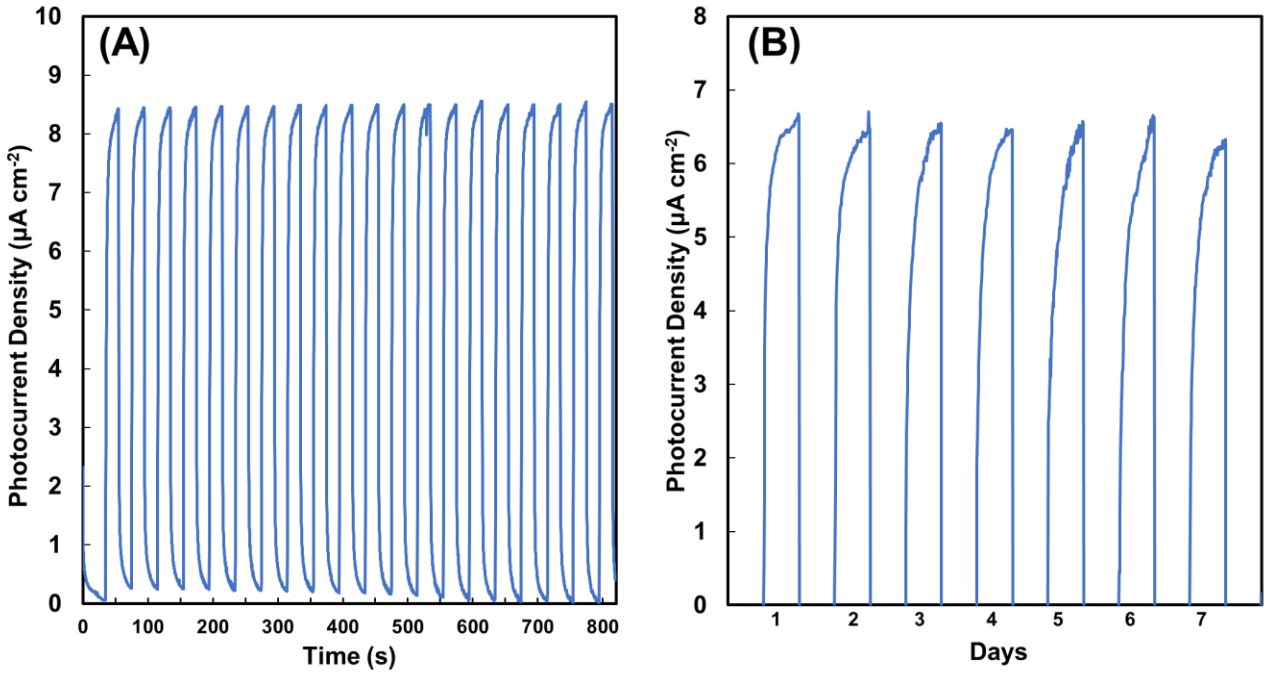

Figure 4-6. Evaluation of the stability of the PEC biosensor. (A) Photocurrent density measurements for 20 continuous cycles of the bare DHBA-TiO_2 (IPS) photoelectrodes. (B) Photocurrent density measurements following the storage of capture antibody modified DHBA-TiO_2 (IPS) photoelectrodes for 7 days.

The short-term stability of the sensor was evaluated by measuring the photocurrent density for 20 continuous cycles for bare DHBA-TiO_2 (IPS) photoelectrodes (**Figure 4-6A**), demonstrating negligible scan-to-scan variability (signal change of 0.86% over 20 scans and 14 min). The long-term stability was evaluated by storing capture antibody modified photo-electrodes over a period of 7 days and measuring the photocurrent density each day (**Figure 4-6B**). The sensor demonstrates good long-term stability, with a∼6% signal decrease after 7 days.

The above data makes it evident that catecholate surface modified TiO_2 nanostructures, specifically DHBA-TiO_2 (IPS), are an excellent material system for use in PEC biosensors with a wide dynamic range and a low LOD. Some recent examples for PEC IL-6 biosensors in literature include TiO_2 nanoparticles dual cosensitized with CdS and CdSe on ITO electrodes (LOD = 0.38 pg mL^{-1}, dynamic range = 0.1−1pg mL^{-1}), and the use of perovskite-type $LaFeO_3$ nanoparticles deposited on fluorine-doped tin oxide electrodes (LOD = 33 fg mL^{-1}, dynamic range = 0.1−100 pg mL^{-1}).[324] The main advantage offered by our system is its wide dynamic range which covers the diagnostic IL-6 concentration range of diseases such as Alzheimer's disease (85−567 pg mL^{-1}), rheumatoid arthritis (17 pg mL^{-1}), myocardial infraction (28.5−46.5 pg mL^{-1}), cachexia (100 pg mL^{-1}), cardiac myxoma (>56 pg mL^{-1}), multiple myeloma (5−33 pg mL^{-1}), hepatocyte carcinoma (7−18.9 pg mL^{-1}), and Burkitt lymphoma (100.3 pg mL^{-1}),[296] while still maintaining clinically acceptable LOD and stability. Commercial IL-6 biosensors (**Table 4-S2**) are typically based on enzyme-linked immunosorbent assays (ELISA).[325] These commercial devices rely on chemiluminescence,[326] electrochemiluminescence,[327] or colorimetry[78] as their principle signal transduction mechanism, which require the use of benchtop plate readers. The LOD of these assays range from 0.2 to 5 pg mL^{-1} putting the LOD of our device (3.6 pg mL^{-1}) well within this range. In contrast to the above-mentioned assays, our newly developed system does not require target labeling, which reduces the number of steps required for assay operation. Furthermore, it would be possible in the future to integrate the assay with hand-held and portable signal readers for point-of-care analysis.

4.4 Conclusions

In this work, we developed an advanced material synthesis process to create photoelectrodes for use in photoelectrochemical biosensors. These photoelectrodes use catecholate-modified TiO_2

nanostructures to provide a 3D architecture, enhanced photoelectrochemical response, and functional ligands for effective biofunctionalization. The chemical structure of the selected multifunctional catecholate molecules is a key factor, which governs the material properties and efficient biosensor performance. Compared to photoelectrodes created from unmodified TiO_2, the catecholate-modified electrodes developed here increase the measured photocurrent by about 2 orders of magnitude. These photoelectrodes were easily modified with antibodies, transforming them into biosensors for detecting IL-6. The fabricated biosensor show great performance with a wide dynamic range of 2−2000 pg mL^{-1}, an LOD of 3.6 pg mL^{-1} in 20% human blood plasma, and good short- and long-term stability. These photoelectrochemical biosensors have the potential to be used in the clinical analysis of Alzheimer's disease, rheumatoid arthritis, myocardial infraction, cachexia, cardiac myxoma, multiple myeloma, hepatocyte carcinoma, and Burkitt lymphoma. The results presented here also provide insights into the development of robust photoactive material systems for the fabrication of high performance PEC biosensors.

4.5 Experimental Section

Materials:

Caffeic acid (CA), 3,4-dihydroxybenzaldehyde (DHBA), titanium (IV) butoxide, and indium tin oxide/poly(ethylene terephthalate) (ITO/PET) substrates (surface resistivity 100Ω sq^{-1})were purchased from Sigma-Aldrich. Hydrochloric acid (37%) was purchased from Caledon Laboratory Chemicals. Milli-Q grade (18.2 MΩ cm) deionized (DI) water was used for all solution preparation and washing steps.

Acid-Hydrothermal Synthesis of Nanostructured TiO_2:

In a teflon container, 20 mL of the reaction solution was prepared by mixing 1 M HCl with 1 mL of titanium (IV) butoxide. The teflon container was inserted into an autoclave and placed in an oven for 2 h at 180°C to prepare TiO_2 nanostructures via hydrothermal synthesis. For samples with in-situ surface modification, 0.05 g of CA or DHBA was also added to the reaction solution. After synthesis, the samples were centrifuged six times at 6000 rpm. This was done to remove reaction byproducts and restore neutral pH in the TiO_2 suspension.

Photoelectrode Fabrication:

ITO/PET substrates were cut into dimensions of 1.2×0.7 cm^2 and a small portion of length was masked with self-adhesive vinyl to preserve electrical contact area. Substrates were subjected to air plasma treatment for 1 min. The substrates were then coated with unmodified TiO_2 or surface modified TiO_2 by dropping 10μL of 0.66 g L^{-1} suspension on the substrate surface and baking them in the oven at 85°C for 6 min. This process was repeated three times to deposit three layers.

Material Characterization:

The morphology of the synthesized nanostructures was analyzed via transmission electron microscopy (TEM) imaging using a Thermo Scientific Talos 200X STEM Microscope. The surface of photoelectrodes fabricated from the nanostructures were analyzed via scanning electron microscope (SEM) imaging using an FEI Magellan 400 FEGSEM Microscope. For SEM imaging the samples were coated with 3 nm thick layer of platinum. Conventional sample preparation was used for both TEM and SEM imaging. A Bruker SMART CCD 600 Diffractometer using a Cu source was used for obtaining X-ray diffraction (XRD) characterization of the synthesized particles. Fourier transform infrared (FTIR) spectroscopy was

performed using a Bruker Vertex 70 spectrometer and Ultraviolet/visible (UV/vis) spectroscopy was performed using a Tecan Evo 200 Plate reader.

Photocurrent measurements were caried out using a Zahner CIMPS-QE/IPCE3 Photoelectrochemical Potentiostat. A standard three-electrode cell setup was used with white light as a photoexcitation source. Platinum (Pt) wire was used as the counter electrode, a silver/silver chloride (Ag/AgCl) electrode for the refence electrode and TiO_2 nanostructure or catecholate-modified TiO_2 nanostructure photoelectrodes acted as the working electrodes. The electrolyte solution was composed of 0.1 M phosphate buffered saline (PBS) and 0.1 M ascorbic acid (AA). The photoexcitation source was a Thorlabs MNWHL4 mounted LED, which has a neutral white color temperature (400−700 nm) and an irradiance of 7.7. uW mm^{-2} (see **Figure 4-S1** for the spectrum of the light source. The photocurrent measurement was done by running the potentiostat in chronopotentiometric mode for 60 s. The potential of the PEC cell was fixed at 0 V, and the working electrode was irradiated with white light at a 20 s interval. Average photocurrent density was measured by taking the running average of the last 10 s of the irradiation period.

Antibody/Antigen Complexation and target Detection:

Photoelectrodes fabricated from DHBA-modified TiO_2 nanostructures with both in situ and post situ modification were used for PEC-based protein detection testing. The immunoassay format utilized was a direct assay that made use of anti-IL-6 as its single capture antibody and IL-6 as the target antigen. After fabricating the photoelectrodes, their photocurrents were measured to obtain the bare signal. In the first step, a 125 μg mL^{-1}solution of capture Ab was prepared from stock by diluting in 1 M PBS. Then, 15 mL of the capture Ab solution was deposited on top of the photoelectrodes and incubated for 24 h at 20° C. After this incubation period, the

photoelectrodes were washed with 1 M PBS. Photocurrent was once again measured at this point to get the after-capture-Ab signal. In the next step, various concentrations of the target Ag ranging from 2 to 2000 pg mL^{-1} was prepared by diluting from stock in 1 M PBS. Then, 15 mL of the target Ag solution was deposited on top of the photoelectrode and further incubated for 1 h at 20°C. The photoelectrodes were washed with 1x Tris-buffered saline (TBS) and again washed with a mixture of 1x TBS and 0.5% v/v Tween20 (TBST). The photocurrent was measured for a final time to obtain the after-target-Ag signal.

Limit of Detection Calculation:

A calibration curve was plotted as a function of the photocurrent density and the concentration of the IL-6 target Ag, which was used to complex with the Anti-IL-6 capture Ag immobilized on the photoelectrode. To simulate the effect ofnon specific absorption of nontarget proteins, one of the measurements contained 2000 pg mL^{-1} of bovine serum albumin (BSA), instead of IL-6; this measurement was treated as the blank signal. Limit of blank (LOB) is calculated using the equation:

$$(1) \quad LOB = I_{Blank} + 3 \times \sigma_{Blank}$$

where, σ_{blank} is the standard deviation of the blank signal and the factor 3 is used to calculate the LOD within a 95% confidence interval. The LOD is then calculated from the regression line by substituting the signal (y-value) with the LOB.

4.6 Acknowledgements

This research was funded by the Natural Sciences and Engineering Research Council of Canada. L.S. is the Canada Research Chair in Miniaturized Biomedical Devices. Scanning Electron Microscopy was performed at the Canadian Centre for Electron Microscopy.

4.7 Supporting Information

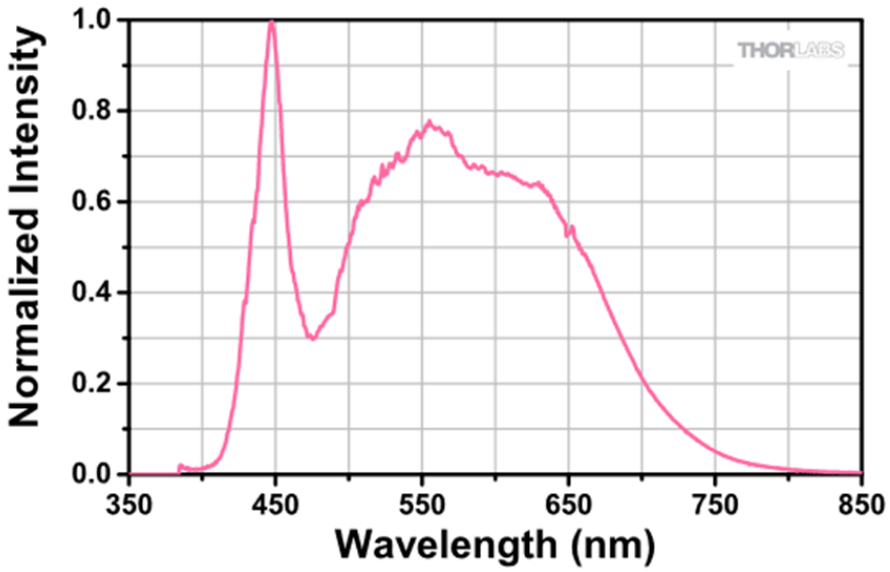

Figure 4-S1. Spectrum of the photoexcitation source.[16]

Table 4-S1. 3D nanostructure photoelectrodes used in photoelectrochemical biosensing.

Photoelectrode material	Nanostructure description	Functionalization	Fabrication method	Application	Ref.
TiO_2	Branched hierarchical NR array	N/A	Seed-assisted hydrothermal synthesis	Water splitting	[313]
ZnO	Nanospindles	Cu_2O film	Electroseposition	Glutathione detection	[321]
TiO_2	Mesoporous film	Au NP, MoS_2 film	Layer-by-layer self assembly through air drying	Glucose detection	[315]

ZnO	Flower rod-like architecture	N/A	Seed-assisted hydrothermal synthesis	DNA sensing	[314]
ZnO	NR array	CdS:Mn quantum dots	Seed-assisted hydrothermal synthesis	Immuno-sensor	[318]
BiOI	Nanoflakes	TiO_2 NP	Successive ionic layer adsorption and reaction	Enzymatic analysis	[320]
TiO_2	Branched hierarchical NR array	Au NP	Surface plasma chemical vapor deposition	Water splitting	[319]

NP = nanoparticles, NR = nanorods

Table 4-S2. Examples of Commercial IL-6 Immunoassays.

Company name	Test name	Assay Type	Signal trans-duction	LOD	Dynamic range	Assay Speed	Sample volume required	Ref.
Beckman Coulter	Access IL-6 Assay	Sandwich ELISA	CL	0.5 pg mL^{-1}	0.5-1500 pg mL^{-1}	≥ 35 mins	110 uL	[328]
Roche Diagnostics	Elecsys ® IL-6	ELISA	ECL	5 pg mL^{-1}	1.5-5000 pg mL^{-1}	18 mins	30 uL	[329]
R&D Systems	Human IL-6	ELISA	CL	0.2 pg mL^{-1}	0.2-10 pg mL^{-1}	4 hrs	100 uL	[330]

	Quantikine HS ELISA Kit							
Abcam	Human IL-6 ELISA Kit	Sandwich ELISA	Colorimetry	1.6 pg mL^{-1}	7.8–500 pg mL^{-1}	90 mins	100 uL	[331]
Invitrogen	IL-6 Human ELISA Kit	ELISA	Colorimetry	0.92 pg mL^{-1}	1.56–100 pg mL^{-1}	3 hrs	50 uL	[332]
PerkinElmer	IL-6 (human) AlphaLISA Detection Kit	AlphaLISA	CL	1.3 pg mL^{-1}	1.3-30000 pg mL^{-1}	3 hrs	5 uL	[333]

CL = chemiluminescence, ECL = electrochemiluminescence,

ELISA = enzyme-linked immunosorbent assay, LOD = limit of detection

Chapter 5

Integration of Photoelectrochemical Signal Transduction with DNAzymes for Culture-free Detection of Bacteria in Lake Water

Preface:

The signal-off biosensing schemes presented in chapter 3 and chapter 4 have generally high performance but are disadvantageous in some instances. The biggest flaw of the signal-off direct bioassays lies in the fact they perform poorly in complex biological media, as background signal reduction from non-specific adsorption can be higher than signal reduction from target detection.[334–337] This severely limits the sensitivity and LOD performance of signal-off PEC biosensors.[334,337] In order to address this issue, this chapter presents the development of a signal-on PEC bacterial assay that uses RNA-cleaving DNAzymes to modulate photocurrent by breaking and then rebuilding of TiO_2 nanomaterial-based heterostructures as a signaling mechanism.

Using the lessons learned about catecholate surface functionalization and morphology tuning of TiO_2 nanostructures from the previous two chapters, we synthesized an ultrasmall (1-6 nm) anatase TiO_2 NP (referred to as TiO_2-nanoparticles in this chapter), through acid-hydrothermal synthesis with *in-situ* addition of CA. When combined with the 3D rutile TiO_2 nanostructures (referred to as TiO_2-assemblies in this chapter) developed in chapter 4, a composite material

system is formed that acts as semiconductor heterostructure in a further development of research objective I. The rutile/anatase/CA heterostructure formed by this material system has significantly higher photoexcitation than the base constituent materials. This is due to the formation co-sensitized band structure whose combined effective bandgap energy nearly half that of the rutile or anatase.[129,338] This improved photoexcitation was demonstrated with photocurrent density measurements and incident photon-to-electron conversion efficiency tests.

A major hurdle in developing such sensors for detecting pathogens such as bacteria is that they require target enrichment or amplification to deliver the required LOD.[23,26,34,339] In order to innovate on novel bioassays for research objective II, this work aimed to solve this problem by coupling TiO_2-nanoparticles with RNA-cleaving DNAzymes to create photoactive biomolecular barcodes that allow automatic molecular signal switching. The result was an ultrasensitive reagent-free signal-on bacterial assay for the detection of *E. Coli* in lake water samples. DNAzymes are a class of functional nucleic acids, have been selected for precisely identifying specific bacterial species without the need for sample processing. DNAzymes cleave a segment of themselves in response to specific bacterial targets. By modifying the DNAzymes with TiO_2-nanoparticles, it was possible to create photoactive barcodes. The PEC bacterial assay was created on a two electrode PEC chip containing - a cleavage electrode and a detection electrode. To achieve bacterial detection, the sample solution is deposited to cover both on-chip electrodes. The *E. coli* target interact with the DNAzyme resulting in the release of the photoactive barcode strand, causing signal decrease at the cleavage electrode. After target interaction, the released DNA barcode is captured by probes at the detection electrode, where signal increases. The specificity of this assay was tested against a panel of several gram-positive and gram-negative bacteria, where it was shown that target *E. Coli* bacteria produced a signal increase by a factor of

~5 compared to non-target-bacteria. A calibration curve was plotted in the range 0-10^6 CFU mL^{-1} and was fitted to logistic curves, resulting in an LOD of 19 CFU mL^{-1} in lake water.

Authors: Sadman Sakib, Zijie Zhang, Enas Osman, Farhaan Kanji, Fatemeh Bahkshandeh, Yingfu Li, Igor Zhitomirsky and Leyla Soleymani

Publication: Submitted for Publication in Nano Today in November 2022

5.1 Abstract

There is a need for rapid and field-based bacterial detection and identification platforms that do not rely on lengthy growth cultures and lab-based techniques such as mass spectroscopy and polymerase chain reaction. Electrochemical techniques have been developed for culture-free bacterial detection; however, biosensors that deliver a low enough limit-of-detection for direct water pathogen sensing remain elusive. Herein, we report a photoelectrochemical biosensor using photoactive DNAzymes for bacterial identification and photoelectrochemical signal transduction. The signal transduction is based on using DNA as a switch that makes and breaks semiconductor heterostructures between TiO_2 nanomaterials for target induced-signal modulation. The developed assay integrating molecular and photoelectrochemical switching is able to detect *Escherichia coli* at a concentration of 18 CFU mL^{-1} and quantify it over five orders-of-magnitude in lake water without target enrichment, addition of reagents, or sample processing and can specifically identify this organism amongst five similar bacterial pathogens.

5.2 Introduction

The rapid detection and identification of bacterial pathogens are critically important for preventing infectious diseases and reducing their spread, as well as for reducing the threats associated with the emergence of antibiotic resistance.[23,24,340] It is well accepted that bacterial testing and monitoring is important in humans and animals, as well as their ecosystems such as water as these systems are intimately intertwined and affect the local and global transmission of infectious diseases.[340,341] The current gold standard for bacterial testing involves growth cultures, which requires incubations times of 4-48 hours.[23,25,26,34] Other clinical laboratory techniques based on mass spectrometry,[342,343] nucleic acid amplification tests (NAAT),[344,345] or enzyme-linked immunosorbent assays (ELISA)[325,346] are more rapid; however, they are not simple and

inexpensive enough for frequent and widespread use for water pathogen testing in the field.[23,25,26,34]

In response to the need for rapid and in-field bacterial testing, biosensors coupled to electrochemical readout have been implemented to create handheld bioanalytical devices that resemble the glucose monitor.[34,59,337,347,348] These devices deliver the required limit-of-detection for clinical testing (1000 CFU mL^{-1}).[34,348] However, they are either non-quantitative,[34,59,337,347,348] incapable of reaching the relevant limits for surface water monitoring (100 CFU mL^{-1})[349] *without* sample processing,[34,350–354] or require extensive sample purification, target extraction and enrichment, or reagent addition,[355–357] failing to deliver a simple solution for in-field use. Electrochemical biosensors that have a low enough limit-of-detection for quantitative analysis of *native* water samples without pre-processing or addition of reagents remain elusive.

Photoelectrochemistry, a method combining electrochemical readout with optical excitation, is an emerging signal transduction approach that offers a low background signal and a high signal-to-noise ratio for biosensing.[9,64,98,306,358] Biosensors utilizing photoelectrochemical (PEC) readout translate the capture of the target analyte by a biorecognition element to a change in photoelectrochemical signal.[64,97,98,134] PEC biosensors generally outperform comparable electrochemical biosensors by achieving lower limits-of-detection.[64,89,302] There are reports of PEC biosensors used for bacterial sensing;[334–336,359–361] however, these systems are either signal-off making them unreliable for use in heterogeneous samples with different backgrounds[334–336,360,361] rely on multi-step labeling or processing with enzymes,[359] or photoactive labels[359,362] by the user to generate the required limit-of-detection, or use semiconductive quantum dots that are unstable in open air.[335,359,362]

To develop a system that exploits the ultrasensitivity of PEC signal readout but is stable, reagent-free, single-step, and simple to operate, we developed a new materials system combining synthetic biology with surface-engineered semi-conductive nanomaterials. We developed a photoactive RNA-cleaving DNAzyme, a synthetic analogue of a protein enzyme,[350,363] that cleaves a segment of itself in response to a specific bacterium.[350,363,364] These DNAzymes are highly specific to their targets[34,350,365] and have been utilized as biorecognition elements to create reagent-less biosensors for multiple bacterial species;[34,350,364,365] however, their integration with PEC signal transduction has not yet been shown.

We designed the photoactive DNAzyme to bear a ligand-modified TiO_2 nanoparticle as the PEC label. The engineering of the TiO_2 nanoparticle with the surface ligand from the catechoalte group enhances its photoactivity[6,9,98] for increasing the biosensing signal. We then house these photoactive DNAzymes on photoactive electrodes made from a different class of TiO_2 nanomaterials to achieve reagent-free and signal-on sensing. This system is designed to modulate the PEC current by breaking TiO_2 heterostructures created between the two TiO_2 nanomaterials on one photoelectrode and building such heterostructure on another closely spaced electrode. The heterostructure manipulation is caused by the cleavage of the photoactive DNAzyme on one electrode followed by the diffusion and capture of the released PEC segment on another electrode. The heterostructures are created and broken in the presence of the bacteria *via* programmed molecular processes and without any external intervention. The resultant PEC DNAzyme assay combines the specificity and reagent-less nature of DNAzymes with the ultrasensitivity of PEC readout to create a simple and sensitive bacterial assay for analyzing the low levels of *Escherichia coli* (*E. coli) bacteria* in water. The results presented herein, demonstrate a new materials system for signal generation, which significantly improves upon our

previous work, where we developed an electrochemical bacterial detection platform based on electroactive DNAzymes.[34] Although the previous assay was able to achieve good clinical performance for the detection of *E. coli* in urine, it achieved a limit-of-detection of 1000 CFU mL^{-1} and relied on threshold-based and non-quantitative detection, not meeting the criteria for environmental monitoring.[34] The present work innovates on our previous design through a novel photoactive materials system, enabling PEC signal readout, to create an ultrasensitive and quantitative assay for bacterial detection.

5.3 Results and Discussion

5.3.1 Engineering TiO_2 Nanomaterials

We sought to develop two classes of photoactive nanomaterials for constructing the photoelectrochemical bacterial assay. The first class was designed as high surface area three-dimensional TiO_2 assemblies (TiO_2-assemblies) for developing a photoelectrode with high efficiency in photocurrent generation. The second class was designed as small nanoparticles (TiO_2-nanoparticles) used as DNA labels for PEC signal modulation, created to minimally affect DNA diffusion and binding. We developed hydrothermal synthesis for creating the two material classes using titanium (IV) butoxide in a highly acidic solution with HCl for the TiO_2-aseemblies, and titanium (IV) oxysulfate and caffeic acid in a low acidity environment with H_2SO_4 for TiO_2-nanoparticles. The TiO_2-assemblies formed as aggregated nanorod clusters that radially extended outwards from a central point with a diameter of 80-100 nm (**Figure 5-1A**). These aggregates are mechanically stable as ultrasonication did not break up the nanorod clusters. The TiO_2-nanoparticles have a spherical geometry with a diameter of 1-6 nm (**Figure 5-1B**). Highly acidic solutions of TiO_2 precursors encourage anisotropic growth, as crystal facets chelated by anions have lower surface energy, which leads to the formation of rutile nanorods,

nanowire and whiskers-like structure.[310,339,366,367] In TiO_2, this leads to accelerated growth of the (110) plane, which is more thermodynamically stable than other planes, leading to the formation of the rutile nanorods observed in TiO_2-assemblies.[310,339] Conversely, low acidity solutions facilitate isotropic growth resulting in the formation of anatase nanoparticles similar to what is observed with TiO_2-nanoparticles.[339,366–368] The small size of the TiO_2-nanoparticles is attributed to the addition of caffeic acid – a member of the catecholate family with an aromatic ring having two adjacent phenolic -OH groups – during synthesis. Caffeic acid also contains a short hydrocarbon chain that ends with a carboxylic group (**Figure 5-1C (i)**).[122,170,187] Catecholate ligands are known to strongly adsorb onto the surface of metal oxides through bidentate-type bonding (**Figure 5-1C (ii)-(iv)**).[9,122,170,369] During hydrothermal synthesis, caffeic acid adsorbs onto the TiO_2 surface upon nucleation and acts as a capping agent which stabilizes TiO_2-nanoparticles and inhibits further growth and agglomeration.[98] To account for caffeic acid degradation during synthesis,[98] we added caffeic acid both before are and after synthesis. As shown in the XRD data (**Figure 5-1D**), both TiO_2 nanomaterials have a high degree of crystallinity. For TiO_2-assemblies, the characteristic peaks of pure rutile phase are observed; whereas, for TiO_2-nanoparticles, the characteristic peaks of pure anatase phase are observed. The presence of Cl^- anions leads to preferential formation of rutile phase,[367,370] whereas SO_4^- anions are known to inhibit rutile formation and encourage growth of anatase,[98,339,367,371] which further explain the phase differences between the two different TiO_2 nanomaterials.

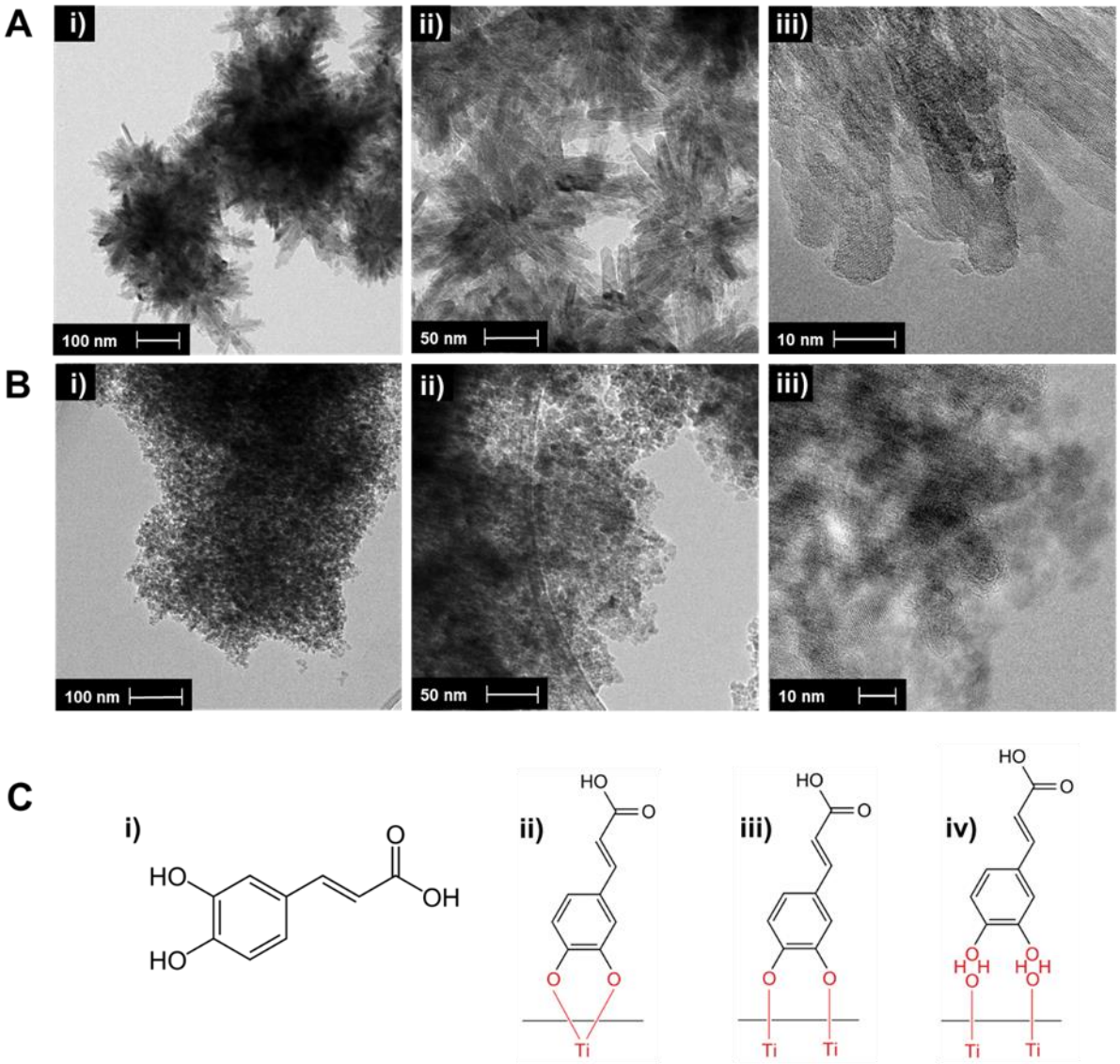
A
i)
ii)
iii)
100 nm
50 nm
10 nm
B
i)
ii)
iii)
100 nm
50 nm
10 nm
C
i)
HO
HO
O
OH
ii)
HO
O
O
O
Ti
iii)
HO
O
O
O
Ti
Ti
iv)
HO
O
H
H
O
O
H
H
O
O
Ti
Ti
D
R – Rutile
A – Anatase
R (110)
R (101)
R (200)
R (111)
R (210)
R (211)
R (220)
R (002)
R (310)
R (301)
R (112)
i)
A (101)
A (004)
A (200)
A (105)
A (211)
A (204)
A (116)
A (220)
A (224)
ii)
Intensity (a.u.)
10
20
30
40
50
60
70
80
2θ (Degrees)

Figure 5-1. Characterization of hydrothermally synthesized TiO_2 materials. Transmission electron micrographs of (A) TiO_2-assemblies and (B) TiO_2-nanoparticles at different magnifications (i-iii). (C) Chemical structure of (i) caffeic acid and it's bonding mechanism to TiO_2 surfaces: (ii) bidentate chelating, (iii) bidentate bridging (inner sphere), and (iv) bidentate bridging (outer sphere). (D) XRD data of (i) TiO_2-assemblies and (ii) TiO_2-nanoparticles.

We hypothesized that combining the two TiO_2 nanomaterials would yield a semiconductor heterostructure, making the combined PEC current higher than either material due to a co-sensitization effect caused by the formation of a type-II band structure.[5,129,130] If this were the case, we could then use the TiO_2-nanoparticles as labels for signal modulation on TiO_2 photoelectrodes. To validate this hypothesis, we characterized hybrid photoelectrodes fabricated using the TiO_2-assemblies (three layers) and coated with a layer of TiO_2-nanoparticles (one layer) using photocurrent density and incident photon-to-electron conversion efficiency (IPCE) measurements (**Figure 5-2**). Four different hybrid photoelectrodes were produced with their fourth layer containing different amounts of TiO_2-nanoparticles (**Figure 5-2A**) and their photocurrent density was measured (**Figure 5-2B**). The photoelectrodes were excited with white light, with photons having energies higher than the TiO_2 bandgap generating electron-hole pairs. The photogenerated holes in the valance band oxidize the ascorbic acid present in the electrolyte, generating an anodic photocurrent.[64,99,122,134] As expected, we observed that the addition of TiO_2-nanoparticles to the photoelectrodes increases the photocurrent, with the current increase being correlated with the increase in the concentration of TiO_2-nanoparticles (**Figure 5-2C**).

The IPCE response (**Figure 5-2D**) of the baseline photoelectrodes (three layers of the TiO_2-aseembly) is typical of TiO_2 materials,[9,313,358,372] with high photoexcitation efficiency in the UV range (< 400 nm) that rapidly drops off in the visible light region (> 400 nm). When one layer of 3.3 % TiO_2-nanoparticles was added to the baseline electrode, the photoexcitation efficiency was significantly enhanced across UV and visible (400-550 nm) ranges. This is

especially remarkable considering that adding a fourth layer of TiO_2-assemblies to the baseline photoelectrode reduced the IPCE across all wavelengths and that TiO_2-nanoparticles alone had a very low IPCE response. The IPCE response of the photoelectrodes demonstrates that the combination of the two different TiO_2 nanomaterials and creation of a semiconductor heterostructure produces a significant improvement in photoexcitation efficiency through increased optical absorption in the visible range and improved photocurrent generation. Interestingly, adding the TiO_2-nanoparticles to the baseline photoelectrode increased the dark and illuminated charge transfer resistance of the hybrid photoelectrodes, indicating the passivation effect of TiO_2-nanoparticles (**Figure 5-S1**). This effect is counteracted by the enhancement in photoexcitation efficiency of the material system.

Based on the above results, a band diagram for the rutile/anatase/caffeic acid semiconductor heterostructure is proposed (**Figure 5-2E**) to describe the photoexcitation process of this system. We believe the enhanced photoexcitation efficiency of this material system is related to the combination of two effects: enhancement in photoabsorption due to catecholate ligand driven electron injection[9,122,184] and a co-sensitization through the formation of a multi-state band structure.[5,129,130] Catecholate ligands like caffeic acid, when adsorbed onto the surface of TiO_2-nanoparticles, improve light absorption in the visible range by forming charge transfer complexes.[122,172,173] In this material system, TiO_2-nanoparticles act as the carrier for caffeic acid. Surface adsorbed catecholate ligands display two types of electron injection mechanisms. In the type-I mechanism, a photoexcited electron first enters an excited state, going from the highest occupied molecular orbital (HOMO) to the lowest unoccupied molecular orbital (LUMO) of the catecholate ligand, and then transferring to the conduction band of the metal oxide[122,184] In the type-II mechanism, there is a direct transition of photoexcited electrons from the HOMO of the

catecholate ligand to the conduction band of the metal oxide.[122,373] The type-II electron injection mechanism is considered to be more efficient due to direct transition from the ligand HOMO to metal oxide conduction band having a lower energy difference than the type-I mechanism.[175,373] A semiconductor co-sensitization structure involves the assembly of two semiconductors with different bandgap energies into a heterostructure. This creates a multi-state bandgap where photogenerated electrons need lower effective energies to enter an excited state, leading to higher electron-hole pair generation and enhancement in photoexcitation efficiency.[130,374] Previous studies show that mixed-phase TiO_2 containing both anatase and rutile can replicate this effect as anatase and rutile have different bandgaps.[130,311,374] Density functional theory models have reported that electron affinity of rutile and anatase are 4.8 eV and 5.1 eV respectively, resulting in the effective bandgap energy of ~2.78 eV for the heterostructure.[129,311,338] In multi-stage band structures like this, electrons typically flow between adjacent conduction bands and holes flow between adjacent valance bands.[129] In our material system, we propose that photoexcited electrons are directly transferred from the HOMO of caffeic acid to the conduction band of TiO_2-nanoparticles (anatase).[5,311] These electrons then flow from the conduction band of TiO_2-nanoparticles to the conduction band of TiO_2-assemblies (rutile) through the co-sensitized semiconductor heterostructure.[129] These studies demonstrate the synergistic interactions between the two TiO_2 nanomaterials toward enhancing the measured photocurrent.

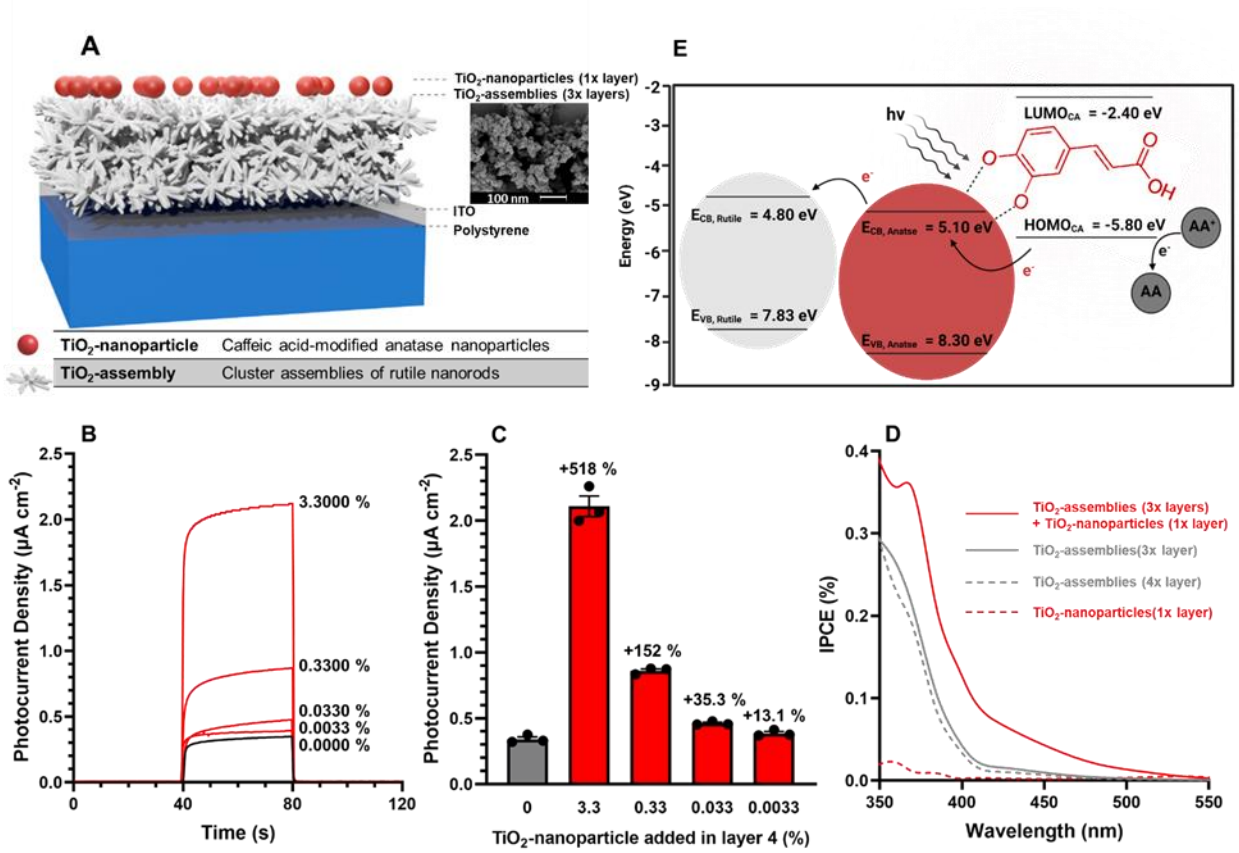

Figure 5-2. Construction and characterization of the TiO_2 heterostructure. (A) Illustration of the cross section of the photoelectrode with TiO_2-nanoparticles deposited on TiO_2-assemblies. The inset demonstrates the top-view SEM of the photoelectrode surface created from TiO_2-assemblies. (B) Photocurrent density measurements and (C) peak photocurrent density summaries generated from the structure illustrated in (A) at different mass ratios of TiO_2-nanoparticles in the top layer to the TiO_2-assemblies in the bottom three layers. (D) IPCE measurements for photoelectrodes fabricated from three layers of TiO_2-assemblies, four layers of TiO_2-assemblies, one layer of TiO_2-nanoparticles, and one layer of TiO_2-nanoparticles on three layers of TiO_2-assemblies. (E) Proposed band diagram of rutile/anatase/caffeic acid heterostructure showing photoelectron injection in the ligand-to-metal oxide charge transfer complex and dual sensitization between rutile and anatase TiO_2.

5.3.2 Designing the PEC DNAzyme Assay

We leveraged the enhancement in photoexcitation efficiency generated by the TiO_2 heterostructure to design a highly sensitive and specific culture-free bacterial sensor. Bacterial identification was achieved using RNA-cleaving DNAzymes that were previously selected for targeting proteins released from *E. coli*,[34,350,364,365] providing a highly specific probe for this

microorganism. To achieve PEC signal transduction, we created photoactive DNAzymes that upon target capture, cleave and release a photoactive single-stranded DNA (ssDNA) barcode. These photoactive DNAzymes were created by attaching streptavidin-modified TiO_2-nanoparticles (discussed above) to biotinylated DNAzymes (**Figure 5-3A**). The TiO_2-nanoparticles were modified with streptavidin through carboxamide bonding between carboxylic acid groups on the caffeic acid ligand and the amino groups on streptavidin.[98,375]

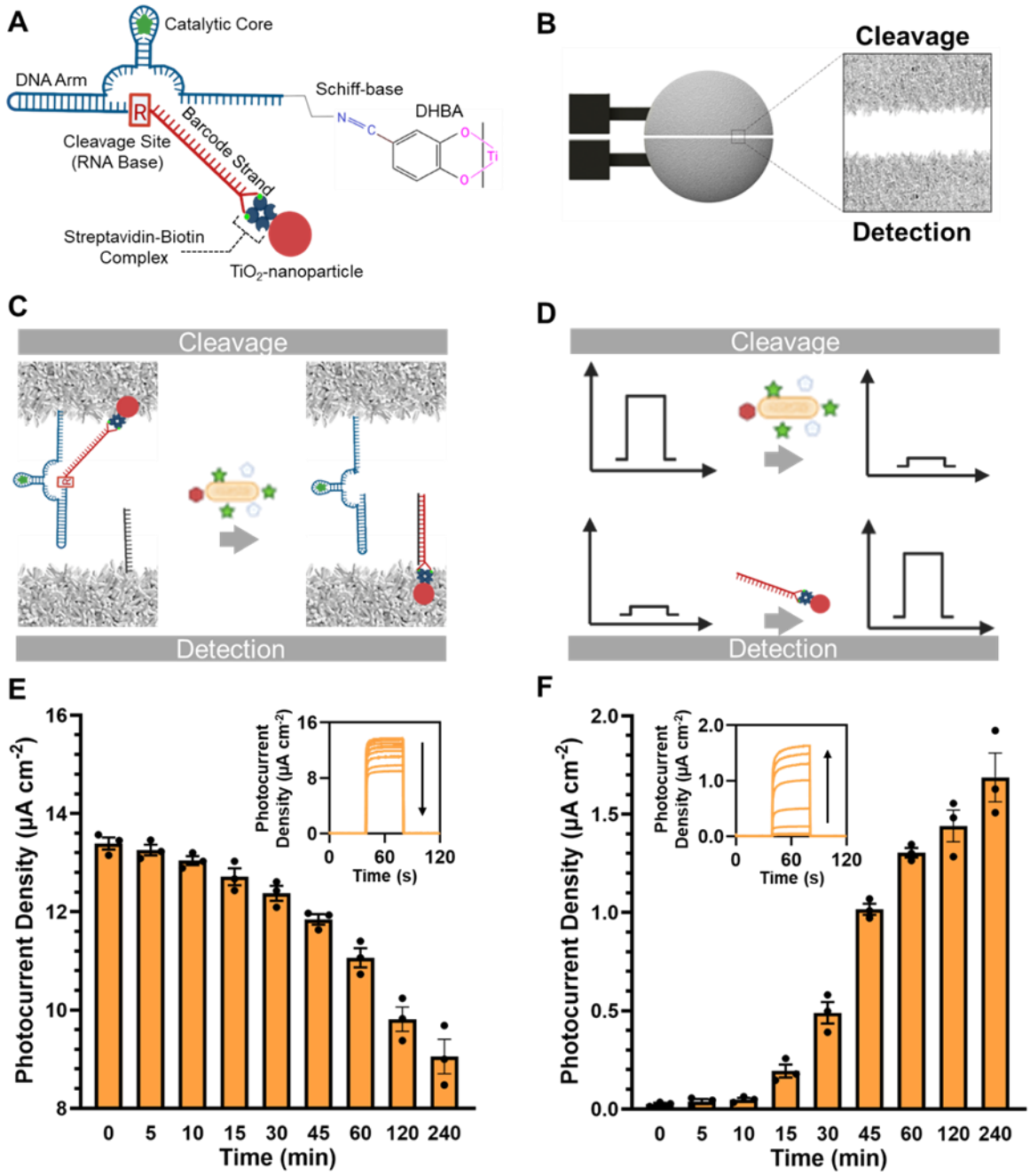

Figure 5-3. Illustration and characterization of the PEC DNAzyme assay. (A) Building blocks of the photoactive DNAzyme strand. (B) Illustration of the TiO_2-assembly photoelectrode. (C) Operation of the PEC DNAzyme assay: In the presence of the target, TiO_2-nanoparticle tagged DNA barcode is released at the cleavage photoelectrode and hybridized at the detection photoelectrode. (D) signal changes on the cleavage and detection photoelectrodes as a result of bacterial target interaction. Kinetics study demonstrating the detection and cleavage of TiO_2-nanoparticle barcodes at the (E) cleavage photoelectrode and the (F) detection electrode. The insets demonstrate the raw PEC curves from 0 to 240 minutes. Average photocurrent density was calculated from buffer solutions spiked with *E. coli* (10^6 CFU mL^{-1}) measured on three different two-electrode PEC chips.

The PEC bacterial assay was created on a two-electrode PEC chip containing cleavage and detection photoelectrodes fabricated from TiO_2-assemblies (**Figure 5-3B**). The geometry of this chip was optimized so that both electrodes would receive equal amount of illumination from mounted LED photoexcitation sources. The cleavage electrode was modified with the DNAzymes and the detection electrode was modified with ssDNA probes to capture the released photoactive DNA barcodes (**Figure 5-3C**). The photoactive DNAzymes and the ssDNA capture probes were modified with 3,4-dihydroxybenzaldehyde (DHBA), another catecholate ligand, through the formation of a Schiff-base link between aldehyde group of DHBA and amine-termination of the DNA sequences.[6,98] The DHBA modification facilitated immobilization of the two different DNA probes onto their respective photoelectrodes, through bidentate-type bonding.[9,122,170] Photoelectrode characterization using electrochemical impedance spectroscopy indicated successful DNAzyme immobilization on the cleavage electrode and ssDNA probe modification on the detection electrode (**Figure 5-S3**). To achieve bacterial detection, the sample solution is deposited to cover both on-chip electrodes. The targets from the bacteria (proteins in the crude intracellular mixture of *E. coli*) interact with the catalytic core of the photoactive DNAzyme resulting in the cleavage of the DNAzyme, releasing the photoactive DNA barcode. After target interaction, the released DNA barcode is captured by the ssDNA probes at the detection electrode. This results in breaking of the rutile TiO_2 assemblies/anatase TiO_2-nanoparticle/caffeic acid heterostructure on the cleavage electrode and its reformation on the detection electrode, which decreases the signal on the cleavage electrode and increases the signal on the detection electrode (**Figure 5-3C** and **5-3D**).

To understand the assay operation, we performed a kinetics study on both photoelectrodes, in which the amount of photoactive barcodes released and captured was indirectly measured

through photocurrent density induced on the two photoelectrodes (**Figure 5-3E** and **5-3F**). These studies indicate that starting at 10 minutes, barcode cleavage is initiated and it continues to increase until 240 minutes. Interestingly, barcode capture is evident starting at 15 minutes on the detection electrode and continues until 240 minutes, which is line with past studies performed with redox barcodes and is linked to the diffusion time between the two electrodes.[34,364] Based on the results of this kinetics study, the target incubation period was chosen as 60 min, which presents an appropriate trade-off between reducing assay time and improving the signal magnitude.

5.3.3 Bacterial Detection

In order to evaluate the ability of the photoelectrochemical DNAzyme assay in detecting environmentally relevant amounts of *E. coli*, we exposed it to buffer or lake water (negative for *E. coli*) spiked with different concentrations of *E. coli* (**Figure 5-4**). *E. coli* was chosen as our target because of its prevalence as a wastewater contaminant.[376–378]; however, this assay can detect other types of bacteria using different photoactive DNAzymes.[350,363,364] The photocurrent change was measured on both electrodes and documented as fold change (ratio of post-target signal (J_T) to pre-target signal (J_{PT})) and plotted for each set of photoelectrodes for the 0-10^6 CFU mL^{-1} range for both buffer and lake water samples (**Figure 5-4A and 5-4B**). As expected, the photocurrent decreases on the cleavage electrode and increases on the detection electrode after exposing the chip to an increasing concentration of *E. coli* mixtures (**Figure 5-4A**). For both buffer and spiked lake water samples analyzed on the detection electrode, a semi-log plot of fold change as a function of target concentration is produced as a calibration curve (**Figure 5-4B, (ii) and (vi)**).[379,380] The limit-of-detection for this assay, calculated using the detection photoelectrode is 21 CFU mL^{-1} in buffer and 18 CFU mL^{-1} in lake water; whereas, the limit-of-

detection calculated using the cleavage photoelectrode is 442 CFU mL^{-1} in buffer, and 2694 CFU mL^{-1} in lake water (**Figure 5-S4**). The lower limit-of-detection observed on the detection photoelectrode compared to the cleavage photoelectrode demonstrates the benefit of our two-photoelectrode design. Such low limit-of-detection is achieved in the absence of growth cultures, target amplification, or the additional of reagents or labels during assay operation, which are common practices used in bacterial cultures, nucleic acid amplification tests (NAAT),[344,345] or enzyme-linked immunosorbent assays (ELISA),[325,346] respectively.

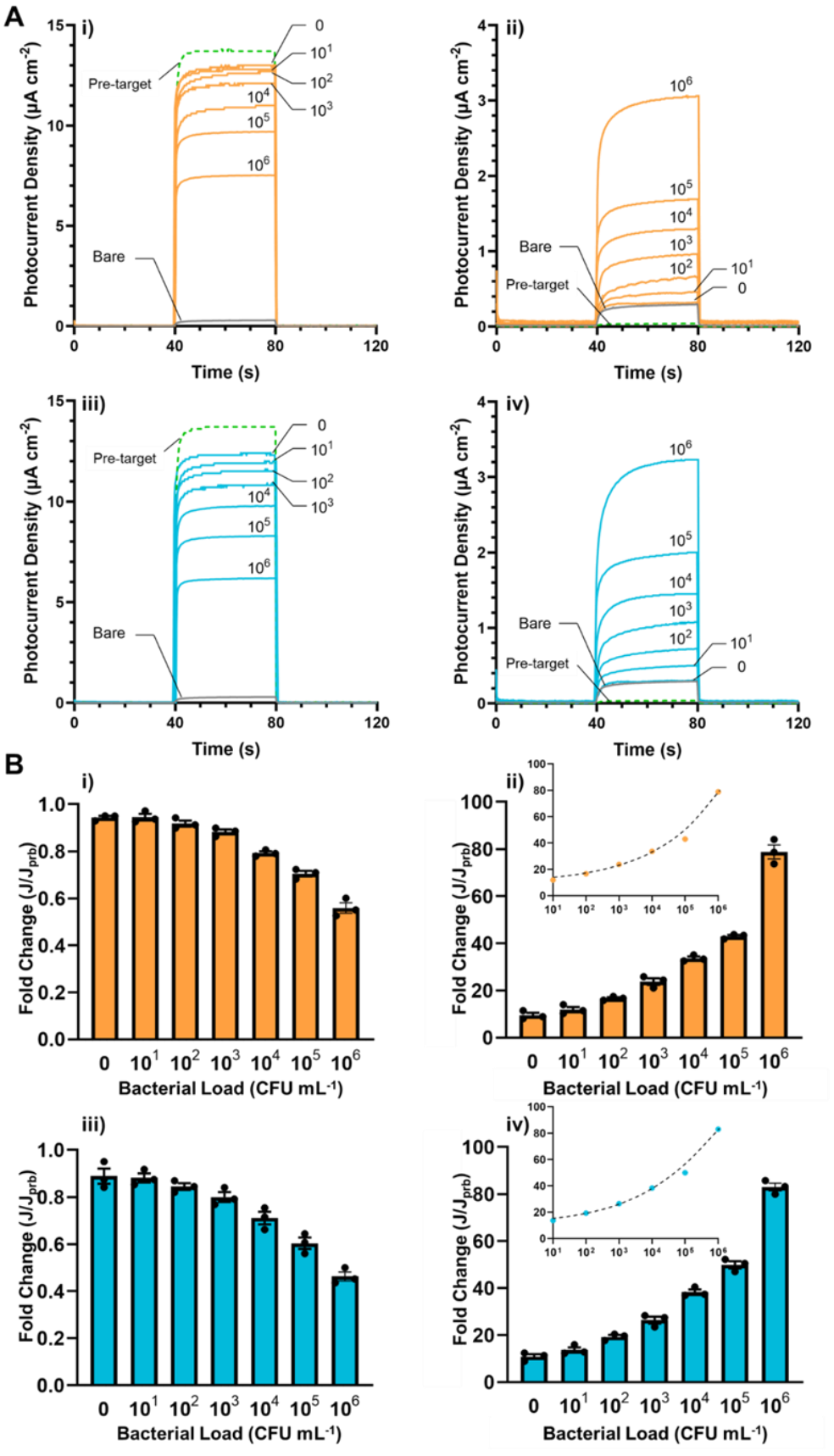
A
i)
ii)
iii)
iv)
Photocurrent Density (μA cm-2)
Time (s)
Pre-target
Bare
0
10^1
10^2
10^3
10^4
10^5
10^6
B
Fold Change (J/Jprb)
Bacterial Load (CFU mL-1)

Figure 5-4. Quantifying the limit-of-detection of the PEC DNAzyme assay. (A) PEC curves at varying *E. coli* concentrations for (i) cleavage photoelectrode in buffer, (ii) detection photoelectrode in buffer, (iii) cleavage photoelectrode in lake water, and (iv) detection photoelectrode in lake water. (B) The fold change of the PEC DNAzyme assay at varying concentrations of *E. Coli* for (i) cleavage photoelectrode in buffer, (ii) detection photoelectrode in buffer, (iii) cleavage photoelectrode in lake water, and (iv) detection photoelectrode in lake water. Fold change is calculated as the ratio of post-target photocurrent to pre-target photocurrent, J_T/J_{PT}. The insets show calibration curves plotted as detection electrode fold change as a function of target concentration, which are fitted to curves (ii) $(J_T/J_{PT})_D = (707[C_{CIM}]^{0.25}/(8.18\times10^9)^{0.25} + [C_{CIM}]^{0.25}) + 8.98$; $R^2 = 0.99$ for buffer and (iv) $(J_T/J_{PT})_D = (186[C_{CIM}]^{0.28}/(5.01\times10^5)^{0.28} + [C_{CIM}]^{0.28}) + 10.8$; $R^2 = 0.98$ for lake water.

After confirming that the PEC DNAzyme assay is capable of detecting environmentally-relevant concentrations of *E. Coli* contamination in both buffer and lake water, we assessed the specificity of this assay. For this assessment, we compared the fold change of *E. coli* to a panel of Gram-positive and Gram-negative bacteria targets: *Bacillus subtilis, Staphylococcus aureus, Legionella pneumophila, Enterobacter aerogenes, and Klebsiella pneumoniae* (**Figure 5-5**). The bacterial load used for all the targets for this assessment was 10^6 CFU mL^{-1} (**Figure 5-5**). Using both photoelectrodes, we were able to identify *E. coli* relative to other bacteria in buffer and lake water. Samples containing *E. coli* displayed fold changes of 79 and 82 in buffer and in lake water, respectively on the detection photoelectrode. In contrast, the non-target bacteria did not result in a fold change higher than 18 in either medium, showing that this assay has a high degree of specificity. Similarly, the cleavage photoelectrode fold change for *E. coli* samples showed a value of 0.56 in buffer and 0.47 in lake water. The minimum cleavage photoelectrode fold change for the non-target did not go lower than 0.84 in either medium, indicating low rates of non-specific cleavage for the non-specific bacteria. This further supports the high specificity of the PEC DNAzyme assay.

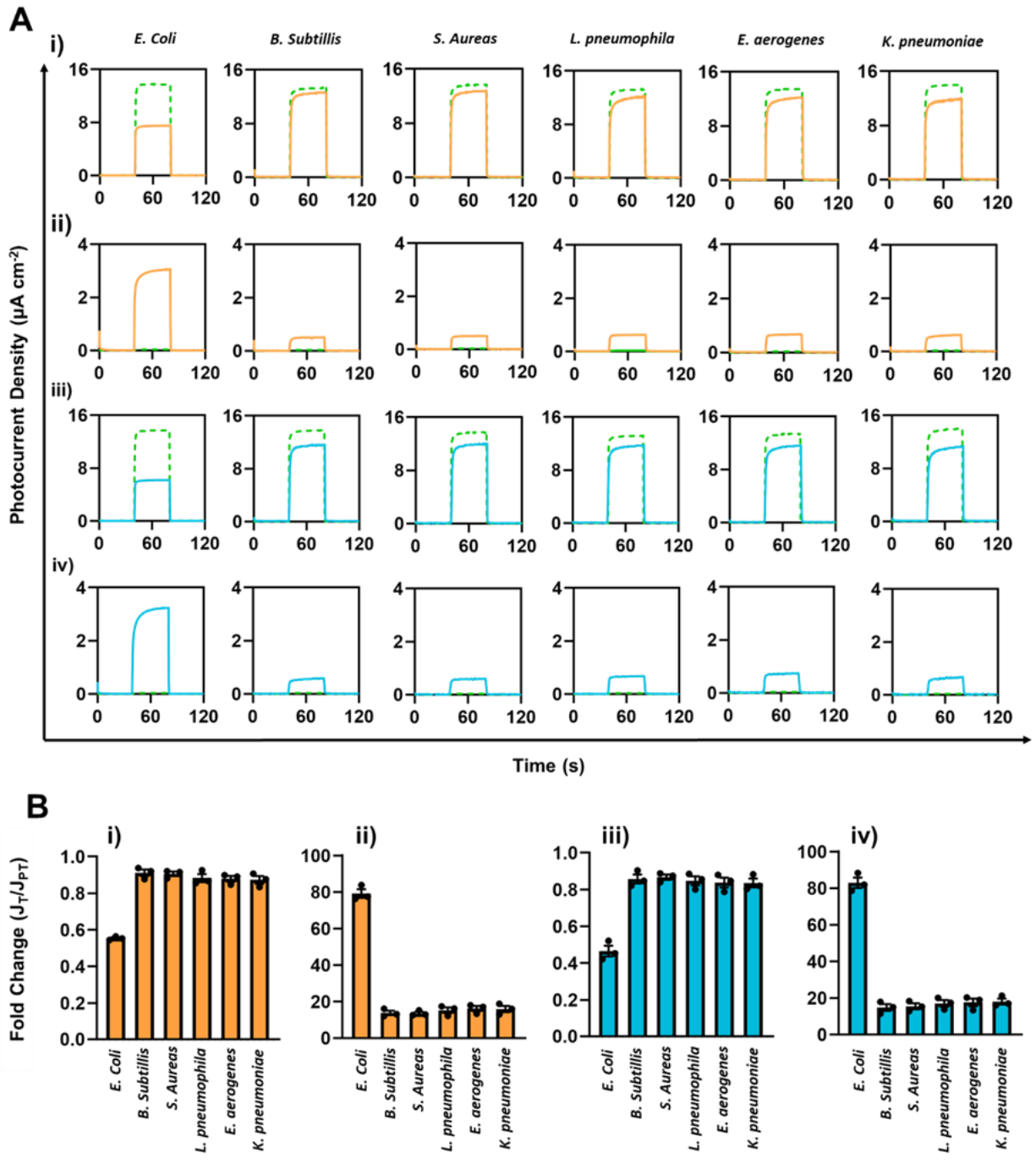

Figure 5-5. Specificity of the PEC DNAzyme assay. (A) Post (solid) and pre (dotted) target PEC curves of different bacteria for (i) cleavage photoelectrode in buffer, (ii) detection photoelectrode in buffer, (iii) cleavage photoelectrode in lake water, and (iv) detection photoelectrode in lake water. (B) Quantification of cross-reactivity of the PEC DNAzyme assay with different bacteria for (i) cleavage photoelectrode in buffer, (ii) detection photoelectrode in buffer, (iii) cleavage photoelectrode in lake water, and (iv) detection photoelectrode in lake water. Fold change is a

ratio of post-target photocurrent to pre-target photocurrent, J_T/J_{PT}. The bacteria concentration is $C_{CIM} = 10^6$ CFU mL^{-1} for all the tested organisms.

The stability of this assay was also evaluated through photocurrent measurements over an eight-week period, while the detection electrode was modified with photoactive DNAzymes and the cleavage electrode was modified with ssDNA capture probes (**Figure 5-S5**). The detection electrode displayed a ~30 % signal decrease over the first two weeks but demonstrates excellent stability from week 2 through to week 8. The cleavage electrode remains highly stable, with the signal decreasing by only ~14 % by the end of week 8.

5.4 Conclusions

We designed a sensitive, specific, reagent-free, and culture-free bacterial assay by integrating PEC signal transduction with RNA-cleaving DNAzymes. This assay is founded on a rationally-designed material system composed of two classes of TiO_2 nanomaterials: TiO_2-assemblies – three-dimensional rutile nanorod clusters (80-100 nm) and TiO_2-nanoparticles – caffeic acid modified anatase nanoparticles (1-6 nm). The combination of TiO_2-assemblies and TiO_2-nanoparticles gives rise to a semiconductor heterostructure, which is broken and reformed in response to the target for creating a bacterial detection assay.

The bacterial assay consists of two photoelectrodes fabricated from TiO_2-assemblies, with a cleavage photoelectrode modified with photoactive DNAzymes, and a detection photoelectrode modified with ssDNA capture probes. Upon target interaction, a photoactive reporter strand is cleaved from the DNAzyme and is captured by the DNA probes. This causes the breaking up of the TiO_2 heterostructures on the cleavage photoelectrode and its subsequent reformation on the detection photoelectrode. The result is a signal decrease on the cleavage photoelectrode and a signal increase on the detection photoelectrode.

The PEC DNAzyme assay detects *E. coli* with a limit-of-detection of 21 CFU mL^{-1} in buffer and 18 CFU mL^{-1} in lake water, surpassing the limit-of-detections offered by other amplification-free, culture-free, and reagent-free electrochemical (1000 CFU mL^{-1})[34] and photoelectrochemical (24 CFU mL^{-1})[334] assays used for bacterial sensing. The assay also demonstrates a wide dynamic range and is responsive until 10^6 CFU mL^{-1}. Additionally, the assay shows a high degree of specificity when compared against a panel of both Gram-positive and Gram-negative bacteria, demonstrating a signal that was at least 4 times higher for *E. coli* compared to interfering bacteria, confirming the effectiveness of this assay in bacterial identification.

The assay presented herein directly improves upon our previous work, which used electroactive DNAzyme labels and electrochemical signal transduction.[34,59,337,347,348] The synthesis of novel photoactive TiO_2 nanomaterials and combining them with DNAzymes allowed for the integration of PEC signal transduction with this assay, which significantly enhanced sensitivity and dynamic range, and enabled quantitative rather than threshold-based analysis. . As such, our newly-developed assay meets the criteria for effective environmental monitoring and can be integrated with handheld photoelectrochemical readers for in-field water analysis.[62,381] Lastly, the new findings made herein with respect to "heterostructure engineering" and the development of "photoactive DNAzymes" are applicable to the sensing of other biologically-relevant targets in a wide range of applications.

5.5 Experimental Section

Materials:

1-ethyl-3-(3-dimethylaminopropyl)carbodiimide hydrochloride (EDC, ≥98.0%), 2-(N-morpholino)ethanesulfonic acid (MES, ≥99.0%), 3,4-Dihydroxybenzaldehyde (DHBA), caffeic acid, L-ascorbic acid (AA, 99.0%) magnesium chloride ($MgCl_2$, ≥99.0%), N-

hydroxysulfosuccinimide (NHS, ≥98.0%) phosphate buffer solution (PBS, 1.0 M, pH 7.4), potassium chloride (KCl, ≥99.0%), potassium ferrocyanide ($K_4Fe(CN)_6$, ≥99.5%), potassium ferricyanide ($K_3Fe(CN)_6$, ≥99.5%) sodium chloride (NaCl, ≥99.0%), streptavidin from *Streptomyces avidinii*, titanium (IV) butoxide (97.0%), and titanium (IV) sulfate (~15 wt. % in dilute sulfuric acid) were purchased from Sigma-Aldrich. Hydrochloric acid (HCl, 37%) was purchased from Caledon Laboratory Chemicals. Polystyrene sheets (1 mm thickness) were sourced from Grafix Arts. Vinyl films were obtained from DFC Graphic Films. Lake water samples were obtained from Lake Erie at Port Dover, Ontario, Canada. Milli-Q grade (18.2 MΩ cm) deionized (DI) water was used for all solution preparation and washing steps. All oligonucleotides were purchased from Integrated DNA Technologies. The modified mTEC agar was purchased from Hach Canada (London, ON) and the Omnipore 0.45 µm PTFE membranes was purchased from Millipore-Sigma (Boston, MA).

Acid-Hydrothermal Synthesis of TiO_2 Nanostructures:

For the synthesis of TiO_2-assemblies, 20 mL of the reaction solution was prepared in a Teflon container, by mixing titanium (IV) butoxide (1 mL) in HCl (1 M). The Teflon container was inserted into an autoclave and placed in an oven for 2 h at 180 ºC to prepare TiO_2-assemblies *via* hydrothermal synthesis. After synthesis, the TiO_2-assembly suspension produced in the oven was centrifuged six times at 6000 rpm. This was done to remove reaction by-products and restore neutral pH in the suspension. The TiO_2-assembly synthesis process and results are further described in our previous work.[98] For the synthesis of TiO_2-nanoparticles, 30 mL of the reaction solution containing ~15% titanium (IV) sulfate (1 mL) solution and caffeic acid (31 g) was prepared in a Teflon container. No acid was added, because as-received titanium (IV) sulfate solution contained sulfuric acid. The parameters for hydrothermal synthesis of TiO_2-

nanoparticles in the oven and its post-synthesis treatment are the same as the preparation method for TiO_2-assemblies.

Photoelectrode Fabrication:

The dual electrode PEC chip was fabricated on polystyrene sheets. The polystyrene was cleaned with ethanol and DI water, after which a vinyl mask was applied onto the sheet. The vinyl mask was cut into the desired electrode pattern (designed on Adobe Illustrator) using a Graphtec Robo Pro CE5000-40-CRP craft cutter. A 100 nm film of indium tin oxide (ITO) was sputtered onto the masked substrate by radio frequency sputtering using a Torr International Magnetron Sputtering System. The resulting chips consist of two half-circle ITO/PS substrates, each with a geometric surface area of 0.166 cm^{-2}. The substrates were coated by drop-depositing TiO_2-assemblies suspension (5 uL, 0.4 g L^{-1}) on each substrate. This process is repeated four times to deposit four layers.

Material Characterization:

The morphology of the synthesized nanostructures was analyzed by transmission electron microscopy (TEM) imaging using a Thermo Scientific Talos 200X STEM Microscope. The surface of photoelectrodes fabricated from the nanostructures was analyzed by scanning electron microscope (SEM) imaging using an FEI Magellan 400 FEGSEM Microscope. For SEM imaging, the samples were coated with a 3 nm thick layer of platinum. Conventional sample preparation was used for both TEM and SEM imaging. A Bruker SMART CCD 600 Diffractometer with a Cu source was used for obtaining X-ray diffraction (XRD) characterization of the synthesized particles.

Photoelectrochemical Characterization:

Photocurrent density measurements, electrochemical impedance spectroscopy (EIS) and incident photon to current efficiency (IPCE) investigations were carried out using a Zahner CIMPS-QE/IPCE3 Photoelectrochemical Potentiostat. For all three of these tests, a standard three-electrode cell setup was used. Platinum (Pt) wire was used as the counter electrode, a silver/silver chloride (Ag/AgCl) electrode for the reference electrode and the TiO_2 nanomaterial based photoelectrodes acted as the working electrodes. The photoexcitation source for the photocurrent measurements and EIS tests was a Thorlabs MNWHL4 mounted LED, which has a neutral white color temperature (400−700 nm) and an irradiance of 7.7 uW mm^{-2}. The photocurrent density measurement was done by running the potentiostat in chronopotentiometric mode for 120 s. The electrolyte solution used for the photocurrent measurement was composed of PBS (0.1 M) and AA (0.1 M). The potential of the PEC cell was fixed at 0 V, and the working electrode was irradiated with white light at a 40 s interval. Average photocurrent density was measured by taking the running average of the last 10 s of the irradiation period. Room temperature EIS measurements were performed at an open-circuit potential and the electrolyte used for the EIS measurements contained potassium ferricyanide (2 mM), potassium ferrocyanide (2 mM), and KCl (0.1 M) in 10 mM PBS. The excitation amplitude was 10 mV and the frequency range used was 100 kHz - 100 mHz. IPCE measurements were carried out with the same electrolyte solution as the photocurrent measurement test. The built-in variable wavelength LED of the Zahner potentiostat was used as the photoexcitation source during the IPCE testing. The following formula was used to convert photocurrent values at specific measured light wavelengths into IPCE:

$$(1) \quad IPCE(\%) = \frac{1240 \times J_{photo}(mA\ cm^{-2})}{\lambda(nm) \times I_{inc}(mW\ cm^{-2})}$$

TiO_2-nanoparticle tagged DNAzyme preparation:

The DNAzyme sequences were produced by ligating biotinylated part of DNAzyme sequences (DZ1) to aminated part of DNAzyme sequence (DZ2), using a ligation template (LT) assisted method adapted from Aguirre et al.[382] This process produced the *E. Coli* DNAzyme sequence without TiO_2-nanoparticle tagging (DZ). A solution of DZ is prepared and an amount DHBA solution was added to it to achieve 1:1 molar ratio of DHBA to DNAzyme, which is then incubated for 1 hour in 4 ºC temperature. This DHBA-DZ solution was set aside. A suspension of TiO_2-nanoparticles was prepared and caffeic acid solution was added to it to achieve 5% mass ratio of caffeic acid to TiO_2-nanoparticle. The TiO_2-nanoparticlesuspension was then mixed with EDC (20 mM), NHS (10 mM) and MES (10 mM) and incubated for 1 hour in 4 ºC temperature. Then streptavidin was added to the suspension to achieve 1:1 ratio of streptavidin molecule to TiO_2-nanoparticle and incubated for 1 hour in 4 ºC temperature. The suspension was then centrifuged at 4000 rpm for 30 s and the supernatant was replaced with DI water. The centrifugation was repeated four times. This process binds streptavidin molecules to TiO_2-nanoparticle through caffeic acid ligands to produce the Streptavidin-caffeic acid-TiO_2 suspension. An additional amount of caffeic acid solution is added to this suspension to achieve 35% mass ratio of caffeic acid to TiO_2-nanoparticle. The Streptavidin-caffeic acid-TiO_2 suspension and DHBA-DZ solution were mixed at a 12:10 molar ratio to produce the final TiO_2-nanoparticle tagged photoactive DNAzyme sequences (TDZ). **Table 5-S1** in Supplementary Information shows full list of all the sequences involved in this process.

Probe immobilization and bacteria detection:

In the initial probe immobilization step, capture probe (CP) solution (7.5 μL, 1.5 μM) and 2 μM TDZ suspension (7.5 μL, 1.5 μM) were deposited onto the detection electrode and the cleavage

electrode of the dual electrode PEC chip, respectively. The chip was incubated overnight at 4 ºC temperature, and then washed with 25:25 buffer (25 mM PBS and 25 mM NaCl). Afterwards, the photocurrents were measured to get the pre-target stage signals. In the next stage, various concentrations of crude intercellular matrix (CIM) from *E. Coli* bacteria were deposited as the target. For all experiments,100 µL of the target solution was deposited to cover both electrodes. The PEC chip was then incubated for 1 h at 37.5 ºC. During the incubation the PEC chips were rested at 15 º incline, with the cleavage electrode elevated above the detection electrode. The photocurrents were measured at this stage to get the post-target stage signals.

The CIM from different *E. coli* cultures (biological replicates) with concentrations of 10^7 CFU mL^{-1} were obtained by centrifugation at 11,000 × g for 5 min at 4 °C, followed by heating at 65 °C for 10 min to demonstrate the feasibility of the assay. The target solutions were prepared by spiking the bacterial samples in 25:25:100 buffer (25 mM PBS, 25 mM NaCl and 100 mM $MgCl_2$) and lake water. The signal generated with *E. coli* was compared with a panel of five control bacteria CIM (10^6 CFU ml^{-1}), including *B. subtilis, S. aureas, L. pneumophila, E. aerogenes* and *K. pneumoniae* to assess the specificity of the technique towards *E. coli*. The lakewater used for the spiking study was determined as negative by following method 1603 from the United States Environmental Protection Agency using modified membrane-thermotolerant Escherichia coli agar (modified mTEC) using 0.45 µm PTFE membranes.[383]

Limit-of-detection calculation:

Calibration curves were plotted as a function of the fold change [post-target signal (J) /pre-target signal (J_{prb})] and the concentration of the *E. Coli* CIM. This was done for both *E. coli* spiked in buffer solution and *E. coli* spiked in lake water. The curves fitted to the fold change data took the form of a logistic function that result from the law-of-mass-action for surface biosensors.[379]

Specifically, the calibration curves were fitted as a four-parameter non-linear logistic curve, known as the Hill equation which is generally used for translating ligand binding to a signal response.[384–386] The Hill equation used had the following forms:

$$(2) \quad (J/J_{prb})_D = \frac{A[C_{CIM}]^n}{(K_A)^n + [C_{CIM}]^n} + b$$

$$(3) \quad (J/J_{prb})_C = 1 - \frac{A[C_{CIM}]^n}{(K_A)^n + [C_{CIM}]^n} - b$$

Equation (2) and (3) were fitted to detection photoelectrode and cleavage photoelectrode fold change data, respectively. The variable C_{CIM} represents the bacterial target concentration in CFU mL^{-1}. Limit of blank (LOB) is calculated using the equation:

$$(4) \quad LOB = \left(\frac{J}{J_{prb}}\right) + 3\sigma_{blank}$$

Where, σ_{blank} is the standard deviation of the blank signal and the limit-of-detection was calculated within a 95% confidence interval. The blank signals were generated from target samples with 0 CFU mL^{-1} of *E. coli* CIM. The limit-of-detection was then calculated from the regression line by substituting the signal (y-value) with the LOB.[387]

Statistical analysis:

Statistical analysis were condcuted via GraphPad Prism 8.0, and the results were presented as mean±standard deviation. Average photocurrent density was calculated from photocurrents measured on three different photoelectrodes. Curve fitting was performed using the SciPy API in Python 3.8.

5.6 Acknowledgements

This research was funded by the National Sciences and Engineering Research Council of Canada. L.S. is the Canada Research Chair in Miniaturized Biomedical Devices. I.Z. is the Canada

Research Chair in Micro-nano Technologies. Transmission Electron Microscopy was performed at the Canadian Centre for Electron Microscopy.

5.7 Supporting Information

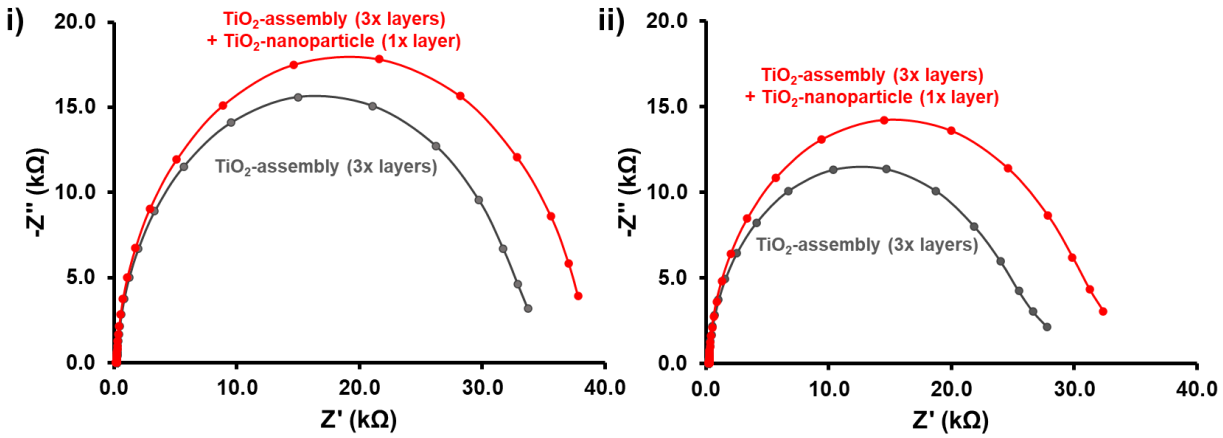

		R_S	R_{CT}	C_{DL}
Dark	3 layers	0.267 kΩ	32.8 kΩ	3.93 μF
	4 layers	0.28 kΩ	35.4 kΩ	4.08 μF
Light	3 layers	0.298 kΩ	25.6 kΩ	3.9 μF
	4 layers	0.299 kΩ	30.7 kΩ	4.08 μF

Figure 5-S1. Nyquist plot of photoelectrode complex impedances fabricated from three layers of TiO_2-assemblies and one layer of TiO_2-nanoparticle on top of three layers of TiO_2-assemblies: (i) dark condition, (ii) illuminated condition, (iii) equivalent circuit, and (iv) impedance values.

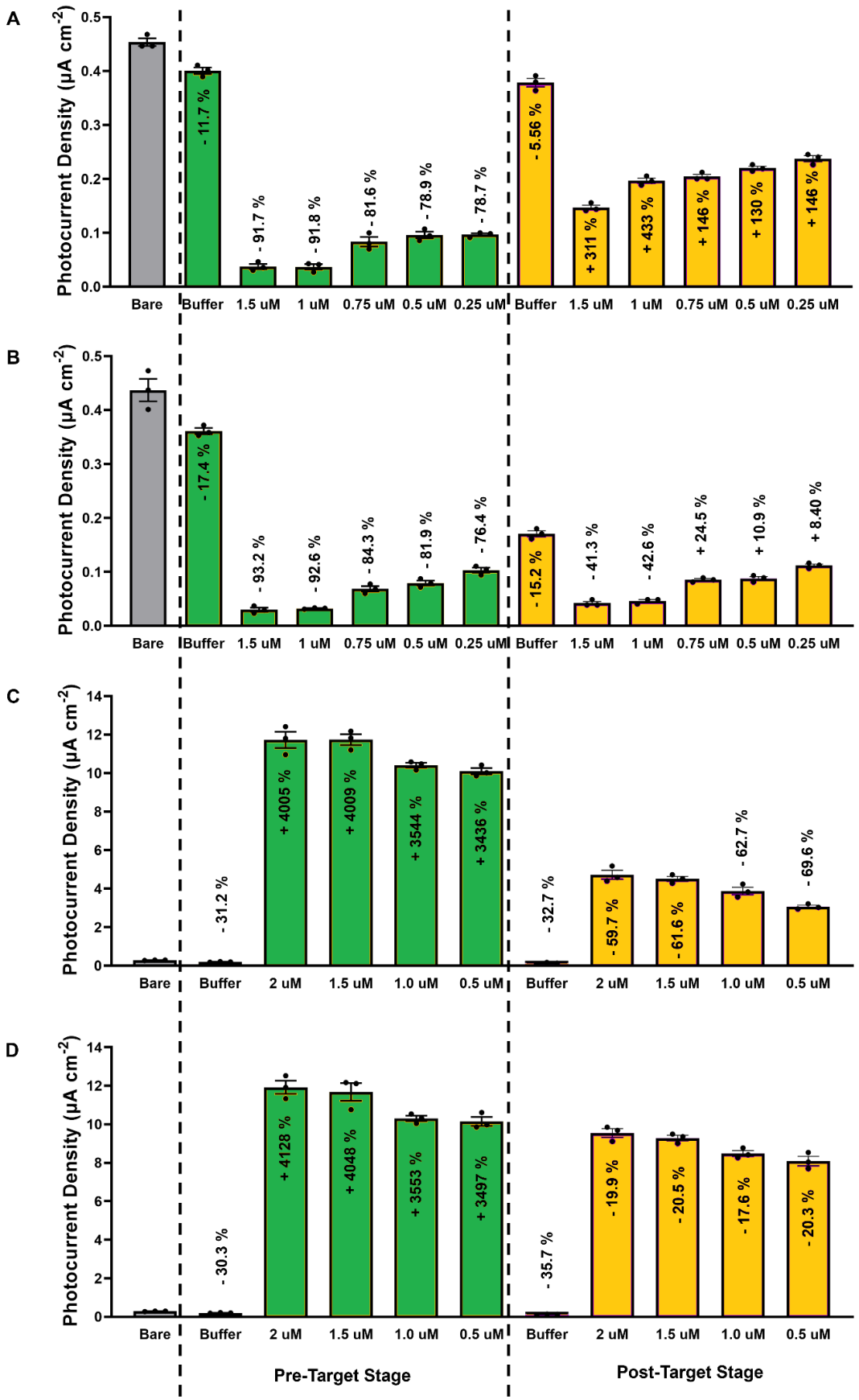
A
B
C
D
Photocurrent Density (μA cm-2)
Bare
Buffer
1.5 uM
1 uM
0.75 uM
0.5 uM
0.25 uM
2 uM
1.0 uM
- 11.7 %
- 91.7 %
- 91.8 %
- 81.6 %
- 78.9 %
- 78.7 %
- 5.56 %
+ 311 %
+ 433 %
+ 146 %
+ 130 %
+ 146 %
- 17.4 %
- 93.2 %
- 92.6 %
- 84.3 %
- 81.9 %
- 76.4 %
- 15.2 %
- 41.3 %
- 42.6 %
+ 24.5 %
+ 10.9 %
+ 8.40 %
- 31.2 %
+ 4005 %
+ 4009 %
+ 3544 %
+ 3436 %
- 32.7 %
- 59.7 %
- 61.6 %
- 62.7 %
- 69.6 %
- 30.3 %
+ 4128 %
+ 4048 %
+ 3553 %
+ 3497 %
- 35.7 %
- 19.9 %
- 20.5 %
- 17.6 %
- 20.3 %
Pre-Target Stage
Post-Target Stage

Figure 5-S2. Optimization of the DNAzyme and ssDNA probe concentrations. (A) Detection photoelectrode with ssDNA capture probe using (A) 10 nM of TiO_2-nanoparticle labelled complementary ssDNA and 100 nM of unlabeled non-complimentary DNAand (B) 100 nM of TiO_2-nanoparticle labelled non-complementary. (C) Cleavage photoelectrode with photoactive DNAzyme deposition using (A) 10^6 CFU mL^{-1} of *E. Coli* CIM (positive control), and (D) 10^6 CFU mL^{-1} of *E. Cloacae* (negative control). The initial bar shows photocurrent density of bare TiO_2-assembly photoelectrodes without any surface probe modification (grey). The middle set of bar plots (green) show photocurrent density of the TiO_2-assembly photoelectrodes at the pre-target stage with various probe concentrations on the surface. The last set of bar plots (yellow) shows the photocurrent density after target interaction.

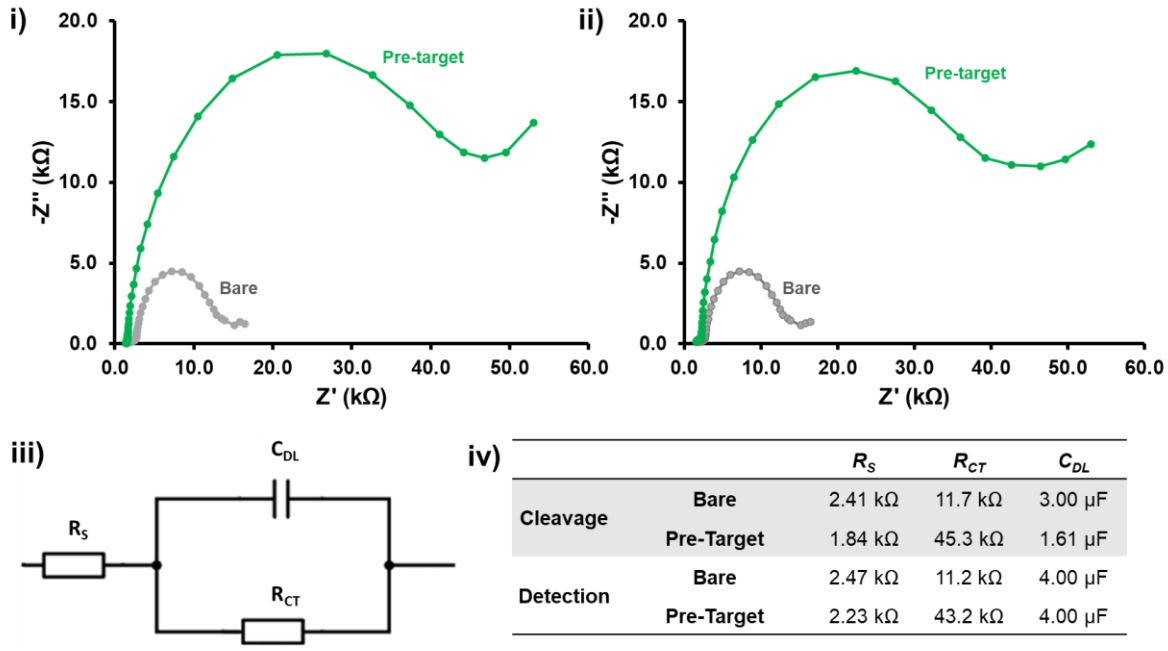

		R_S	R_{CT}	C_{DL}
Cleavage	Bare	2.41 kΩ	11.7 kΩ	3.00 μF
	Pre-Target	1.84 kΩ	45.3 kΩ	1.61 μF
Detection	Bare	2.47 kΩ	11.2 kΩ	4.00 μF
	Pre-Target	2.23 kΩ	43.2 kΩ	4.00 μF

Figure 5-S3. Nyquist plot of TiO_2-asembly photoelectrode complex impedances at various stages of PEC DNAzyme assay operation: (i) cleavage electrode, (ii) detection electrode, (iii) equivalent circuit, and (iv) impedance values. All EIS measurements were done in illuminated condition.

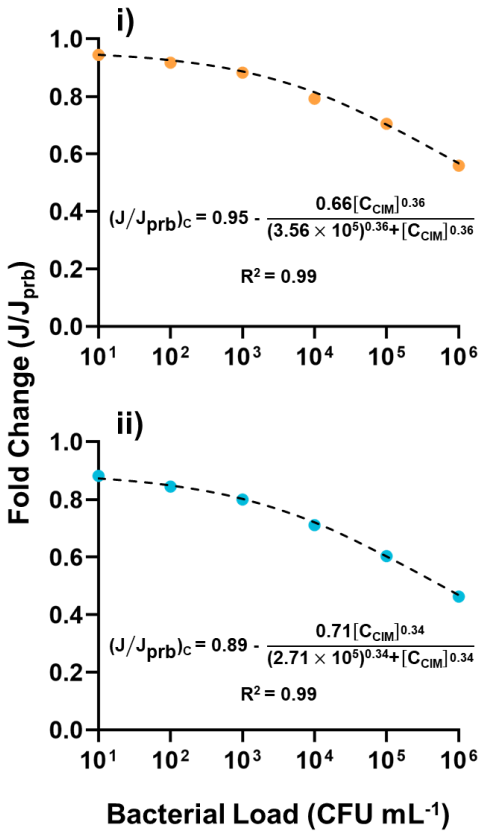

Figure 5-S4. Calibration curves plotted as cleavage electrode fold change as a function of target concentration, which are fitted to a sigmoidal curves by equation (i) $(J_T/J_{PT})_C = 0.95 - (0.66[C_{CIM}]^{0.36}/(3.56\times10^5)^{0.36} + [C_{CIM}]^{0.36})$; $R^2 = 0.99$ for buffer and (ii) $(J_T/J_{PT})_C = 0.89 - (0.71[C_{CIM}]^{0.34}/(2.71\times10^5)^{0.34} + [C_{CIM}]^{0.34})$; $R^2 = 0.99$ for lake water.

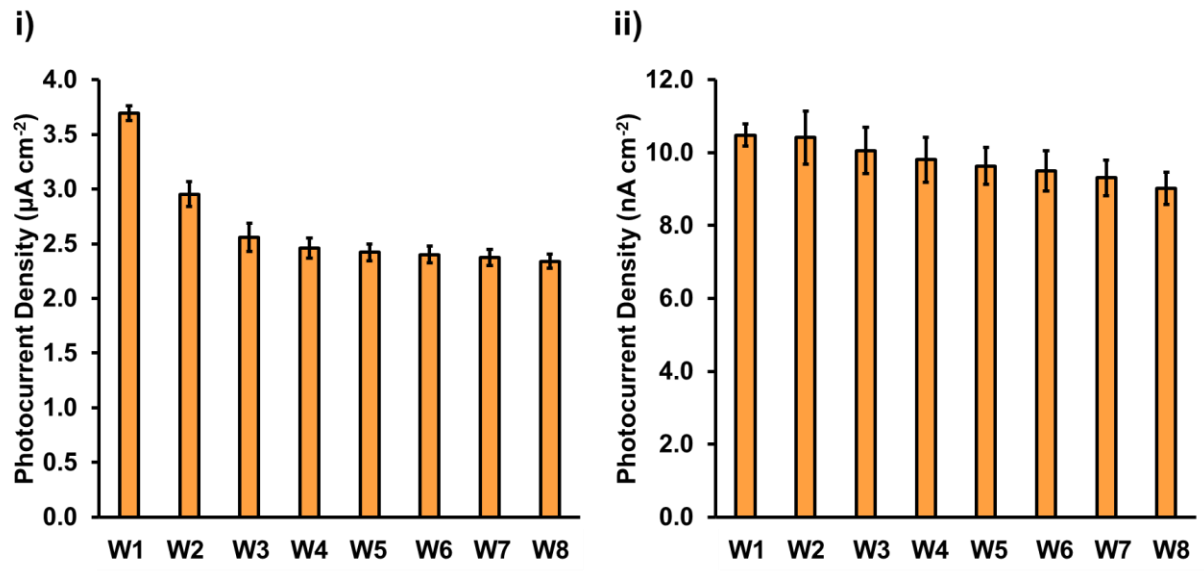

Figure 5-S5. Evaluation of the long-term stability of the PEC DNAzyme assay through photocurrent density measurements during an eight-week period: (i) detection electrode modified with ssDNA capture probes, and (ii) cleavage electrode modified with photoactive DNAzymes.

Table 5-S1. Summary of all the oligonucleotides used in the design of Photoactive DNAzyme.

Name	Labels	Sequence (5'-3')	Note
DZ1	5'- Dual Biotin; rA = riboA	2Bio/TTT TTT GTG TGA CTC TTC CTA GCT rATG GTT CGA TCA AGA	DNAzyme Part 1; Biotinylated part of DNAzyme
DZ2	3' - Amine	GAT GTG CGT CTT GAT CGA GAC CTG CGA CCG TTT TTT TTT T/Am	DNAzyme Part 2; Aminated part of DNAzyme
DZ	5'- Dual Biotin; rA = riboA; 3' - Amine	2Bio/TTT TTT GTG TGA CTC TTC CTA GCT rATG GTT CGA TCA AGA GAT GTG CGT CTT GAT CGA GAC CTG CGA CCG TTT TTT TTT T/Am	*E. Coli* e-RCD after ligation; no TiO_2-nanoparticle tagging
TDZ	NP = TiO_2-nanoparticle; Strp = Streptavidin; 5'-Dual Biotin; rA = riboA; 3'-Amine	NP-Strp-2Bio/TTT TTT GTG TGA CTC TTC CTA GCT rATG GTT CGA TCA AGA GAT GTG CGT CTT GAT CGA GAC CTG CGA CCG TTT TTT TTT T/Am	TiO_2-nanoparticle tagged *E. Coli* photoactive DNAzyme sequences
RS	NP = TiO_2-nanoparticle; Strp = Streptavidin; 5'-Dual Biotin; rA = riboA;	NP-Strp-2Bio/TTT TTT GTG TGA CTC TTC CTA GCT rA	Cleaved TiO_2-nanoparticle tagged reporter strand
LT		CAA GAC GCA CAT CTC TTG ATC GAA CC	Ligation template
CP	3'-Amine	TAG CTA GGA AGA GTC ACA CA/Am	Capture Probe

Chapter 6

Catecholate Dye-assisted Decoration of Ag on TiO_2 Nanoparticles for the Detection of Cancer-related MicroRNA Biomarkers on a Multiplexed Photoelectrochemical Platform

Preface:

A significant aspect of objective I of this thesis is to develop photoactive materials that allow PEC biosensors to be easy-to-use while remaining highly sensitive. An effective method of accomplishing this is to have easily biofunctionalizable photoelectrodes, where biomolecule reagents can be easily linked to its surface.[109–111] Chapter 6 addresses this need by exploring decoration of plasmonic metal NPs onto TiO_2 nanostructures. The presence of metal NPs enable biofunctionalization through formation of thiol-metal complexes, [306,391] which in turn allowed us to create an ultrasensitive PEC biosensor with simple operation procedure. In this work, we describe a rapid one-pot synthesis method for the decoration of sub-nanometer ranged silver (Ag) NPs onto the surface of TiO_2 NPs, by using a catecholate-assisted photoreduction technique. In this method, Hematoxylin (HTX) – a catecholate dye acts as a multifunctional molecule that readily adsorbs onto the surface of TiO_2 to provide photoexcitation enhancement, while also acting as a reducing agent for silver precursors. HTX provided an initial boost in the optical absorption of TiO_2 in the visible and UV light range, to produce higher photocurrent for more efficient photoreduction of Ag NPs onto the surface of TiO_2 NPs. This resulted in the production of TiO_2/HTX/Ag NPs - a hybrid semiconductor heterostructure with significantly

enhanced photocurrent generation due to the combined effects of photoelectron injection from HTX and localized surface plasmon resonance decay from the Ag NPs. This synthesis method allowed for size tunability of the Ag NPs by adjusting the ratio of HTX to silver nitrate, and thereby allowing the level of photocurrent enhancement to be controlled. This was a direct continuation of the techniques used for catecholate-assisted synthesis and morphology tuning of TiO_2 nanomaterials developed in chapter 4 and 5, but instead applied for depositing new materials onto the TiO_2 nanomaterials.

The TiO_2/HTX/Ag NPs were used to fabricate photoelectrodes for a PEC biosensor the detection of cancer-related microRNA biomarkers. This assay was able to achieve a high degree of specificity when compared against other non-specific microRNA targets and achieved a LOD of 172 fM in diluted urine samples. While the design of this biosensor reverts to signal-off design of chapter 4 and 4, it still furthers objective II by detecting a new type of biomarker, having a simple operation and achieving ultrasensitivity. Furthermore, this design achieved multiplexing with PEC biosensing for the first time, which innovates towards objective III. Multiplexing allows for the detection of a panel of biomarkers rather than a single biomarker, which will enable acquiring of detailed prognostic information about diseases at the PoC setting.

Authors: Sadman Sakib, Leyla Soleymani and Igor Zhitomirsky

Publication: Submitted for publication in ACS Nano in December 2022

6.1 Abstract

Effective management of cancer requires continuous and frequent monitoring of associated biomarkers to monitor its progression during treatment. Recent advances in cancer management have shown non-coding nucleic acids such as microRNAs to be effective biomarkers for aiding in diagnosis, prognosis, and treatment monitoring. There is a growing interest in using rapid, simple, and point-of-care biosensing technology to implement a more patient-centric approach to cancer treatment, rather than relying on current standards of lengthy laboratory-based nucleic acid amplification processes. Photoelectrochemical (PEC) signal transduction has emerged as a powerful technique for ultrasensitive detection with low background in complex media, that is able to meet this shift in cancer-related healthcare. Despite this, it nevertheless remains challenging to create PEC biosensors founded on stable material systems that are also easily biofunctionalized. Herein, we report the development of a novel one-pot synthesis method for TiO_2 nanoparticles (NPs) decorated with Ag NPs. In this method, TiO_2 NPs were surface modified with Hematoxylin (HTX) dye to achieve enhanced photoreduction and direct nucleation of Ag NPs on TiO_2 surfaces. The resulting TiO_2/HTX/Ag NP heterostructure showed significantly enhanced photocurrent generation, necessary for achieving high sensitivity in PEC biosensing, through the combined effects of localized surface plasmon resonance and photoelectron injection. The TiO_2/HTX/Ag NP material system was very easily biofunctionalized through thiol-metal complexation. This material system was used to construct signal-off multiplexing PEC microRNA sensor for analysis of urine samples, that demonstrated low limit-of-detection of 172 fM, and a high dynamic range of 100 fM – 100 nM, while showing a high degree of specificity.

6.2 Introduction

In response to the need for rapid and point-of-patient testing for cancer management, biosensors coupled to electrochemical readout have been implemented to create handheld bioanalytical devices that resemble the glucose monitor.[60,64,388–390] Photoelectrochemistry (PEC) is an emerging signal transduction method that has shown great potential for ultrasensitive detection with low background in complex media, that is perfectly suited for analyzing complex media from liquid biopsy samples.[9,62,98,391,392] PEC biosensors combine electrochemical signal readout with optical excitation, which decouples the mode signal excitation from the mode of signal readout.[62,64,133] This decoupling allows PEC biosensors to a high signal generation combined with very low background signal, which results in high sensitivity, low limit-of-detection (LOD), and high dynamic range.[64,133,392]

Compared to conventional mechanisms for bioanalyte detection such as electrochemistry, chemiluminescence or colorimetry for bioanalyte detection, PEC signal transduction offers significantly higher signal-to-noise ratios. [64,96,97,133,392,393] This makes it possible use PEC signal reading to implement simpler, more reliable and easy-to-use bioassays without sacrificing performance.[64,96,97,133,392,393] Despite this advantage, it nevertheless remains challenging to create PEC biosensors founded on stable material systems that are also easily biofunctionalized for sensing applications.[64,96,97,109,122,230] It is desirable for photoelectrodes, the transducing element in PEC biosensing to have high incident photon-to-converted electron efficiency to increase the electrochemical reaction rate and the resultant photocurrent. Conventional PEC biosensors have typically relied on fabricating photoelectrodes from TiO_2 nanoparticles (NP) due to their high photocatalytic efficiency, chemical stability, tunable morphology, water insolubility, low toxicity, low cost, and ideal conduction and valence band levels for driving electrochemical reactions.[64,122,394] However, unmodified TiO_2 has poor light absorption in the visible light range

along with high photogenerated charge carrier recombination rate, limiting its photocurrent generation efficiency, due to its intrinsic wide bandgap physical properties.[9,64,98,122] Furthermore, TiO_2, like most PEC-suitable materials, is problematic for facilitating bioconjugation because of its chemical inertness. This makes it difficult to immobilize the necessary biomolecules on TiO_2, which are needed to capture target biomarkers.[9,64,122,170]

To overcome the drawbacks of TiO_2-based photoelectrodes in PEC biosensors, we sought to develop a novel material system which improves photocurrent generation in addition to facilitating easier bioconjugation. Coupling TiO_2 with plasmonic NPs made from noble metals such as silver or gold can further amplify photocurrent by providing a mechanism for capturing hot-electrons generated from the localized surface plasmon resonance (LSPR) effect, which reduces electron-hole pair recombination and improves UV/visible light absorption.[128,306,391,395] Additionally, noble metals are useful for bioconjugation, as thiolated biomolecules can be easily immobilized onto them through the formation of thiol-metal complexes.[306,391,395,396] Amongst noble metal nanoparticles, silver nanoparticles (Ag NP) are particularly desirable due to their low cost and simple preparation..[397–399] Traditionally, Ag NP are decorated onto TiO_2 nanostructures through conventional photoreduction techniques. However, this method presents several disadvantages such as weak bonds at the Ag/TiO_2 interface making the structure unstable and the tendency to form Ag aggregates which decreases photoconversion efficiency.[400,401] Other methods for Ag NP decoration include hydrothermal reduction,[402] atomic layer deposition,[403] spin coating,[404] evaporation method,[405] and pulsed current deposition.[406] These methods come with disadvantages of either being complex multistage processes that are costly and time consuming, unsuitable for decorating nanoscale particles needed for PEC biosensing or resulting in only limited improvement in photoconversion efficiency. Herein, we present a novel one-pot

process for the synthesis of stable Ag NP decorated TiO_2 nanoparticles through catecholate dye-assisted photoreduction, referred to as TiO_2/HTX/Ag NP. This process takes commercially available "P25"-TiO_2 NP and directly grows sub-nanometer sized Ag NP by taking advantage of the innate PEC current of the TiO_2 NP. In this process TiO_2 nanostructures are first modified with hematoxylin (HTX), a dye with catecholate groups. Here, HTX is a multifunctional molecule that readily adsorbs onto the surface of TiO_2 to provide photoexcitation enhancement, while also acting as a reducing agent for silver precursors.[9,98,170,407] HTX is used to give an initial boost in the optical absorption of TiO_2 in the visible light range, to produce higher photocurrent for more efficient photoreduction of Ag NPs onto the surface of TiO_2 NPs, resulting in a hybrid semiconductor heterostructure with significant enhanced photocurrent generation.

The objective of this investigation was to develop a highly photoactive and easily biofunctionalizable material system as a foundation for a high-performance signal transducer in a PEC biosensing platform for the detection of microRNA (miRNA) biomarkers related to prostate cancer. These biomarkers are a type of nucleic acid that regulates RNA expression in the cell and various cell functions such as cell growth, cell death, cell differentiation, and cell-to-cell communication.[408–410] The importance of miRNAs in cellular function make them an effective indicator for the presence of cancer and tumor cells, and detection of miRNAs can provide a clear profile of cancer prognosis to give information about the patient's disease stage.[408,410–412] Herein, we developed a novel catechol-assisted synthesis method for Ag NP-decorated TiO_2 NP that was rapid, one-pot and reliable. This material system was used to fabricate multifunctional photoelectrodes that served as the foundation for a signal-off multiplexed PEC miRNA sensor, that demonstrated high sensitivity, a large dynamic range and a low LOD. [10,12,14,58] The presence

of silver converted TiO_2 NPs into a material that is very easily biofunctionalized through thiol-metal complexation. This property combined with the ultra high signal generation allowed for the design of a very simple two-step assay that can deliver rapid sample-to-result time and ultrasensitivity. Additionally, the designed assay shows how PEC biosensors can be implemented with multiplexing to monitoring a wide variety of different biomarkers to perform miRNA expression profiling. This material developed herein is highly promising for the improved performance and robustness it brings to PEC biosensing.

6.3 Results and Discussion

With the purpose of fabricating Ag NP-decorated TiO_2 NP for achieving noble metal/semiconductor interfaces,[128,413] we developed a novel catecholate-assisted photoreduction synthesis technique for decorating TiO_2 NP with Ag NP. The initial step in this method involved using HTX, [38,42] a novel dye material for the surface modification of TiO_2 NP. [122,170] Here various concentrations of HTX were added to TiO_2 suspensions, resulting in the TiO_2/HTX NP suspensions. The proceeding step involved the addition of $AgNO_3$ as the silver precursor to the TiO_2/HTX suspensions. After samples were exposed to white light irradiation for 1 hour in a dark chamber, the photoreduction process resulted in the nucleation of Ag NPs on the surfaces of TiO_2 NP, creating the TiO_2/HTX/Ag NP suspensions. Seven different TiO_2 NP samples with various amounts of HTX and starting $AgNO_3$ concentrations were analyzed to understand the synthesis mechanism and characterize the properties of TiO_2/HTX/Ag NP material system (**Table 6-1**).

Table 6-1. Nomenclature used for various TiO_2 suspensions and initial reagent concentrations used during their synthesis.

Sample Name	TiO_2 NP concentration	HTX Concentration	$AgNO_3$ Precursor Concentration

TiO_2	0.66 g L^{-1}	N/A	N/A
TiO_2/HTX-5	0.66 g L^{-1}	0.033 g L^{-1}	N/A
TiO_2/HTX-10	0.66 g L^{-1}	0.066 g L^{-1}	N/A
TiO_2/HTX-15	0.66 g L^{-1}	0.099 g L^{-1}	N/A
TiO_2/HTX-5/Ag-5	0.66 g L^{-1}	0.033 g L^{-1}	0.033 g L^{-1}
TiO_2/HTX-10/Ag-10	0.66 g L^{-1}	0.066 g L^{-1}	0.066 g L^{-1}
TiO_2/HTX-15/Ag-15	0.66 g L^{-1}	0.099 g L^{-1}	0.099 g L^{-1}

Transmission electron microscopy (TEM) imaging was performed to analyze the morphologies of the final TiO_2/HTX/Ag NP particles (**Figure 1A and 1B**). All the samples contained P25-TiO_2 NP as the base material, which presented as highly monodispersed nanoparticles with an average size of 21 nm. The TEM micrographs for all three TiO_2/HTX/Ag NP samples showed successful decoration of Ag NPs on the surface of the TiO_2 NPs. The Ag NPs could be identified as bright white particles contrasted against the TiO_2 in dark-field images and as dark particles in bright-field images. The Ag NP size ranges for each of the samples were as follows: TiO_2/HTX-5/Ag-5 – 0.35-3.5 nm (median = 1.8 nm), TiO_2/HTX-10/Ag-10 – 1.0-4.5 nm (median = 2.8 nm), and TiO_2/HTX-10/Ag-10 – 2-10 nm (median = 3.0 nm) (**Figure 6-1C**). Increasing the amount of HTX and $AgNO_3$ precursor correlated with increasing average Ag NP size and polydispersity. In addition to the sub-nanometer sized Ag NPs, the three samples also contained Ag NP aggregates with a size range of 50-250 nm (**Figure 6-S2**). X-ray diffraction (XRD) analysis was performed to identify the phase compositions of the TiO_2/HTX/Ag NP samples (**Figure 6-1D**). All three samples exhibit the characteristic peaks for anatase, rutile and silver-3C, and display a high degree of crystallinity. The anatase and rutile peaks are characteristic of P25-TiO_2 NPs, which are typically known to have a composition of 80% anatase and 20% rutile.[9,407,414] The only peaks observed that indicated the presence of silver in the samples were of the face-centered cubic 3C polytype, which is typical to bulk silver.[415] The

peaks associated with silver-3C were shown to be more prominent for the samples prepared with larger amounts of HTX and $AgNO_3$ precursor. This was particularly apparent with the (111) plane of Ag-3C, which is hard to distinguish from the (004) plane of anatase in the TiO_2/HTX-5/Ag-5 sample but is easily identified in the TiO_2/HTX-10/Ag-10 and TiO_2/HTX-15/Ag-15 samples. the increasing silver content resulted in increasing Ag NP size on the TiO_2 NP surface. The TEM images and the XRD data demonstrate how HTX-assisted photoreduction synthesis process can be used to produce different sizes of Ag NP decoration.

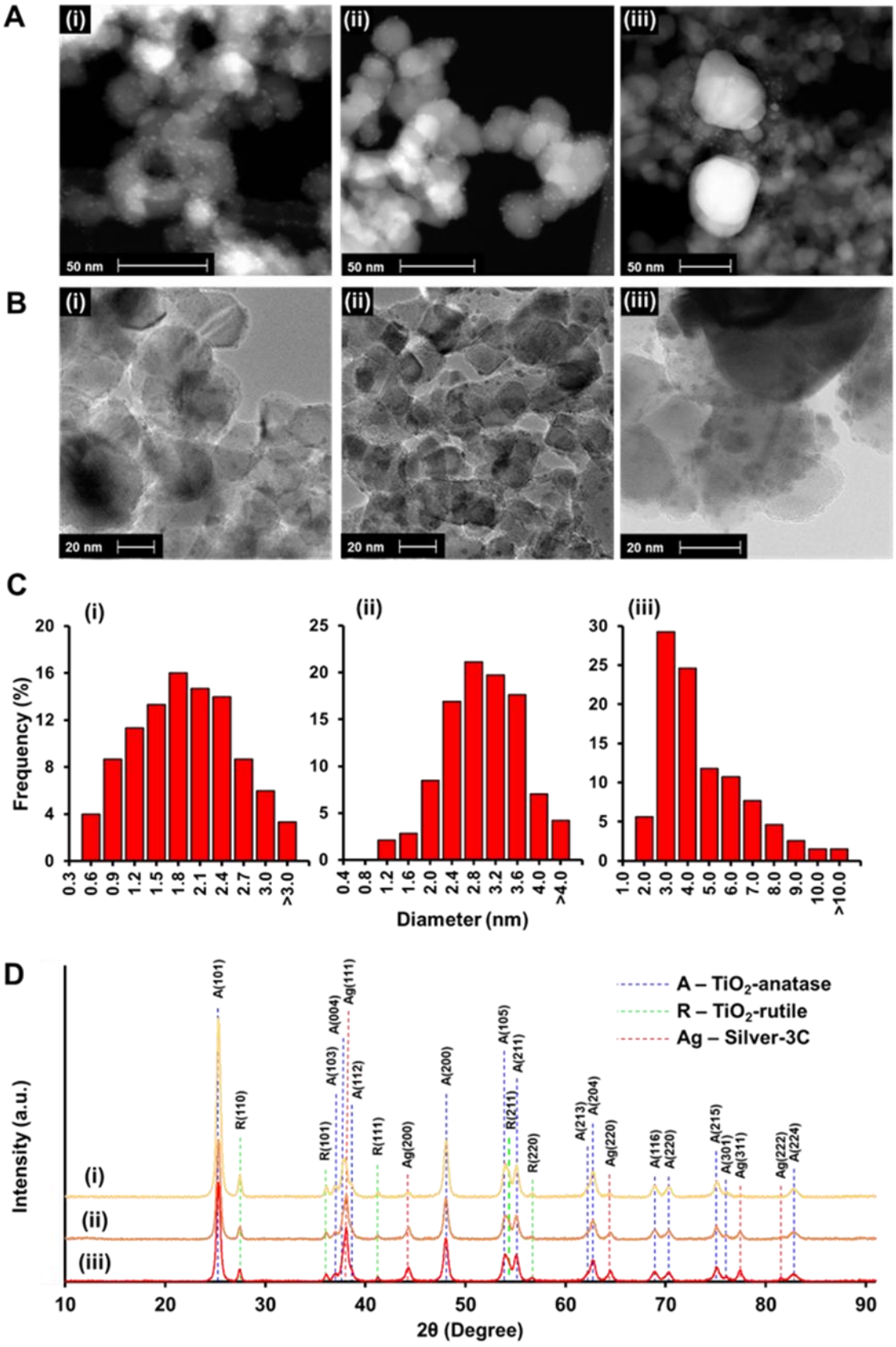
A
(i)
(ii)
(iii)
50 nm
B
20 nm
C
Frequency (%)
Diameter (nm)
D
Intensity (a.u.)
2θ (Degree)
A – TiO2-anatase
R – TiO2-rutile
Ag – Silver-3C
A(101)
R(110)
A(004)
A(103)
Ag(111)
A(112)
R(101)
R(111)
Ag(200)
A(200)
A(105)
A(211)
R(211)
R(220)
A(213)
A(204)
Ag(220)
A(116)
A(220)
A(215)
A(301)
Ag(311)
Ag(222)
A(224)

Figure 6-1. Morphology characterization of the TiO_2/HTX/Ag NP material system. (A) HAADF-STEM images, and (B) bright-field TEM images. (C) Size distribution of decorated Ag NP for (i) TiO_2/HTX-5/Ag-5, (ii) TiO_2/HTX-5/Ag-5, and (iii) TiO_2/HTX-15/Ag-15. (D) XRD data for (i) TiO_2/HTX-5/Ag-5, (ii) TiO_2/HTX-10/Ag-10 and (iii) TiO_2/HTX-15/Ag-15 (peaks correspond to the JCPDS files 21-1276, 64-0863, and 04-0783 for rutile, anatase and silver-3C, respectively).

HTX is a dye from the catecholate family of molecules and is characterized by the presence of aromatic rings with two adjacent phenolic hydroxide groups on opposite sides in its chemical structure (**Figure 6-2A-(i)**).[9,98,122,170] Catecholate molecules can adsorb onto metal oxide surfaces through their aforementioned hydroxide groups. This property makes them useful as colloidal dispersants and molecular linkers for metal oxide nanostructures.[122,170,187,416] Similar to other catecholate molecules, HTX binds to TiO_2 NP surfaces through the bidentate chelation bonding (**Figure 6-2A-(ii)**).[122,170] In metal oxides like TiO_2, dissociation of water molecules near their surface plane creates hydroxide groups in order to minimize surface Gibbs energy.[98,122,200] In the bidentate chelating bonding configuration, the phenolic hydroxide groups of catecholate molecules deprotonate and coordinate with the metal cation through a dehydration reaction.[98,122,200] In previous studies, catecholate molecules have been shown to act as reducing agents for silver precursors based on the chelation between two phenolic hydroxide groups of the catecholate functional groups and silver ions. [417–419] It is proposed that surface-bound HTX, which contain two catecholate functional groups, acts as a reducing agent for silver nitrate and this process was enhanced by the photogenerated current of the TiO_2/HTX NP system.[417–419] This results in silver nucleating onto the surface of TiO_2/HTX NP during photoreduction synthesis, and binding to HTX through bidentate chelation to form the TiO_2/HTX/Ag NP heterostructure.[419]

While XRD was used confirm the presence of silver in the TiO_2/HTX/Ag NP in the bulk samples, energy-dispersive X-ray spectroscopy (EDS) analysis was also employed to verify the

distribution of colloidal silver on the surface of TiO_2 NPs. (**Figure 6-2B**). Specifically, the EDS analysis was performed on the TiO_2/HTX-10/Ag-10 samples (the analysis area shown in **Figure 6-2B-(i)**) to gain insight about the deposition pattern of Ag NP.[420,421] The emission spectra was measured from a region containing a large aggregate particle (**Figure 6-2B-(ii)**) and a region containing decorated TiO_2 NPs (**Figure 6-2B-(iii)**). Both emission spectra contained characteristic X-ray peaks related to titanium (Ti), oxygen (O) and silver (Ag). The measured silver peaks are significantly stronger than the titanium and oxygen peaks in the aggregate particle region, indicating that the large aggregates are indeed composed of silver. Conversely, the silver peaks were weaker than the titanium and oxygen peaks, when focused on the TiO_2 NP region, which indicates that the TiO_2 NPs are decorated with sub-nanoscopic Ag NPs. As the samples were deposited on a copper TEM grid, the emission spectra contain background peaks related to copper. There is a small peak related to carbon seen in the TiO_2 NP region which can be attributed to the presence of HTX in the samples; this peak is superimposed with the Ag-M peak in the aggregate region emission spectra and is hard to distinguish. The deposition pattern of Ag NP in the TiO_2/HTX/Ag NP samples were further mapped out by using electron energy loss spectroscopy (EELS) to perform elemental mapping of a single Ag NP-decorated TiO_2 NP (**Figure 6-2C**).[420,421] The distribution of titanium and oxygen clearly outlines boundaries and space occupied by the TiO_2 NP. HTX can be mapped out by correlating it to distribution of carbon; the hollow core-shell distribution of carbon is indicative of the surface adsorption of HTX on TiO_2 NPs. The distribution of silver clearly maps out decoration pattern of Ag NPs on the TiO_2 NP surface, showing nanoparticles in the 0.5-2.5 nm size range.[38,65] In order to achieve successful decoration of silver onto TiO_2 NP, two conditions needed to be met: dispersion of TiO_2 NPs and a driving force for precipitation of silver on the surface of TiO_2. Not meeting these

conditions would result in Ag precipitating in the bulk as large aggregate particles only (**Figure 6-S3**).[417–419] Our approach was able to successfully meet both of these prerequisite conditions by making use of the multifunctional HTX dye. Catecholate molecules like HTX are known for improving colloidal stability by reducing agglomeration in metal oxides after surface adsorption.[122,170] The phenolic hydroxide groups of catechol molecules have also been proven to reduce silver nitrate. Thus surface-bound HTX acts as the driving force for the nucleation of Ag NP onto TiO_2 NPs, rather than only precipitating in the solution.[417–419] This process can be enhanced through applying an external anodic current. Our synthesis method attempted to take advantage of these known properties of HTX to enhance the photocurrent generation of TiO_2 NP for highly efficient decoration of Ag NP.[422]

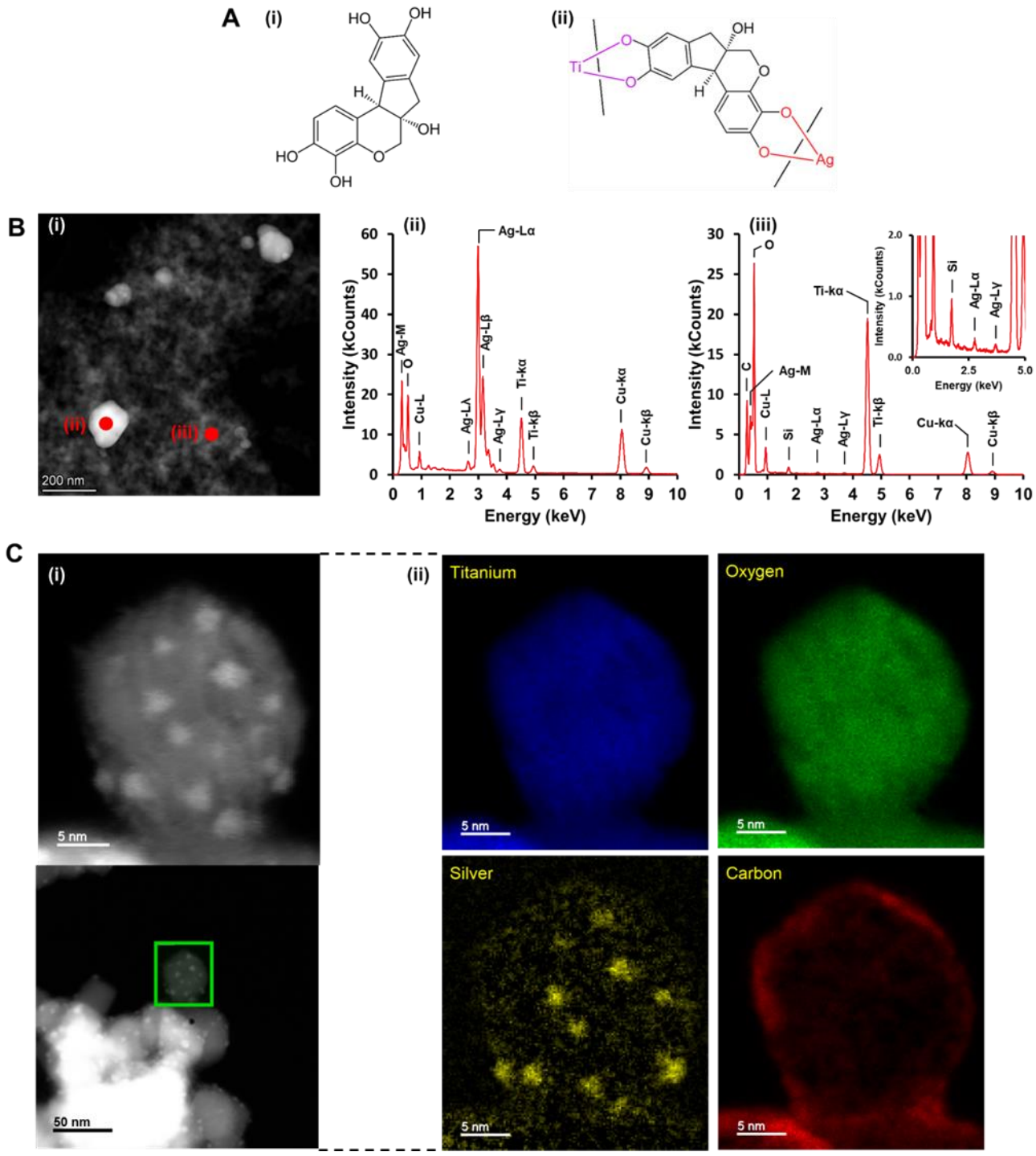

Figure 6-2. (A) Chemical structure of (i) HTX and (ii) its proposed binding mechanism to TiO_2 NP and Ag NP through bidentate chelation. (B) EDS data confirming the presence of Ag NP in TiO_2/HTX-10/Ag-10 NP material system: (i) TEM images showing the location of EDS spectra, (ii) EDS spectra of silver aggregates, and (iii) EDS spectra of TiO_2 NP decorated with subnanometer sized Ag NP. (C) EELS microscopy mapping out the elemental distribution of an Ag-decorated TiO_2 NP from the TiO_2/HTX-10/Ag-10 NP material system: (i) TEM image of the

of the region that was mapped (area bounded by the green box in the bottom image, which is magnified 10x in top image), and (ii) EELS data showing the distribution of titanium, oxygen, silver and carbon.

Photoelectrodes fabricated from all seven TiO_2 NP samples (**Table 6-1**) were optically and photoelectrochemically characterized (**Figure 6-3**). Ultraviolet-visible (UV/vis) spectroscopy of the solid photoelectrode samples (**Figure 6-3A**) showed unmodified TiO_2 NP having an optical absorption peak at 319 nm and having comparatively higher light absorption in the UV range (<400 nm) than in the visible range (400-700 nm). The absorbance of all modified TiO_2 NP samples greatly improved across all wavelengths. Both the TiO_2/HTX NP samples and the TiO_2/HTX/Ag NP showed a redshifting in the absorbance peak to ~342 nm and ~365 nm, respectively. Samples with higher amount of HTX and/or Ag NP demonstrated increased overall absorbance. The TiO_2/HTX/Ag NP samples have lower absorbance peaks than their TiO_2/HTX NP counterparts, but their absorbance peaks are wider leading to higher overall absorbance in the near-UV/blue light (400 – 450 nm) range. Photocurrent density measurements were performed by exciting the TiO_2 NP photoelectrodes with UV light (405 nm) (**Figure 6-3B**). Photons with energies higher than the work function of TiO_2 are absorbed to generate electron-hole pairs. The holes in the valence band migrate to the photoelectrode/electrolyte interface and oxidize L-ascorbic acid resulting in an anodic photocurrent.[9,95,98] The photocurrent density of the TiO_2 NP samples when ordered from the highest to the lowest are TiO_2/HTX-15/Ag-15 > TiO_2/HTX-5 > TiO_2/HTX-10/Ag-10 > TiO_2/HTX-15 > TiO_2/HTX-10 > TiO_2/HTX-5/Ag-5 > TiO_2. Modification of TiO_2 NP significantly increased its photocurrent density from 38.1 μA cm^{-2} up to a maximum of 346 μA cm^{-2} with the TiO_2/HTX-15/Ag-15 sample. HTX concentration of 5 % resulted in the highest phototocurrent density at 320 μA cm^{-2} in the TiO_2/HTX samples, which is consistent with the HTX concentration optimization experiment (**Figure 6-S4**). The

TiO_2/HTX/Ag NP samples have higher photocurrent than their TiO_2/HTX counterparts, which can be attributed their wider UV/vis absorbance peaks. The exception to this is TiO_2/HTX-5/Ag-5, which is nearly half that of TiO_2/HTX-5 and could potentially be attributed to the quantum confinement effect becoming dominant in Ag atomic clusters.[423–425] Photocurrent measurements with white light were also performed, but current density was found to be much lower than with UV excitation not suitable for PEC sensing (**Figure 6-S6**).

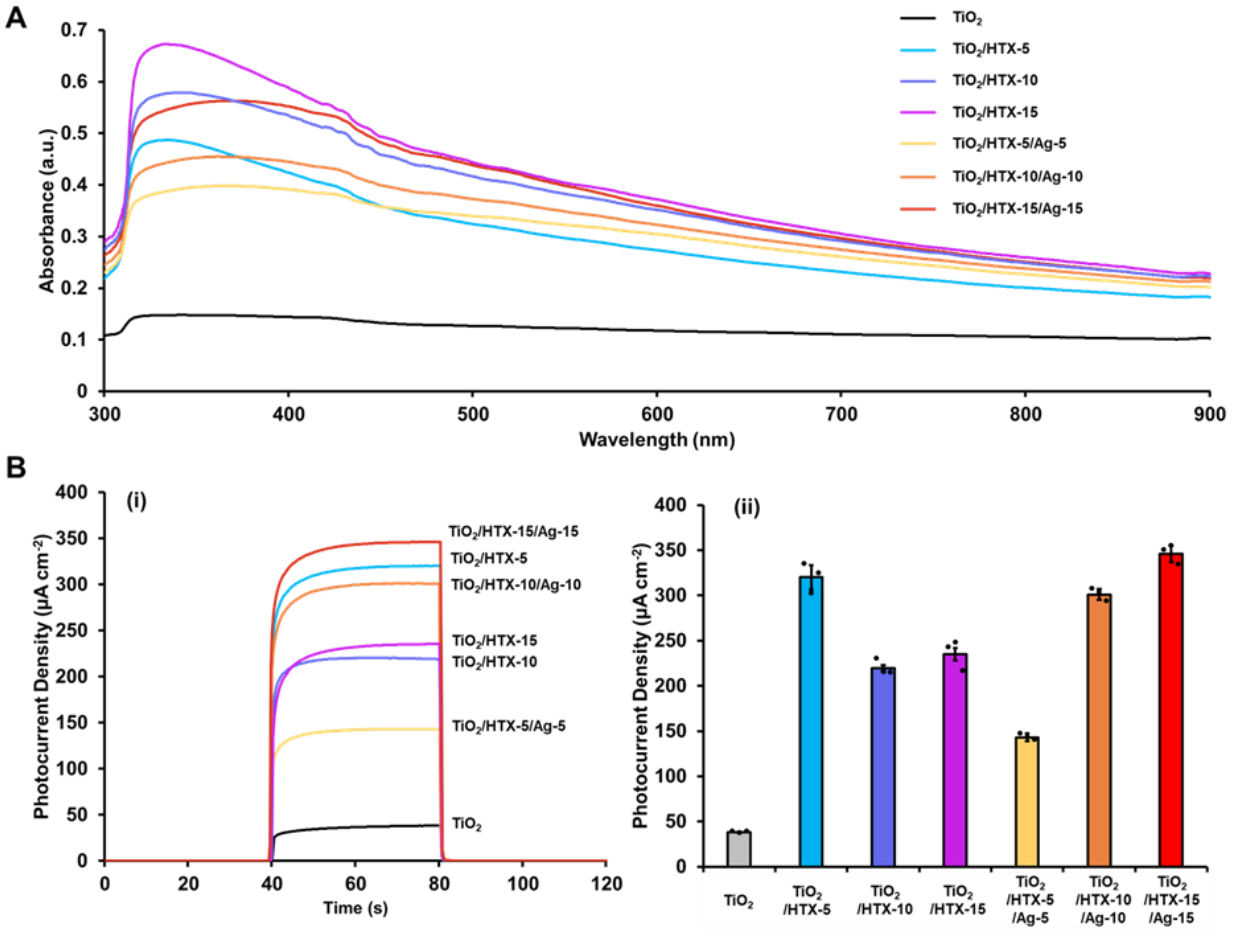

Figure 6-3. Optical and photoelectrochemical characterization of photoelectrodes fabricated from various TiO_2/HTX/Ag NP suspensions. (A) Solid UV-vis spectroscopy data. (B) Photoelectrochemical current density measurements: (i) chronoamperometric curves of the photocurrent densities shown both with and without optical excitation, and (ii) summary of photocurrents density measurements showing the mean value obtained from three measurements, with the error bars representing standard deviation. The photocurrent density measurements were performed at 0 V potential vs. Ag/AgCl reference electrode using 0.1 M L-ascorbic acid and 0.1 M phosphate buffered saline (PBS) as the electrolyte solution. The photoelectrodes were excited

with a mounted UV LED (405 nm), and the average photocurrent density of each sample was calculated by taking the running average of the last 10 s of the light excitation period.

In order to explain the UV/vis spectroscopy and photocurrent density measurements data, and to correlate them with the observations from the TEM and EELS images, a band structure for the TiO_2/HTX/Ag NP heterostructure was proposed (**Figure 6-4A**). We believe that the improved photoexcitation efficiency of this metal-molecule-semiconductor junction can be explained through the combined interaction two effects: enhancement in photoabsorption due to catecholate ligand driven electron injection from the TiO_2 surface-bound HTX[122,175,184] and hot electron generation from the Ag NPs through LSPR decay.[128,413,426] When catecholate molecules are adsorbed onto the surface of metal oxide semiconductors like TiO_2, they form charge transfer complexes that greatly improve UV/vis optical absorption by improving photoexcited electron injection into the metal oxide conduction band.[122,184,427] The highest occupied molecular orbital (HOMO) level and lowest energy molecular orbital (LUMO) level of HTX are -5.64 eV and -0.19 eV.[427] Likewise, in unmodified P25-TiO_2, the bandgap has been determined to be 3.20 eV and the conduction band level is approximately at -4.2 eV.[427,428] As the HOMO level of HTX is higher than the conduction band level of TiO_2, photoexcitation is made more efficient through type-I photoelectron injection process, where electrons can directly transition from the LUMO of a photoexcited surface-adsorbed dye to conduction band of a semiconductor.[122,184,427] Since dyes like HTX are able to be photoexcited at a wide range different frequencies in both UV and visible light, the type-I photoelectron injection process is able to significantly enhance the photoexcitation efficiency of the TiO_2/HTX NP heterostructure.[9,98,184,407] When plasmonic Ag NPs are added to this system, it results in the formation of a Schottky barrier between the Ag NP and the HTX-modified TiO_2, where Fermi level equilibration of TiO_2 and Ag produce band bending in the conduction and valance bands of TiO_2.[128,413,426] Following light absorption,

LSPRs are generated in the Ag NPs, which undergo non-radiative electromagnetic decay to produce hot electrons.[128,413,429] Plasmonic NPs can generate hot electrons at a wide range of frequencies correlating to their extinction spectra, which means the presence of plasmonic Ag NPs within TiO_2/HTX/Ag NP directly enhances the IPCE of this material system in both UV and visible light.[128,413,429] Despite there being a molecular layer of HTX lies in between the TiO_2/Ag junction, the proximity of Ag NPs to TiO_2 NPs would still result in Fermi level equilibration and band bending of the TiO_2 conduction and valence bands.[430,431] In this scheme, initial light absorption by Ag NPs results in LSPR generation which decays by direct injection of a hot electron into the LUMO of HTX. The excited HTX molecule then undergoes type-I photoelectron injection to excite TiO_2. [43,79,82] The transfer of hot electron leaves the Ag NPs positively charged, which helps reduce hole scavengers like L-ascorbic acid used in our experiments.[9,128]. This band structure is able to explain the behavior seen in TiO_2/HTX-10/Ag-10 NP and TiO_2/HTX-15/Ag-15 NP, which have improved photoexcitation efficiency compared to their TiO_2/HTX counterparts but is not consistent with the photocurrent density observations for TiO_2/HTX-5/Ag-5 NP. To explain this discrepancy, we need to consider how the band structure of Ag NPs change as they become smaller in size to become atomic clusters (**Figure 6-4B**). Silver and other noble metal NPs of sufficiently large sizes behave like plasmonic NPs, as depicted in the proposed TiO_2/HTX/Ag NP band diagram (**Figure 6-4A**).[106,128,423] However, it has been predicted via electronic structure studies that as plasmonic NPs approach the sub-nanometer range (under 5 nm for silver), they start to develop a bandgap and quantum dot-like properties.[106,423] This can be explained via the quantum confinement effect, where as the Ag NPs get smaller, their density of states also gets reduced which discretizes the conduction band and valance band of silver.[423–425] The addition of a third large bandgap structure can create a larger

effective bandgap for the TiO_2/HTX/Ag NP heterostructure, rather than reducing it like in the case with TiO_2/HTX NP, which would reduce the photocurrent density.[431,432] Based on the polydispersity observed in the TEM images, all TiO_2/HTX/Ag NP samples contained quantum dot-like Ag NPs. Only TiO_2/HTX-5/Ag-5 NP did not contain enough plasmonic Ag NP, which reduced their photoexcitation efficiency. Additionally, a portion of the Ag atomic clusters could have very large bandgaps that make them behave as insulators. It is possible that the TiO_2/HTX-5/Ag-5 NP sample contain a concentration of insulating Ag atomic clusters that are higher than its percolation threshold, thereby reducing the conductivity of this material which lowers the photocurrent density.[433]

In order to further verify the proposed TiO_2/HTX/Ag NP band structure and the presence of quantum dot-like or insulating Ag atomic clusters, incident photo-to-electron conversion efficiency (IPCE) and electrochemical impedance spectroscopy (EIS) were performed. The IPCE response (**Figure 6-4C**) showed that all seven samples have high photoexcitation efficiency in the UV range (< 400 nm) that rapidly drops off in the visible light region (> 400 nm), as expected for TiO_2-based materials.[6,9,306] The addition of HTX increased the photoexcitation efficiency of TiO_2 NPs. Increasing the amount of HTX added correlated to higher improvement in photoexcitation efficiency in the TiO_2/HTX NP samples and their corresponding TiO_2/HTX/Ag NP counterparts. The IPCE enhancement observed in each sample corresponded to their measured photocurrent density levels. As with the chronoamperometry data, the addition of Ag NPs improved the IPCE of TiO_2/HTX-10/Ag-10 NP and TiO_2/HTX-15/Ag-15 NP, particularly in the UV and blue light range, while having the opposite effect for TiO_2/HTX-5/Ag-5 NP. The IPCE response of TiO_2/HTX-10/Ag-10 NP and TiO_2/HTX-15/Ag-15 NP have peaks at ~380 nm and ~590 nm. The peaks in the UV region can be attributed to the extinction spectra

of silver; UV range peaks corresponds to decorated Ag NP, and visible corresponds to the large Ag NP aggregates.[106,128,413] The broad peak widths reflect the polydispersity of Ag NPs.[106]

The Nyquist plots from EIS show that the TiO_2 NP samples can be modeled through a Randles cell equivalent circuit with a constant phase element (CPE) representing the double layer (**Figure 6-4E**). Addition of HTX results in samples gaining higher charge transfer resistance. More HTX results in higher charge transfer resistance which reduces photocurrent density, but is counterbalanced by improved photoexcitation efficiency, leading to optimal HTX concentration at 5 % for maximizing highest photocurrent density in the TiO_2/HTX NP samples (**Figure 6-S4**). In TiO_2/HTX-10/Ag-10 NP and TiO_2/HTX-15/Ag-15 NP, the charge transfer resistance is reduced compared to their TiO_2/HTX counterparts. The exception to this is TiO_2/HTX-5/Ag-5 NP, where the charge transfer resistance significantly increases compared to TiO_2/HTX-5 NP, which indicates an increased presence of quantum dot-like or insulating Ag NPs. These observations combined with the IPCE response are further evidence for plasmonic NPs enhancing photoelectron injection (**Figure 6-4A**) and quantum dot-like/insulating Ag atomic clusters hindering photoexcitation (**Figure 6-4B**).

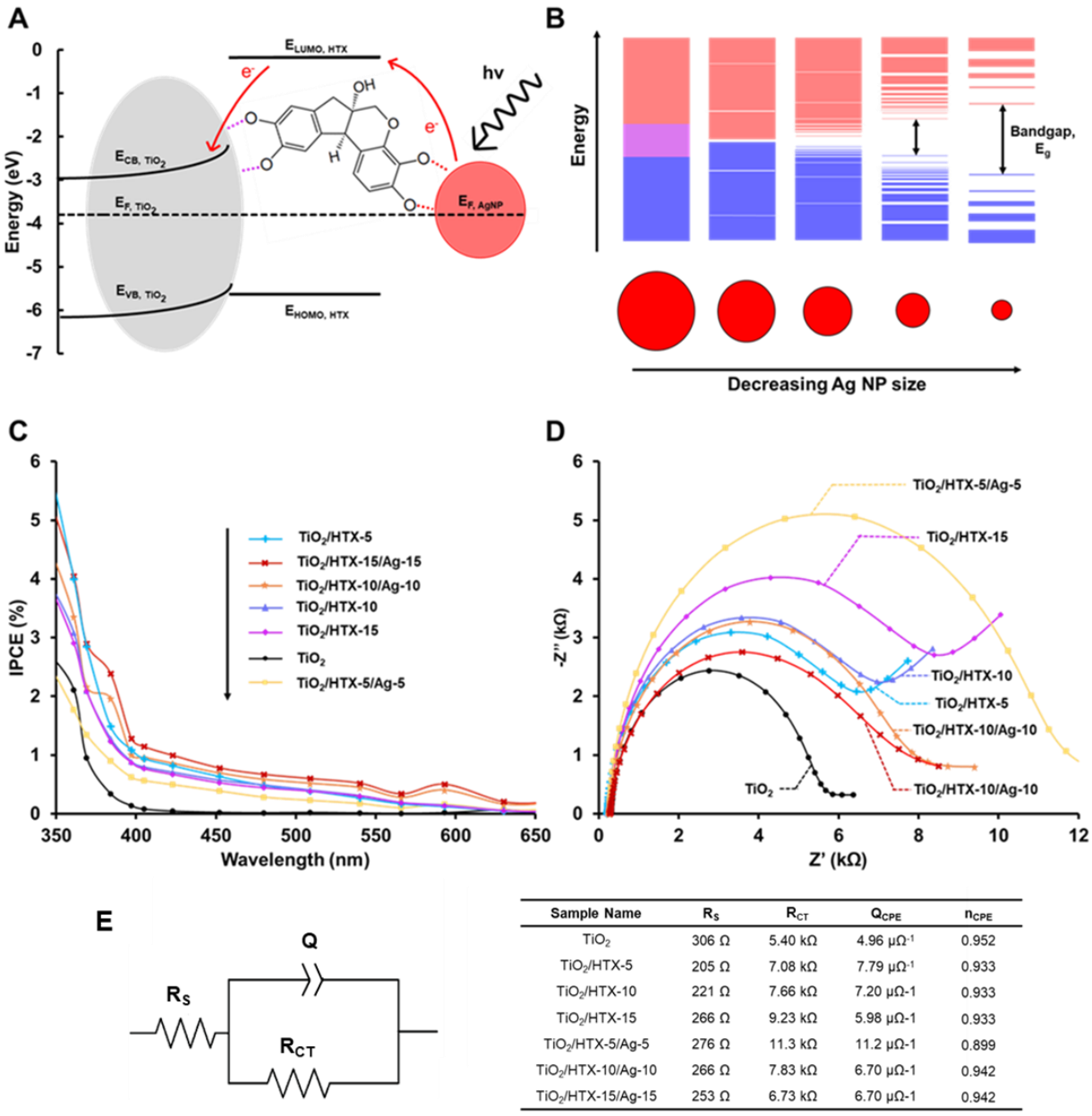

Sample Name	R_S	R_{CT}	Q_{CPE}	n_{CPE}
TiO_2	306 Ω	5.40 kΩ	4.96 μΩ^{-1}	0.952
TiO_2/HTX-5	205 Ω	7.08 kΩ	7.79 μΩ^{-1}	0.933
TiO_2/HTX-10	221 Ω	7.66 kΩ	7.20 μΩ-1	0.933
TiO_2/HTX-15	266 Ω	9.23 kΩ	5.98 μΩ-1	0.933
TiO_2/HTX-5/Ag-5	276 Ω	11.3 kΩ	11.2 μΩ-1	0.899
TiO_2/HTX-10/Ag-10	266 Ω	7.83 kΩ	6.70 μΩ-1	0.942
TiO_2/HTX-15/Ag-15	253 Ω	6.73 kΩ	6.70 μΩ-1	0.942

Figure 6-4. (A) Proposed band structure of TiO_2/HTX-10/Ag-10 NP and TiO_2/HTX-15/Ag15 NP. (B) Quantum confinement effect resulting in the formation of large bandgaps as Ag NP size decreases. (C) IPCE of photoelectrodes fabricated from various TiO_2/HTX/Ag NP suspensions. (D) EIS of photoelectrodes fabricated from various TiO_2/HTX/Ag NP suspensions during UV (405 nm) photoexcitation, and (E) Equivalent Randles cell circuit with CPE parameters fitted to the Nyquist plots from the EIS data.

The TiO_2/HTX-15/Ag-15 NPs were used as the basis for the PEC miRNA biosensor, as this material produces the highest photocurrent density and possesses Ag NPs for

biofunctionalization, making it ideal for PEC biosensing.[64,133,392] We designed a direct signal-off assay consisting of three-photoelectrodes fabricated from the TiO_2/HTX-15/Ag-15 NP (**Figure 6-5A**). To functionalize the photoelectrodes for capturing specific DNA strands, single-stranded DNA (ssDNA) capture probes were immobilized onto the photoelectrode surfaces. This biofunctionalization was achieved by thiol-metal bonds between thiol functionalized ssDNA and the decorated Ag NPs on the photoelectrode.[396,434,435] In the target capture stage, target miRNA interacts with the ssDNA capture probes through DNA hybridization and is immobilized onto the photoelectrode. The detection scheme here relies on steric hinderance, where photocurrent signal decreases as a result accumulation of ssDNA capture probe and target miRNA on the photoelectrode making charge transfer between the photoelectrode and the electrolyte less efficient.[9,64,98] In order to validate each step in the operation of the assay, the photocurrent density was measured before and after each step, in both buffer solution and in 20 % urine diluted in PBS (**Figure 6-5B and 6-5C**). On the chip, the leftmost photoelectrode (T1) is specific to target miRNA 1, the rightmost photoelectrode (T2) is specific to target miRNA 2, and the middle electrode serves as a control (CTL) that isn't specific to any target, as there is no capture probe on it. During target deposition, the solution containing targets are deposited to cover all three photoelectrodes simultaneously. The two miRNA targets used (see Table 3) were key prostate cancer biomarkers, commonly found analyzed through urine biopsies.[391,408,436] The immobilization of capture probe decreased the signal by ~40 % relative to bare photocurrent density, which indicated successful biofunctionalization of the photoelectrodes. In the target stage, four sets of target solution were deposited, which were repeated for buffer and urine media: no target miRNA, target miRNA 1 (100 nM), target miRNA 2 (100 nM), and target miRNA 1 + 100 nM target miRNA 2 (both 100 nM). In the buffer set, when no target was

deposited, the T1 and T2 signal only decreased by ~5.5 %. When the targets were deposited, the photoelectrodes corresponding to each target showed a signal decrease of ~32 %, and if the photoelectrodes did not have a corresponding target (in the case of only target miRNA 1 or only target miRNA 2), their signal decreased by only ~3.5 %. The signal for photoelectrode B only decreased by ~3.2 % after any target in buffer solution was deposited. Similar observations can be made for the targets suspended in urine, except all the photocurrent densities are slightly elevated. This is particularly noticeable with when no target in urine deposited where the control photoelectrode signal increased by 7.3 %, relative to bare photocurrent; this effect can be attributed to the reduction of various electrolytes species present in urine such as urea and citrate.[437] These results demonstrate the high specificity and multiplexing capability of this assay. The design of the three-photoelectrode chip can be easily modified to detect more than two miRNA target sequences.

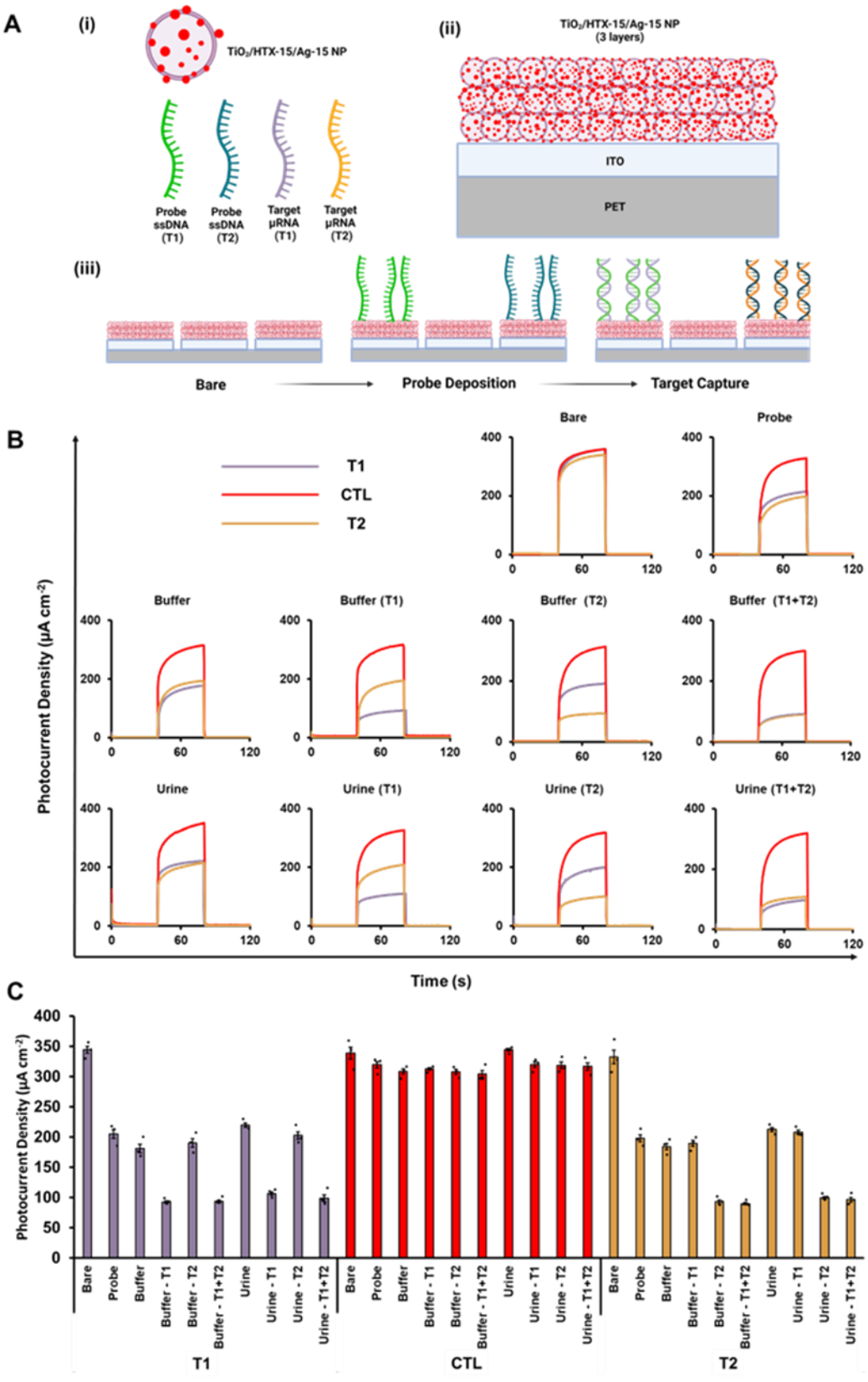
A
(i)
TiO2/HTX-15/Ag-15 NP
Probe ssDNA (T1)
Probe ssDNA (T2)
Target µRNA (T1)
Target µRNA (T2)
(ii)
TiO2/HTX-15/Ag-15 NP (3 layers)
ITO
PET
(iii)
Bare
Probe Deposition
Target Capture
B
T1
CTL
T2
Photocurrent Density (µA cm-2)
Time (s)
Bare
Probe
Buffer
Buffer (T1)
Buffer (T2)
Buffer (T1+T2)
Urine
Urine (T1)
Urine (T2)
Urine (T1+T2)
C
Photocurrent Density (µA cm-2)
Bare
Probe
Buffer
Buffer - T1
Buffer - T2
Buffer - T1+T2
Urine
Urine - T1
Urine - T2
Urine - T1+T2
T1
CTL
T2

Figure 6-5. (A) Illustration of the working principle of the PEC miRNA assay: (i) legend of photoelectrode materials, (ii) side profile of the TiO_2/HTX-15/Ag-15 photoelectrode used for the assay, and (iii) operational stages of the assay showing the signal-off detection scheme with probe deposition and target capture. (B) Chronoamperometric curves from photocurrent density measurements corresponding to the specificity/multiplexing data above. (C) Demonstration of the specificity and multiplexing of the PEC microRNA assay through photocurrent density measurements at the bare, probe deposition and target capture stages.

In order to evaluate the ability of the multiplexed PEC miRNA assay in detecting clinically relevant amounts of prostate cancer biomarkers, we exposed it to 20% urine spiked with different concentrations of miRNA 200b target sequences (miRNA Target 1) in the range of 100 fM – 100 nM (**Figure 6-6A and 6-6B**). Each target sample also contained 100 nM of miRNA 21 (miRNA Target 2) to simulate the effect of non-specific adsorption. The photocurrent change was measured as fold change (ratio of target-stage signal ($J_{T,T1}$) to probe-stage signal ($J_{P,T1}$) for photoelectrode T1) and a calibration curve was plotted to show fold change as a function of concentration. The limit-of-detection was calculated to be 172 fM within a 95 % confidence interval.[391,438,439]

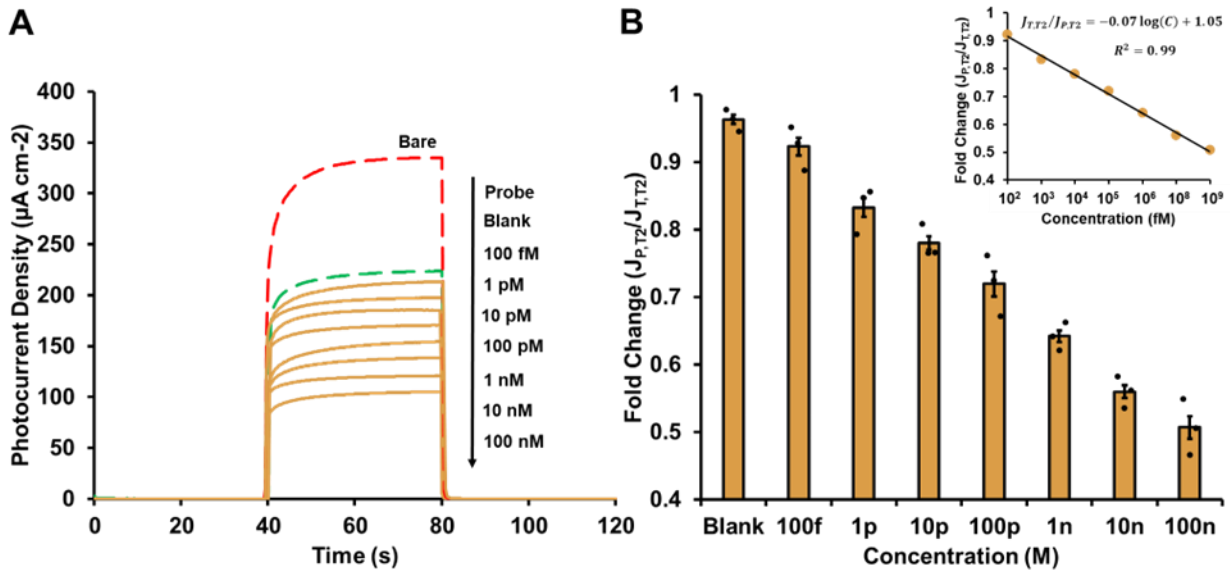

Figure 6-6. Quantifying the limit-of-detection for the PEC microRNA assay. PEC signal response curves at microRNA target concentration ranging from 100 fM – 100 nM in 20% urine: (A) chronoamperometric curves, and (B) mean fold change obtained from three measurements, where fold change is calculated as the ratio between T1 electrode probe-stage photocurrent ($J_{P,T1}$)

and T1 electrode target-stage photocurrent ($J_{T,T1}$). Inset shows the calibration curves plotted as fold change as a function of concentration in fM, which is fitted to curve, $(J_{T,T1}/J_{P,T1}) = -0.07log(C) + 1.05$; $R^2 = 0.99$.

6.4 Conclusions

In this work, we developed a material synthesis method for rapid and one-pot decoration of TiO_2 NPs with Ag NPs, using catecholate-assisted photoreduction. Our method utilized HTX, a dye from the catecholate family of ligands, to provide initial improvement in the photoactive properties of TiO_2 NPs. The photoenhanced TiO_2 NPs, with the help of surface-bound HTX molecules promoted the direct nucleation of sub-nanometer sized Ag NPs onto the TiO_2 surface. The resultant TiO_2/HTX/Ag NP material system demonstrated enhanced photocurrent generation, through the combined effect of LSPR from the Ag NPs and photoelectron injection through charge transfer complexes formed through HTX. Additionally, the presence of silver in this material allowed for easily interfacing with biomolecules needed as biorecognition agents in biosensors through the formation of thiol-metal complexes.

This material system was demonstrated for use as a PEC miRNA detection platform. This biosensor was used to specifically detect cancer related miRNA biomarkers in urine and a LOD of 172 fM and a linear dynamic range of 100 fM – 100 nM. Additionally, the biosensor demonstrated a high degree of specificity, showing a signal decrease of only 3.2 % in the presence of non-specific targets. Multiplexed biosensing was also demonstrated using this system through the development of multiple PEC sensing electrodes on a single chip. The assay presented here, requiring no target labeling and the use of a simple readout buffer containing ascorbic acid, can be integrated with recently developed handheld PEC readers for future potential applications in point-of-care sensing.[62,381]

6.5 Experimental Section

Materials:

Hematoxylin (HTX), L-ascorbic acid (AA, 99.0%), magnesium chloride ($MgCl_2$, ≥99.0%), phosphate buffered saline (PBS, 1.0 M, pH 7.4), potassium chloride (KCl, ≥99.0%), potassium ferrocyanide ($K_4Fe(CN)_6$, ≥99.5%), potassium ferricyanide ($K_3Fe(CN)_6$, ≥99.5%), silver nitrate ($AgNO_3$, ≥99.0%), sodium chloride (NaCl, ≥99.0%), tris(2-carboxyethyl)phosphine (TCEP), were purchased from Sigma-Aldrich. Titanium(IV) dioxide (TiO_2, P25 containing 80% anatase and 20% rutile) nanoparticles (NP) were obtained from Nippon Aerosil Co. Ltd. Polyethylene terephthalate (PEC) sheets of 0.8 mm thickness were sourced from Acme Plastics Inc. Adhesive vinyl films were obtained from DFC Graphic Films. All oligonucleotides were purchased from Integrated DNA Technologies. Milli-Q grade (18.2 MΩ cm) deionized (DI) water was used for all solution preparation and washing steps.

Photoreduction Synthesis of TiO_2/HTX/Ag NP Suspensions:

The synthesis of all seven material system varieties presented in this work, started with the preparation of TiO_2 NP suspensions as the base. The final concentration of TiO_2 NP in all seven of samples was 0.66 g L^{-1}. The concentrations of reagents used in the preparation of each sample can be found in Table 1. To prepare TiO_2/HTX suspensions, HTX solution was added to TiO_2 NP suspensions and mixed.

In order to decorate TiO_2/HTX NP with silver nanoparticles (Ag NP) and produce suspensions of TiO_2/HTX/Ag NP, a photoreduction synthesis technique was implemented. A 200 mL suspension of TiO_2/HTX NP was prepared in a clear glass beaker, with added prerequisite amount of $AgNO_3$ solution. The beaker was placed on a magnetic stirrer inside a photoreduction chamber (i.e. a chamber with reflective inner lining). The suspension was exposed to 100 W

white LED floodlight for 1 hour while being stirred, resulting in the formation of the TiO_2/HTX/Ag NP suspension.

Photoelectrode Fabrication:

The photoelectrodes used for the material characterization experiments and miRNA detection experiments were fabricated on PET substrates sputtered with indium-tin oxide (ITO) to make them conductive. The PET sheet substrates were cleaned with ethanol and DI water, after which an adhesive vinyl mask was applied onto them. The vinyl mask was cut into the desired electrode pattern (designed on Adobe Illustrator) using a Graphtec Robo Pro CE5000-40-CRP craft cutter. A 100 nm film of indium tin oxide (ITO) was sputtered onto the masked substrate by radio frequency sputtering using a Torr International Magnetron Sputtering System to form ITO/PET substrates. The chips used for the material characterization consisted of a single rectangular electrode measuring 80 cm X 70 mm. The chips used for the DNA detection experiments consisted of three rectangular electrodes, each measuring 80 mm X 50 mm and having a 10 mm non-conductive (i.e. no ITO layer) gap between them. The ITO/PET substrates were cleaned with air plasma for 1 minute. They were then coated with TiO_2 NP, TiO_2/HTX NP or TiO_2/HTX/Ag NP by drop depositing the respective suspension at the concentration of 0.66 g L^{-1} and a volume of 17.8 μL cm^{-2}. This process was repeated three times to deposit three layers.

Characterization:

The morphology of the synthesized nanostructures was analyzed by transmission electron microscopy (TEM) imaging using a Thermo Scientific Talos F200X STEM Microscope through both standard bright-field TEM and high-angle annular dark-field scanning transmission electron microscopy (HAADF-STEM). Ag NP size distribution analysis was carried out using the ImageJ software. Additionally, Energy-dispersive X-ray spectroscopy (EDS) and electron energy loss

spectroscopy (EELS) were also carried out using the Talos F200X STEM Microscope. Conventional sample preparation was used for imaging techniques. A Bruker SMART CCD 600 Diffractometer with a Cu source was used for obtaining X-ray diffraction (XRD) characterization of the synthesized particles in dried powder form.

Photocurrent density measurements, electrochemical impedance spectroscopy (EIS) and incident photon to current efficiency (IPCE) investigations were carried out using a Zahner CIMPS-QE/IPCE3 Photoelectrochemical Potentiostat. For all three of these tests, a standard three-electrode cell setup was used. Platinum (Pt) wire was used as the counter electrode, a silver/silver chloride (Ag/AgCl) electrode for the reference electrode and the TiO_2 NP based photoelectrodes acted as the working electrodes. The photoexcitation source for the photocurrent measurements and EIS tests was a Thorlabs M405L4 mounted LED, which has a peak wavelength of 405 nm and an irradiance of 14.53 uW mm^{-2} (Figure S5). Some supplemental experiments used Thorlabs MNWHL4 mounted LED, which has a neutral white color temperature (400−700 nm) and an irradiance of 7.7. uW mm^{-2} (Figure S5). The photocurrent density measurement was done by running the potentiostat in chronopotentiometric mode for 120 s. The electrolyte solution used for the photocurrent measurement was composed of 0.1 M phosphate buffered saline (PBS) and 0.1 M L-ascorbic acid. The potential of the PEC cell was fixed at 0 V, and the working electrode was irradiated with white light at a 40 s interval. Average photocurrent density was measured by taking the running average of the last 10 s of the irradiation period. Room temperature EIS measurements were performed at an open-circuit potential and the electrolyte used for the EIS measurements contained 2 mM potassium ferricyanide, 2mM potassium ferrocyanide, and 0.1 M KCl in 10 mM PBS. The excitation amplitude was 10 mV and the frequency range used was 100 mHz – 100 kHz. IPCE

measurements were carried out with the same electrolyte solution as the photocurrent measurement test. The built-in variable wavelength LED of the Zahner potentiostat was used as the photoexcitation source during the IPCE testing. The following formula was used to convert photocurrent values at specific measured light wavelengths into IPCE:

$$(1) \qquad IPCE(\%) = \frac{1240 \times J_{photo}(mA\ cm^{-2})}{\lambda(nm) \times I_{inc}(mW\ cm^{-2})}$$

Detection of MicroRNA (miRNA):

Three-electrode chips fabricated from TiO_2/HTX-15/Ag-15 NP suspensions were used for all miRNA detection experiments. The full sequences of all the oligonucleotides used can be found in **Table 6-2**. After fabricating the three-electrode chip, the photocurrents for all three electrodes were measured to get their bare-stage signal. In the probe immobilization step, 10 μL solution of 1 μM capture probe and 10 μM TCEP was deposited onto the electrodes. The capture probes are thiolated, and TCEP acts as reducing agent to facilitate bonding between silver and thiol groups. Capture probe 1 (CP1) and capture probe 2 (CP2) were deposited onto electrode T1 (leftmost electrode) and electrode T2 (rightmost electrode), while nothing was deposited onto electrode B (middle electrode). The chip was incubated overnight at 4 ºC temperature, and then washed with 25:25 buffer (25 mM PBS and 25 mM NaCl). Afterwards, the photocurrent measurements of all three electrodes were taken to get the probe-stage currents. In the last target capture stage, a solution containing various concentrations of two different target miRNA (TM1 and TM2) dissolved in either 25:25 buffer or 5x diluted urine (healthy no-growth samples, pH 6.4) was deposited onto the three-electrode chip. The target solution was deposited in way to cover all three electrodes simultaneously. The chips are once again incubated for 1 hour at room

temperature and washed with 25:25 buffer. Photocurrent measurements were performed again to get the target-stage currents for three electrodes.

Table 6-2. Full sequences of all the oligonucleotides used in the miRNA sensor.

Name	Sequence (5'-3')	Note
CP1	SH/ TCA TCA TTA CCA GGC AGT ATT A/	Capture probe 1
CP2	SH/ TCA ACA TCA GTC TGA TAA GCT A/	Capture probe 2
TM1	/rUAA rUAC rUGC CrUG GrUA ArUG ArUG A/	Target 1; miRNA 200b
TM2	/rUAG CrUrU ArUC AGA CrUG ArUG rUrUG A/	Target 2; miRNA 21

SH – Thiolation, rU – deoxyUridine base

Limit-of-detection (LOD) Calculation:

Calibration curves were plotted as a function of the fold change [target-stage signal ($J_{P,T2}$) / probe-stage signal ($J_{T,T2)}$] and the concentration of target sequence TM2 spiked in 5x diluted urine. To simulate the effect of non-specific target absorption, the target solutions were spiked with an additional 100 nM of target sequence TM1. The regression line fitted to the fold change data took the form of a linear-log function. The blank signal was derived from a target sample with 100 nM of TM1 and no TM2. Limit of blank (LOB) is calculated using the equation:

$$(2) \quad LOB = \left(\frac{J_{T,T2}}{J_{P,T2}}\right) + 3\sigma_{blank}$$

Where, σ_{blank} is the standard deviation of the blank signal and the LOD was calculated within a 95% confidence interval. The limit-of-detection was then calculated from the regression line by substituting the signal (y-value) with the LOD.[440]

6.6 Acknowledgements

This research was funded by the National Sciences and Engineering Research Council of Canada. I.Z. is the Canada Research Chair in Micro-nano Technologies. L.S. is the Canada Research Chair in Miniaturized Biomedical Devices. Transmission Electron Microscopy was performed at the Canadian Centre for Electron Microscopy.

6.7 Supporting Information

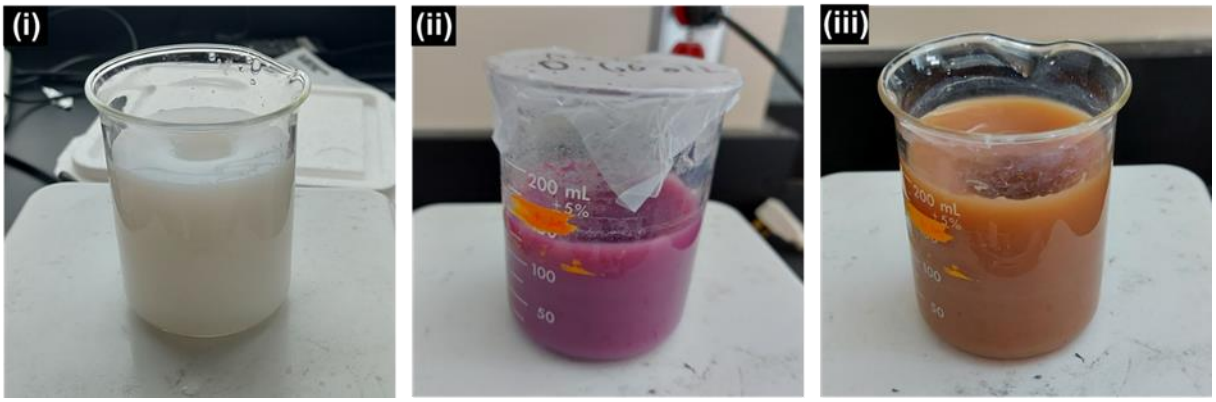

Figure 6-S1. Pictures of TiO_2 nanoparticle suspensions: (i) unmodified TiO_2 NP, (ii) TiO_2/HTX NP, and (iii) TiO_2/HTX/Ag NP.

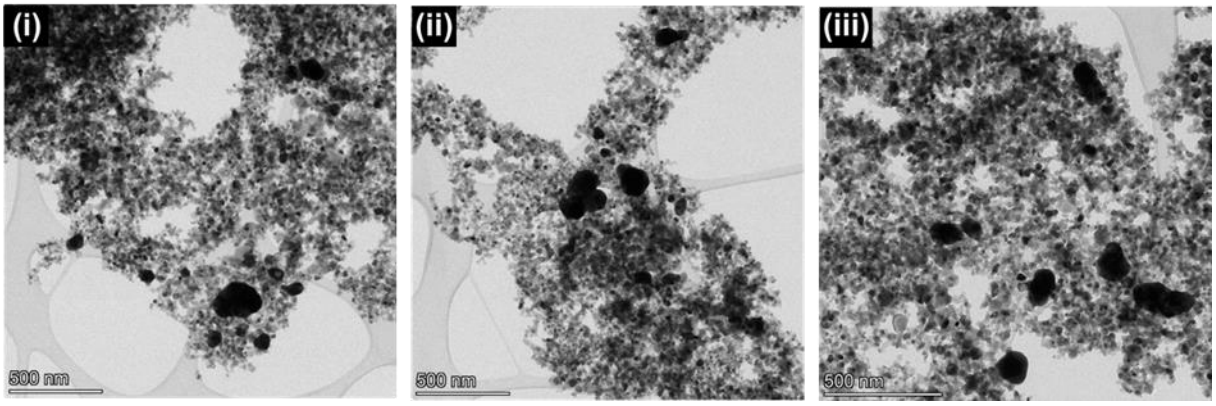

Figure 6-S2. Low magnification bright-field TEM micrographs TiO_2/HTX/Ag NP samples: (i) TiO_2/HTX-5/Ag-5, (ii) TiO_2/HTX-10/Ag-10 and (iii) TiO_2/HTX-15/Ag-15.

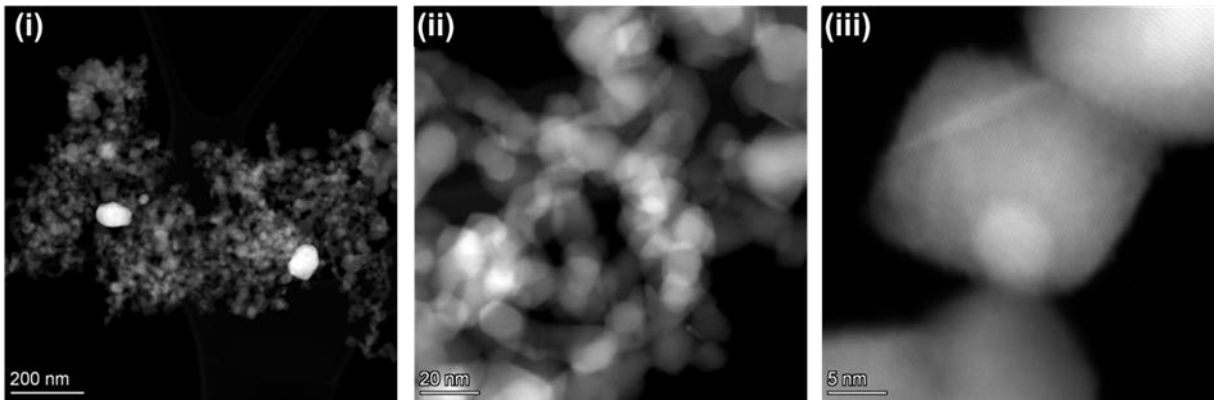

Figure 6-S3. HAADF STEM micrographs TiO_2/Ag NP samples which were synthesized through the photoreduction process without the surface modification of TiO_2 NPs with HTX.

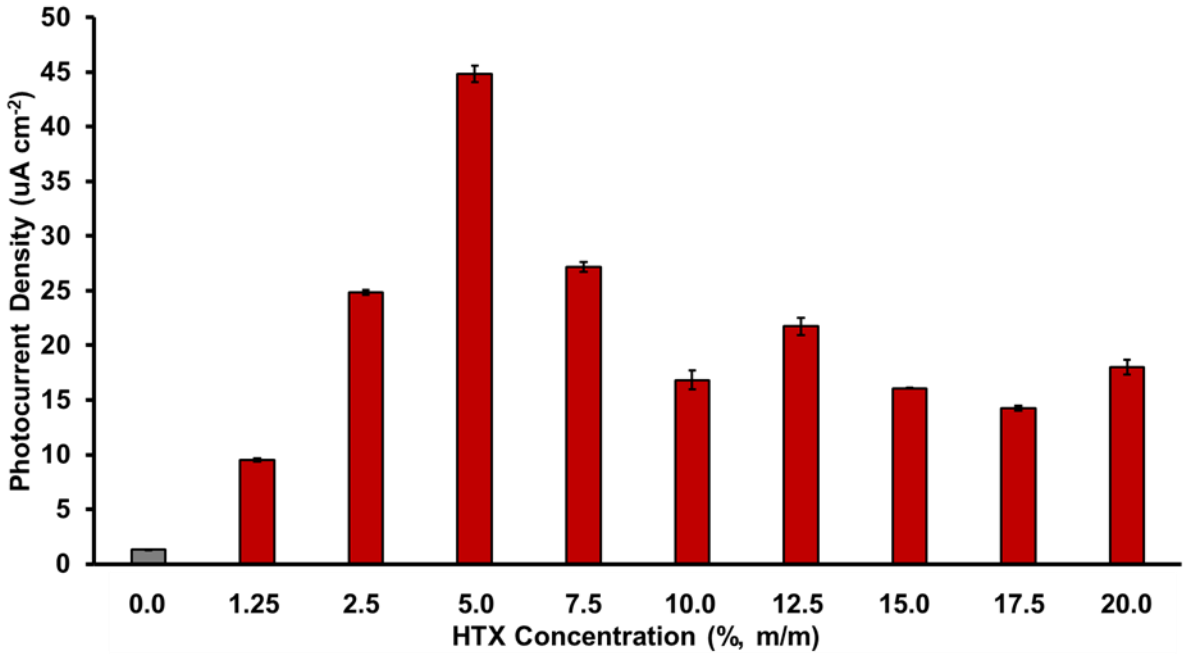

Figure 6-S4. Optimization of the photocurrent density of the TiO_2/HTX NP material system through varying the amount of HTX. The concentration of HTX is represented as the percentage mass ratio between HTX and TiO_2 NP, where the concentration of TiO_2 NP is all suspensions is 0.66 g L^{-1}.

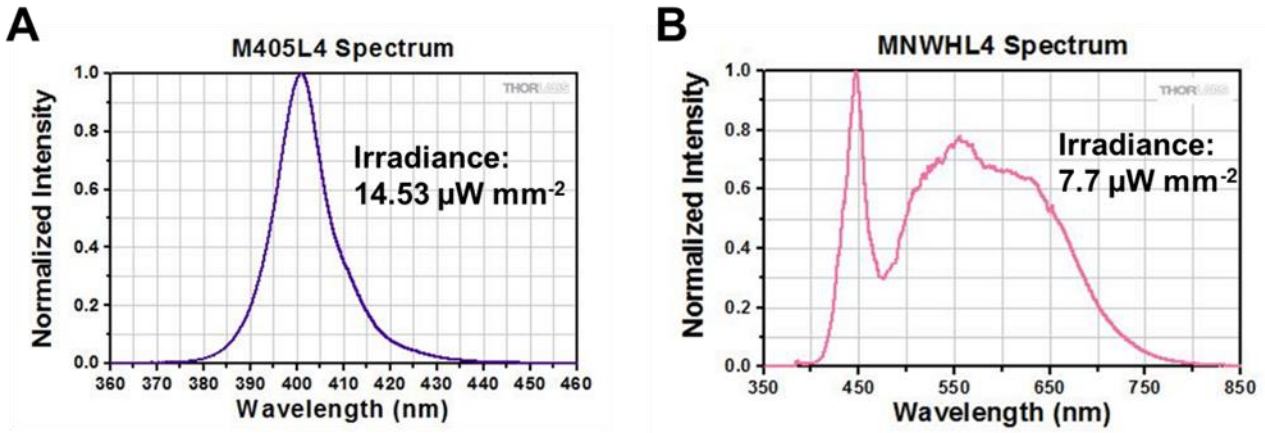

Figure 6-S5. (A) Spectrum of the UV LED photoexcitation source and (B) Spectrum of the white LED photoexcitation source.

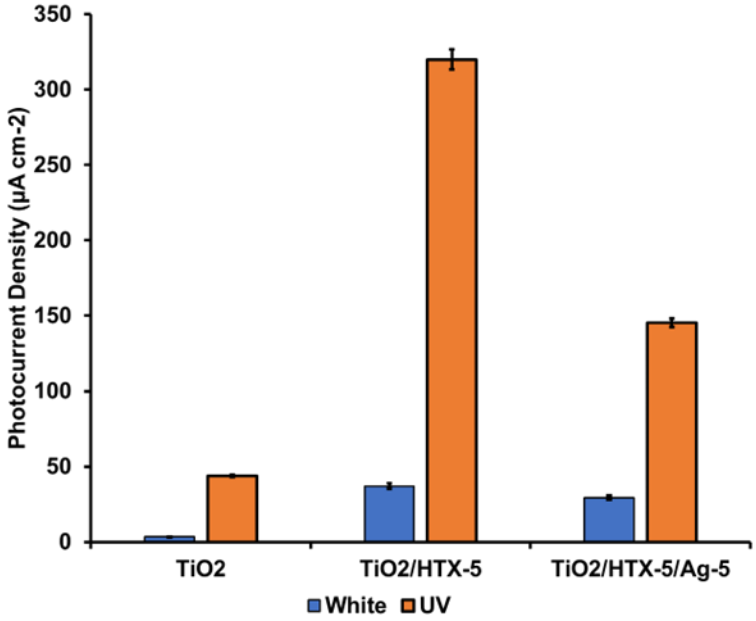

Figure 6-S6. Photocurrent density measurements of photoelectrodes fabricated from TiO_2/HTX/Ag NP suspensions in UV (405 nm) and white light.

Chapter 7

A Portable and Smartphone-operated Photoelectrochemical Reader for Point-of-care Biosensing

Preface:

Chapter 7 mainly focuses on research objective III, in making PEC biosensors point-of-care (PoC) capable. Driven by recent advancements in the field of biosensing, there has been growing interest in the development of PoC readout instruments. The practice of PoC testing involves performing diagnostic or prognostic tests near a patient with the promise of rapid results. PoC-capable devices aim to provide rapid diagnostic information outside of a typical laboratory setting[44,57] and prove to be substantially more affordable and faster than gold standard techniques.[39,44] Amongst the various signal transduction strategies employed in the design of biosensors, PEC biosensors are particularly known for producing low limit of detection, high sensitivity and broad dynamic ranges.[94,96,97,100] In PEC signal transduction, the mode of signal excitation (optical) and signal readout (electrical) are decoupled, allowing for high performance to co-exist with simple, more reliable bioassays.[94] Despite this, PEC biosensors have seen limited commercial success, and this can be attributed to the lack of low-cost, portable, and user-friendly PEC readout devices.[64,94,441] In this work, we focused on designing a portable handheld potentiostat for PEC applications with the following requirements:

1. Capable of supporting a broad range of PEC-based bioassays. In particular, the reader should be able to apply adjustable bias voltages, measure both anodic & cathodic photocurrent, and should have minimal input-referred noise

2. Interface with illumination sources suitable for PEC applications and support variable illumination periods.

3. Feature an approachable user-interface to streamline much of the experimental process.

Our PEC readout system, referred to as PECsense, can be controlled remotely via an accompanying smartphone application through the Bluetooth Low Energy communication protocol. PECsense interfaces with a custom LED matrix circuit which can be used as an optical excitation source to facilitate PEC biosensing. The smartphone-based app interfaces with the PECsense via the Bluetooth Low Energy communication protocol. The app enables enables the user to adjust the experimental parameters (including the applied bias, scan duration, illumination period, among others), provides instructions to the user, and features in-app data processing. This eliminates the need for bulky external hardware and ensures that PECsense is PoC ready. The performance of the PECsense was validated by running the signal-off PEC DNA hybridization detection assay from chapter 3, as well as using it in experiments that demonstrate its variable illumination periods, anodic/cathodic biasing capabilities, and low signal-to-noise ratio. We found that the PECsense was able to match the performance of conventional benchtop potentiostats, while offering PoC capabilities.

Authors: Alexander Scott, Sadman Sakib, Sudip Saha, Igor Zhitomirsky and Leyla Soleymani (Equal contribution with Alexander Scott)

Publication: Published in Electrochimica Acta in July 2022

7.1 Abstract

In recent years, a number of lab-made potentiostats have been developed as alternatives to the expensive commercial options to facilitate point-of-care (PoC) electrochemical biosensing. However, these devices have no means of interfacing with and controlling optical excitations sources, an essential component in photoelectrochemical (PEC) biosensing. Accordingly, this sensing modality has been relegated to laboratory applications only and can only be conducted using expensive photoelectrochemical workstations. To address this limitation, we have designed and validated a portable reader for PoC PEC biosensing (PECsense). The device can perform chronoamperometry while synchronously controlling an optical excitation source. PECsense is remotely controlled by a smartphone via the Bluetooth Low Energy communication protocol. This photoelectrochemical reader can be used in several different PEC sensing applications, including experiments with variable illumination periods, those that yield cathodic or anodic photocurrents, and those that require applied biases.

7.2 Introduction

Biosensors are devices that bring together biorecognition and signal transduction elements for analyzing biologically-relevant analytes.[42,64,104,442] These devices are ideally suited for use in point-of-care (PoC) diagnostics and health monitoring systems and are being extensively researched for diagnosing infectious diseases,[443,444] cancers,[445–449] cardiovascular diseases,[448,450] and neurological diseases,[447,451] to name a few. The rapid sample-to-result time of these devices at the point-of-need enables effective intervention by clinicians, which is expected to increase patient survivability and minimize the rates of disease transmission.[452,453]

Multiple signal transduction strategies – electrochemical,[444,454] photoelectrochemical,[455–458] electronic,[459,460] optical,[461,462] and mechanical[460,463] – have been widely used in biosensing.[464]

Among these, photoelectrochemical (PEC) signal transduction, combining optical excitation with electrochemical readout, has generated tremendous interest in recent years due to its low limit-of-detection (LOD),[302] high sensitivity,[465] and broad linear dynamic range.[466] The decoupling of the mode of signal excitation from the signal readout reduces the background signals that are generated at high voltage biases, enhancing the signal-to-background ratio and limit-of-detection of PEC biosensors.[457,465,467–469]

Despite increasing number of PEC biosensors reported in the literature (from 35 search results up to 2011 on Pubmed to an additional 764 results up to 2021), these devices are far from being utilized in real-world applications and are unavailable in commercial markets. In many cases, this can be attributed to the limited number of suitable photoactive materials that meet the stringent chemical stability requirements of biosensors and the challenges resulting from the poor photostability of common reagents and analytes (e.g. DNA probes, antibodies, antigens) under high energy optical excitation.[457,468,470] Such issues are being addressed by researchers through the development of new chemically-stable photoactive materials such as semiconductor metal oxides,[314,458,468,471] quantum dots[472–475] and carbon-based nanomaterials[108,476,477] and the use of photocurrent enhancing strategies such as creating hybrid plasmonic nanoparticle-metal oxide heterostructures,[80,455,478–481] using carbon nanomaterials as highly conductive scaffolds,[256,482] using organic ligands/dyes to improve optical absorption[122,175,483] and dual sensitization via the coupling of large and small bandgap semiconductors heterostructures[125,303,484] for exciting these materials at lower energies (i.e. visible wavelengths). The limited commercial success of PEC biosensors is further compounded by the challenges associated with employing existing PEC readout devices for PoC use. While PEC workstations are commercially available, they are both prohibitively expensive and are not portable. These devices are also feature-rich, consisting of

frequency analyzers, potentiostats, photodiode sensors, and tunable light sources. While many of these features are needed in research settings, they are of no use in a PoC capacity. Conversely, none of the commercially available portable potentiostats[485,486] support PEC biosensing, and their functionality cannot be expanded given their black-box nature.[487] Excluding a recent PEC measurement system with surface-mounted light-emitting diodes (LEDs) controlled by a smartphone for optical excitation,[488] none of the lab-made potentiostats reported in the literature[142,487,489–492] can interface *directly* with optical-excitation sources to support PEC biosensing.

We sought to develop a portable and low-cost smartphone-operated PEC readout system to help expedite the translation of PEC biosensors from the laboratory to the real world. In particular, this device, referred to hereon as PECsense, can perform chronoamperometric measurements while synchronously controlling an optical-excitation source. This solution is made possible due to the increased processing power and decreasing cost of both smartphones and microcontrollers alongside both the widespread global adoption of smartphones in recent years and the development of low-energy consumption communication protocols like Bluetooth Low Energy (BLE). Cathodic/anodic currents were measured in response to different biases, and both rapid PEC cycling tests and long-term optical exposure tests were conducted in order to demonstrate the versatility and robustness of PECsense. The performance of PECsense was further compared to a commercial PEC workstation. Finally, to demonstrate the applicability of this newly-developed PEC reader, we used it for PEC DNA biosensing with surface-modified TiO_2 photoelectrodes. In order to distinguish between matched and mismatched DNA, we used PECsense to measure the change in photocurrent before and after DNA capture, creating a handheld PEC DNA biosensor.

7.3 Experimental

Materials:

Caffeic acid (CA), phosphate buffered saline (PBS), L-ascorbic acid (AA), sodium hydroxide (NaOH), 1-ethyl-3-(3-dimethylaminopropyl)carbodiimide hydrochloride (EDC), N-hydroxysulfosuccinimide (NHS), 2-(N-morpholino)ethanesulfonic acid (MES), and 100 nm indium tin oxide coated poly(ethylene terephthalate) (ITO/PET) were purchased from Sigma-Aldrich. TiO_2 nanoparticles (P25, containing 80% anatase and 20% rutile) were obtained from Nippon Aerosil Co. Ltd. Anhydrous ethanol was purchased from Greenfield Global. Synthetic DNA sequences used capture probe and target were obtained from Integrated DNA Technologies.

Photoelectrode fabrication:

An aqueous suspension of 0.66 g L^{-1} TiO_2 nanoparticles was prepared, to which a solution of CA dissolved in 5% ethanol in DI water solution was added to produce CA-surface-modified TiO_2 nanoparticles (CA-TiO_2). The mass ratio of TiO_2 to CA in the CA-TiO_2 suspension was 10:1. ITO/PET substrates with dimensions of 1.2 cm × 0.7 cm were masked with vinyl to preserve the electrical contact area. Substrates were subjected to (oxygen) plasma treatment for 1 min. The substrates were then coated with CA-TiO_2 by depositing 10 μL of the suspension on the substrate surface and incubating in the oven at 85°C for 6 min. This process was repeated three times to deposit three layers.

Device Engineering:

For PEC biosensing, PECsense performs voltammetric techniques while synchronously controlling an LED matrix circuit which is used as an optical excitation source. This LED matrix circuit consists of four QT-Brightek PLCC6 white LEDs that have a neutral white color

temperature (typically 4240K) and a typical intensity of 6000mcd. Detailed specifications of the QT-Brightek PLCC6 white LED as retrieved from the manufacturer's datasheet, namely the LED spectrum and luminous intensity with respect to ambient temperature, can be found in **Figure 7-S1 and 7-S2** respectively. These LEDs have a maximum optical power of 324 mW and are driven by the 3.3V supply of the Arduino Nano 33 BLE. The overall luminous intensity of the LED matrix circuit is controlled directly via pulse width modulation (PWM) pins on the Arduino Nano 33 BLE development board. Printed circuit boards (PCB) for PECsense and the LED matrix circuit were designed using Eagle Autodesk and manufactured by JLCPCB based out of Shenzhen, Guangdong, China. The electronic components were then hand-soldered onto the PCBs. While many commercial potentiostats make use of multiple feedback resistors to adjust the current measurement range and sensitivity, to reduce device complexity, we chose to use a single resistor. This yields a current measurement range of -10 µA to 10 µA and it was specifically in accordance with the photocurrent levels previously reported using the CA surface modified TiO_2 biosensor.[458] The firmware was created using the Arduino integrated development environment. To facilitate debugging and access the serial monitor, PECsense was connected to a laptop running the Arduino IDE. The accompanying Android application was written in Java using the Android Studio integrated development environment.

Device characterization:

A standard three-electrode cell setup was used with the custom-made LED matrix circuit consisting of white light as a photoexcitation source. A platinum (Pt) wire was used as the counter electrode, a silver/silver chloride (Ag/AgCl) electrode for the reference electrode and the CA-TiO_2 photoelectrodes served as the working electrodes. The custom-made LED matrix circuit was used as an optical excitation source, with a PWM duty cycle of 100%. The LED

matrix circuit was placed 50 mm from the working electrodes. The electrolyte solution used for the biasing experiment was composed of 0.5 M NaOH solution, whereas the electrolyte solution used for both the rapid PEC cycling and long-term exposure experiments was composed of 0.1 M PBS and 0.1 M AA. The photocurrent measurement was done by running PECsense in chronoamperometric mode. The potential of the PEC cell (DAC output) was fixed at a 0 V bias relative to an Ag/AgCl reference electrode, except for in the biasing experiment where the potential was varied. The performance of PECsense was compared to the Zahner CIMPS-QE/IPCE PEC workstation. All measurements recorded using PECsense were conducted in ambient conditions (22 °C with minimal effort to reduce background illumination) without the use of a Faraday cage to better reflect PoC environments. Conversely, measurements conducted with the Zahner CIMPS-QE/IPCE PEC workstation made use of the manufacturer's Faraday cage. An experiment was conducted to quantify the amount of background signal suppression offered by a Faraday cage while performing photocurrent measurements with PECsense (**Figure 7-S3**). Finally, the LED matrix circuit luminous intensity was modulated by applying different PWM duty cycles and the resulting photocurrent was measured using PECsense (**Figure 7-S4**).

DNA hybridization and detection experiment:

A solution of 20 mM EDC, 10 mM NHS, and 10 mM MES was deposited onto the photoelectrodes and incubated for 1 hour. This was done in order to facilitate carboxamide linking between CA and amine-terminated probe single-stranded DNA (ssDNA). Subsequently, 1 μM amine-terminated probe DNA was deposited on the photoelectrode surface and incubated for 2.5 hours. The photocurrent was measured at this point to get the after-probe photocurrent. For detecting DNA hybridization, the PEC signal was read out before and after incubation of the functionalized electrodes with a 100 nM target ssDNA solution for 1 hour. DNA hybridization

detection was conducted using ssDNA-functionalized CA-TiO_2 photoelectrodes prepared using protocols described previously.[458] Signal readout was performed using a PBS/AA electrolyte solution, and the LED matrix circuit as a photoexcitation source, with a PWM duty cycle of 100%. The LED matrix circuit was placed 50mm from the working electrodes. When measuring the photocurrent of the PEC cell, the potential was kept constant at 0 V bias relative to an Ag/AgCl reference electrode, and the working electrode was irradiated for 40 s in the middle of a 120 s runtime. To test non-specific adsorption, some samples were spiked with 100 nM non-complementary ssDNA and/or 10% human blood plasma. The photoelectrodes were washed between each deposition step with deionized water. All the photocurrents were normalized by performing baseline subtraction of the dark current. Finally, PECsense was directly compared to the Zahner CIMPS-QE/IPCE PEC workstation by recording the post-target peak photocurrent densities for three different target ssDNA concentrations (1 pM, 100 pM, and 10 nM) as shown in **Figure 7-S5**.

7.4 Results and Discussion

7.4.1 Device Design

We have developed a portable (75 mm by 40 mm, <100g including a 3D printed case) and inexpensive (~100 CAD) PEC reader, referred to as PECsense, which is wirelessly controlled by an Android application through the Bluetooth Low Energy (BLE) communication protocol to facilitate away-from-lab PEC experiments. In this design, we capitalize on the widespread global adoption of BLE-supported smartphones, rendering our system both smaller and less expensive than a standalone device. The specifications of PECsense are summarized in **Table 7-1**.

Table 7-1. PECsense specifications.

Current range	-10 µA to 10 µA (-20 µA to 20 µA for differential measurements)
Supply voltage	4.5-21V
Signal generation resolution	16-bit (46 µV quantization error)
ADC resolution	24-bit
Experimental current sensing resolution	36 pA
Sampling rate	Programmable from 20 Hz – 1000 Hz (20 Hz used in this work)
Typical LED matrix color temperature	4240 ºK
Typical LED matrix intensity	6000 mcd

Alongside standard components that commonly make up a potentiostat (**Figure 7-1A**) – a core processing unit (Arduino Nano 33 BLE development board), a digital-to-analog converter (DAC), a reconstruction filter, potentiostat circuitry consisting of a voltage follower (VF), control amplifier (Camp), and transimpedance amplifier (TIA), and an analog-to-digital converter (ADC) – our device also interfaces with a peripheral LED matrix circuit (**Figure 7-1B**) for PEC signal readout. The independence of the LED matrix circuit from the core device allows it to be modified (in terms of wavelength and intensity) to meet the optical requirements of different PEC assays.

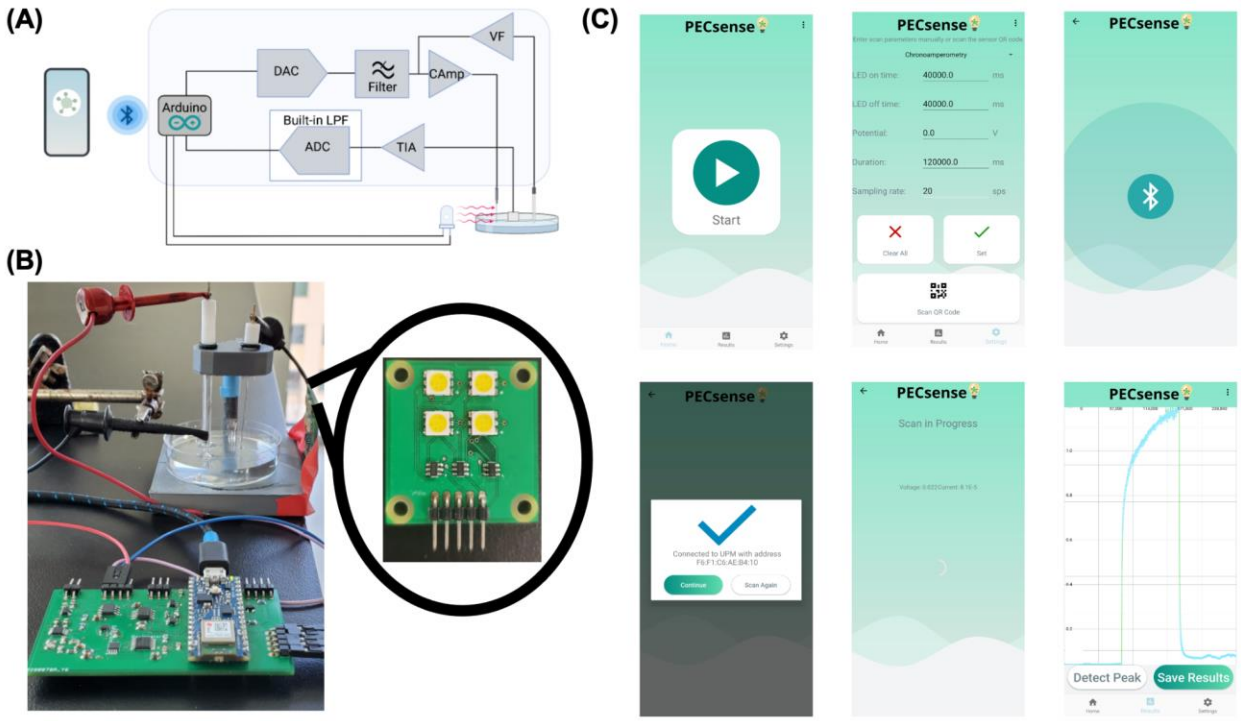

Figure 7-1. Overview of PECsense. (A) A block diagram representation of PECsense consisting of the Arduino Nano 33 BLE development board, digital-to-analog converter (DAC), reconstruction filter, core-potentiostat circuit composed of a voltage follower (VF), control amplifier (CAmp), and transimpedance amplifier (TIA), and analog-to-digital converter (ADC) with a built-in low-pass filter (LPF). (B) Experimental setup including a photograph of the LED matrix circuit. (C) The smartphone application process flow.

We developed a firmware function to perform chronoamperometric scans while synchronously controlling the LED matrix circuit. This function makes use of timer interrupts to toggle the LED matrix circuit ON and OFF. Scan parameters for performing photoelectrochemical readout including the LED on and off time, the total duration of the scan, the voltage bias, pulse amplitude, pulse duration, and the sampling rate are all adjusted using the accompanying smartphone application. We undertook significant effort when designing the smartphone application to ensure it could easily be controlled by inexperienced users. By providing graphical animations, the Android application guides the user through the different stages of a typical PEC experiment (**Figure 7-1C**). The collected scan measurements are then transmitted from

PECsense to the smartphone via BLE for signal processing and to compile the results in a graphical format. In particular, we have developed a function to perform in-app data smoothening using a Savitzky-Golay filter, an algorithm known for smoothening while preserving the shape and key features of the original signal.[493–495]

7.4.2 Device Characterization

Experiments were conducted to demonstrate the versatility of PECsense and highlight its applicability for a wide array of PEC experiments. In order to demonstrate the ability of PECsense in measuring anodic and cathodic photocurrents, we applied different bias voltages (-1.0V, -0.75V, 0.75V, and 1.0V relative to an Ag/AgCl reference electrode) in an NaOH electrolyte solution and measured the resulting photocurrent. It was expected that the positive biases would yield anodic currents, and the negative biases would generate cathodic currents due to the oxidation of water and reduction of oxygen species, respectively.[496] The working photoelectrodes, constructed via the drop deposition of TiO_2 nanoparticle suspensions onto a conductive polymer substrate, were irradiated with white light using the LED matrix circuit at 30 s intervals for 150 s, in order to generate the chronoamperometric curves (**Figure 7-2**). As expected, the results demonstrated that PECsense could measure cathodic and anodic currents when positive and negative biases were applied. However, in the case of both the -0.75V and 0.75V biases (relative to an Ag/AgCl reference electrode), the signals were obfuscated by noise given their low amplitude. The noise can partly be attributed to the lack of shielding from background illumination and electrical interference. It is well known that the cathodic photocurrent generation of TiO_2 in alkaline solutions saturates in the region of -0.9 V to -1.0 V.[496] This saturation is attributed to the diffusion limitation of oxygen species, thus limiting the reduction reaction.[496] This explains the large

increase in cathodic photocurrent from -0.75 V bias to -1.0 V bias (relative to an Ag/AgCl reference electrode), as the system has not yet reached saturation.

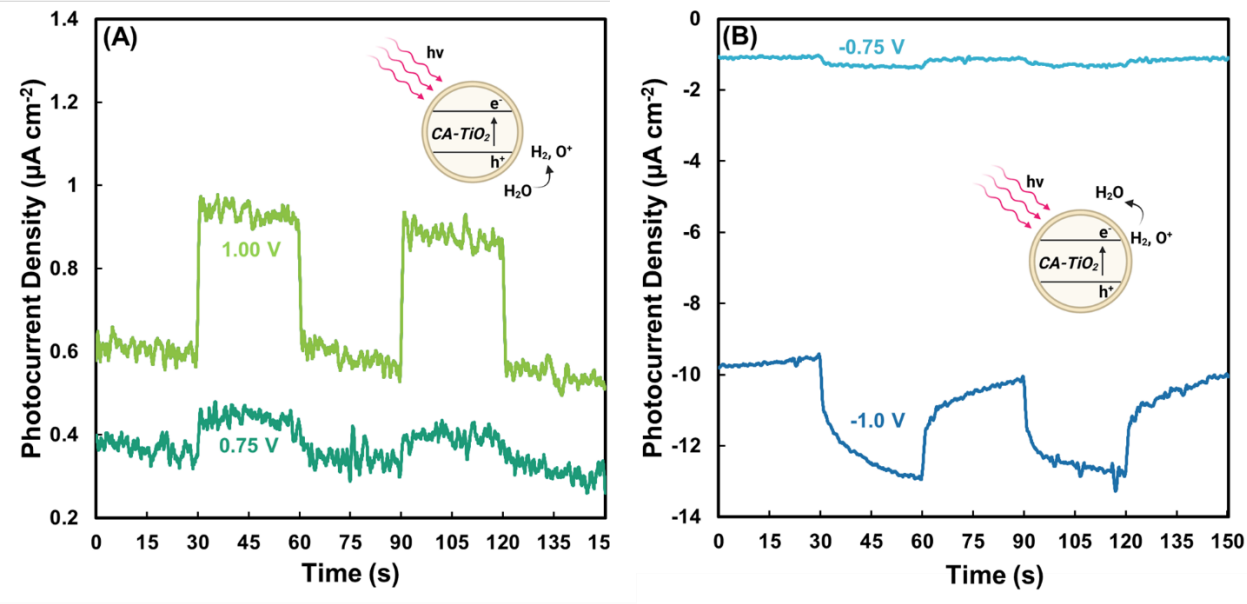

Figure 7-2. Illuminated chronoamperometry experiments using PECsense. (A) Anodic photocurrent generated by CA-TiO_2 photoelectrodes when bias voltages of 0.75 V and 1.0 V were applied relative to an Ag/AgCl reference electrode. The inset illustrates photocurrent generation via oxidation of water. (B) Cathodic photocurrent generated by CA-TiO_2 photoelectrodes at bias voltages of -0.75 V and -1.0 V relative to an Ag/AgCl reference electrode. The inset illustrates photocurrent generation via reduction of oxygen species.

To further demonstrate the robustness of PECsense and showcase its applicability for PEC measurements with variable illumination periods, we conducted a PEC cycling test. The potential of the photoelectrode was held constant at 0 V bias relative to an Ag/AgCl reference electrode and concurrently irradiated with white light using the LED matrix circuit at 20-s intervals for 20 minutes (**Figure 7-3A**). This experiment was performed using the same LED matrix circuit and the Zahner CIMPS-QE/IPCE PEC workstation, a benchtop measurement system used as a control (**Figure 7-3B**). The two systems resulted in similar PEC currents that followed the illumination pattern, with gradual ramping of the photocurrents observed during the first 15 cycles. This behavior is owed to charge carriers getting trapped at the surface of the TiO_2

photoelectrode, producing a transient charging response.[497,498] The short light-ON periods are not enough to reach the steady-state of the trap state induced transient response, and some discharge occurs at a slower rate during the light-OFF periods, resulting in the sawtooth photocurrent waveforms. The small decreases in photocurrent observed near the latter half of the experiment can be attributed to mechanical degradation of the photoelectrodes due to rapid cycling. The differences in the results obtained from PECsense and Zahner CIMPS-QE/IPCE PEC workstation, namely the larger photocurrent density recorded using PECsense during the LED OFF periods, can largely be attributed to the fact that the Zahner CIMPS-QE/IPCE PEC workstation was better shielded from background illumination and interference through the use of a faraday cage. This faraday cage was not used in conjunction with PECsense in order to better replicate the typical conditions associated with PoC measurements.

To investigate the electrical performance of PECsense, the input-referred noise was characterized. This parameter is a measure of the electrical noise induced exclusively by the circuitry and does not include any interference induced by the PEC cell. The working electrode connector was left open and readings were taken for 7 minutes. The ADC sampling rate was set to 20 sample-per-second, thereby enabling the built-in 50/60 Hz low-pass filter. This sampling rate is in line with all other measurements conducted in this work. The standard deviation of the open-circuit noise measurement was found to be 36 pA.

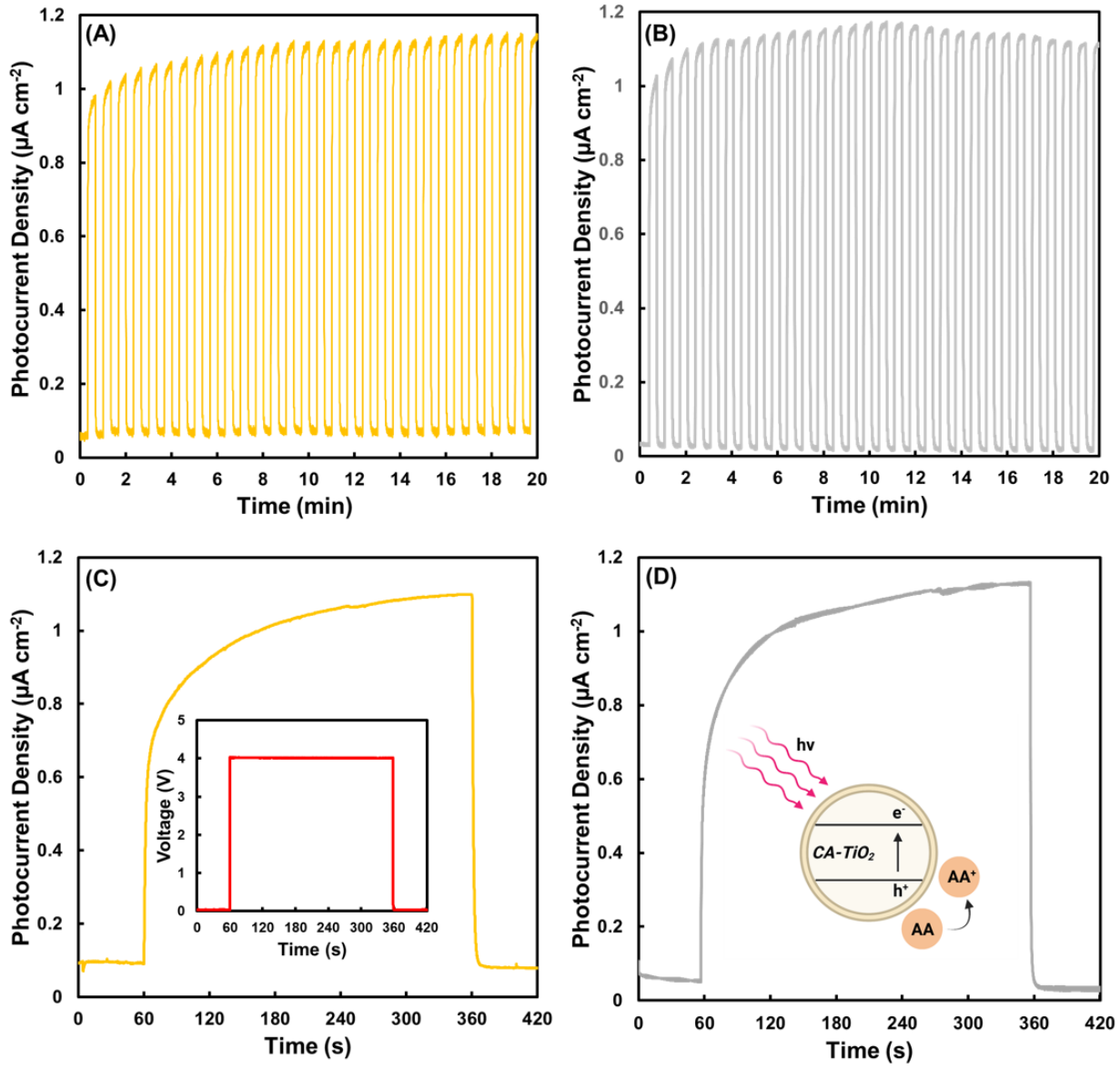

Figure 7-3. Variable illumination experiments conducted using PECsense and a commercial PEC workstation with an applied bias of 0V relative to an Ag/AgCl reference electrode. (A) PEC cycling test conducted using PECsense. (B) PEC cycling test conducted using the Zahner CIMPS-QE/IPCE PEC workstation. (C) Long term exposure test conducted using PECsense. Inset shows the LED matrix circuit intensity measurement by recording the voltage drop across a photocell. (D) Long term exposure test using the Zahner CIMPS-QE/IPCE PEC workstation. Inset illustrates photocurrent generation via the oxidation of ascorbic acid following TiO_2 photoexcitation.

Next, we performed a long-term light exposure test in order to demonstrate that the LED matrix circuit could be used as a stable optical excitation source without significant fluctuations.

Photocurrent measurements were conducted using a PBS/AA electrolyte solution. The AA electrolyte is a hole scavenger and its oxidation at the photoelectrode results in the generation of anodic photocurrent (**Figure 7-3D inset**). The potential of the PEC cell was held constant at a 0 V bias relative to an Ag/AgCl reference electrode, and the working photoelectrode was irradiated with white light using the LED matrix circuit for 5 minutes, in order to generate the chronoamperometric curve (**Figure 7-3C**). The performance was compared to the Zahner CIMPS-QE/IPCE PEC workstation (**Figure 7-3D**). The expected anodic current was generated due to the oxidation of AA at the working electrode when under illumination (**Figure 7-3D inset**). Additionally, the PEC curves measured using PECsense are nearly indistinguishable from those recorded by the Zahner CIMPS-QE/IPCE PEC workstation, featuring similar shapes and peak photocurrents. Using a photocell, we measured the luminosity of the LED matrix circuit over a 5-minute period (**Figure 7-3C inset**) to verify consistent performance of the LED matrix circuit. Throughout this 5-minute period, the resistance of the photocell remained constant, indicating that the luminosity of the LED matrix circuit was stable. The photo-charging effect observed for the PEC cycling test is also present in the long-term exposure test. However, without the intermittent discharging, the photocurrent was able to come close to achieving steady-state within the 5-minute LED matrix circuit ON period.

7.4.3 DNA Hybridization and Detection Experiment

In order to demonstrate the applicability of our newly developed handheld platform for PEC biosensing, we used it to detect signal changes in a DNA hybridization detection assay.[9] To this end, we fabricated photoelectrodes through drop deposition of TiO_2 nanoparticle suspensions onto a conductive polymer substrate. The unmodified photoelectrodes were composed of TiO_2 nanoparticles that were surface-modified with CA to improve photocurrent generation by

enhancing photo-absorption.[9,98,122] The peak photocurrent density of the unmodified stage was 1.12 μA cm^{-2}. The surfaces of the photoelectrodes were modified with aminated single-stranded DNA (ssDNA) capture probes by linking NH_2 groups of the DNA to -COOH groups on the CA-modified TiO_2 nanoparticles (**Figure 7-4A and 7-4B**).[9] DNA hybridization is expected to reduce the anodic current measured on the TiO_2 photoelectrodes by hindering the access of AA in the electrolyte to the electrode surface.[9] To validate the performance of PECsense, we measured the photocurrent density after each stage of the assay development: unmodified; after-probe deposition; and after-target stages (**Figure 7-4C**). Using this data, we calculated the percent reduction in photocurrent relative to the previous stage (**Figure 7-4D**). The deposition of 1 μM probe ssDNA resulted in a 37.7 % average signal decrease. In the after-target stage, deposition of 100 nM non-complementary ssDNA in buffer (NC) as a control resulted in a slight 2.1 % decrease in signal, which can be attributed to non-specific DNA adsorption on the photoelectrode.[72,96] In comparison, when a solution of 100 nM non-complementary and 100nM complementary target ssDNA in buffer (Target+NC) was deposited, the observed signal reduction was much larger at 51.8 %, due to DNA hybridization.[64,96] We also challenged the assay with samples of 10% human blood plasma with and without spiking of DNA. The blank samples containing only plasma (Plasma) and those containing 100 nM non-complementary ssDNA spiked in plasma (Plasma+NC) showed a signal decrease of 6.6 % and 8.0 %, respectively. The sample with 100 nM target complementary ssDNA in plasma (Target+Plasma) displayed a 56.5 % signal reduction, whereas the sample with both 100 nM non-complementary ssDNA and 100 nM target complementary ssDNA spiked in plasma (Target+Plasma+NC) showed a higher signal reduction at 60.9 %. While the protocol as presented in this work is slightly modified, these results are in-line with those previously reported by Sakib et al.,[9] which

were recorded using a commercial PEC workstation. Accordingly, this demonstrates that the sensing abilities of PECsense are suitable for PEC DNA Biosensing at the PoC.

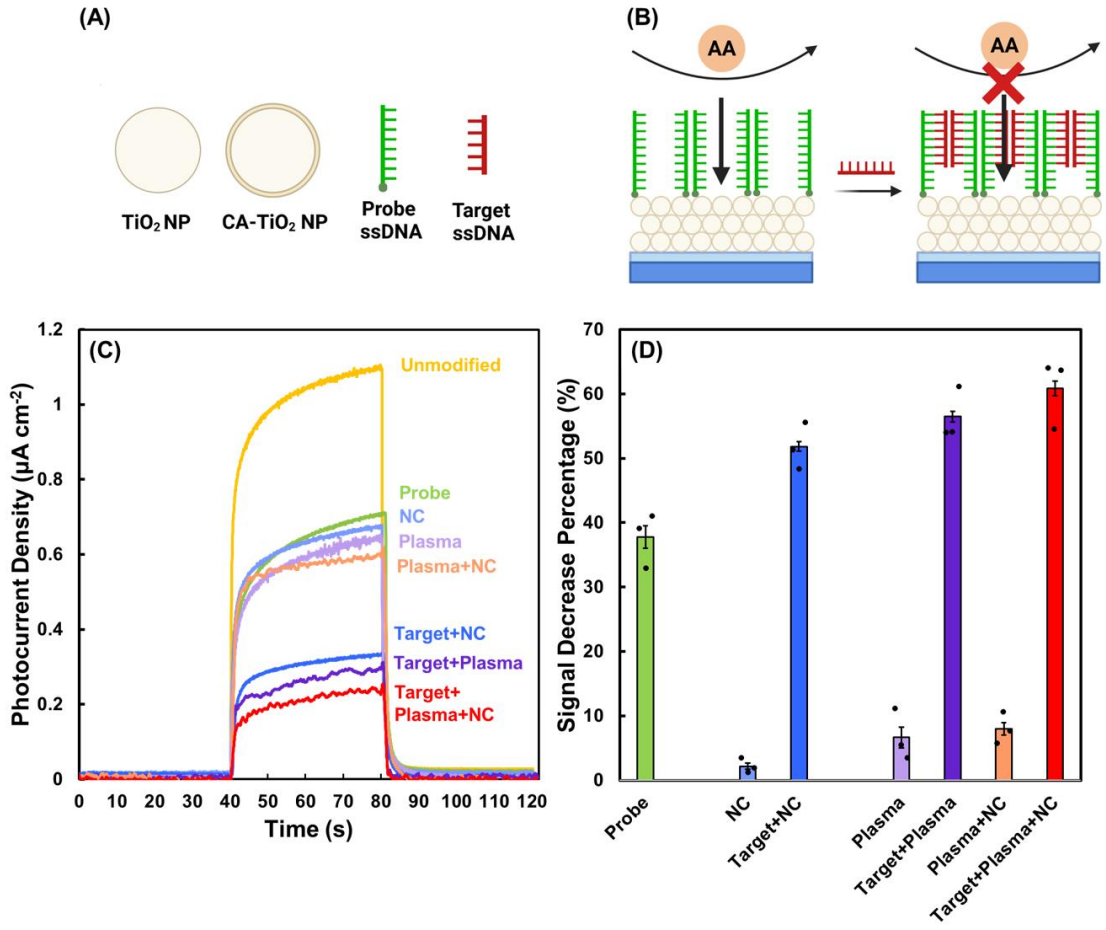

Figure 7-4. DNA biosensor operation and data collection using PECsense. (A) Unmodified TiO_2, CA-modified TiO_2, probe DNA and target DNA. (B) DNA detection scheme. Following hybridization with target DNA, photocurrent decreases due to steric hinderance in the presence of ascorbic acid. (C) Photocurrent densities at unmodified, after-probe and after-target stages of signal-OFF DNA biosensor operation when a 0 V bias was applied to the PEC cell relative to an Ag/AgCl reference electrode. The after-target samples include: only non-complementary target in buffer (NC), non-complementary target & complementary target in buffer (Target+NC), only human blood plasma (Plasma), complementary target in human blood plasma (Target+Plasma), non-complementary target in human blood plasma (Plasma+NC), and both non-complementary target & complementary target in human blood plasma. (D) Summary of photocurrent signal decrease at each stage of the signal-OFF DNA biosensor operation.

7.5 Conclusions

Herein, we developed a portable PEC reader (PECsense) to enable photoelectrochemical biological sensing assays to be performed at the point-of-care. This device is compact (75 mm x 100 mm, <100g), inexpensive (~100CAD) and is wirelessly (with Bluetooth low energy) controlled using a smartphone application. All measurements, data processing, and data analysis are performed using PECsense while wirelessly connected to a smartphone. Unlike other portable potentiostats reported in the literature[58,142,489,490,499,500] and even many commercial systems[501,502], this device directly interfaces with a custom LED to enable PEC experiments. In our study, PECsense offered a similar level of performance to a commercially available PEC workstation, at a fraction of the cost and in a significantly smaller form factor. We demonstrated that PECsense could be used in a number of different PEC applications, including experiments with variable illumination periods, those that yield cathodic and anodic currents, and those that operate under different potential biases. PECsense was also used as the readout system in a DNA hybridization detection assay, demonstrating its potential for use in point-of-care biosensing. We anticipate that the development of PECsense would expedite the translation of a wide range of PEC biosensors to the market.

7.6 Acknowledgements

The authors acknowledge the financial support provided for this work from NSERC and Ontario Ministry of Research and Innovation. Leyla Soleymani is the Canada Research Chair in Miniaturized Biomedical Devices and is supported by the Canada Research Chairs Program. Leyla Soleymani is the recipient of the Ontario Early Researcher Award. All authors listed have made a substantial, direct and intellectual contribution to the work, and approved it for publication.

7.7 Supplementary Materials

The following figures were retrieved from the manufacturer's datasheet.

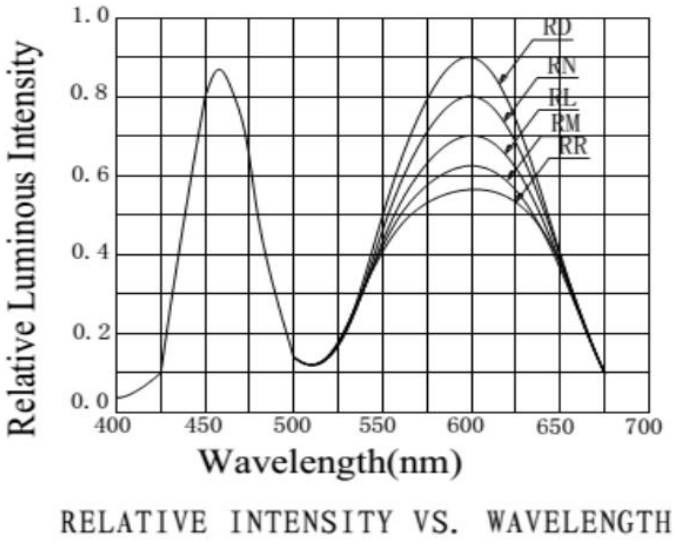

Figure 7-S1. Spectrum of the QT-Brightek PLCC6 white LED.

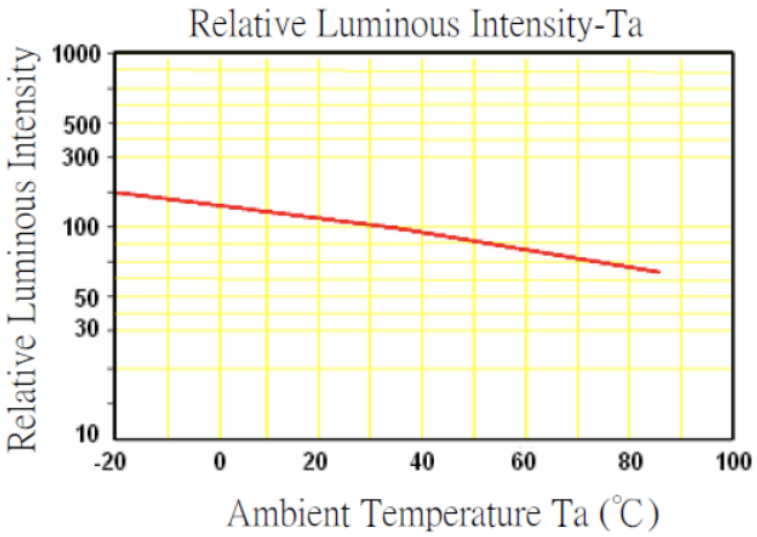

Figure 7-S2. Relative Luminous Intensity of the QT-Brightek PLCC6 white LED as a function of Ambient Temperature.

To further characterize the sensing abilities of PECsense, photocurrent measurements were conducted using bare CA-TiO_2 with and without the use of a Faraday cage for background signal shielding. In this experiment, the working electrode was irradiated for 40 s in the middle of a 120 s runtime. As shown in **Figure 7-S3**, there were no significant differences between the two

measurements. Although it is reasonable to assume that the elimination of background illumination would be advantageous in bright environments.

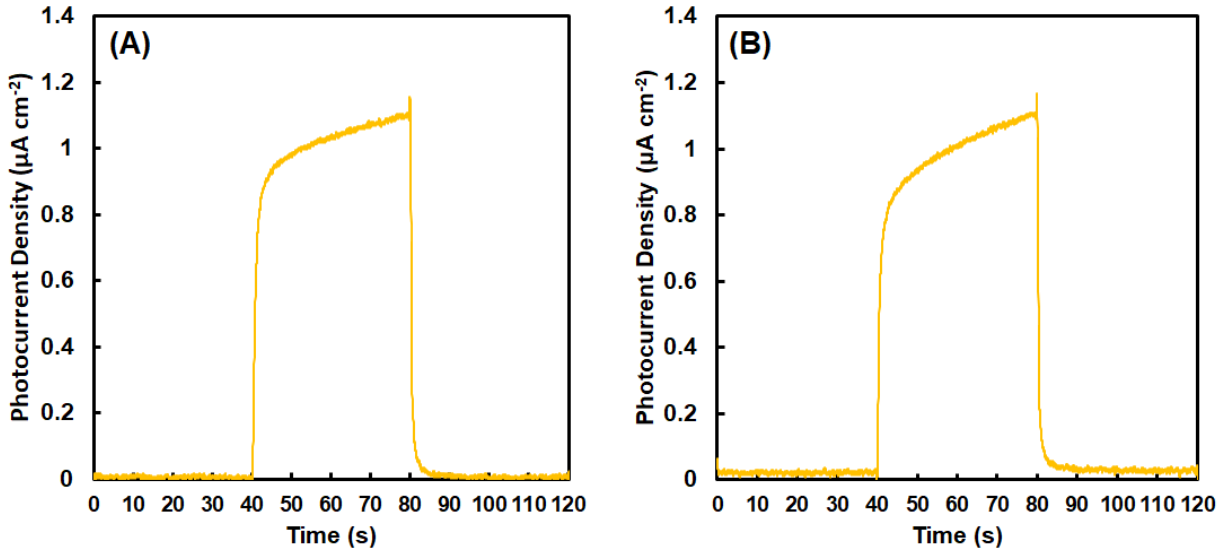

Figure 7-S3. Illuminated chronoamperometry experiments using PECsense (A) with a faraday cage and (B) without a Faraday cage.

The LED matrix circuit is controlled via pulse width modulation (PWM) pins of the Arduino Nano 33 BLE, which operates at 500Hz. By varying the PWM duty cycle (ON/OFF time), the effective LED matrix circuit luminous intensity can be modified. In this experiment, the working electrode was irradiated for 40 s in the middle of a 120 s runtime. As shown in **Figure 7-S4**, the peak photocurrent was found to be directly related to the duty cycle of the PWM signal.

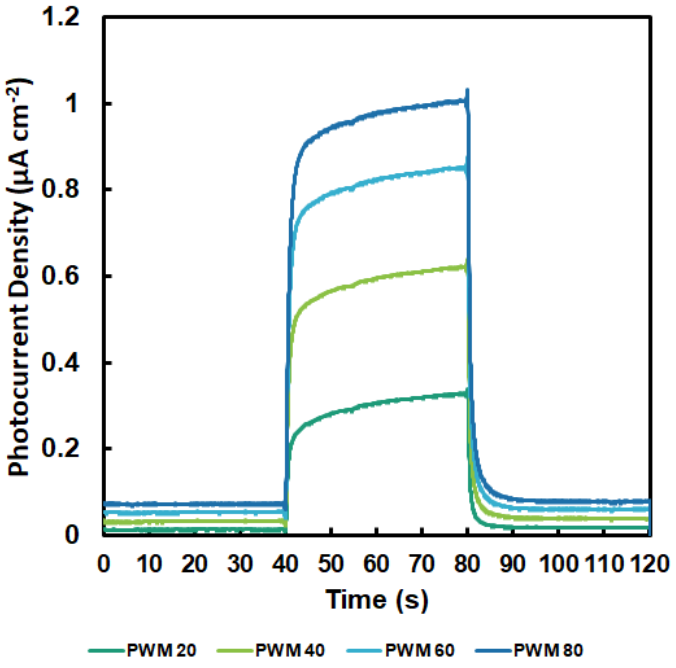

Figure 7-S4. Illuminated chronoamperometry experiments with adjustable LED matrix through variable PWM duty cycling using bare CA-TiO_2 photoelectrodes.

A partial limit of detection study was performed to demonstrate PECsense's performance in an analytical capacity. PECsense's ability to measure different target analyte concentration was assessed and compared against Zahner CIMPS-QE/IPCE PEC workstation, a commercially available potentiostat. Different target samples of various concentrations of complementary single-stranded DNA (ssDNA) in buffer solution were used. All the target samples also contained 100 nM non-complementary ssDNA to simulate the effect of non-specific absorption.

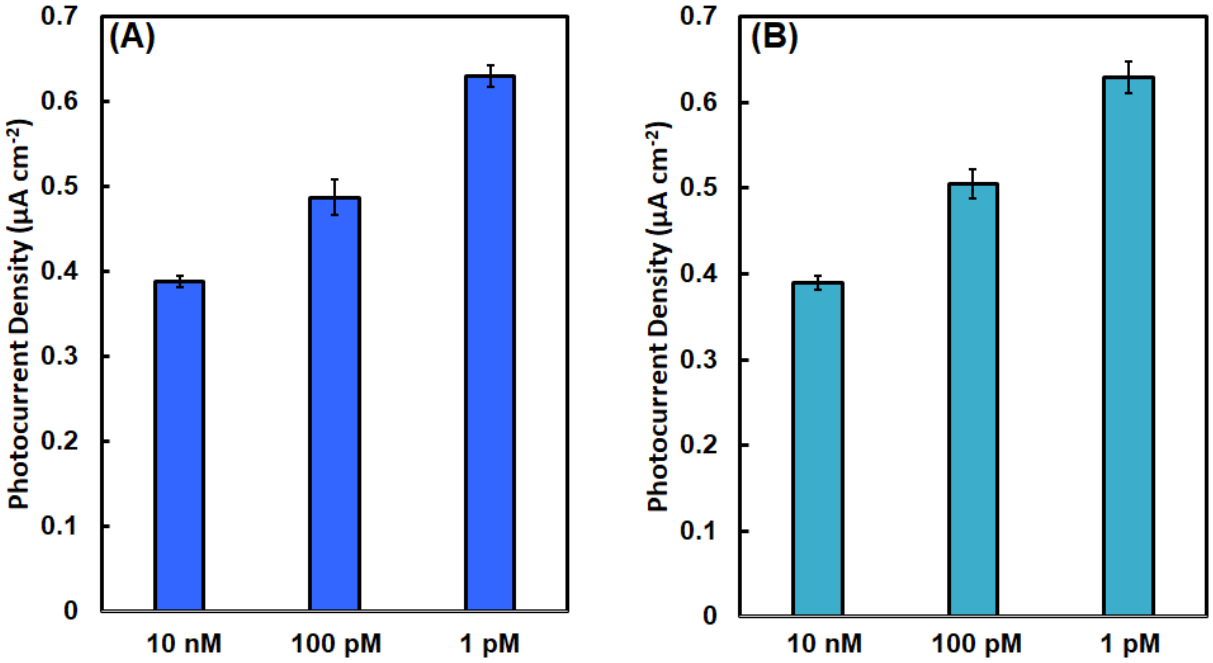

Figure 7-S5. Illuminated chronoamperometry experiments with different DNA target hybridization on the photoelectrode measured using (A) PECsense and (B) the Zahner CIMPS-QE/IPCE PEC workstation.

Chapter 8

Summary, Conclusions, Limitations and Future Work

Preface:

This final chapter briefly summarizes the outcome of this thesis and the potential to use the conclusions drawn from this work for developing highly effective PEC biosensors for PoC applications. Additionally, the limitations of this work and future directions are discussed.

8.1 Thesis Summary

The objective of this thesis was to develop new strategies to improve on PEC signal transduction so that it could be applied to build PoC-enabled biosensors that are ultrasensitive, simple to operate, have a high dynamic range and a low LOD. The overarching goal was to designe biosensors that are robust enough to reliably detect a wide variety of different disease biomarkers in complex biological matrices by enhancing analytical sensitivity, decreasing response time and enabling reagent-less biomolecular detection.

Photoelectrodes fabricated from TiO_2 nanomaterials are widely used in PEC biosensing due to their availability, chemical stability, tunable morphology, high catalytic efficiency and ideal band levels for driving useful EC reactions. However, unmodified TiO_2 is a wide bandgap semiconductor that has poor photoabsorbtion in the visible range and high charge carrier combination rates. This limits its photocurrent signal generation, and therefore PEC biosensors made from this material are limited in their performance. Towards the goal of improving TiO_2 nanomaterial-based PEC biosensors, we used catecholate molecules for the surface modification of TiO_2 nanomaterials to enhance their photoactivity. Catecholate molecules such as DHBA, CA and HTX were found to have a high binding affinity for TiO_2 and were easily adsorbed through solutions-based processing. Surface modification via catecholate molecules significantly enhanced photoabsorbtion in the visible range and overall IPCE of TiO_2, resulting in considerable enhancement in photocurrent density from unmodified TiO_2. Additionally, the catecholate molecules provided many useful functional groups for easier functionalization such as amines, carboxylates and aldehydes to TiO_2 nanoparticles. Furthermore, the high binding affinity of catecholates for TiO_2 surfaces was taken advantage of to develop novel synthesis methods for multifunctional nanostructures with a high degree of tunability. These catecholate-

modified TiO_2 nanomaterials were used as the foundation material on which all our PEC biosensors were built to deliver high performance.

The phase composition of the various synthesized TiO_2 nanostructures were studied using XRD analysis. In order to confirm the surface adsorption of catecholate molecules on TiO_2, we relied on FTIR and UV/Vis absorbance studies. The nanostructure morphologies and photoelectrode surface morphologies were studied using TEM and SEM imaging. PEC characterization of the photoelectrodes were achieved through chopped light amperometry to measure their photocurrent densities and IPCE measurements. All of this work was done to understand the impact of catecholates on the morphological and photoactive properties of TiO_2 nanostructures. When assessing the performance of the biosensors fabricated from catecholate-modified TiO_2 nanostructures, kinetics studies were often performed to study the response times. EIS was performed to verify successful immobilization of biomolecular probes and target interaction on the photoelectrodes. For each of our biosensors, we constructed calibration curves of signal as a function of target concentration in order to quantify the LOD.

Solution-based fabrication photoelectrodes from catecholate-modified TiO_2 nanomaterials allowed for designs of bioassays that were amenable to low cost, mass-scalability, rapid processing and industrial manufacture. Photoelectrodes fabricated from catecholate-modified TiO_2 nanomaterials used in the bioassays showed continuous enhancement in photocurrent density compared to those made from unmodified TiO_2 NP under both white light and UV illumination. The following samples showed the maximum photocurrent density in each of our works: CA-modified TiO_2 NP (J = 22.5 µA cm^{-2}), DHBA-TiO_2 (IPS) (J = 8.23 µA cm^{-2}), TiO_2-assembly/TiO_2-nanoparticle heterostructure (J = 2.15 µA cm^{-2}), and TiO_2/HTX-15/Ag-15 NP (J = 346 µA cm^{-2}). The high photocurrent signals of these material systems were leveraged to

create reagent-less and operationally simple PEC biosensors that achieved similar or better levels of performance compared to typical EC and PEC biosensors found in literature which are more complex and less reliable. This resulted in the creation of direct signal-off bioassays that were able to detect DNA biomarkers (LOD = 1.38 pM) and Il-6 antigens (LOD = 3.6 pg mL^{-1}) in blood plasma. We also engineered a hybrid semiconductor structure by coupling TiO_2 nanomaterials of different phases that have different bandgap energies to achieve photocurrent enhancement. By combining this material system with functional DNAzymes, we designed a molecular switch that modulated photocurrent signal by breaking and remaking semiconductor heterostructures. This was used to design a bacterial detection assay that was able to detect E. coli in lake water (LOD = 18 CFU mL^{-1}). Additionally, using catecholate molecules, we developed a novel method for rapid one-pot synthesis of Ag-decorated TiO_2 NP. The resultant TiO_2/HTX/Ag NP hybrid structures enhanced photocurrent through the combined effect of LSPR and photoelectron injection. The presence of Ag allowed for easy biofunctionalization through thiol-silver complexes, which was used to construct a highly sensitive direct signal-off bioassay for detecting microRNA biomarkers associated with prostate cancer in urine (LOD = 172 fM).

Aside from improving the sensitivity and reliability, we made strides towards PoC testing by exploring miniaturization and multiplexing in our PEC biosensors. All of our biosensors require small sample volumes (<100 µL) and have rapid sample-to-result time (<1 hr) which is crucial for PoC-capable biosensors. Additionally, we designed a portable smartphone-operated potentiostat for PEC signal reading that removes the barrier of bulky instrumentation preventing PEC biosensors from being commercialized. In conclusion, we have addressed the technical challenges associated with the advancement of biomolecular detection and PoC diagnostics by designing ultrasensitive, easy-to-use, reliable and portable TiO_2 nanomaterial-based PEC

biosensors that are able to detect a wide range of different biomarkers in complex biological matrices.

8.2 Thesis Conclusions

i. Several catecholate and gallate molecules were use to modify the surface of TiO_2 NPs for photosensitization through forming charge transfer complexes. The molecules used were DOPA, THB, DHB, THBA, DHPL, DHBA and CA, which were shown to improve visible light photoabsorbtion and photocurrent density of TiO_2 NPs, in that order, from lowest to highest. FTIR study was used to verify the bidentate chelation or bidentate bridging bonding mechanisms between the catecholates and gallates. The highest photocurrent density measurement was from the CA-modified TiO_2 NP (J = 22.5 µA cm^{-2}), which was used to fabricate photoelectrodes for a PEC DNA biosensor. Probe ssDNA was immobilized onto the photoelectrode through the formation of carboxamide bond amine-termination of the ssDNA probes and the carboxyl functional group of CA. The probes would then capture target ssDNA through DNA hybridization, forming the basis of a simple but effective direct signal-off biosensor. Higher concentration of captured target DNA inversely correlated to a reduction in the photocurrent of the CA-TiO_2 photoelectrodes, due to steric hinderance. This bioassay required a sample volume of 15 mL and demonstrated a linear range of 1 pM – 100 nM and an LOD of 1.38 pM in blood plasma within a 95 % confidence interval. The bioassay also showed a high degree of specificity when compared against plasma samples spiked with 100 nM non-complementary ssDNA.

ii. A novel synthesis method for TiO_2 nanostructures was developed through in-situ addition of catecholate molecules during hydrothermal synthesis. Catecholates were found to

preferentially bind to specific crystal facets during synthesis, acting as capping agents, resulting highly anisotropic growth. This method could be used tune the morphology of TiO_2 into multifunctional 3D nanostructures (radial clusters of nanorods) with enhanced electronic properties such as improved photoabsorbtion/photoexcitation due to higher charge carrier separation, reduced charge carrier recombination rates, and lower charge transfer resistance, compared to conventional NP morphologies that is typically used. Using the DHBA-TiO_2 (IPS) nanostructures (J = 8.23 μA cm^{-2}), photoelectrodes were fabricated for use in a PEC IL-6 immunoassay. Probe anti-IL-6 antigen was immobilized onto the photoelectrode through the formation of Schiff-base between the aldehyde group of the DHBA on TiO_2 surfaces and free amine groups in the antigens. The anti-IL-6 captured the IL-6 proteins through anti-body/antigen complexation, forming the basis for direct signal-off immunoassay, where higher target concentration inversely correlated to photocurrent of the photoelectrode due to steric hindrance. This assay required a sample volume of 15 mL and demonstrated a linear range of 2-2000 pg mL^{-1} and an LOD of 3.6 pg mL^{-1} in plasma. The bioassay also showed a high degree of specificity when compared against plasma samples spiked with 2000 pg mL^{-1} BSA. Lastly this assay showed excellent short-term and long-term stability, with signal degradation of only 0.86 % over 14 minutes and ~6 % over a seven-day period, respectively.

iii. A highly specific and ultrasensitive bacterial assay was designed by integrating TiO_2-based PEC signal transduction with RNA-cleaving DNAzymes. This assay capable of performing rapid sample analysis without culture-growth or biomolecule amplification. For this PEC DNAzyme assay, we designed a material system composed of two different TiO_2 nanomaterials: TiO_2-assemblies – three-dimensional rutile nanorod clusters (80-100

nm) and TiO_2-nanoparticles – caffeic acid modified anatase nanoparticles (1-6 nm). The combination of TiO_2-assemblies and TiO_2-nanoparticles gave rise to a semiconductor heterostructure that massively improves the photoexcitation efficiency of the combined material system and was shown to improve photocurrent generation by up to 518 %. This effect in conjunction with DNAzymes - which are highly specific biorecognition elements for bacterial samples, was utilized as the signaling mechanism in this assay. To achieve PEC signal transduction, photoactive DNAzymes were created by linking them to TiO_2-nanoparticles. The assay consisted of two electrodes fabricated from TiO_2-assemblies: cleavage electrode – modified with photoactive DNAzymes, and detection electrode – modified with ssDNA capture probes. Upon target interaction, a photoactive reporter strand is cleaved from the DNAzyme and is captured by the probes. This caused the breaking up of the TiO_2 heterostructure on the cleavage electrode and its subsequent reformation on the detection electrode, resulting in cleavage electrode signal decrease and detection electrode signal increase. The PEC DNAzyme assay was able to detect *E. Coli* contamination with high sensitivity and achieved a very low limit of detection of 21 CFU mL^{-1} in buffer and 18 CFU mL^{-1} in lake water. Additionally, the assay showed a high degree of specificity when compared against a panel of both gram-positive and gram-negative bacteria.

iv. A novel manufacturing method that uses catecholate-assisted photoreduction for decorating TiO_2 NP with plasmonic Ag NPs to implement photoenhancement through LSPR was developed. In this method, TiO_2 NPs were first surface modified with HTX, a catecholate dye. The resulting TiO_2/HTX NP has enhanced photocurrent generation which was taken advantage of to reduce an Ag precursor to directly nucleate Ag NPs

onto the TiO_2 surface, resulting in the TiO_2/HTX/Ag NP material system. XRD, TEM, EELS analysis were used to study the morphology and distribution of the Ag NP decoration. It was found that the deposited Ag NP were highly crystalline silver-3C and ranged in size from 0.5 nm – 10 nm. By varying the amount of HTX and silver precursor, size tunability could be achieved with this manufacturing method. Samples that had larger Ag NPs (2 - 10 nm) showed improvement in photocurrent from TiO_2/HTX, while samples with smaller Ag NP (0.5 – 2.5 nm) did the opposite. IPCE, UV/Vis absorbance, and photocurrent density measurements was used to propose a possible band diagram describing the TiO_2/HTX/Ag NP heterostructure with larger Ag NPs. The proposed band structure involved high energy electron generation through LSPR decay in Ag NP cascading and enhancing type-II photoelectron injection between TiO_2 and HTX. This material system was used as the basis for a multiplexing PEC biosensor the detection of multiple miRNA biomarkers associated with prostate cancer. This was a signal-off assay, where thiolated ssDNA probes were immobilized onto the photoelectrode through the formation of thiol-metal complexes, and captured the miRNA targets through DNA hybridization. This bioassay required a sample volume of 15 mL and demonstrated a linear range of 100 fM – 100 nM and an LOD of 172 fM in urine within a 95 % confidence interval. The bioassay also showed a high degree of specificity when compared against plasma samples spiked with 100 nM non-complementary miRNA.

v. We developed a portable PEC signal reader for more seamless integration of PEC biosensing in PoC settings. Our PEC readout system, referred to as PECsense, can be controlled remotely via an accompanying smartphone application through the Bluetooth Low Energy communication protocol. PECsense interfaces with a custom LED matrix

circuit which can be used as an optical excitation source to facilitate PEC biosensing. The smartphone-based app interfaces with the PECsense via the Bluetooth Low Energy communication protocol. The app enables enables the user to adjust the experimental parameters (including the applied bias, scan duration, illumination period, among others), provides instructions to the user, and features in-app data processing. This eliminates the need for bulky external hardware and ensures that PECsense is PoC ready. The performance of the PECsense was validated by running a signal-off PEC DNA hybridization detection assay, as well as using it in experiments that demonstrate its variable illumination periods, anodic/cathodic biasing capabilities, and low signal-to-noise ratio. We found that the PECsense was able to match the performance of conventional benchtop potentiostats. The PECsense runs on a 24-bit ADC which gives it a a current resolution of 36 pA within a current measurement range of of -10 µA to 10 µA (-20 µA to 20 µA for differential measurements). The sampling rate can be programmed from 20 – 1000 Hz. The color temperature of the built-in LED matrix is 4240 ^{o}K, and its intensity 6000 mcd.

8.3 Contributions to the Field

Surface modification of TiO_2 by catecholates for enhancing photocurrent and improved biofunctionalization

TiO_2 nanomaterials are very popular as photoelectrode material for use in PEC, photocatalytic and photovoltaic applications due to their high photocatalytic activity and ideal band levels for driving useful electrochemical reactions.[94,137] Despite this, TiO_2 has poor visible light absorption and high charge carrier recombination rates, which limits in IPCE and photocurrent generation.[64,94,278] We explored surface modification of TiO_2 with catecholate molecules as a

photoenhancement strategy. Catecholates were found to adsorb onto TiO_2 surfaces very readily by simply mixing them and without any other special procedures. Catecholates form bidentate chelating or bidentate bridging type bonds on the surface of TiO_2, which results in charge transfer complexes that significantly improved photoabsorption in the visible range and photocurrent generation. We fine-tuned the ratio of catecholates to TiO_2 to produce optimal photoenhancement. Catecholate-modified TiO_2 also displayed enhanced colloidal stability, improving the morphology of photoelectrodes made from them. Catecholates also added functional groups on TiO_2, which was useful for interfacing with biomolecules for bioassays. This work paved the way for a fast, easy and cost-effective method for producing large amounts of high quality photoelectrodes for the PEC biosensing application of this thesis. The initial exploration of catecholate modified TiO_2 nanomaterials is described in chapter 3. However, this became the foundational material for all subsequent PEC biosensors and was further developed throughout the work described in chapter 4, 5 and 6.

Catecholate-assisted Hydrothermal Synthesis allowing for a high-degree of tunability in TiO_2 nanomaterials

Our work on surface modification of TiO_2 nanomaterials with catecholates highlighted the very high binding affinity of catecholate molecules for TiO_2 surfaces.[242,503] This led us to develop novel synthesis methods where catecholates were used as surfactants to tune the structural morphology of TiO_2 nanomaterials. By adding catecholates in-situ during hydrothermal synthesis alongside the TiO_2 precursor, we could change the growth pattern of TiO_2. It was found that catecholates preferentially bind to specific crystal facets of TiO_2, leading to highly anisotropic growth which can form large 3D morphologies or sub-nanoscale particles. In chapter 4, this synthesis technique was used to develop the 3D TiO_2 nanostructures used to fabricate

nanoporous photoelectrodes. In chapter 5, the synthesis technique was also used to make the ultrasmall rutile TiO_2-nanoparticles (1-6 nm), which was used in conjunction with the previously developed 3D TiO_2 nanostructures in the PEC DNAzyme assay.

Inorganic semiconductor heterostructure made from two different TiO_2 nanomaterials

Multistage bandgap heterostructure resulting from hybrid semiconductor are utilized to extend the photoabsorbtion spectra and charge separation efficiency of PEC systems.[64,504] Usually, these heterostructures are created by coupling two or more inorganic semiconductors with different bandgap energies.[96,97,504] In chapter 5, we described the engineering of a hybrid semiconductor heterostructure by coupling two different polymorphs of TiO_2 nanostructures. The semiconductor heterostructure was formed by drop depositing rutile TiO_2-nanoparticles on photoelectrodes made from anatase TiO_2-assemblies. The rutile and anatase phase of TiO_2 have electron affinity values of 4.8 eV and 5.1 eV, and therefore when combined into a heterostructure, have an effective bandgap of ~2.78 eV, which significantly improved the photoabsorbtion spectra and IPCE of the combined material system. The photoreduction synthesis process resulted in CA surface functionalization on the rutile TiO_2-nanoparticles, which further the photoexcitation properties through formation of charge transfer complexes. This material system showed remarkable enhancement in photoexcitation, with only 0.0033 % TiO_2-nanoparticle added (compared to mass amount of TiO_2 assemblies) leading to a noticeable 13.1 % increase in photocurrent; a maximum photocurrent increase of 518 % was observed.

High sensitivity in signal-off biosensing

Signal-off schemes for biosensors, where higher target concentration decreases signal output from the transducer element in generally not preferred due to their high background

signals.[41,60,64] In EC or PEC biosensors, these assays typically rely on steric hinderance, where target analytes build-up on the transducer surface hinder interaction between the electrolyte and the electrode/photoelectrode, thereby reducing signal.[122,334] Despite this, the signal-off approach is one of the simplest and most repeatable mechanisms for biomolecular detection, since it does not require additional reagents or labeling stages.[64,505,506] In chapter 3, 4, and 6, we developed several signal-off PEC biosensors for detecting bioanalytes (i.e. ssDNA, Il-6 antigen and miRNA) that were cost-effective, easy-to-operate and reliable without sacrificing any performance. This could be achieved due to the development of various photoactive materials with high signal generation which negated the high background signal associated with signal-off detection schemes.

PEC signal modulation with photoactive DNAzymes

A major hurdle in developing sensors for detecting pathogens such as bacteria is that they require target enrichment or amplification to deliver the required LOD.[25,27,53,54] RNA-cleaving DNAzymes, are a class of synthetic nucleic acids, that have emerged as a high-precision biorecognition element for detection of specific bacterial species without the need for sample processing.[350,363,507] These molecules work by acting as molecular switches by cleaving off a segment of themselves in response to particular bacterial targets. [350,363,507] In chapter 5, for the first time, we developed photoactive RCDs by tagging them with TiO_2 nanomaterials for combining these molecular switches with photoelectrochemical signal readout. We designed these molecular switches to make and then break semiconductive heterostructures in response to bacterial targets. The result is a photoelectrochemical bacterial sensor with a record sensitivity of 18 CFU mL^{-1}, a new record for amplification-free detection of bacteria, that does not rely on

target enrichment, reagent addition, or sample processing. This presents a new tool for rapid and in-field water testing.

Catechol-assisted photoreduction synthesis technique for decoration of TiO_2 NP with Ag NP

The success of the catechol-assisted hydrothermal synthesis of TiO_2 nanomaterials, led us to explore other ways the high binding affinity of catecholates could be used to create new materials. In chapter 6, this led us to develop a novel one-pot catecholate-assisted photoreduction method for decorating TiO_2 NP with Ag NPs that is both fast and has a high yield. In typical photoreduction synthesis, Ag or other plasmonic metal NPs can be directly deposited onto photoactive metal oxides by using their intrinsic photocurrent to reduce a precursor.[400,508] This process is very slow, often requiring several hours of irradiation to produce decorations and produces inconsistent results. We directly improved this process by first modifying TiO_2 – our metal oxide of choice – with HTX, a catechol dye. TiO_2/HTX NPs have significantly enhanced photocurrent generation which made the photoreduction of Ag precursor much more efficient. By varying the amount of HTX and Ag precursor we could tune the average size and polydispersity of the Ag NP, leading to materials with different properties. TiO_2/HTX/Ag NP with larger Ag NP (2 – 10 nm) showed excellent photoexcitation properties through the combined effects of LSPR and photoelectron injection. Their enhanced photoabsorbtion and photocurrent generation was very useful for achieving high performance in signal-off PEC biosensors. TiO_2/HTX/Ag NP with larger Ag NP (0.5 – 2.5 nm) had reduced photoexcitation, likely due to the quantum confinement effect resulting in the formation of bandgaps in the sub-nanometer sized Ag NP. This interesting material property could potentially be applied to create frequency-based signal-reading for biosensors (see section 8.4).

Multiplexing in PEC biosensors

Detection of single biomarkers is a useful form of diagnostic testing. However being able to detect a panel of multiple biomarkers can be even more valuable by providing much more detailed diagnosic and prognosic information.[509,510] In chapter 6, we demonstrated multiplexing with PEC signal transduction in biosensors for the first time. While this specific assay was biomolecular detection of microRNA, it can be expanded for the detection of any biomolecules such as DNA or proteins, as long it relies on steric hinderance-based signal-off assays. The high photocurrent of the PEC biosensor built on TiO_2/HTX/Ag NP material system, and the resulting ultrasensitivity mean that multiplexing can be implemented with simple assays for a high degree of reliability in PoC settings.

Portable Smartphone-interfacing PEC reader

PEC biosensors have seen limited commercial success, and this can be attributed to the lack of low-cost, portable, and user-friendly PEC readout devices.[62] To overcome this challenge, we focused on designing a portable smartphone-interfacing potentiostat for PEC applications. In chapter 7, we described our device called the PECsense which was designed for support PoC signal-reading in a broad range of PEC-based bioassays. In particular, the reader was able to apply adjustable bias voltages, measure both anodic & cathodic photocurrent, and had minimal input-referred noise. Unlike other potentiostats in the market, the PECsense was able to interface with illumination sources (built-in LED matrix) suitable for PEC applications and support variable illumination periods. The smartphone app which was designed with a helpful user-interface, allows any user with minimal training to operate PEC biosensors and process output data very easily.

8.4 Future Work

Automation of photoelectrode fabrication

The layer-by-layer drop deposition process for the fabrication of photoelectrodes for use in PEC biosensors was described in chapter 3,4, 5 and 6. This process was done manually one-by-one for each photoelectrode. Moreover, the photoelectrode substrates were also prepared by manually cutting them out from large sheets. The manual handing in these processes introduced variability in the photocurrent density measurements used for PEC biomolecular detection. Automation of the fabrication process will help reduce standard deviation in the signal measurements, leading to more accurate and sensitive PEC biosensors. Automation is also the next step preparing these biosensors for batch processing in industrial manufacturing.

Alternate photoactive materials

While TiO_2 remains one of the most versatile materials for use in PEC biosensing, using other materials can open up new avenues of photoenhancement strategies that can potentially be used to attain greater improvement in PEC biosensor performance. Aside from TiO_2, other inorganic metal oxides such as ZnO, WO_3 and SnO_2 should be explored as material used for fabricating photoelectrode signal transducers. The catecholate-assisted morphology tuning discussed in chapter 4 and 5 can be used to synthesize new types of 3D nanomaterial architectures when used with conjunction with alternate metal oxides since they different crystal structures and surface binding affinities compared to TiO_2.[114] More variety in nanostructure architecture will result in the fabrication photoelectrodes with new types of morphologies that may offer higher photocurrent generation. The HOMO levels, LUMO levels and bandgap energy of alternate metal oxides are different from TiO_2. This opens up opportunities to further optimize the

photoenhancement strategies presented in this thesis such as ligand/dye sensitization, coupling between two different semiconductors, and coupling a semiconductor with plasmonic NP.

Multiplexing in Biosensing combined with machine learning (ML) algorithms

Diseases often impact different biochemical and immune pathways, which interact in countless and unexpected ways.[509,510] By detecting multiple biomarkers corresponding to different biochemical mechanisms, we can achieve a significantly more powerful diagnostic and prognostic indicators compared to the detection of a single biomarker.[509,510] We showed the implementation of multiplexing combined with ultrasensitive PEC biosensing in chapter 6. The next step the advancement in biomolecular sensing should be to take advantage of multiplexing to apply ML to algorithms to parse more accurate diagnostic and prognostic information from PEC biosensors. ML algorithms such as support vector machines, κ-nearest neighbours, convolutional neural networks and feedforward neural networks are well suited for multiplexed biosensing for adding non-linear regression and classification functionality after post-processing.[511] Proper deployment of ML algorithms can uncover hidden relations between sample parameters and through data visualization, and mine interrelations between signals and biochemical pathways.[511] Moreover, benefits of using ML can allow working with reasonable analytical performance even with noisy or low-resolution data.[511]

Wearable EC signal readers with skin-patchable electrodes

The next step in portable signal reading lies in converting these devices into a wearable sensor for continuous monitoring of biomarkers. Recently, there have been significant development towards skin-patchable electrodes for biosensing electrodes such as conductive polymer-based microneedle patches useful for analysis of metabolites such as cholesterol and glucose in skin

interstitial fluid.[512,513] These wearable electrodes are typically used for offline analysis, which does not fully realize their potential. We can turn the PECsense into a wearable EC signal-reader by miniaturizing it after stripping out unneeded features, which reduces the profile of the PCB and device housing. The modified device will sit on top of and connect to the skin-patchable electrode. The smartphone-based user interface of the modified PECsense will enable this device to be easy-to-use while delivering fast continuous response.

Bacterial detection platforms for common pathogens

We demonstrated a highly sensitive PEC biosensor for the detection of *E. coli* in environmental monitoring capacity in chapter 5. The photoactive DNAzyme-based signal modulation used in this assay was sensitive enough to detect quantities as low as 2 CFU within 100 µL sample volume and accurately quantify bacterial concentration due low standard deviations in the signal measurements. There exists DNAzymes that respond to many different pathogenic bacteria such as *L. pneumophila, K. pneumoniae, H. pylori, C. difficile, S. typhimurium and L monocytogenes*.[507,514] The next step should be to design new versions of the PEC DNAzyme sensor which can use alternate DNAzymes to detect a panel of different bacteria both in environmental samples and biological matrices.

Frequency-based PEC biosensing through Ag NP size modulation via photocurrent-driven chemical oscillations

Typically, it is expected that decorating metal oxides via noble metal NPs increases their photoexcitation due to the LSPR effect. One of the more interesting observations made during the work on the TiO_2/HTX/Ag NP material system described in chapter 6, is that decoration via sub-nanometer range Ag NP actually decreases the cathodic photocurrent of TiO_2 NPs. The typical improvement in photoexcitation was still observed with TiO_2/HTX/Ag NP that contained

larger sized Ag NPs (~10 nm). This led us to believe that we were observing the quantum confinement effect, where as the Ag NPs got smaller, their density of states was reduced which discretized the CB and VB of silver.[423–425] This essentially resulted in the formation of a bandgap for the Ag NPs, leading them to exhibit QD-like properties.[106,423] The reduction in photoexcitation in these samples likely stemmed from misalignment of band energy levels between TiO_2, HTX and Ag NPs.[515] It could be possible to turn this reduction in cathodic photocurrent into an anodic photocurrent by changing the metal oxide and catechol dye of choice. In the presence of a silver salt, an anodic photocurrent can oxidize the Ag NP to produce Ag^+ ions. The photocurrent would reverse polarity when sufficient Ag NP is removed from the metal oxide surface, turning Ag^+ back into redeposited Ag NP. By coupling the metal oxide nanomaterials with biorecognition elements, this type of chemical oscillation could pave the way for the frequency-based signal-reading for biosensors.

8.5 Final remarks

We started this work with the aim of developing signal amplification strategies for PEC biosensors and improve current understandings of surface modification of metal oxides with ligands and dyes. Throughout the course of this thesis, the scope of our work grew to become a highly interdisciplinary project that bridged the gaps between various engineering disciplines such as biotechnology, nanotechnology, crystallography, electrochemistry, photonics, microelectronics and embedded systems. Aside from PoC biosensing, the innovations and advancements presented in this work can be applied to many other technologies such as smart surfaces, ultracapacitors, fuel cells, photovoltaics, nanoactuators, microelectromechanical systems, and other forms of data acquisition systems.

References

1. Global Biosensors Market Size to Reach USD 50.7 Billion in 2030 | Rising Need for Real-Time Monitoring Devices and Increasing Demand for Point of Care Healthcare Services are Some Key Factors Driving Industry Demand, Says Emergen Research. https://www.prnewswire.com/news-releases/global-biosensors-market-size-to-reach-usd-50-7-billion-in-2030--rising-need-for-real-time-monitoring-devices-and-increasing-demand-for-point-of-care-healthcare-services-are-some-key-factors-driving-industry-demand-says-emergen--301551217.html.

2. Biosensors Market Size & Share Report, 2022-2030. https://www.grandviewresearch.com/industry-analysis/biosensors-market.

3. Biosensors Market Size to Surpass US$ 49.6 Billion by 2030. https://www.globenewswire.com/en/news-release/2022/05/05/2437016/0/en/Biosensors-Market-Size-to-Surpass-US-49-6-Billion-by-2030.html.

4. Moina, C. & Ybarra, G. *Fundamentals and Applications of Immunosensors*. www.intechopen.com.

5. Li, J. & Wu, N. Semiconductor-Based Photocatalysts and Photoelectrochemical Cells for Solar Fuel Generation: A Review. *Catal Sci Tech* **5**, 1360–1384 (2015).

6. Victorious, A., Clifford, A., Saha, S., Zhitomirsky, I. & Soleymani, L. Integrating TiO2 Nanoparticles within a Catecholic Polymeric Network Enhances the Photoelectrochemical Response of Biosensors. *J Phys Chem C* **123**, 16186–16193 (2019).

7. Burger, A. *et al.* Synergy of Catechol-Functionalized Zinc Oxide Nanorods and Porphyrins in Layer-by-Layer Assemblies. *Chem Eur J* **24**, 7896–7905 (2018).

8. Clifford, A., Lee, B. E. J., Grandfield, K. & Zhitomirsky, I. Biomimetic modification of poly-L-lysine and electrodeposition of nanocomposite coatings for orthopaedic applications. *Colloids Surf B* **176**, 115–121 (2019).

9. Sakib, S., Pandey, R., Soleymani, L. & Zhitomirsky, I. Surface modification of TiO_2 for photoelectrochemical DNA biosensors. *Med Dev Sens* **3**, e10066 (2020).

10. Zhang, B., Wang, H., Xi, J., Zhao, F. & Zeng, B. In situ formation of inorganic/organic heterojunction photocatalyst of WO_3/Au/polydopamine for immunoassay of human epididymal protein 4. *Electrochim Acta* **331**, 135350 (2020).

11. Yang, Y. & Hu, W. Bifunctional polydopamine thin film coated zinc oxide nanorods for label-free photoelectrochemical immunoassay. *Talanta* **166**, 141–147 (2017).

12. Higashimoto, S. *et al.* Photocatalysis of titanium dioxide modified by catechol-type interfacial surface complexes (ISC) with different substituted groups. *J Catal* **329**, 286–290 (2015).

13. Kim, J. H., Joshi, M. K., Lee, J., Park, C. H. & Kim, C. S. Polydopamine-assisted immobilization of hierarchical zinc oxide nanostructures on electrospun nanofibrous membrane for photocatalysis and antimicrobial activity. *J Colloid Interface Sci* **513**, 566–574 (2018).

14. Wettstein, C. M. & Sánchez, C. G. Characterization of ZnO as substrate for DSSC. *Phys Chem Chem Phys* **20**, 21910–21916 (2018).

15. Nam, H. J. *et al.* A new mussel-inspired polydopamine sensitizer for dye-sensitized solar cells: Controlled synthesis and charge transfer. *Chem Eur J* **18**, 14000–14007 (2012).

16. Thorlabs - MNWHL4 4900 K, 740 mW (Min) Mounted LED, 1225 mA. https://www.thorlabs.com/thorproduct.cfm?partnumber=MNWHL4.

17. Noncommunicable diseases. *World Health Organization* https://www.who.int/news-room/fact-sheets/detail/noncommunicable-diseases (2021).

18. *Global Health Estimates 2020: Deaths by Cause, Age, Sex, by Country and by Region, 2000-2019*. (2020).

19. Bennett, J. E. *et al.* NCD Countdown 2030: worldwide trends in non-communicable disease mortality and progress towards Sustainable Development Goal target 3.4. *The Lancet* **392**, 1072–1088 (2018).

20. About Global NCDs | Division of Global Health Protection | Global Health | CDC. https://www.cdc.gov/globalhealth/healthprotection/ncd/global-ncd-overview.html.

21. Jaspers, L. *et al.* The global impact of non-communicable diseases on households and impoverishment: a systematic review. *Eur J Epidemiol* **30**, 163–188 (2014).

22. Gakidou, E. *et al.* Global, regional, and national comparative risk assessment of 84 behavioural, environmental and occupational, and metabolic risks or clusters of risks, 1990–2016: a systematic analysis for the Global Burden of Disease Study 2016. *Lancet* **390**, 1345–1422 (2017).

23. Castillo-Henríquez, L. *et al.* Biosensors for the detection of bacterial and viral clinical pathogens. *Sensors* **20**, 1–26 (2020).

24. Chen, J., Andler, S. M., Goddard, J. M., Nugen, S. R. & Rotello, V. M. Integrating recognition elements with nanomaterials for bacteria sensing. *Chem Soc Rev* **46**, 1272–1283 (2017).

25. Zhao, X., Lin, C. W., Wang, J. & Oh, D. H. Advances in rapid detection methods for foodborne pathogens. *J Microbiol Biotechnol* **24**, 297–312 (2014).

26. Law, J. W. F., Mutalib, N. S. A., Chan, K. G. & Lee, L. H. Rapid methods for the detection of foodborne bacterial pathogens: Principles, applications, advantages and limitations. *Front Microbiol* **5**, 770 (2014).

27. Pandey, P. K., Kass, P. H., Soupir, M. L., Biswas, S. & Singh, V. P. Contamination of water resources by pathogenic bacteria. *AMB Express* **4,** (2014).

28. Lake, I. R. *et al.* Climate change and food security: Health impacts in developed countries. *Environ Health Perspect* **120**, 1520–1526 (2012).

29. Boxall, A. B. A. *et al.* Impacts of climate change on indirect human exposure to pathogens and chemicals from agriculture. *Environ Health Perspect* **117**, 508–514 (2009).

30. Hellberg, R. S. & Chu, E. Effects of climate change on the persistence and dispersal of foodborne bacterial pathogens in the outdoor environment: A review. *Crit Rev Microbiol* **42**, 548–572 (2016).

31. Zoonoses. *World Health Organization* https://www.who.int/news-room/fact-sheets/detail/zoonoses (2020).

32. Background to the WHO R&D blueprint pathogens. https://www.who.int/observatories/global-observatory-on-health-research-and-development/analyses-and-syntheses/who-r-d-blueprint/background.

33. Bloom, D. E. & Cadarette, D. Infectious disease threats in the twenty-first century: Strengthening the global response. *Front Immunol* **10**, 549 (2019).

34. Pandey, R. *et al.* Integrating programmable DNAzymes with electrical readout for rapid and culture-free bacterial detection using a handheld platform. *Nat Chem* **13**, 895-901 (2021).

35. Aminov, R. I. A brief history of the antibiotic era: Lessons learned and challenges for the future. *Front Microbiol* **1**, 134 (2010).

36. Mehand, M. S., Al-Shorbaji, F., Millett, P. & Murgue, B. The WHO R&D Blueprint: 2018 review of emerging infectious diseases requiring urgent research and development efforts. *Antiviral Res* **159**, 63–67 (2018).

37. Alexandru, A., Ianculescu, M. & Coardos, D. Improved patient engagement in self-management of health, a key to sustainable preventative healthcare systems. *Lecture Notes of the Institute for Computer Sciences, Social-Informatics and Telecommunications Engineering, LNICST* **247**, 129–137 (2018).

38. Rey, J. *et al.* Towards a common definition of global health. *Lancet* **373**, 1993–1995 (2009).

39. Omidfar, K., Ahmadi, A., Syedmoradi, L., Khoshfetrat, S. M. & Larijani, B. Point-of-care biosensors in medicine: a brief overview of our achievements in this field based on the conducted research in EMRI (endocrinology and metabolism research Institute of Tehran University of medical sciences) over the past fourteen years. *J Diabetes Metab Disord* 1–5 (2020).

40. Kaushik, A. & Mujawar, M. A. Point of Care Sensing Devices: Better Care for Everyone. *Sensors* **18**, 4303 (2018).

41. Turner, A. P. F. Biosensors: Sense and sensibility. *Chem Soc Rev* **42**, 3184–3196 (2013).

42. Mohanty, S. P. & Koucianos, E. Biosensors: A tutorial review. *IEEE Potentials* **25**, 35–40 (2006).

43. Grady, P. A. & Gough, L. L. Self-Management: A Comprehensive Approach to Management of Chronic Conditions. *Am J Public Health* **104**, e25 (2014).

44. Nayak, S., Blumenfeld, N. R., Laksanasopin, T. & Sia, S. K. Point-of-care diagnostics: Recent developments in a connected age. *Anal Chem* **89,** 102–123 (2016).

45. Kosack, C. S., Page, A. L. & Klatser, P. R. A guide to aid the selection of diagnostic tests. *Bull World Health Organ* **95**, 639–645 (2017).

46. Syedmoradi, L. *et al.* Point of care testing: The impact of nanotechnology. *Biosens Bioelectron* **87**, 373–387 (2017).

47. Mabey, D., Peeling, R. W., Ustianowski, A. & Perkins, M. D. Diagnostics for the developing world. *Nat Rev Microbiol* **2**, 231–240 (2004).

48. Nayak, S., Blumenfeld, N. R., Laksanasopin, T. & Sia, S. K. Point-of-Care Diagnostics: Recent Developments in a Connected Age. *Anal Chem* **89**, 102–123 (2017).

49. Ronkainen, N. J., Halsall, H. B. & Heineman, W. R. Electrochemical biosensors. *Chem Soc Rev* **39**, 1747–1763 (2010).

50. Rakotosamimanana, N. *et al.* GeneXpert for the diagnosis of COVID-19 in LMICs. *Lancet Glob Health* **8**, e1457–e1458 (2020).

51. Peto, T. *et al.* COVID-19: Rapid antigen detection for SARS-CoV-2 by lateral flow assay: A national systematic evaluation of sensitivity and specificity for mass-testing. *eClinicalMedicine* **36**, 100924 (2021).

52. Ding, X., Srinivasan, B. & Tung, S. Development and Applications of Portable Biosensors. *J Lab Autom* **20**, 365–389 (2015).

53. Sandbhor Gaikwad, P. & Banerjee, R. Advances in point-of-care diagnostic devices in cancers. *Analyst* **143**, 1326–1348 (2018).

54. Manocha, A. & Bhargava, S. Emerging challenges in point-of-care testing. *Curr Med Res Pract* **9**, 227–230 (2019).

55. Sher, M., Zhuang, R., Demirci, U. & Asghar, W. Paper-based analytical devices for clinical diagnosis: recent advances in the fabrication techniques and sensing mechanisms. *Expert Rev Mol Diagn* **17**, 351–366 (2017).

56. Wang, S. Q., Chinnasamy, T., Lifson, M. A., Inci, F. & Demirci, U. Flexible Substrate-Based Devices for Point-of-Care Diagnostics. *Trends Biotechnol* **34**, 909–921 (2016).

57. Harpaz, D., Eltzov, E., Seet, R. C. S., Marks, R. S. & Tok, A. I. Y. Point-of-care-testing in acute stroke management: An unmet need ripe for technological Harvest. *Biosensors* **7**, 30 (2017).

58. Sun, A. C. & Hall, D. A. Point-of-Care Smartphone-based Electrochemical Biosensing. *Electroanalysis* **31**, 2–16 (2019).

59. Altintas, Z., Akgun, M., Kokturk, G. & Uludag, Y. A fully automated microfluidic-based electrochemical sensor for real-time bacteria detection. *Biosens Bioelectron* **100**, 541–548 (2018).

60. Wang, J. Electrochemical biosensors: Towards point-of-care cancer diagnostics. in *Biosens Bioelectron* **21**, 1887–1892 (2006).

61. Ding, X., Srinivasan, B. & Tung, S. Development and Applications of Portable Biosensors. *J Lab Autom* **20**, 365–389 (2015).

62. Scott, A., Sakib, S., Saha, S., Zhitomirsky, I. & Soleymani, L. A portable and smartphone-operated photoelectrochemical reader for point-of-care biosensing. *Electrochim Acta* **419**, 140347 (2022).

63. Hao, N., Hua, R., Zhang, K., Lu, J. & Wang, K. A Sunlight Powered Portable Photoelectrochemical Biosensor Based on a Potentiometric Resolve Ratiometric Principle. *Anal Chem* **90**, 13207–13211 (2018).

64. Victorious, A., Saha, S., Pandey, R., Didar, T. F. & Soleymani, L. Affinity-Based Detection of Biomolecules Using Photo-Electrochemical Readout. *Front Chem* **7**, 617 (2019).

65. He, L. *et al.* Current signal amplification strategies in aptamer-based electrochemical biosensor: A review. *Chin Chem Lett* **32**, 1593–1602 (2021).

66. Giljohann, D. A. & Mirkin, C. A. Drivers of biodiagnostic development. *Nature* **462,** 461–464 (2009).

67. Syedmoradi, L. *et al.* Point of care testing: The impact of nanotechnology. *Biosens Bioelectron* **87**, 373–387 (2017).

68. Shrivastava, S., Trung, T. Q. & Lee, N. E. Recent progress, challenges, and prospects of fully integrated mobile and wearable point-of-care testing systems for self-testing. *Chem Soc Rev* **49**, 1812–1866 (2020).

69. Wang, S. *et al.* Advances in addressing technical challenges of point-of-care diagnostics in resource-limited settings. *Expert Rev Mol Diagn* **16**, 449–459 (2016).

70. Fan, B. *et al.* Photoelectrochemical Biosensor for Sensitive Detection of Soluble CD44 Based on the Facile Construction of a Poly(ethylene glycol)/Hyaluronic Acid Hybrid Antifouling Interface. *ACS Appl Mater Interfaces* **11**, 24764–24770 (2019).

71. Sabaté del Río, J., Henry, O. Y. F., Jolly, P. & Ingber, D. E. An antifouling coating that enables affinity-based electrochemical biosensing in complex biological fluids. *Nat Nanotechnol* **14**, 1143–1149 (2019).

72. Li, Y. *et al.* Impact of anti-biofouling surface coatings on the properties of nanomaterials and their biomedical applications. *J Mater Chem B* **6**, 9–24 (2017).

73. Pang, J., Chia, P. Y., Lye, D. C. & Leo, Y. S. Progress and challenges towards pointof-care diagnostic development for dengue. *J Clin Microbiol* **55** 3339–3349 (2017).

74. Chan, V., Graves, D. J. & McKenzie, S. E. The biophysics of DNA hybridization with immobilized oligonucleotide probes. *Biophys J* **69**, 2243–2255 (1995).

75. Squires, T. M., Messinger, R. J. & Manalis, S. R. Making it stick: Convection, reaction and diffusion in surface-based biosensors. *Nat Biotechnol* **26**, 417–426 (2008).

76. Pashchenko, O., Shelby, T., Banerjee, T. & Santra, S. A Comparison of Optical, Electrochemical, Magnetic, and Colorimetric Point-of-Care Biosensors for Infectious Disease Diagnosis. *ACS Infect Dis* **4**, 1162–1178 (2018).

77. Piriya V.S, A. *et al.* Colorimetric sensors for rapid detection of various analytes. *Mater Sci Eng C* **78**, 1231–1245 (2017).

78. Thiha, A. & Ibrahim, F. A colorimetric Enzyme-Linked Immunosorbent Assay (ELISA) detection platform for a point-of-care dengue detection system on a lab-on-compact-disc. *Sensors* **15**, 11431–11441 (2015).

79. Li, R., Liu, Q., Jin, Y. & Li, B. Sensitive colorimetric determination of microRNA let-7a through rolling circle amplification and a peroxidase-mimicking system composed of trimeric G-triplex and hemin DNAzyme. *Microchim Acta* **187**, 139 (2020).

80. Špačková, B., Wrobel, P., Bocková, M. & Homola, J. Optical Biosensors Based on Plasmonic Nanostructures: A Review. *Proc IEEE* **104**, 2380–2408 (2016).

81. Damborský, P., Švitel, J. & Katrlík, J. Optical biosensors. *Essays Biochem* **60**, 91–100 (2016).

82. Khlebtsov, N. G. & Dykman, L. A. Optical properties and biomedical applications of plasmonic nanoparticles. *J Quant Spectrosc Radiat Transf* **111**, 1–35 (2010).

83. Ramanathan, K. & Danielsson, B. Principles and applications of thermal biosensors. *Biosens Bioelectron* **16**, 417–423 (2001).

84. Mosbach, K. Thermal biosensors. *Biosens Bioelectron* **6**, 179–182 (1991).

85. Haun, J. B., Yoon, T. J., Lee, H. & Weissleder, R. Magnetic nanoparticle biosensors. *Wiley Interdiscip Rev Nanomed Nanobiotechnol* **2**, 291–304 (2010).

86. Rocha-Santos, T. A. P. Sensors and biosensors based on magnetic nanoparticles. *Trends Analyt Chemi* **62**, 28–36 (2014).

87. Pohanka, M. The Piezoelectric Biosensors: Principles and Applications, a Review. *Int. J. Electrochem. Sci* **12**, 496–506 (2017).

88. Pohanka, M. Overview of piezoelectric biosensors, immunosensors and DNA sensors and their applications. *Materials* **11**, 448 (2018).

89. Yildiz, H. B., Freeman, R., Gill, R. & Willner, I. Electrochemical, photoelectrochemical, and piezoelectric analysis of tyrosinase activity by functionalized nanoparticles. *Anal Chem* **80**, 2811–2816 (2008).

90. Cesewski, E. & Johnson, B. N. Electrochemical biosensors for pathogen detection. *Biosens Bioelectron* **159**, 112214 (2020).

91. Bard, A. J., Faulkner, L. R. & White, H. S. *Electrochemical methods: Fundamentals and applications*. (John Wiley & Sons, Inc, 2022).

92. Salacinski, A. J., Alford, M., Drevets, K., Hart, S. & Hunt, B. E. Validity and reliability of a glucometer against industry reference standards. *J Diabetes Sci Technol* **8**, 95–99 (2014).

93. Connelly, N. R., Magee, M. & Kiessling, B. The use of the Istat portable analyzer in patients undergoing cardiopulmonary bypass. *J Clin Monit* **12,** 311–315 (1996).

94. Devadoss, A., Sudhagar, P., Terashima, C., Nakata, K. & Fujishima, A. Photoelectrochemical biosensors: New insights into promising photoelectrodes and signal amplification strategies. *J Photochem Photobiol C Photochemi Rev* **24**, 43–63 (2015).

95. Grätzel, M. Photoelectrochemical cells. *Solar Energy Conversion and Storage: Photochemical Modes* **414**, 29–53 (2015).

96. Zhao, W.-W., Xu, J.-J. & Chen, H.-Y. Photoelectrochemical DNA Biosensors. *Chem Rev* **114**, 7421–7441 (2014).

97. Zhao, W. W., Xu, J. J. & Chen, H. Y. Photoelectrochemical Immunoassays. *Anal Chem* **90**, 615–627 (2018).

98. Sakib, S., Hosseini, A., Zhitomirsky, I. & Soleymani, L. Photoelectrochemical IL-6 Immunoassay Manufactured on Multifunctional Catecholate-Modified TiO_2 Scaffolds. *ACS Appl Mater Interfaces* **13**, 50851–50861 (2021).

99. Hodes, G. Photoelectrochemical cell measurements: Getting the basics right. *J Phys Chem Lett* **3**, 1208–1213 (2012).

100. Ge, L., Liu, Q., Hao, N. & Kun, W. Recent developments of photoelectrochemical biosensors for food analysis. *J Mater Chem B* **7**, 7283–7300 (2019).

101. Tryk, D., Fujishima, A., Honda, K. Recent topics in photoelectrochemistry: achievements and future prospects. *Electrochim Acta* **45**, 236 (2000).

102. Nozik, A. J. & Memming, R. Physical Chemistry of semiconductor−liquid interfaces. *J Phys Chem* **100,** 13061–13078 (1996).

103. Chen, K., Bell, A. T. & Iglesia, E. The relationship between the electronic and redox properties of dispersed metal oxides and their turnover rates in oxidative dehydrogenation reactions. *J Catal* **209**, 35–42 (2002).

104. Soleymani, L. & Li, F. Mechanistic Challenges and Advantages of Biosensor Miniaturization into the Nanoscale. *ACS Sensors* **2**, 458–467 (2017).

105. Imani, S. M. *et al.* Hierarchical Structures, with Submillimeter Patterns, Micrometer Wrinkles, and Nanoscale Decorations, Suppress Biofouling and Enable Rapid Droplet Digitization. *Small* **16**, 2004886 (2020).

106. Sun, B. & Barnard, A. S. The impact of size and shape distributions on the electron charge transfer properties of silver nanoparticles. *Nanoscale* **9**, 12698–12708 (2017).

107. Qiu, Z. & Tang, D. Nanostructure-based photoelectrochemical sensing platforms for biomedical applications. *J Mater Chem B* **8**, 2541–2561 (2020).

108. Gergeroglu, H., Yildirim, S. & Ebeoglugil, M. F. Nano-carbons in biosensor applications: an overview of carbon nanotubes (CNTs) and fullerenes (C60). *SN Appl Sci* **2**, (2020).

109. Zang, Y., Lei, J. & Ju, H. Principles and applications of photoelectrochemical sensing strategies based on biofunctionalized nanostructures. *Biosens Bioelectron* **96**, 8–16 (2017).

110. Mendes, P. M. Stimuli-responsive surfaces for bio-applications. *Chem Soc Rev* **37**, 2512–2529 (2008).

111. Li, D. *et al.* Surface Functionalization, Bioanalysis, and Applications: Progress of New Magnetoelastic Biosensors. *Adv Eng Mater* **24**, 2101216 (2022).

112. Jiang, Y. & Tian, B. Inorganic semiconductor biointerfaces. *Nat Rev Mater* **3**, 473–490 (2018).

113. Yao, W. T. & Yu, S. H. Synthesis of semiconducting functional materials in solution: From II-VI semiconductor to inorganic-organic hybrid semiconductor nanomaterials. *Adv Funct Mater* **18**, 3357–3366 (2008).

114. Devan, R. S., Patil, R. A., Lin, J. H. & Ma, Y. R. One-dimensional metal-oxide nanostructures: Recent developments in synthesis, characterization, and applications. *Adv Funct Mater* **22**, 3326–3370 (2012).

115. Nelson, J. Organic photovoltaic films. *Mater Today* **5,** 20–27 (2002).

116. Chen, F. C. Organic Semiconductors. *Encyclopedia of Modern Optics* **1–5**, 220–231 (2018).

117. Da, H., Liu, H., Zheng, Y., Yuan, R. & Chai, Y. A highly sensitive VEGF165 photoelectrochemical biosensor fabricated by assembly of aptamer bridged DNA networks. *Biosens Bioelectron* **101**, 213–218 (2018).

118. Shi, X. M. *et al.* Energy Transfer between Semiconducting Polymer Dots and Gold Nanoparticles in a Photoelectrochemical System: A Case Application for Cathodic Bioanalysis. *Anal Chem* **90**, 4277–4281 (2018).

119. Nelson, J. Organic photovoltaic films. *Mater Today* **5,** 20–27 (2002).

120. Imani, S. M. *et al.* Hierarchical Structures, with Submillimeter Patterns, Micrometer Wrinkles, and Nanoscale Decorations, Suppress Biofouling and Enable Rapid Droplet Digitization. *Small* **16**, 2004886 (2020).

121. Feng, J. *et al.* Ultrasensitive Double-Channel Microfluidic Biosensor-Based Cathodic Photo-electrochemical Analysis via Signal Amplification of SOD-Au@PANI for Cardiac Troponin i Detection. *Anal Chem* **93**, 14196–14203 (2021).

122. Sakib, S., Bakhshandeh, F., Saha, S., Soleymani, L. & Zhitomirsky, I. Surface Functionalization of Metal Oxide Semiconductors with Catechol Ligands for Enhancing Their Photoactivity. *Solar RRL* **5**, 2100512 (2021).

123. Kus, M. *et al.* Synthesis of nanoparticles. in *Handbook of Nanomaterials for Industrial Applications* 392–429 (Elsevier, 2018). doi:10.1016/B978-0-12-813351-4.00025-0.

124. Dyer-Smith, C. & Nelson, J. Organic Solar Cells. in *Practical Handbook of Photovoltaics* 543–569 (Elsevier Ltd, 2012). doi:10.1016/B978-0-12-385934-1.00016-7.

125. Sarkar, S. *et al.* Dual-sensitization via electron and energy harvesting in CdTe quantum dots decorated ZnO nanorod-based dye-sensitized solar cells. *J Phys Chem C* **116**, 14248–14256 (2012).

126. Jiang, Y. *et al.* Effective TiO2 hybrid heterostructure fabricated on nano mesoporous phenolic resol for visible-light photocatalysis. *J Mater Chem* **22**, 23642–23649 (2012).

127. Brolo, A. G. Plasmonics for future biosensors. *Nat Photonics* **6**, 709–713 (2012).

128. Clavero, C. Plasmon-induced hot-electron generation at nanoparticle/metal-oxide interfaces for photovoltaic and photocatalytic devices. *Nat Photonics* **8**, 95–103 (2014).

129. Scanlon, D. O. *et al.* Band alignment of rutile and anatase TiO_2. *Nat Mater* **12**, 798–801 (2013).

130. Song, J., Song, X., Ling, T., Du, X. & Qiao, S. Z. Enhancing the Conversion Efficiency of Semiconductor Sensitized Solar Cells via the Cosensitization of Dual-Sized Quantum Dots. *Ind Eng Chem Res* **51**, 10074–10078 (2012).

131. Hernández, S. *et al.* Comparison of photocatalytic and transport properties of TiO_2 and ZnO nanostructures for solar-driven water splitting. *Physical Chemistry Chemical Physics* **17**, 7775–7786 (2015).

132. Ni, M., Leung, M. K. H., Leung, D. Y. C. & Sumathy, K. A review and recent developments in photocatalytic water-splitting using TiO2 for hydrogen production. *Renew Sust Energ Rev* **11**, 401–425 (2007).

133. Devadoss, A., Sudhagar, P., Terashima, C., Nakata, K. & Fujishima, A. Photoelectrochemical biosensors: New insights into promising photoelectrodes and signal amplification strategies. *J Photochem Photobiol C Photochem Rev* **24**, 43–63 (2015).

134. Zhao, W. W., Xu, J. J. & Chen, H. Y. Photoelectrochemical DNA biosensors. *Chem Rev* **114**, 7421–7441 (2014).

135. Holzinger, M., Goff, A. le & Cosnier, S. Nanomaterials for biosensing applications: A review. *Front Chem* **2**, 63 (2014).

136. Yu, Y. *et al.* The design of TiO_2 nanostructures (nanoparticle, nanotube, and nanosheet) and their photocatalytic activity. *J Phys Chem C* **118**, 12727–12733 (2014).

137. Fujishima, A., Rao, T. N. & Tryk, D. A. Titanium dioxide photocatalysts. *J Photochem Photobiol C Photochem* **1**, 1–21 (2000).

138. Thanh, N. T. K. & Green, L. A. W. Functionalisation of nanoparticles for biomedical applications. *Nano Today* **5**, 213–230 (2010).

139. Beltrán Lopez, A. P. DNA Biosensors and Biomarkers to Cancer Detection. *Int J Biosens Bioelectron* **4**, 20–21 (2018).

140. Chikkaveeraiah, B. v., Bhirde, A. A., Morgan, N. Y., Eden, H. S. & Chen, X. Electrochemical immunosensors for detection of cancer protein biomarkers. *ACS Nano* **6**, 6546–6561 (2012).

141. Tribolet, L. *et al.* MicroRNA Biomarkers for Infectious Diseases: From Basic Research to Biosensing. *Front Microbiol* **11**, 1197 (2020).

142. Adams, S. D., Doeven, E. H., Quayle, K. & Kouzani, A. Z. MiniStat: Development and Evaluation of a Mini-Potentiostat for Electrochemical Measurements. *IEEE Access* (2019) doi:10.1109/ACCESS.2019.2902575.

143. Gong, J., Liang, J. & Sumathy, K. Review on dye-sensitized solar cells (DSSCs): Fundamental concepts and novel materials. *Renewable and Sustainable Energy Reviews* vol. 16 5848–5860 Preprint at https://doi.org/10.1016/j.rser.2012.04.044 (2012).

144. Ismail, A. A. & Bahnemann, D. W. Photochemical splitting of water for hydrogen production by photocatalysis: A review. *Solar Energy Materials and Solar Cells* vol. 128 85–101 Preprint at https://doi.org/10.1016/j.solmat.2014.04.037 (2014).

145. Lee, J. *et al.* Direct access to thermally stable and highly crystalline mesoporous transition-metal oxides with uniform pores. *Nat Mater* **7**, 222–228 (2008).

146. Bolink, H. J., Coronado, E., Orozco, J. & Sessolo, M. Efficient polymer light-emitting diode using air-stable metal oxides as electrodes. *Adv Mater* **21**, 79–82 (2009).

147. Miyauchi, M., Nakajima, A., Fujishima, A., Hashimoto, K. & Watanabe, T. Photoinduced surface reaction on TiO2 and SrTiO3 films: Photocatalytic oxidation and photoinduced hydrophilicity. *Chem Mater* **12**, 3–5 (2000).

148. Kröger, M. *et al.* P-type doping of organic wide band gap materials by transition metal oxides: A case-study on Molybdenum trioxide. *Org Electron* **10**, 932–938 (2009).

149. Emeline, A. v. *et al.* Effect of surface photoreactions on the photocoloration of a wide band gap metal oxide: Probing whether surface reactions are photocatalytic. *J Phys Chem B* **109**, 5175–5185 (2005).

150. Sysoev, V. v., Button, B. K., Wepsiec, K., Dmitriev, S. & Kolmakov, A. Toward the nanoscopic 'electronic nose': Hydrogen vs carbon monoxide discrimination with an array of individual metal oxide nano- and mesowire sensors. *Nano Lett* **6**, 1584–1588 (2006).

151. Zhu, M., Zhang, Z. & Miao, W. Intense photoluminescence from amorphous tantalum oxide films. *Appl Phys Lett* **89**, 021915 (2006).

152. Dev, A. *et al.* Enhancement of the near-band-edge photoluminescence of ZnO nanowires: Important role of hydrogen incorporation versus plasmon resonances. *Appl Phys Lett* **98**, (2011).

153. Karthik, P. *et al.* A visible-light active catechol-metal oxide carbonaceous polymeric material for enhanced photocatalytic activity. *J Mater Chem A Mater* **5**, 384–396 (2017).

154. Concina, I. & Vomiero, A. Metal oxide semiconductors for dye- and quantum-dot-sensitized solar cells. *Small* **11**, 1744–1774 (2015).

155. Liu, A. Towards development of chemosensors and biosensors with metal-oxide-based nanowires or nanotubes. *Biosens Bioelectron* **24**, 167–177 (2008).

156. Zhang, L. *et al.* Small-molecule surface-modified bismuth-based semiconductors as a new class of visible-light-driven photocatalytic materials: Structure-dependent photocatalytic properties and photosensitization mechanism. *Chem Eng J* **380**, 122546 (2020).

157. Džunuzović, E. S. *et al.* Influence of surface modified TiO_2 nanoparticles by gallates on the properties of PMMA/TiO_2 nanocomposites. *Eur Polym J* **48**, 1385–1393 (2012).

158. Kawaguti, C. A., Santilli, C. v. & Pulcinelli, S. H. Effect of the surfactant nature on the thermo-stability of surface modified SnO_2 nanoparticles. *J Non Cryst Solids* **354**, 4790–4794 (2008).

159. Abugazleh, M. K., Rougeau, B. & Ali, H. Adsorption of catechol and hydroquinone on titanium oxide and iron (III) oxide. *J Environ Chem Eng* **8**, 104180 (2020).

160. Li, Y.-H., Li, J.-Y. & Xu, Y.-J. Bimetallic nanoparticles as cocatalysts for versatile photoredox catalysis. *EnergyChem* **3**, 100047 (2021).

161. Zhang, N., Yang, M.-Q., Liu, S., Sun, Y. & Xu, Y.-J. Waltzing with the Versatile Platform of Graphene to Synthesize Composite Photocatalysts. *Chem Rev* **115**, 10307–10377 (2015).

162. Tvrdy, K., Frantsuzov, P. A. & Kamat, P. v. Photoinduced electron transfer from semiconductor quantum dots to metal oxide nanoparticles. *Proc Natl Acad Sci U S A* **108**, 29–34 (2011).

163. ben Saber, N., Mezni, A., Alrooqi, A. & Altalhi, T. A review of ternary nanostructures based noble metal/semiconductor for environmental and renewable energy applications. *J Mater Res Tech* **9**, 15233–15262 (2020).

164. Hod, I. & Zaban, A. Materials and interfaces in quantum dot sensitized solar cells: Challenges, advances and prospects. *Langmuir* **30**, 7264–7273 (2014).

165. Sharma, K., Sharma, V. & Sharma, S. S. Dye-Sensitized Solar Cells: Fundamentals and Current Status. *Nanoscale Res Lett* **13**, (2018).

166. Wu, C., Chen, B., Zheng, X. & Priya, S. Scaling of the flexible dye sensitized solar cell module. *Sol Energy Maters Sol Cells* **157**, 438–446 (2016).

167. Chen, X., Zhou, P., Yan, H. & Chen, M. Systematically investigating solar absorption performance of plasmonic nanoparticles. *Energy* **216**, 119254 (2021).

168. Rajh, T. *et al.* Surface restructuring of nanoparticles: An efficient route for ligand-metal oxide crosstalk. *J Phys Chem B* **106**, 10543–10552 (2002).

169. Janković, I. A., Šaponjić, Z. v., Čomor, M. I. & Nedeljkovic, J. M. Surface modification of colloidal tiO2 nanoparticles with bidentate benzene derivatives. *J Phys Chem C* **113**, 12645–12652 (2009).

170. Ata, M. S., Liu, Y. & Zhitomirsky, I. A review of new methods of surface chemical modification, dispersion and electrophoretic deposition of metal oxide particles. *RSC Adv* **4**, 22716–22732 (2014).

171. Huang, W. M., Jiang, P., Wei, C. Y., Zhuang, D. K. & Shi, J. Low-temperature one-step synthesis of covalently chelated ZnO/dopamine hybrid nanoparticles and their optical properties. *J Mater Res* **23**, 1946–1952 (2008).

172. Varaganti, S. & Ramakrishna, G. Dynamics of interfacial charge transfer emission in small molecule sensitized TiO2 nanoparticles: Is it localized or delocalized? *Journal of Physical Chemistry C* **114**, 13917–13925 (2010).

173. Orchard, K. L. *et al.* Catechol-TiO_2 hybrids for photocatalytic H2 production and photocathode assembly. *Chem Comm* **53**, 12638–12641 (2017).

174. Rangan, S., Theisen, J. P., Bersch, E. & Bartynski, R. A. Energy level alignment of catechol molecular orbitals on ZnO(110) and TiO2 (110) surfaces. *Appl Surf Sci* **256**, 4829–4833 (2010).

175. Arbouch, I. *et al.* Influence of the nature of the anchoring group on electron injection processes at dye-titania interfaces. *Phys Chem Chem Phys* **19**, 29389–29401 (2017).

176. Fischer, M. J. E. Amine coupling through EDC/NHS: a practical approach. *Methods Mol Biol* **627**, 55–73 (2010).

177. Zhang, X., Li, S., Jin, X. & Li, X. Aptamer based photoelectrochemical cytosensor with layer-by-layer assembly of CdSe semiconductor nanoparticles as photoelectrochemically active species. *Biosens Bioelectron* **26**, 3674–3678 (2011).

178. Wang, R. *et al.* Photoelectrochemical sensitive detection of insulin based on CdS/polydopamine co-sensitized WO3 nanorod and signal amplification of carbon nanotubes@polydopamine. *Biosens Bioelectron* **96**, 345–350 (2017).

179. Gnichwitz, J. F. *et al.* Efficient synthetic access to cationic dendrons and their application for ZnO nanoparticles surface functionalization: New building blocks for dye-sensitized solar cells. *J Am Chem Soc* **132**, 17910–17920 (2010).

180. An, B. K., Hu, W., Burn, P. L. & Meredith, P. New type II catechol-thiophene sensitizers for dye-sensitized solar cells. *J Phys Chem C* **114**, 17964–17974 (2010).

181. Higashimoto, S. Titanium-Dioxide-Based Visible-Light-Sensitive Photocatalysis: Mechanistic Insight and Applications. *Catalysts* **9**, 201 (2019).

182. Peter, L. M. Dynamic aspects of semiconductor photoelectrochemistry. *Chem Rev* **90**, 753–769 (1990).

183. Nozik, A. J. Photoelectrochemistry: application to solar energy conversion. *Ann. Rev. Phys. Chern.* 189–222 (1978).

184. Sánchez-de-Armas, R., San-Miguel, M. A., Oviedo, J. & Sanz, J. F. Direct vs. indirect mechanisms for electron injection in DSSC: Catechol and alizarin. *Comput Theor Chem* **975**, 99–105 (2011).

185. Tachan, Z., Hod, I. & Zaban, A. The TiO_2-catechol complex: Coupling type II sensitization with efficient catalysis of water oxidation. *Adv Energy Mater* **4**, 1301249 (2014).

186. Tae, E. L. *et al.* A strategy to increase the efficiency of the dye-sensitized TiO_2 solar cells operated by photoexcitation of dye-to-TiO_2 charge-transfer bands. *J Phys Chem B* **109**, 22513–22522 (2005).

187. Wu, K., Wang, Y. & Zhitomirsky, I. Electrophoretic deposition of TiO2 and composite TiO2-MnO2 films using benzoic acid and phenolic molecules as charging additives. *J Colloid Interface Sci* **352**, 371–378 (2010).

188. Cheng, F. *et al.* Lyotropic ‘hairy’ TiO2 nanorods. *Nanoscale Adv* **1**, 254–264 (2019).

189. Wang, X., Li, Z., Shi, J. & Yu, Y. One-Dimensional Titanium Dioxide Nanomaterials: Nanowires, Nanorods, and Nanobelts. *Chem Rev* **114**, 9346–9384 (2014).

190. Zander, Z., Yagloski, R., DeCoste, J., Zhang, D. & DeLacy, B. G. One-pot synthesis of high aspect ratio titanium dioxide nanorods using oxalic acid as a complexing agent. *Mater Lett* **163**, 39–42 (2016).

191. Zhang, T., Wojtal, P., Rubel, O. & Zhitomirsky, I. Density functional theory and experimental studies of caffeic acid adsorption on zinc oxide and titanium dioxide nanoparticles. *RSC Adv* **5**, 106877–106885 (2015).

192. Lin, W., Haderlein, M., Walter, J., Peukert, W. & Segets, D. Spectra Library: An Assumption-Free In Situ Method to Access the Kinetics of Catechols Binding to Colloidal ZnO Quantum Dots. *Angew Chem* **128**, 944–947 (2016).

193. Đorđević, V. *et al.* Visible light absorption of surface-modified Al2O3 powders: A comparative DFT and experimental study. *Microporous Mesoporous Mater* **273**, 41–49 (2019).

194. Yu, Z., Zeng, H., Min, X. & Zhu, X. High-performance composite photocatalytic membrane based on titanium dioxide nanowire/graphene oxide for water treatment. *J Appl Polym Sci* **137**, (2020).

195. Gulley-Stahl, H. *et al.* Surface complexation of catechol to metal oxides: An ATR-FTIR, adsorption, and dissolution study. *Environ Sci Technol* **44**, 4116–4121 (2010).

196. Araujo, P. Z., Morando, P. J. & Blesa, M. A. Interaction of catechol and gallic acid with titanium dioxide in aqueous suspensions. 1. Equilibrium studies. *Langmuir* **21**, 3470–3474 (2005).

197. Lana-Villarreal, T., Rodes, A., Pérez, J. M. & Gómez, R. A spectroscopic and electrochemical approach to the study of the interactions and photoinduced electron transfer between catechol and anatase nanoparticles in aqueous solution. *J Am Chem Soc* **127**, 12601–12611 (2005).

198. de La Garza, L., Saponjic, Z. v., Dimitrijevic, N. M., Thurnauer, M. C. & Rajh, T. Surface states of titanium dioxide nanoparticles modified with enediol ligands. *J Phys Chem B* **110**, 680–686 (2006).

199. Li, S. C. *et al.* Correlation between bonding geometry and band gap states at organic-inorganic interfaces: Catechol on rutile TiO_2(110). *J Am Chem Soc* **131**, 980–984 (2009).

200. Syres, K. L. *et al.* Adsorbate-induced modification of surface electronic structure: Pyrocatechol adsorption on the anatase TiO_2 (101) and rutile TiO_2 (110) surfaces. *J Phys Chem C* **116**, 23515–23525 (2012).

201. Li, S. C., Chu, L. N., Gong, X. Q. & Diebold, U. Hydrogen bonding controls the dynamics of catechol adsorbed on a TiO_2(110) surface. *Science (1979)* **328**, 882–884 (2010).

202. Zhang, L., Xu, L. & Li, J. First Principles Study on Structurally Resolved Titanium Dioxide Nanoparticles Functionalized by Organic Ligands. *J Struct Chem* **60**, 671–677 (2019).

203. Savić, T. D. *et al.* The effect of substituents on the surface modification of anatase nanoparticles with catecholate-type ligands: A combined DFT and experimental study. *Phys Chem Chem Phys* **16**, 20796–20805 (2014).

204. Lin, W. *et al.* Influence of Tail Groups during Functionalization of ZnO Nanoparticles on Binding Enthalpies and Photoluminescence. *Langmuir* **33**, 13581–13589 (2017).

205. Deng, X., Huang, Z., Wang, W. & Davé, R. N. Investigation of nanoparticle agglomerates properties using Monte Carlo simulations. *Adv Powder Technol* **27**, 1971–1979 (2016).

206. Wang, W., Banerjee, S., Jia, S., Steigerwald, M. L. & Herman, I. P. Ligand control of growth, morphology, and capping structure of colloidal CdSe nanorods. *Chem Mater* **19**, 2573–2580 (2007).

207. Silva, R. M. E., Poon, R., Milne, J., Syed, A. & Zhitomirsky, I. New developments in liquid-liquid extraction, surface modification and agglomerate-free processing of inorganic particles. *Adv Colloid Interface Sci* **261**, 15–27 (2018).

208. Schindler, T. *et al.* Evolution of the Ligand Shell Around Small ZnO Nanoparticles During the Exchange of Acetate by Catechol: A Small Angle Scattering Study. *ChemNanoMat* **5**, 116–123 (2019).

209. Park, J. Y., Choi, E. S., Baek, M. J. & Lee, G. H. Colloidal stability of amino acid coated magnetite nanoparticles in physiological fluid. *Mater Lett* **63**, 379–381 (2009).

210. Burger, A. *et al.* Layer-by-Layer Assemblies of Catechol-Functionalized TiO_2 Nanoparticles and Porphyrins through Electrostatic Interactions. *Chem Eur J* **21**, 5041–5054 (2015).

211. Geiseler, B. & Fruk, L. Bifunctional catechol based linkers for modification of TiO_2 surfaces. *J Mater Chem* **22**, 735–741 (2012).

212. Lash, T. D. Benziporphyrins, a unique platform for exploring the aromatic characteristics of porphyrinoid systems. *Org Biomol Chem* **13**, 7846–7878 (2015).

213. Kesters, J. *et al.* Porphyrin-Based Bulk Heterojunction Organic Photovoltaics: The Rise of the Colors of Life. *Adv Energy Mater* **5**, 1–20 (2015).

214. Valverde-Aguilar, G. *et al.* Photoconductivity studies on nanoporous TiO2/dopamine films prepared by sol-gel method. *Appl Phys A Mater Sci Process* **116**, 1075–1084 (2014).

215. Janković, I. A., Šaponjić, Z. v., Džunuzović, E. S. & Nedeljković, J. M. New Hybrid Properties of TiO 2 Nanoparticles Surface Modified With Catecholate Type Ligands. *Nanoscale Res Lett* **5**, 81–88 (2010).

216. Connor, P. A., Dobson, K. D. & Mcquillan, A. J. *New Sol-Gel Attenuated Total Reflection Infrared Spectroscopic Method for Analysis of Adsorption at Metal Oxide Surfaces in Aqueous Solutions. Chelation of TiO_2, ZrO_2, and A203 Surfaces by Catechol, 8-Quinolinol, and Acetylacetone*. *Langmuir* **11**, 4193-4195 (1995).

217. Klitsche, F. *et al.* Synthesis of tripodal catecholates and their immobilization on zinc oxide nanoparticles. *Beilstein J Org Chem* **11**, 678–686 (2015).

218. Zeininger, L., Portilla, L., Halik, M. & Hirsch, A. Quantitative Determination and Comparison of the Surface Binding of Phosphonic Acid, Carboxylic Acid, and Catechol Ligands on TiO2Nanoparticles. *Chem Eur J* **22**, 13506–13512 (2016).

219. Bhui, D. K. *et al.* Synthesis and UV-vis spectroscopic study of silver nanoparticles in aqueous SDS solution. *J Mol Liq* **145**, 33–37 (2009).

220. Ahmadi, M., Rad-Moghadam, K. & Hatami, M. Investigation of morphological aspects and thermal properties of ZnO/poly(amide–imide) nanocomposites based on levodopa-mediated diacid monomer. *Polym Bull* **76**, 53–72 (2019).

221. Calzolari, A., Ruini, A. & Catellani, A. Anchor group versus conjugation: Toward the gap-state engineering of functionalized ZnO($10\bar{1}0$) surface for optoelectronic applications. *J Am Chem Soc* **133**, 5893–5899 (2011).

222. Velmurugan, R. & Incharoensakdi, A. Nanoparticles and Organic Matter: Process and Impact. in *Nanomaterials in Plants, Algae, and Microorganisms* vol. 1 407–428 (Elsevier Inc., 2018).

223. Monllor-Satoca, D. & Gómez, R. A photoelectrochemical and spectroscopic study of phenol and catechol oxidation on titanium dioxide nanoporous electrodes. *Electrochim Acta* **55**, 4661–4668 (2010).

224. Dong, Y., Liu, T., Sun, S., Chang, X. & Guo, N. Preparation and characterization of SiO_2/polydopamine/Ag nanocomposites with long-term antibacterial activity. *Ceram Int* **40**, 5605–5609 (2014).

225. Lee, Y. L., Chi, C. F. & Liau, S. Y. CdS/CdSe Co-Sensitized TiO_2 photoelectrode for efficient hydrogen generation in a photoelectrochemical cell. *Chem Mater* **22**, 922–927 (2010).

226. Baker, K., Sikkema, R. & Zhitomirsky, I. Application of bile acids for biomedical devices and sensors. *Med Devices Sens* **3**, 1–9 (2020).

227. Schechtel, E. *et al.* Mixed Ligand Shell Formation upon Catechol Ligand Adsorption on Hydrophobic TiO_2 Nanoparticles. *Langmuir* **35**, 12518–12531 (2019).

228. Anithaa, A. C., Lavanya, N., Asokan, K. & Sekar, C. WO_3 nanoparticles based direct electrochemical dopamine sensor in the presence of ascorbic acid. *Electrochim Acta* **167**, 294–302 (2015).

229. Burger, A., Srikantharajah, R., Peukert, W. & Hirsch, A. Individualization and Stabilization of Zinc Oxide Nanorods by Covalent Functionalization with Positively Charged Catechol Derivatives. *Chem Eur J* **23**, 17257–17268 (2017).

230. Calzolari, A., Ruini, A. & Catellani, A. Surface effects on catechol/semiconductor interfaces. *J Phys Chem C* **116**, 17158–17163 (2012).

231. Das, P. & Reches, M. Revealing the role of catechol moieties in the interactions between peptides and inorganic surfaces. *Nanoscale* **8**, 15309–15316 (2016).

232. Eda, T., Fujisawa, J. I. & Hanaya, M. Inorganic Control of Interfacial Charge-Transfer Transitions in Catechol-Functionalized Titanium Oxides Using $SrTiO_3$, $BaTiO_3$, and TiO_2. *J Phys Chem C* **122**, 16216–16220 (2018).

233. Finkelstein-Shapiro, D. *et al.* Direct Evidence of Chelated Geometry of Catechol on TiO2 by a Combined Solid-State NMR and DFT Study. *J Phys Chem C* **120**, 23625–23630 (2016).

234. Li, X. *et al.* Salicylic acid complexed with TiO2 for visible light-driven selective oxidation of amines into imines with air. *Appl Catal B* **244**, 758–766 (2019).

235. Mowbray, D. J. & Migani, A. Optical Absorption Spectra and Excitons of Dye-Substrate Interfaces: Catechol on TiO_2(110). *J Chem Theory Comput* **12**, 2843–2852 (2016).

236. Murata, Y., Hori, H., Taga, A. & Tada, H. Surface charge-transfer complex formation of catechol on titanium(IV) oxide and the application to bio-sensing. *J Colloid Interface Sci* **458**, 305–309 (2015).

237. Nauth, A. M., Schechtel, E., Dören, R., Tremel, W. & Opatz, T. TiO2 nanoparticles functionalized with non-innocent ligands allow oxidative photocyanation of amines with visible/near-infrared photons. *J Am Chem Soc* **140,** 14169–14177 (2018).

238. Ronchi, C., Datteo, M., Kaviani, M., Selli, D. & di Valentin, C. Unraveling Dynamical and Light Effects on Functionalized Titanium Dioxide Nanoparticles for Bioconjugation. *J Phys Chem C* **123**, 10130–10144 (2019).

239. Ronchi, C., Selli, D., Pipornpong, W. & di Valentin, C. Proton Transfers at a Dopamine-Functionalized TiO_2 Interface. *J Phys Chem C* **123**, 7682–7695 (2019).

240. Sadowski, R., Strus, M., Buchalska, M., Heczko, P. B. & Macyk, W. Visible light induced photocatalytic inactivation of bacteria by modified titanium dioxide films on organic polymers. *Photochem Photobiol Sci* **14**, 514–519 (2015).

241. Sadowski, R., Wach, A., Buchalska, M., Kuśtrowski, P. & Macyk, W. Photosensitized TiO 2 films on polymers – Titania-polymer interactions and visible light induced photoactivity. *Appl Surf Sci* **475**, 710–719 (2019).

242. Savić, T. D. *et al.* Surface modification of anatase nanoparticles with fused ring catecholate type ligands: a combined DFT and experimental study of optical properties. *Nanoscale* **4**, 1612 (2012).

243. Sharker, S. M. *et al.* Functionalized biocompatible WO3 nanoparticles for triggered and targeted in vitro and in vivo photothermal therapy. *J Control Release* **217**, 211–220 (2015).

244. Wang, Y., Hang, K., Anderson, N. A. & Lian, T. Comparison of electron transfer dynamics in molecule-to-nanoparticle and intramolecular charge transfer complexes. *J Phys Chem B* **107**, 9434–9440 (2003).

245. Wang, G. L., Xu, J. J. & Chen, H. Y. Dopamine sensitized nanoporous TiO_2 film on electrodes: Photoelectrochemical sensing of NADH under visible irradiation. *Biosens Bioelectron* **24**, 2494–2498 (2009).

246. Sallem, F., Villatte, L., Geffroy, P. M., Goglio, G. & Pagnoux, C. Surface modification of titania nanoparticles by catechol derivative molecules: Preparation of concentrated suspensions. *Colloids Surf A Physicochem Eng Asp* **602**, 125167 (2020).

247. Ahmadi, M., Monji, D. & Taromi, F. A. Bio-inspired surface modification of iron oxide nanoparticles for active stabilization in hydrogels. *Soft Matter* **17**, 955–964 (2021).

248. Zhang, B., Zou, W. & Zhang, J. In situ surface modification of colloidal TiO2 nanoparticles with catechol. *Research on Chemical Intermediates* **41**, 3157–3170 (2015).

249. Paramasivam, I., Jha, H., Liu, N. & Schmuki, P. A review of photocatalysis using self-organized TiO_2 nanotubes and other ordered oxide nanostructures. *Small* **8**, 3073–3103 (2012).

250. Hou, W. & Cronin, S. B. A review of surface plasmon resonance-enhanced photocatalysis. *Adv Funct Mater* **23**, 1612–1619 (2013).

251. Reddy, C. V. *et al.* Hetero-nanostructured metal oxide-based hybrid photocatalysts for enhanced photoelectrochemical water splitting – a review. *Int J Hydrog Energy* **45,** 18331–18347 (2020).

252. Zhang, J. Z. & Noguez, C. Plasmonic optical properties and applications of metal nanostructures. *Plasmonics* **3**, 127–150 (2008).

253. Saha, S., Chan, Y. & Soleymani, L. Enhancing the Photoelectrochemical Response of DNA Biosensors Using Wrinkled Interfaces. *ACS Appl Mater Interfaces* **10**, 31178–31185 (2018).

254. Finkelstein-Shapiro, D. *et al.* CO_2 preactivation in photoinduced reduction via surface functionalization of TiO2 nanoparticles. *J Phys Chem Lett* **4**, 475–479 (2013).

255. Karimi-maleh, H., Tahernejad-javazmi, F. & Kumar, V. A novel biosensor for liquid phase determination of glutathione and amoxicillin in biological and pharmaceutical samples using a ZnO / CNTs nanocomposite / catechol derivative modified electrode. *J Mol Liq* **196**, 258–263 (2014).

256. Han, C. *et al.* Surface/Interface Engineering of Carbon-Based Materials for Constructing Multidimensional Functional Hybrids. *Solar RRL* **4**, 1–25 (2020).

257. Li, S. H., Qi, M. Y., Tang, Z. R. & Xu, Y. J. Nanostructured metal phosphides: From controllable synthesis to sustainable catalysis. *Chem Soc Rev* **50**, 7539–7586 (2021).

258. Adineh, M., Tahay, P., Ameri, M., Safari, N. & Mohajerani, E. Fabrication and analysis of dye-sensitized solar cells (DSSCs) using porphyrin dyes with catechol anchoring group. *RCS Advances* **6**, 14512–14521 (2016).

259. Liu, J., Wang, Y. & Sun, D. Enhancing the performance of dye-sensitized solar cells by benzoic acid modified TiO2 nanorod electrode. *Renew Energy* **38**, 214–218 (2012).

260. Richhariya, G., Kumar, A., Tekasakul, P. & Gupta, B. Natural dyes for dye sensitized solar cell: A review. *Renew Sust Energ Rev* **69**, 705–718 (2017).

261. Sima, C., Grigoriu, C. & Antohe, S. Comparison of the dye-sensitized solar cells performances based on transparent conductive ITO and FTO. *Thin Solid Films* **519**, 595–597 (2010).

262. Hagfeldt, A. & Grätzel, M. Molecular photovoltaics. *Acc Chem Res* **33**, 269–277 (2000).

263. Ullah, N., Shah, S. M., Hussain, H., Ansir, R. & Hussain, M. N. Pyrocatechol violet sensitized Ho-TiO_2/ZnO nanostructured material: As photoanode for dye sensitized solar cells. *Mater Res Express* **7**, 35003 (2020).

264. Ding, C., Li, H., Li, X. & Zhang, S. A new strategy of photoelectrochemical analysis without an external light source based on isoluminol chemiluminescence probe. *Chem Comm* **46**, 7990–7992 (2010).

265. Abolhasan, R., Mehdizadeh, A., Rashidi, M. R., Aghebati-Maleki, L. & Yousefi, M. Application of hairpin DNA-based biosensors with various signal amplification strategies in clinical diagnosis. *Biosens Bioelectron* **129**, 164–174 (2019).

266. Krishnan, S. K., Singh, E., Singh, P., Meyyappan, M. & Nalwa, H. S. A review on graphene-based nanocomposites for electrochemical and fluorescent biosensors. *RSC Advances* **9**, 8778–8781 (2019).

267. Sai-Anand, G. *et al.* Recent progress on the sensing of pathogenic bacteria using advanced nanostructures. *Bull Chem Soc Jpn* **92**, 216–244 (2019).

268. Drummond, T. G., Hill, M. G. & Barton, J. K. Electrochemical DNA sensors. *Nature Biotechnology* **21**, 1192–1199 (2003).

269. Lu, W., Jin, Y., Wang, G., Chen, D. & Li, J. Enhanced photoelectrochemical method for linear DNA hybridization detection using Au-nanopaticle labeled DNA as probe onto titanium dioxide electrode. *Biosens Bioelectron* **23**, 1534–1539 (2008).

270. Zhou, W. J., Halpern, A. R., Seefeld, T. H. & Corn, R. M. Near infrared surface plasmon resonance phase imaging and nanoparticle-enhanced surface plasmon resonance phase imaging for ultrasensitive protein and DNA biosensing with oligonucleotide and aptamer microarrays. *Anal Chem* **84**, 440–445 (2012).

271. Marie, R., Jensenius, H., Thaysen, J., Christensen, C. B. & Boisen, A. Adsorption Kinetics and mechanical properties of thiol-modified DNA-oligos on gold investigated by microcantilever sensors. *Ultramicroscopy* **91,** 29–36 (2002).

272. Shen, S. *et al.* Titanium dioxide nanostructures for photoelectrochemical applications. *Prog Mater Sci* **98**, 299–385 (2018).

273. Abdullah, H., Khan, M. M. R., Ong, H. R. & Yaakob, Z. Modified TiO_2 photocatalyst for CO_2 photocatalytic reduction: An overview. *J CO_2 Util* 22, 15–32 (2017).

274. Yan, P. *et al.* Photoelectrochemical water splitting promoted with a disordered surface layer created by electrochemical reduction. *ACS Appl Mater Interfaces* **7**, 3791–3796 (2015).

275. Li, S. *et al.* 'Signal-off' photoelectrochemical DNA sensing strategy based on target dependent DNA probe conformational conversion using CdS quantum dots sensitized TiO2 nanorods array as photoactive material. *J Electroanal Chem* **759**, 38–45 (2015).

276. Kumar, S. G. & Rao, K. S. R. K. Comparison of modification strategies towards enhanced charge carrier separation and photocatalytic degradation activity of metal oxide semiconductors (TiO_2, WO_3 and ZnO). *Appl Surf Sci* **391**, 124–148 (2017).

277. Verma, S., Ghosh, A., Das, A. & Ghosh, H. N. Exciton-coupled charge-transfer dynamics in a porphyrin J-aggregate/TiO_2 complex. *Chem Eur J* **17**, 3458–3464 (2011).

278. Valverde-Aguilar, G. *et al.* Photoconductivity studies on nanoporous TiO2/dopamine films prepared by sol-gel method. *Appl Phys A Mater Sci Process* **116**, 1075–1084 (2014).

279. Wang, G. L., Xu, J. J. & Chen, H. Y. Dopamine sensitized nanoporous TiO2 film on electrodes: Photoelectrochemical sensing of NADH under visible irradiation. *Biosens Bioelectron* **24**, 2494–2498 (2009).

280. Tunesi, S. & Anderson, M. A. Surface effects in photochemistry: An in situ cylindrical internal reflection-fourier transform infrared investigation of the effect of ring substituents on chemisorption onto Titania ceramic membranes. *Langmuir* **8,** 487–495 (1992).

281. Barreto, W. J., Ando, R. A., Estevão, B. M. & Zanoni, K. P. D. S. Adsorption of caffeic acid on titanium dioxide: A spectroscopic study. *Spectrochim Acta A Mol Biomol Spectrosc* **92**, 16–20 (2012).

282. Chong, D., Wan, X. & Zhang, J. Charge-transfer complexes of dinuclear ruthenium compounds/polyoxometalates for multistate electrochromism covering ultraviolet, visible, and near-infrared region. *J Mater Chem C Mater* **5**, 6442–6449 (2017).

283. Liu, Y., Dadap, J. I., Zimdars, D. & Eisenthal, K. B. Study of interfacial charge-transfer complex on TiO_2 particles in aqueous suspension by second-harmonic generation. *J Phys Chem B* **103**, 2480–2486 (1999).

284. Li, Y., Wu, K. & Zhitomirsky, I. Electrodeposition of composite zinc oxide-chitosan films. *Colloids Surf A Physicochem Eng Asp* **356**, 63–70 (2010).

285. Belay, A., Kim, H. K. & Hwang, Y. H. Binding of caffeine with caffeic acid and chlorogenic acid using fluorescence quenching, UV/vis and FTIR spectroscopic techniques. *Luminescence* **31**, 565–572 (2016).

286. Fan, D. *et al.* An ultrasensitive label-free immunosensor based on CdS sensitized Fe-TiO_2 with high visible-light photoelectrochemical activity. *Biosens Bioelectron* **74**, 843–848 (2015).

287. Morris, A. J. & Meyer, G. J. TiO2 surface functionalization to control the density of states. *J Phys Chem C* **112**, 18224–18231 (2008).

288. Peng, H., Zhang, L., Kjällman, T. H. M., Soeller, C. & Travas-Sejdic, J. DNA hybridization detection with blue luminescent quantum dots and dye-labeled single-stranded DNA. *J Am Chem Soc* **129**, 3048–3049 (2007).

289. Yan, K., Liu, Y., Yang, Y. & Zhang, J. A Cathodic 'signal-off' Photoelectrochemical Aptasensor for Ultrasensitive and Selective Detection of Oxytetracycline. *Anal Chem* **87**, 12215–12220 (2015).

290. Galasso, K., Livache, T., Roget, A. & Vieil, E. Electrogravimetric detection of DNA hybridization on polypyrrole copolymer. *Journal de Chimie Physique et de Physico-Chimie Biologique* **95,** 1514–1517 (1998).

291. Contreras-Naranjo, J. & Aguilar, O. Suppressing non-specific binding of proteins onto electrode surfaces in the development of Electrochemical Immunosensors. *Biosensors* **9,** 15 (2019).

292. Zang, Y., Lei, J., Hao, Q. & Ju, H. CdS/MoS2 heterojunction-based photoelectrochemical DNA biosensor via enhanced chemiluminescence excitation. *Biosens Bioelectron* **77**, 557–564 (2016).

293. Zhang, L. *et al.* Ag nanoclusters could efficiently quench the photoresponse of CdS quantum dots for novel energy transfer-based photoelectrochemical bioanalysis. *Biosens Bioelectron* **85**, 930–934 (2016).

294. Shu, J., Qiu, Z., Lv, S., Zhang, K. & Tang, D. Plasmonic Enhancement Coupling with Defect-Engineered TiO2-x: A Mode for Sensitive Photoelectrochemical Biosensing. *Anal Chem* **90**, 2425–2429 (2018).

295. Jun, Y.-wook *et al.* Surfactant-assisted elimination of a high energy facet as a means of controlling the shapes of TiO_2 nanocrystals. *J Am Chem Soc* **125,** 15981–15985 (2003).

296. Khan, M. A. & Mujahid, M. Recent advances in electrochemical and optical biosensors designed for detection of Interleukin 6. *Sensors* **20**, 1–27 (2020).

297. Rubin, E. J., Longo, D. L. & Baden, L. R. Interleukin-6 Receptor Inhibition in Covid-19 — Cooling the Inflammatory Soup. *New England Journal of Medicine* **384**, 1564–1565 (2021).

298. Metkar, S. K. & Girigoswami, K. Diagnostic biosensors in medicine – A review. *Biocatal Agric Biotechnol* **17**, 271–283 (2019).

299. Ronkainen, N. J. & Okon, S. L. Nanomaterial-based electrochemical immunosensors for clinically significant biomarkers. *Materials* **7**, 4669–4709 (2014).

300. Yáñez-Sedeño, P., Campuzano, S. & Pingarrón, J. M. Multiplexed electrochemical immunosensors for clinical biomarkers. *Sensors* **17**, (2017).

301. Wu, J., Fu, Z., Yan, F. & Ju, H. Biomedical and clinical applications of immunoassays and immunosensors for tumor markers. *Trends Analyt Chem* **26**, 679–688 (2007).

302. Golub, E., Pelossof, G., Freeman, R., Zhang, H. & Willner, I. Electrochemical, photoelectrochemical, and surface plasmon resonance detection of cocaine using supramolecular aptamer complexes and metallic or semiconductor nanoparticles. *Anal Chem* **81**, 9291–9298 (2009).

303. Fan, G. C., Ren, X. L., Zhu, C., Zhang, J. R. & Zhu, J. J. A new signal amplification strategy of photoelectrochemical immunoassay for highly sensitive interleukin-6 detection based on TiO_2/CdS/CdSe dual co-sensitized structure. *Biosens Bioelectron* **59**, 45–53 (2014).

304. Huo, X., Liu, P., Zhu, J., Liu, X. & Ju, H. Electrochemical immunosensor constructed using TiO2 nanotubes as immobilization scaffold and tracing tag. *Biosens Bioelectron* **85**, 698–706 (2016).

305. Yang, W. *et al.* Photoelectrochemical Glucose Biosensor Based on the Heterogeneous Facets of Nanocrystalline TiO_2/Au/Glucose Oxidase Films. *ACS Appl Nano Mater* **3**, 2723–2732 (2020).

306. Saha, S. *et al.* Differential photoelectrochemical biosensing using DNA nanospacers to modulate electron transfer between metal and semiconductor nanoparticles. *ACS Appl Mater Interfaces* **12**, 36895–36905 (2020).

307. Zhou, H., Liu, J. & Zhang, S. Quantum dot-based photoelectric conversion for biosensing applications. *Trends Analyt Chem* **67**, 56–73 (2015).

308. Huang, J., Harvey, J., Derrick Fam, W. H., Nimmo, M. A. & Alfred Tok, I. Y. Novel biosensor for interleukin-6 detection. in *Procedia Engineering* vol. 60 195–200 (Elsevier Ltd, 2013).

309. Wang, G., He, X., Chen, L., Zhu, Y. & Zhang, X. Ultrasensitive IL-6 electrochemical immunosensor based on Au nanoparticles-graphene-silica biointerface. *Colloids Surf B Biointerfaces* **116**, 714–719 (2014).

310. Zhou, W. *et al.* Control synthesis of rutile TiO_2 microspheres, nanoflowers, nanotrees and nanobelts via acid-hydrothermal method and their optical properties. *CrystEngComm* **13**, 4557–4563 (2011).

311. Su, R. *et al.* How the anatase-to-rutile ratio influences the photoreactivity of TiO_2. *J Phys Chem C* **115**, 24287–24292 (2011).

312. Swierk, J. R., Regan, K. P., Jiang, J., Brudvig, G. W. & Schmuttenmaer, C. A. Rutile TiO_2 as an Anode Material for Water-Splitting Dye-Sensitized Photoelectrochemical Cells. *ACS Energy Lett* **1**, 603–606 (2016).

313. Cho, I. S. *et al.* Branched TiO_2 Nanorods for Photoelectrochemical Hydrogen Production. *Nano Lett* **11**, 4978–4984 (2011).

314. Han, Z. *et al.* A photoelectrochemical biosensor for determination of DNA based on flower rod-like zinc oxide heterostructures. *Microchim Acta* **184**, 2541–2549 (2017).

315. Çakıroğlu, B. & Özacar, M. A Photoelectrochemical Biosensor Fabricated using Hierarchically Structured Gold Nanoparticle and MoS_2 on Tannic Acid Templated Mesoporous TiO_2. *Electroanalysis* **32**, 166–177 (2020).

316. Lindgren, T. *et al.* Aqueous photoelectrochemistry of hematite nanorod array. *Sol Energy Mater Sol Cells* **71**, 231–243 (2002).

317. Woo, S. M., Gabardo, C. M. & Soleymani, L. Prototyping of wrinkled nano-/microstructured electrodes for electrochemical DNA detection. *Anal Chem* **86**, 12341–12347 (2014).

318. Liu, A. *et al.* A novel photoelectrochemical immunosensor by integration of nanobody and ZnO nanorods for sensitive detection of nucleoside diphosphatase kinase-A. *Anal Chim Acta* **973**, 82–90 (2017).

319. Li, H. *et al.* Surface-plasmon-resonance-enhanced photoelectrochemical water splitting from au-nanoparticle-decorated 3D TiO_2 nanorod architectures. *J Phys Chem C* **121,** 12071–12079 (2017).

320. Zhao, W. W. *et al.* Acetylcholine esterase antibodies on BiOI nanoflakes/TiO_2 nanoparticles electrode: A case of application for general photoelectrochemical enzymatic analysis. *Anal Chem* **85**, 11686–11690 (2013).

321. Li, J., Li, H., Xue, Y., Fang, H. & Wang, W. Facile electrodeposition of environment-friendly Cu_2O/ZnO heterojunction for robust photoelectrochemical biosensing. *Sens Actuators B Chem* **191**, 619–624 (2014).

322. Li, W., Sheng, P., Cai, J., Feng, H. & Cai, Q. Highly sensitive and selective photoelectrochemical biosensor platform for polybrominated diphenyl ether detection using the quantum dots sensitized three-dimensional, macroporous ZnO nanosheet photoelectrode. *Biosens Bioelectron* **61**, 209–214 (2014).

323. Yan, Z., Wang, Z., Miao, Z. & Liu, Y. Dye-Sensitized and Localized Surface Plasmon Resonance Enhanced Visible-Light Photoelectrochemical Biosensors for Highly Sensitive Analysis of Protein Kinase Activity. *Anal Chem* **88**, 922–929 (2016).

324. Liu, X. P. *et al.* Photoelectrochemical immunoassay for human interleukin 6 based on the use of perovskite-type $LaFeO_3$ nanoparticles on fluorine-doped tin oxide glass. *Microchim Acta* **185**, 1–6 (2018).

325. Aydin, S. A short history, principles, and types of Elisa, and our laboratory experience with peptide/protein analyses using Elisa. *Peptides* **72,** 4–15 (2015).

326. Cinquanta, L., Fontana, D. E. & Bizzaro, N. Chemiluminescent immunoassay technology: what does it change in autoantibody detection? *Autoimmun Highlights* **8**, 9 (2017).

327. Zanut, A. *et al.* Insights into the mechanism of coreactant electrochemiluminescence facilitating enhanced bioanalytical performance. *Nat Commun* **11**, 1–9 (2020).

328. Access IL-6 Assay | Beckman Coulter. https://www.beckmancoulter.com/products/immunoassay/access-il-6-assay#/documents.

329. Elecsys® IL-6. https://diagnostics.roche.com/global/en/products/params/elecsys-il-6.html.

330. Human IL-6 Quantikine HS ELISA Kit HS600C: R&D Systems. https://www.rndsystems.com/products/human-il-6-quantikine-hs-elisa-kit_hs600c.

331. Human IL-6 ELISA Kit (ab178013) | Abcam. https://www.abcam.com/human-il-6-elisa-kit-ab178013.html?productWallTab=ShowAll.

332. IL-6 Human ELISA Kit - Invitrogen. https://www.thermofisher.com/elisa/product/IL-6-Human-ELISA-Kit/BMS213-2.

333. IL-6 (human) AlphaLISA Detection Kit, 500 Assay Points | PerkinElmer. https://www.perkinelmer.com/product/alphalisa-il6-kit-500-assay-pts-al223c.

334. Chen, X. *et al.* Signal-off Photoelectrochemical Aptasensor for S. aureus Detection Based on Graphite-like Carbon Nitride Decorated with Nickel Oxide. *Electroanalysis* **34**, 310–315 (2022).

335. Jiang, D. *et al.* Ultra-sensitive photoelectrochemical aptamer biosensor for detecting E. coli O157:H7 based on nonmetallic plasmonic two-dimensional hydrated defective tungsten oxide nanosheets coupling with nitrogen-doped graphene quantum dots (dWO3•H2O@N-GQDs). *Biosens Bioelectron* **183**, (2021).

336. Yin, M. *et al.* Paper-supported near-infrared-light-triggered photoelectrochemical platform for monitoring Escherichia coli O157:H7 based on silver nanoparticles-sensitized-upconversion nanophosphors. *Biosens Bioelectron* **203**, (2022).

337. Wang, R. *et al.* Rapid, sensitive and label-free detection of pathogenic bacteria using a bacteria-imprinted conducting polymer film-based electrochemical sensor. *Talanta* **226**, 122135 (2021).

338. Xiong, B. G. *et al.* Photoemission Electron Microscopy of TiO_2 Anatase Films Embedded with Rutile Nanocrystals**. *Adv Funct Mater* **17**, 2133–2138 (2007).

339. Zhao, B., Lin, L. & He, D. Phase and morphological transitions of titania/titanate nanostructures from an acid to an alkali hydrothermal environment. *J Mater Chem A Mater* **1**, 1659–1668 (2013).

340. A route out of resistance. *Nature Microbiology* vol. 1 Preprint at https://doi.org/10.1038/nmicrobiol.2016.89 (2016).

341. Hernando-Amado, S., Coque, T. M., Baquero, F. & Martínez, J. L. Defining and combating antibiotic resistance from One Health and Global Health perspectives. *Nat Microbiol* **4**, 1432–1442 (2019).

342. Ho, Y. P. & Muralidhar Reddy, P. Identification of pathogens by mass spectrometry. *Clin Chem* **56**, 525–536 (2010).

343. Singhal, N., Kumar, M., Kanaujia, P. K. & Virdi, J. S. MALDI-TOF mass spectrometry: An emerging technology for microbial identification and diagnosis. *Front Microbiol* **6**, 791 (2015).

344. Kaur, N. & Toley, B. J. Paper-based nucleic acid amplification tests for point-of-care diagnostics. *Analyst* **143**, 2213–2234 (2018).

345. Monis, P. T. & Giglio, S. Nucleic acid amplification-based techniques for pathogen detection and identification. *Infect Genet Evol* **6**, 2–12 (2006).

346. Pang, B. *et al.* Development of a low-cost paper-based ELISA method for rapid Escherichia coli O157:H7 detection. *Anal Biochem* **542**, 58–62 (2018).

347. Castle, L. M., Schuh, D. A., Reynolds, E. E. & Furst, A. L. Electrochemical Sensors to Detect Bacterial Foodborne Pathogens. *ACS Sensors* **6**, 1717–1730 (2021).

348. Amiri, M., Bezaatpour, A., Jafari, H., Boukherroub, R. & Szunerits, S. Electrochemical methodologies for the detection of pathogens. *ACS Sens* **3**, 1069–1086 (2018).

349. van Nevel, S. *et al.* Flow cytometric bacterial cell counts challenge conventional heterotrophic plate counts for routine microbiological drinking water monitoring. *Water Res* **113**, 191–206 (2017).

350. Tram, K., Kanda, P., Salena, B. J., Huan, S. & Li, Y. Translating bacterial detection by DNAzymes into a litmus test. *Angew Chem Int Ed* **53**, 12799–12802 (2014).

351. Ma, F. *et al.* Glycosylation of quinone-fused polythiophene for reagentless and label-free detection of E. coli. *Anal Chem* **87**, 1560–1568 (2015).

352. Mannoor, M. S. *et al.* Graphene-based wireless bacteria detection on tooth enamel. *Nat Commun* **3**, (2012).

353. Zelada-Guillén, G. A., Sebastián-Avila, J. L., Blondeau, P., Riu, J. & Rius, F. X. Label-free detection of Staphylococcus aureus in skin using real-time potentiometric biosensors based on carbon nanotubes and aptamers. *Biosens Bioelectron* **31**, 226–232 (2012).

354. Brosel-Oliu, S. *et al.* Novel impedimetric aptasensor for label-free detection of Escherichia coli O157:H7. *Sens Actuators B Chem* **255**, 2988–2995 (2018).

355. Wang, J., Leong, M. C., Leong, E. Z. W., Kuan, W. sen & Leong, D. T. Clinically Relevant Detection of Streptococcus pneumoniae with DNA-Antibody Nanostructures. *Anal Chem* **89**, 6900–6906 (2017).

356. Tiwari, I., Singh, M., Pandey, C. M. & Sumana, G. Electrochemical genosensor based on graphene oxide modified iron oxide-chitosan hybrid nanocomposite for pathogen detection. *Sens Actuators B Chem* **206**, 276–283 (2015).

357. Li, Q. *et al. Rapid and Sensitive Strategy for Salmonella Detection Using an InvA Gene-Based Electrochemical DNA Sensor*. *Int J Electrochem Sci* 7, 844-856 (2012).

358. Saha, S., Victorious, A. & Soleymani, L. Modulating the photoelectrochemical response of titanium dioxide (TiO_2) photoelectrodes using gold (Au) nanoparticles excited at different wavelengths. *Electrochim Acta* **380**, 138154 (2021).

359. Zhu, L. *et al.* A novel photoelectrochemical aptamer sensor based on CdTe quantum dots enhancement and exonuclease I-assisted signal amplification for Listeria monocytogenes detection. *Foods* **10**, 2896 (2021).

360. Yang, Z., Wang, Y. & Zhang, D. An integrated multifunctional photoelectrochemical platform for simultaneous capture, detection, and inactivation of pathogenic bacteria. *Sens Actuators B Chem* **274**, 228–234 (2018).

361. Yang, Z., Wang, Y., Zhang, D. & Chen, C. A sensitizing photoelectrochemical sensing platform strategy based on bio-etching preparation of Bi_2S_3/BiOCl p–n heterojunction. *Talanta* **190**, 357–362 (2018).

362. Yang, Z., Wang, Y. & Zhang, D. A novel signal-on photoelectrochemical sensing platform based on biosynthesis of CdS quantum dots sensitizing ZnO nanorod arrays. *Sens Actuators B Chem* **261**, 515–521 (2018).

363. Zhang, W., Feng, Q., Chang, D., Tram, K. & Li, Y. In vitro selection of RNA-cleaving DNAzymes for bacterial detection. *Methods* **106**, 66–75 (2016).

364. Ali, M. M., Aguirre, S. D., Lazim, H. & Li, Y. Fluorogenic DNAzyme probes as bacterial indicators. *Angew Chem Int Ed* **50**, 3751–3754 (2011).

365. Zaouri, N., Cui, Z., Peinetti, A. S., Lu, Y. & Hong, P.-Y. DNAzyme-based biosensor as a rapid and accurate verification tool to complement simultaneous enzyme-based media for *E. coli* detection. *Environmental Science: Water Research & Technology* **5,** 2260–2268 (2019).

366. Kobayashi, M., Petrykin, V., Kakihana, M. & Tomita, K. Hydrothermal synthesis and photocatalytic activity of whisker-like rutile-type titanium dioxide. *J Am Ceram Soc* **92**, S21-S26 (2009).

367. Cano-Casanova, L., Amorós-Pérez, A., Ouzzine, M., Lillo-Ródenas, M. A. & Román-MartİNez, M. C. One step hydrothermal synthesis of TiO_2 with variable HCl concentration: Detailed characterization and photocatalytic activity in propene oxidation. *Appl Catal B* **220**, 645–653 (2018).

368. Zhitomirsky, I. & Gal-Or, L. Cathodic Electrosynthesis of Ceramic Deposits. *J Eur Ceram Soc* **16**, 819–824 (1996).

369. Džunuzović, E. S. *et al.* Influence of surface modified TiO_2 nanoparticles by gallates on the properties of PMMA/TiO_2 nanocomposites. *Eur Polym J* **48**, 1385–1393 (2012).

370. Wu, M. *et al.* Sol-Hydrothermal Synthesis and Hydrothermally Structural Evolution of Nanocrystal Titanium Dioxide. *Chem Mater* **14**, 1974–1980 (2002).

371. Zhang, Z., Ouyang, Y., Cheng, Y., Chen, J. & Li, N. Size-dependent phononic thermal transport in low-dimensional nanomaterials. *Phys Rep* **860**, 1–26 (2020).

372. Warnan, J. *et al.* A compact diketopyrrolopyrrole dye as efficient sensitizer in titanium dioxide dye-sensitized solar cells. *J Photochem Photobiol A Chem* **226**, 9–15 (2011).

373. Tachan, Z., Hod, I. & Zaban, A. The TiO_2-catechol complex: Coupling type II sensitization with efficient catalysis of water oxidation. *Adv Energy Mater* **4**, (2014).

374. Skliri, E., Vanvasakis, I., Papadas, I. T., Choulis, S. A. & Armatas, G. S. Mesoporous Composite Networks of Linked MnFeO4 and Reduction of Cr(VI). *Catalysts* **11**, 199 (2021).

375. Traynor, S. M., Wang, G. A., Pandey, R., Li, F. & Soleymani, L. Dynamic Bio-Barcode Assay Enables Electrochemical Detection of a Cancer Biomarker in Undiluted Human Plasma: A Sample-In-Answer-Out Approach. *Angew Chem* **132**, 22806–22811 (2020).

376. Shahraki, A. H., Chaganti, S. R. & Heath, D. D. Diel Dynamics of Freshwater Bacterial Communities at Beaches in Lake Erie and Lake St. Clair, Windsor, Ontario. *Microb Ecol* **81**, 1–13 (2021).

377. Anastasi, E. M., Matthews, B., Stratton, H. M. & Katouli, M. Pathogenic Escherichia coli found in sewage treatment plants and environmental waters. *Appl Environ Microbiol* **78**, 5536–5541 (2012).

378. Navab-Daneshmand, T. *et al.* Escherichia coli contamination across multiple environmental compartments (soil, hands, drinking water, and handwashing water) in urban Harare: Correlations and risk factors. *Am J Trop Med Hygiene* **98**, 803–813 (2018).

379. Rant, U. Binding Theory Equations for Affinity and Kinetics Analysis. *Dynamic Biosensors* **1**, 1–6 (2017).

380. Quinn, J. G. A rebinding-assay for measuring extreme kinetics using label-free biosensors. *Sci Rep* **11**, 1–14 (2021).

381. Zhang, Q. *et al.* Smartphone-based photoelectrochemical biosensing system with graphitic carbon nitride/gold nanoparticles modified electrodes for matrix metalloproteinase-2 detection. *Biosens Bioelectron* **193**, 113572 (2021).

382. Aguirre, S. D., Ali, M. M., Salena, B. J. & Li, Y. A Sensitive DNA Enzyme-Based Fluorescent Assay for Bacterial Detection. *Biomolecules* **3**, 563–577 (2013).

383. *United States Environmental Protection Agency. Method 1603: Escherichia coli (E. coli) in Water by Membrane Filtration Using Modified membrane-Thermotolerant Escherichia coli Agar (Modified mTEC). https://www.epa.gov/sites/default/files/2015-08/documents/method_1603_2009.pdf (2014).*

384. Gadagkar, S. R. & Call, G. B. Computational tools for fitting the Hill equation to dose-response curves. *J Pharmacol Toxicol Methods* **71**, 68–76 (2015).

385. Gesztelyi, R. *et al.* The Hill equation and the origin of quantitative pharmacology. *Arch Hist Exact Sci* **66**, 427–438 (2012).

386. Stefan, M. I. & le Novère, N. Cooperative Binding. *PLoS Comput Biol* **9**, 2–7 (2013).

387. Armbruster, D. A. & Pry, T. Limit of Blank , Limit of Detection and Limit of Quantitation. *Clin Biochem Rev* **29**, 49–52 (2008).

388. Bohunicky, B. & Mousa, S. A. Biosensors: The new wave in cancer diagnosis. *Nanotechnol Sci Appl* **4**, 1–10 (2011).

389. Arakawa, T., Dao, D. V. & Mitsubayashi, K. Biosensors and Chemical Sensors for Healthcare Monitoring: A Review. *IEEJ Trans Electr Electron Eng* **17**, 626–636 (2022).

390. Bohunicky, B. & Mousa, S. A. Biosensors: The new wave in cancer diagnosis. *Nanotechnol Sci and Appl* **4**, 1–10 (2011).

391. Saha, S. *et al.* Two-Step Competitive Hybridization Assay: A Method for Analyzing Cancer-Related microRNA Embedded in Extracellular Vesicles. *Anal Chem* **93**, 15913–15921 (2021).

392. Zhang, L., Loh, X. J. & Ruan, J. Photoelectrochemical nanosensors: An emerging technique for tumor liquid biopsy. *J Photochem Photobiol A Chem* **429**, 113942 (2022).

393. Shi, J. *et al.* Photoelectrochemical biosensing platforms for tumor marker detection. *Coord Chem Rev* **469**, 214675 (2022).

394. Ma, X., Wang, C., Wu, F., Guan, Y. & Xu, G. TiO_2 Nanomaterials in Photoelectrochemical and Electrochemiluminescent Biosensing. *Topics in Current Chemistry* 378, 1-17 (2020).

395. Saha, S., Victorious, A. & Soleymani, L. Modulating the photoelectrochemical response of titanium dioxide (TiO2) photoelectrodes using gold (Au) nanoparticles excited at different wavelengths. *Electrochim Acta* **380**, 138154 (2021).

396. Gan, W., Xu, B. & Dai, H. L. Activation of thiols at a silver nanoparticle surface. *Angew Chem Int Ed* **50**, 6622–6625 (2011).

397. Wang, X. *et al.* Silver-Decorated TiO_2 Nanorod Array Films with Enhanced Photoelectrochemical and Photocatalytic Properties. *J Electrochem Soc* **163**, H943–H950 (2016).

398. Chen, K. *et al.* Effect of Ag nanoparticle size on the photoelectrochemical properties of Ag decorated TiO_2 nanotube arrays. *J Alloys Compd* **554**, 72–79 (2013).

399. Temerov, F. *et al.* Silver-Decorated TiO2Inverse Opal Structure for Visible Light-Induced Photocatalytic Degradation of Organic Pollutants and Hydrogen Evolution. *ACS Appl Mater Interfaces* **12**, 41200–41210 (2020).

400. Guin, D., Manorama, S. v., Latha, J. N. L. & Singh, S. Photoreduction of silver on bare and colloidal TiO_2 nanoparticles/nanotubes: Synthesis, characterization, and tested for antibacterial outcome. *J Phys Chem C* **111**, 13393–13397 (2007).

401. Wahyuni, E. T. & Roto, R. Silver nanoparticle incorporated titanium oxide for bacterial inactivation and Dye degradation. *Titanium Dioxide - Material for a Sustainable Environment* (2018). doi:10.5772/intechopen.75918

402. Sirivallop, A., Areerob, T. & Chiarakorn, S. Enhanced visible light photocatalytic activity of N and Ag doped and co-doped TiO_2 synthesized by using an in-situ solvothermal method for gas phase ammonia removal. *Catalysts* **10**, 251 (2020).

403. Assaud, L. *et al.* Atomic Layer Deposition of Pd Nanoparticles on TiO_2 Nanotubes for Ethanol Electrooxidation: Synthesis and Electrochemical Properties. *ACS Appl Mater Interfaces* **7**, 24533–24542 (2015).

404. Salman Hamdi, S. Synthesis of Ag-TiO_2 Thin Films by Spin Coating process. *Eng Tech J* **34**, 13 (2016).

405. Temerov, F., Ankudze, B. & Saarinen, J. J. TiO2 inverse opal structures with facile decoration of precious metal nanoparticles for enhanced photocatalytic activity. *Mater Chem Phys* **242**, (2020).

406. Chen, Z. *et al.* Inverse opal structured Ag/TiO2 plasmonic photocatalyst prepared by pulsed current deposition and its enhanced visible light photocatalytic activity. *J Mater Chem A Mater* **2**, 824–832 (2014).

407. Bakhshandeh, F., Saha, S., Sakib, S., Zhitomirsky, I. & Soleymani, L. TiO_2 Nanoparticles Co-Sensitized with Graphene Quantum Dots and Pyrocatechol Violet for Photoelectrochemical Detection of Cr(VI). *J Electrochem Soc* **169**, 057520 (2022).

408. Quirico, L. & Orso, F. The power of microRNAs as diagnostic and prognostic biomarkers in liquid biopsies. *Cancer* **3**, 117–139 (2020).

409. Rapisuwon, S., Vietsch, E. E. & Wellstein, A. Circulating biomarkers to monitor cancer progression and treatment. *Comput Struct Biotechnol J* **14**, 211–222 (2016).

410. Jansson, M. D. & Lund, A. H. MicroRNA and cancer. *Mol Oncol* **6**, 590–610 (2012).

411. Schwarzenbach, H., Nishida, N., Calin, G. A. & Pantel, K. Clinical relevance of circulating cell-free microRNAs in cancer. *Nat Rev Clin Oncol* **11**, 145–156 (2014).

412. Tkach, M. & Théry, C. Communication by Extracellular Vesicles: Where We Are and Where We Need to Go. *Cell* **164**, 1226–1232 (2016).

413. ben Saber, N., Mezni, A., Alrooqi, A. & Altalhi, T. A review of ternary nanostructures based noble metal/semiconductor for environmental and renewable energy applications. *J Mater Res Technol* **9**, 15233–15262 (2020).

414. Ohtani, B., Prieto-Mahaney, O. O., Li, D. & Abe, R. What is Degussa (Evonic) P25? Crystalline composition analysis, reconstruction from isolated pure particles and photocatalytic activity test. *J Photochem Photobiol A Chem* **216**, 179–182 (2010).

415. Chakraborty, I. *et al.* Novel hexagonal polytypes of silver: Growth, characterization and first-principles calculations. *J Phys Condens Matter* **23**, 325401 (2011).

416. Ata, M. S., Milne, J. & Zhitomirsky, I. Fabrication of Mn_3O_4–carbon nanotube composites with high areal capacitance using cationic and anionic dispersants. *J Colloid Interface Sci* **512**, 758–766 (2018).

417. Huang, X., Bao, X., Liu, Y., Wang, Z. & Hu, Q. Catechol-Functional Chitosan/Silver Nanoparticle Composite as a Highly Effective Antibacterial Agent with Species-Specific Mechanisms. *Sci Rep* **7**, 1860 (2017).

418. Black, K. C. L., Liu, Z. & Messersmith, P. B. Catechol redox induced formation of metal core-polymer shell nanoparticles. *Chem Mater* **23**, 1130–1135 (2011).

419. Liu, G. *et al.* Fabrication of silver nanoparticle sponge leather with durable antibacterial property. *J Colloid Interface Sci* **514**, 338–348 (2018).

420. Li, L. *et al.* Phase Engineering of a Ruthenium Nanostructure toward High-Performance Bifunctional Hydrogen Catalysis. *ACS Nano 14885-14894* (2022).

421. Yu, H. *et al.* Tracking Nanoparticle Degradation across Fuel Cell Electrodes by Automated Analytical Electron Microscopy. *ACS Nano* **16**, 19 (2022).

422. Timakwe, S., Silwana, B. & Matoetoe, M. C. Electrochemistry as a Complementary Technique for Revealing the Influence of Reducing Agent Concentration on AgNPs. *ACS Omega* **7**, 4921–4931 (2022).

423. Dong, R. *et al.* Towards ultra small noble metal nanoparticles: Testing Jellium model for ligand protected copper and silver M13 core nanoparticles. *Physical Chemistry Chemical Physics* **13**, 3274–3280 (2011).

424. Blackman, G. N. & Genov, D. A. Bounds on quantum confinement effects in metal nanoparticles. *Phys Rev B* **97**, 115440 (2018).

425. Doménech-Carbó, A., Galian, R. E., Aguilera-Sigalat, J. & Pérez-Prieto, J. Electrochemistry of metal nanoparticles and quantum dots. in *Handbook of Nanoparticles* 715–743 (Springer International Publishing, 2015). doi:10.1007/978-3-319-15338-4_28.

426. Scanlon, M. D., Peljo, P., Méndez, M. A., Smirnov, E. & Girault, H. H. Charging and discharging at the nanoscale: Fermi level equilibration of metallic nanoparticles. *Chem Sci* **6**, 2705–2720 (2015).

427. Kooh, M. R. R., Yoong, V. N. & Ekanayake, P. Density functional theory (DFT) and time-dependent density functional theory (TDDFT) studies of selected ancient colourants as sensitizers in dye-sensitized solar cells. *J Natl Sci Found* **42**, 169–175 (2014).

428. Zouzelka, R. & Rathousky, J. Photocatalytic abatement of NOx pollutants in the air using commercial functional coating with porous morphology. *Appl Catal B* **217**, 466–476 (2017).

429. Khanam, S. & Rout, S. K. A Photocatalytic Hydrolysis and Degradation of Toxic Dyes by Using Plasmonic Metal–Semiconductor Heterostructures: A Review. *Chemistry* **4**, 454–479 (2022).

430. Vezzoli, A., Brooke, R. J., Higgins, S. J., Schwarzacher, W. & Nichols, R. J. Single-Molecule Photocurrent at a Metal-Molecule-Semiconductor Junction. *Nano Lett* **17**, 6702–6707 (2017).

431. Liu, Y., Ma, H., Han, X. X. & Zhao, B. Metal-semiconductor heterostructures for surface-enhanced Raman scattering: Synergistic contribution of plasmons and charge transfer. *Mater Horizons* **8**, 370–382 (2021).

432. Zhang, C., Qiao, F., Wan, J. & zi, J. Enlargement of nontransmission frequency range in photonic crystals by using multiple heterostructures. *J Appl Phys* **87**, 3174–3176 (2000).

433. Pokhrel, S., Waters, B., Felton, S., Huang, Z. F. & Nadgorny, B. Percolation in metal-insulator composites of randomly packed spherocylindrical nanoparticles. *Phys Rev B* **103**, 134110 (2021).

434. Pacchioni, G. A not-so-strong bond. *Nat Rev Mater* **4**, 226 (2019).

435. Steinbrück, A. *et al.* Gold-silver and silver-silver nanoparticle constructs based on DNA hybridization of thiol- and amino-functionalized oligonucleotides. *J Biophotonics* **1**, 104–113 (2008).

436. Ramirez-Garrastacho, M. *et al.* Extracellular vesicles as a source of prostate cancer biomarkers in liquid biopsies: a decade of research. *Br J Cancer* **126**, 331-350(2021).

437. Sarigul, N., Korkmaz, F. & Kurultak, İ. A New Artificial Urine Protocol to Better Imitate Human Urine. *Sci Rep* **9**, 20159 (2019).

438. de Souza, M. F. *et al.* Circulating mRNAs and miRNAs as candidate markers for the diagnosis and prognosis of prostate cancer. *PLoS One* **12**, e0184094 (2017).

439. Salido-Guadarrama, A. I. *et al.* Urinary microRNA-based signature improves accuracy of detection of clinically relevant prostate cancer within the prostate-specific antigen grey zone. *Mol Med Rep* **13**, 4549–4560 (2016).

440. Armbruster, D. A. & Pry, T. Limit of Blank , Limit of Detection and Limit of Quantitation. *Clinical Biochemist Reviews* **29**, 49–52 (2008).

441. Yagura, T., Makita, K., Yamamoto, H., Menck, C. F. M. & Schuch, A. P. Biological sensors for solar ultraviolet radiation. *Sensors* **11**, 4277–4294 (2011).

442. Mehrotra, P. Biosensors and their applications - A review. *J Oral Biol Craniofac Res* **6**, 153–159 (2016).

443. Hosseini, A. *et al.* Roadmap to the Bioanalytical Testing of COVID-19: From Sample Collection to Disease Surveillance. *ACS Sens* **5**, 3328–3345 (2020).

444. Pandey, R. *et al.* Integrating programmable DNAzymes with electrical readout for rapid and culture-free bacterial detection using a handheld platform. *Nat Chem* **13**, 895-901(2021).

445. Beltrán Lopez, A. P. DNA Biosensors and Biomarkers to Cancer Detection. *Int J Biosens Bioelectron* **4**, 20–21 (2018).

446. Traynor, S. M. *et al.* Review—Recent Advances in Electrochemical Detection of Prostate Specific Antigen (PSA) in Clinically-Relevant Samples. *J Electrochem Soc* **167**, 037551 (2020).

447. Khan, M. A. & Mujahid, M. Recent advances in electrochemical and optical biosensors designed for detection of Interleukin 6. *Sensors* **20**, 1–27 (2020).

448. Metkar, S. K. & Girigoswami, K. Diagnostic biosensors in medicine – A review. *Biocatal Agric Biotechnol* **17**, 271–283 (2019).

449. Bianchi, V. *et al.* A self-calibrating IOT portable electrochemical immunosensor for serum human epididymis protein 4 as a tumor biomarker for ovarian cancer. *Sensors* **20**, (2020).

450. King, K. R. *et al.* Point-of-Care Technologies for Precision Cardiovascular Care and Clinical Research: National Heart, Lung, and Blood Institute Working Group. *JACC Basic Transl Sci* **1**, 73–86 (2016).

451. Harpaz, D., Eltzov, E., Seet, R. C. S., Marks, R. S. & Tok, A. I. Y. Point-of-care-testing in acute stroke management: An unmet need ripe for technological Harvest. *Biosensors* **7**, 30 (2017).

452. Quinchia, J., Echeverri, D., Cruz-Pacheco, A. F., Maldonado, M. E. & Orozco, J. A. Electrochemical biosensors for determination of colorectal tumor biomarkers. *Micromachines* **11**, 1–46 (2020).

453. Cesewski, E. & Johnson, B. N. Electrochemical biosensors for pathogen detection. *Biosens Bioelectron* **159**, 112214 (2020).

454. Cesewski, E. & Johnson, B. N. Electrochemical biosensors for pathogen detection. *Biosens Bioelectron* **159**, 112214 (2020).

455. Saha, S. *et al.* Differential photoelectrochemical biosensing using DNA nanospacers to modulate electron transfer between metal and semiconductor nanoparticles. *ACS Appl Mater Interfaces* **12**, 36895–36905 (2020).

456. Sakib, S., Bakhshandeh, F., Saha, S., Soleymani, L. & Zhitomirsky, I. Surface Functionalization of Metal Oxide Semiconductors with Catechol Ligands for Enhancing Their Photoactivity. *Solar RRL* **5**, 2100512 (2021).

457. Victorious, A., Saha, S., Pandey, R., Didar, T. F. & Soleymani, L. Affinity-Based Detection of Biomolecules Using Photo-Electrochemical Readout. *Front Chem* **7**, 617 (2019).

458. Sakib, S., Pandey, R., Soleymani, L. & Zhitomirsky, I. Surface modification of TiO_2 for photoelectrochemical DNA biosensors. *Med Devices Sens* **3**, (2020).

459. Roy, S. & Gao, Z. Nanostructure-based electrical biosensors. *Nano Today* **4**, 318–334 (2009).

460. Chalklen, T., Jing, Q. & Kar-Narayan, S. Biosensors based on mechanical and electrical detection techniques. *Sensors* **20**, 26–37 (2020).

461. Chen, J. X. *et al.* A Dynamic DNA Machine via Free Walker Movement on Lipid Bilayer for Ultrasensitive Electrochemiluminescent Bioassay. *Anal Chem* **91**, 14125–14132 (2019).

462. Escobedo, P. *et al.* General-purpose passive wireless point–of–care platform based on smartphone. *Biosens Bioelectron* **141**, 1–23 (2019).

463. Arlett, J. L., Myers, E. B. & Roukes, M. L. Comparative advantages of mechanical biosensors. *Nat Nanotechnol* **6**, 203–215 (2011).

464. Vigneshvar, S., Sudhakumari, C. C., Senthilkumaran, B. & Prakash, H. Recent advances in biosensor technology for potential applications - an overview. *Front Bioeng Biotechnol* **4**, 1–9 (2016).

465. Zhao, W. W., Xu, J. J. & Chen, H. Y. Photoelectrochemical Immunoassays. *Anal Chem* **90**, 615–627 (2018).

466. Saha, S., Chan, Y. & Soleymani, L. Enhancing the Photoelectrochemical Response of DNA Biosensors Using Wrinkled Interfaces. *ACS Appl Mater Interfaces* **10**, 31178–31185 (2018).

467. Zhao, W. W., Xu, J. J. & Chen, H. Y. Photoelectrochemical DNA biosensors. *Chem Rev* **114**, 7421–7441 (2014).

468. Devadoss, A., Sudhagar, P., Terashima, C., Nakata, K. & Fujishima, A. Photoelectrochemical biosensors: New insights into promising photoelectrodes and signal amplification strategies. *J Photochem Photobiol C Photochem Rev* **24**, 43–63 (2015).

469. Sakib, S., Hosseini, A., Zhitomirsky, I. & Soleymani, L. Photoelectrochemical IL-6 Immunoassay Manufactured on Multifunctional Catecholate-Modified TiO_2 Scaffolds. *ACS Appl Mater Interfaces* **13**, 50851-50861 (2021).

470. Yagura, T., Makita, K., Yamamoto, H., Menck, C. F. M. & Schuch, A. P. Biological sensors for solar ultraviolet radiation. *Sensors* **11**, 4277–4294 (2011).

471. Zhang, X., Zhao, Y., Li, S. & Zhang, S. Photoelectrochemical biosensor for detection of adenosine triphosphate in the extracts of cancer cells. *Chem Comm* **46**, 9173–9175 (2010).

472. Wang, W., Bao, L., Lei, J., Tu, W. & Ju, H. Visible light induced photoelectrochemical biosensing based on oxygen-sensitive quantum dots. *Anal Chim Acta* **744**, 33–38 (2012).

473. Zhang, X. *et al.* Synthesis of CdS quantum dots decorated graphene nanosheets and non-enzymatic photoelectrochemical detection of glucose. *Electrochim Acta* **133**, 615–622 (2014).

474. Yue, Z. *et al.* Quantum-dot-based photoelectrochemical sensors for chemical and biological detection. *ACS Appl Mater Interfaces* **5**, 2800–2814 (2013).

475. Sabir, N. *et al.* Photo-electrochemical Bioanalysis of Guanosine Monophosphate Using Coupled Enzymatic Reactions at a CdS/ZnS Quantum Dot Electrode. *Small* **11**, 5844–5850 (2015).

476. Zhang, X. *et al.* A new signal-on photoelectrochemical biosensor based on a graphene/quantum-dot nanocomposite amplified by the dual-quenched effect of bipyridinium relay and AuNPs. *Chem Eur J* **18**, 16411–16418 (2012).

477. Li, Z. *et al.* Carbon dots based photoelectrochemical sensors for ultrasensitive detection of glutathione and its applications in probing of myocardial infarction. *Biosens Bioelectron* **99**, 251–258 (2018).

478. Altenschmidt, L. *et al.* Aerogelation of Polymer-Coated Photoluminescent, Plasmonic, and Magnetic Nanoparticles for Biosensing Applications. *ACS Appl Nano Mater* **4**, 6678–6688 (2021).

479. Zhao, S. *et al.* Introducing visible-light sensitivity into photocatalytic CeO2nanoparticles by hybrid particle preparation exploiting plasmonic properties of gold: Enhanced photoelectrocatalysis exemplified for hydrogen peroxide sensing. *Nanoscale* **13**, 980–990 (2021).

480. Riedel, M., Höfs, S., Ruff, A., Schuhmann, W. & Lisdat, F. A Tandem Solar Biofuel Cell: Harnessing Energy from Light and Biofuels. *Angew Chem* **133**, 2106–2111 (2021).

481. Lahav, M. *et al.* Photoelectrochemistry with integrated photosensitizer-electron acceptor and Au-nanoparticle arrays. *J Am Chem Soc* **122**, 11480–11487 (2000).

482. Kongkanand, A., Domınguez, R. M. & Kamat, P. V. Single Wall Carbon Nanotube Scaffolds for Photoelectrochemical Solar Cells. Capture and Transport of Photogenerated Electrons. *Nano Lett* **7**, 676–680 (2007).

483. Parker, S. G. *et al.* A photoelectrochemical platform for the capture and release of rare single cells. *Nat Commun* **9**, 2288 (2018).

484. Zhang, J., Bang, J. H., Tang, C. & Kamat, P. V. Tailored TiO_2-$SrTiO_3$ heterostructure nanotube arrays for improved photoelectrochemical performance. *ACS Nano* **4**, 387–395 (2010).

485. Palmsens. Palmsens 4 - Palmsens. https://www.palmsens.com/product/palmsens4/ (2021).

486. Palmsens. Sensit Smart - Palmsens.

487. Dryden, M. D. M. & Wheeler, A. R. DStat: A versatile, open-source potentiostat for electroanalysis and integration. *PLoS One* **10**, 1–17 (2015).

488. Zhang, Q. *et al.* Smartphone-based photoelectrochemical biosensing system with graphitic carbon nitride/gold nanoparticles modified electrodes for matrix metalloproteinase-2 detection. *Biosens Bioelectron* **193**, 113572 (2021).

489. Rowe, A. A. *et al.* Cheapstat: An open-source, 'do-it-yourself' potentiostat for analytical and educational applications. *PLoS One* **6**, e23783 (2011).

490. Ainla, A. *et al.* Open-Source Potentiostat for Wireless Electrochemical Detection with Smartphones. *Anal Chem* **90**, 6240–6246 (2018).

491. Sun, A., Wambach, T., Venkatesh, A. G. & Hall, D. A. A low-cost smartphone-based electrochemical biosensor for point-of-care diagnostics. in *IEEE 2014 Biomedical Circuits and Systems Conference, BioCAS 2014 - Proceedings* (2014). doi:10.1109/BioCAS.2014.6981725.

492. Sun, A. C. & Hall, D. A. Point-of-Care Smartphone-based Electrochemical Biosensing. *Electroanalysis* **31**, 2–16 (2019).

493. Feuerstein, D., Parker, K. H. & Boutelle, M. G. Practical methods for noise removal: Applications to spikes, nonstationary quasi-periodic noise, and baseline drift. *Anal Chem* **81**, 4987–4994 (2009).

494. Gonçalves, W. D., Lanfredi, A. J. C. & Crespilho, F. N. Development of numerical methods for signal smoothing and noise modeling in single wire-based electrochemical biosensors. *Journal of Physical Chemistry C* **115**, 16172–16179 (2011).

495. Acharya, D., Rani, A., Agarwal, S. & Singh, V. Application of adaptive Savitzky–Golay filter for EEG signal processing. *Perspect Sci* **8**, 677–679 (2016).

496. Tsujiko, A. *et al.* Observation of cathodic photocurrents at nanocrystalline TiO2 film electrodes, caused by enhanced oxygen reduction in alkaline solutions. *J Phys Chem B* **106**, 5878–5885 (2002).

497. Dumortier, M., Bosserez, T., Rongé, J., Martens, J. A. & Haussener, S. Combined Experimental-Numerical Analysis of Transient Phenomena in a Photoelectrochemical Water Splitting Cell. *J Phys Chem C* **120**, 3705–3714 (2016).

498. Changshi, L. Energy and charge conservation during photo capacitance-voltage. *Energy* **214**, 118899 (2021).

499. Dryden, M. D. M. & Wheeler, A. R. DStat: A versatile, open-source potentiostat for electroanalysis and integration. *PLoS One* **10**, e0140349 (2015).

500. Sun, A., Wambach, T., Vengkatesh, A. G. & Hall, D. A. A Low-Cost Smartphone-Based Electrochemical Biosensor for Point-of-Care Diagnostics. in *2014 IEEE Biomedical Circuits and Systems Conference (BioCAS) Proceedings* (2014).

501. Palmsens. Palmsens 4 - Palmsens. https://www.palmsens.com/product/palmsens4/ (2021).

502. Palmsens. Sensit Smart - Palmsens.

503. Finkelstein-Shapiro, D. *et al.* Direct Evidence of Chelated Geometry of Catechol on TiO2 by a Combined Solid-State NMR and DFT Study. *J Phys Chem C* **120**, 23625–23630 (2016).

504. Wen, G. & Ju, H. Enhanced photoelectrochemical proximity assay for highly selective protein detection in biological matrixes. *Anal Chem* **88**, 8339–8345 (2016).

505. Fu, B. & Zhang, Z. Periodical 2D Photonic–Plasmonic Au/TiOx Nanocavity Resonators for Photoelectrochemical Applications. *Small* **14**, (2018).

506. Pang, X. *et al.* Photoelectrochemical Cytosensing of RAW264.7 Macrophage Cells Based on a TiO2 Nanoneedls@MoO3 Array. *Anal Chem* **89**, 7950–7957 (2017).

507. Ali, M. M., Aguirre, S. D., Lazim, H. & Li, Y. Fluorogenic DNAzyme probes as bacterial indicators. *Angew Chem Int Ed* **50**, 3751–3754 (2011).

508. Masud, S. *et al.* Photoreduction of metallic co-catalysts onto novel semiconducting metal oxides. in *Mater Sci Eng B Solid State Mater Adv Technol* **174**, 66–70 (2010).

509. Bahrmann, P. *et al.* Multiple biomarker strategy for improved diagnosis of acute heart failure in older patients presenting to the emergency department. *Eur Heart J Acute Cardiovasc Care* **4**, 137–147 (2015).

510. Nozaki, T. *et al.* Significance of a Multiple Biomarkers Strategy Including Endothelial Dysfunction to Improve Risk Stratification for Cardiovascular Events in Patients at High Risk for Coronary Heart Disease. *J Am Coll Cardiol* **54**, 601–608 (2009).

511. Cui, F., Yue, Y., Zhang, Y., Zhang, Z. & Zhou, H. S. Advancing Biosensors with Machine Learning. *ACS Sens* **5**, 3346–3364 (2020).

512. Shetti, N. P. *et al.* Skin-Patchable Electrodes for Biosensor Applications: A Review. *ACS Biomater Sci Eng* **6**, 1823–1835 (2020).

513. Zheng, H. *et al.* Hydrogel Microneedle-Assisted Assay Integrating Aptamer Probes and Fluorescence Detection for Reagentless Biomarker Quantification. *ACS Sens* **7**, 2387–2399 (2022).

514. Cozma, I., McConnell, E. M., Brennan, J. D. & Li, Y. DNAzymes as key components of biosensing systems for the detection of biological targets. *Biosens Bioelectron* **177**, (2021).

515. Young, J. L. *et al.* Direct solar-to-hydrogen conversion via inverted metamorphic multi-junction semiconductor architectures. *Nat Energy* **2**, (2017).